Theoretical Investigation of Compounds with Triple Bonds

Dissertation

zur

Erlangung des Doktorgrades

der Naturwissenschaften

(Dr. rer. nat.)

dem

Fachbereich Chemie

der Philipps-Universität Marburg

vorgelegt von

Deepa Devarajan

aus Puthupatti/Indien

Marburg/Lahn 2011

Vom Fachbereich Chemie der Philipps-Universität Marburg
als Dissertation angenommen am 05.07.2011

Erstgutachter	Professor Dr. Gernot Frenking
Zweitgutachter	Dr. Ralf Tonner
Tag der mündlichen Prüfung:	07.07.2011

To

My Parents

Preface

This thesis presents my work at the Department of Chemistry, the Philipps University of Marburg, Germany. This study has been carried out from August 2008 until May 2011, under the supervision of Professor Dr. Gernot Frenking.

I would like to thank Prof. Frenking for his continuous support, guidance, encouragement, and discussions on my research projects. My special thanks go to Thomas Reuter, Gerda Jansonius, Susanne Klein, Nozomi Takagi, Moritz von Hopffgarten, Nicole Holzmann, Shimizu Takayasu, and all the members of the group, "AK Frenking", for their kind help and support.

Thanks to Dr. Rosalyne Cowie for her invaluable effort in correcting this thesis.

I thank my teachers Prof. D. Vimala Devi and Prof. P. Venuvanalingam for their support, encouragement, and inspiring lectures during the days of my Bachelor and Master Degrees, which motivated me to continue on to study a Ph.D. in the field of chemistry.

My heartfelt thanks go to my friends Karthik, Shanthi, Nhung, and Fereshteh and all of my family members for their moral support and encouragement during my stay in Marburg.

I thank the Deutsche Forschungsgemeinschaft (DFG) for the financial assistance.

Deepa Devarajan

Abstract

In this thesis, compounds with potential triple-bonding character involving the heavier main-group elements, Group 4 transition metals, and the actinides uranium and thorium were studied by using molecular quantum mechanics. The triple bonds are described in terms of the individual orbital contributions (σ, $\pi_{\parallel}$, and $\pi_{\perp}$), involving electron-sharing covalent or donor–acceptor interactions between the orbitals of two atoms or fragments. Energy decomposition, natural bond orbital, and atoms in molecules analyses were used for the bonding analysis of the triple bonds. The results of this thesis suggest that the triple-bonding character between the heavier elements of the periodic table is important and worth further study and exploration.

Zusammenfassung

In dieser Dissertation wurden Moleküle der schwereren Hauptgruppenelemente, der Übergangsmetalle der 4. Gruppe und der Actinoide Uran und Thorium auf mögliche Element-Element-Dreifachbindungen hin mit quantenchemischen Methoden überprüft.

Die einzelnen Komponenten der Dreifachbindungen (σ, $\pi_{\perp}$ und $\pi_{\parallel}$) werden dabei entweder als Elektronenpaarbindung oder als Donor-Akzeptor-Bindungen beschrieben. Dazu wurden diese Bindungen wurden mit der Energiedekompositionsanalyse (EDA), der natürlichen Bindungsorbitalanalyse (NBO) und der Quantentheorie der Atome in Molekülen (AIM) untersucht.

Die Ergebnisse dieser Untersuchungen zeigen, dass auch zwischen den schwereren Elementen Bindungen mit nicht zu vernachlässigendem Dreifachbindungscharakter existieren, die auch in Zukunft Teil der Forschung auf dem Gebiet der Bindungsanalyse sein sollten.

Table of Contents

1. Introduction

A triple bond is a chemical bond in which three pairs of electrons are shared between two atoms, for example, H–C≡C–H, N≡N, H–C≡N, C≡O, and C≡S. Acetylene, C_2H_2, is a linear molecule with a CC triple bond. However, the heavier homologues of acetylene, E_2H_2 (E = Si – Pb), have been reported to adopt different equilibrium geometries. The unusual structures of E_2H_2 (E = Si – Pb) were explained by Frenking et al.[1] The chemistry of the triple bond involving the heavier main-group elements[2] is a topic of interest to both synthetic and theoretical chemists. There have been a number of compounds reported with triple-bonding character involving the heavier main-group elements. However, a discussion about these compounds is beyond the scope of this introduction and readers are invited to refer to the review articles by Power and Fischer.[2] This thesis focuses on some of the smaller molecules with potential triple-bonding character that are (or could be) characterized by using spectroscopic techniques.

Hydrogen cyanide is a linear molecule with a CN triple bond. Hydrogen cyanide (HCN) and its isomer, hydrogen isocyanide (HNC), are astronomically interesting molecules.[3] HCN is more stable than HNC. Some of the heavier homologues of HCN and HNC known are HSiN, HNSi,[4] HCP,[5] and HPSi[6]. Unlike the HCN–HNC system, the HSiN–HNSi system has a reverse stability order, that is, HNSi is more stable than HSiN. The formation of HCP as a stable compound with a CP triple bond was first reported by Gier in 1961.[5a] The existence of HPSi was confirmed by using rotational spectroscopic studies in 2010.[6] Quantum chemical calculations suggest that HPSi has a bent geometry with a PSi double bond, a PH single bond, and a donor–acceptor interaction between the HP bond and an empty p orbital on Si.[6] Bent HPSi was predicted to be more stable than the linear isomer, HSiP. The barrier height for the isomerization of HPSi to HSiP was calculated to be about 23.5 kcal/mol.[7] Information from the literature indicates that the heavy atom analogues of HCN behave differently and this raises certain questions: Do they have a linear geometry similar to that of HCN or a bent structure, as in the case of HPSi, or a cyclic (H-bridged structure) geometry? What is the bonding situation between the Group 14 and 15 elements in the heavier analogues of the HCN–HNC system? What are the possible arrangements between them? These questions are addressed in Chapter 3, “Heavier Homologues of HCN–HNC”, by exploring the singlet potential energy surface (PES) of the HCN–HNC system and heavier homologues.

Another common example of a triple bond is carbonmonosulfide, C≡S. Compounds with a CS triple-bond character are rare. C≡S,[8] $F_3C–C≡SF_3$,[9] $F_5S–C≡SF_3$,[10] and HC≡SOH[11] are the only compounds that are known to have a CS triple-bond character. Despite the shorter CS bonds in $F_3C–C≡SF_3$ and $F_5S–C≡SF_3$, the CS bonds in these compounds are reported to have a hidden carbene character.[9c, 12]

The molecule HCSOH was reported by Schreiner et al. in 2009.[11] The IR absorption band corresponding to the CS bond stretching vibration in HCSOH (1201.3 cm^{-1}) is comparable to the CS bond stretching vibration in C≡S (1272 cm^{-1}) and is likely to be higher than the CS stretching vibration

in CS_2 (1097 cm^{-1}). Hence, the molecule HCSOH is viewed as a structure with a strong CS double bond or a weak CS triple bond. Chapter 4 of this thesis focuses on understanding the nature of the CS bond in HCSOH and $F_5S–C{\equiv}SF_3$ by proposing the model systems HCSF and HCSH. Compounds with an NS triple bond are called sulfanenitrile or thiazynes. The nature of the NS triple bond in thiazyenes (NSF, NSH, and NSOH) is also studied. The possibility of the existence of SiS and PS triple bonds in HSiSF and PSF is also explored.

Triple bonds are not only limited to the main-group elements of the periodic table, but are also known to exist between the transition metals and the main-group elements of the periodic table, after the discovery of the transition-metal alkylidyne complexes by Fischer et al. in 1973.[13] The heavier members of the carbon and nitrogen families are also known to form triple bonds with Group 6 transition metals.[14] The unprecedented discovery of $HC{\equiv}UF_3$ by Lyon et al. in 2007[15] opened the door to the synthesis of compounds with triple bonds to actinides. The formation of $N{\equiv}UF_3$, $P{\equiv}UF_3$, and $As{\equiv}UF_3$ were also reported.[16] Triplet pnictinidene molecules, $E{\div}MF_3$, with a triplet triple bond (E÷M) between Group 15 non-metal elements (E = N, P, and As) and Group 4 (M = Ti, Zr, Hf, and Th) transition metals were characterized by using infrared spectroscopy.[17] Bonding analysis of molecules with a triple bond to uranium and terminal pnictinidene molecules of Group 4 metal atoms and some of their related systems are given in Chapter 5.

2. Theoretical Background and Methods

This chapter gives an overview of the theoretical background and methods used in this thesis. A detailed description of the theory and methods used in the field of computational chemistry can be found in quantum chemistry textbooks[18] written by Szabo, Levine, Jensen, and Cramer.

2.1 Schrödinger Equation

In 1926, Erwin Schrödinger proposed an equation, which is now named after him, describing the quantum behavior of matter.[19] A nonrelativistic and time-independent Schrödinger equation of a system is written as given by Equation (2.1):

$$\hat{H}\Psi = E\Psi \tag{2.1}$$

in which, $\hat{H}$ is the Hamiltonian, which is a function of the kinetic and potential energies of particles in the system, Ψ is the molecular wave function, and E is the energy of the system.

2.2 Ab Initio Methods

Ab initio quantum chemical calculations used in computational chemistry involve finding the solution to the Schrödinger equation of molecular systems. Although the Schrödinger equation of a hydrogen atom can be solved exactly, the Schrödinger equation of the systems with more than two particles cannot be solved exactly. There are a number of approximations and methods applied in solving the Schrödinger equation of many-body systems and some of them are described in brief below.

2.2.1 Born–Oppenheimer Approximation[20]

In the Born–Oppenheimer approximation, electronic and nuclear motions are treated separately. Because of the larger nuclear mass, relative to the mass of the electron, "nuclei are expected to move very slowly relative to the motion of electrons" in other words, "nuclei are fixed with respect to electron motion." Hence, the total molecular wave function can be written as a product of the electronic and nuclear wave function, and the Hamiltonian of the nuclei and electrons are separable. The electronic Hamiltonian for a molecule, with M number of nuclei (A, B, …) and N number of electrons (i, j, …), can be written in atomic units as given by Equation (2.2):

$$\hat{H}_{\text{elec}} = -\sum_{i=1}^{N}\frac{1}{2}\nabla_i^2 - \sum_{i=1}^{N}\sum_{A=1}^{M}\frac{Z_{\text{A}}}{r_{iA}} + \sum_{i=1}^{N}\sum_{j>i}^{N}\frac{1}{r_{ij}} \tag{2.2}$$

in which $\nabla_i^2 = \frac{\partial^2}{\partial x_i^2} + \frac{\partial^2}{\partial y_i^2} + \frac{\partial^2}{\partial z_i^2}$ is the Laplacian operator, involving differentiation with respect to the coordinates of the *i*th electron, r_{iA} is the distance between the *i*th electron and *A*th nucleus, r_{ij} is the distance between *i*th and *j*th electrons, and Z_A is the atomic number of nucleus A. The first term of Equation (2.2) represents the kinetic energy of the electrons, the second term shows the columbic attraction between the electrons and nuclei, and the third term represents the repulsion between the electrons. The nuclear repulsion energy of the fixed nuclei in atomic units is given by Equation (2.3):

$$V_{NN} = \sum_{A=1}^{M} \sum_{B>A}^{M} \frac{Z_A Z_B}{r_{AB}} \tag{2.3}$$

The final Hamiltonian of the molecule including the nuclear repulsion is given by $\hat{H}_{elec} + V_{NN}$.

2.2.2 Variation Principle

If Ψ is the trial wave function of a system and $\hat{H}$ is the Hamiltonian, the energy of the system is given by Equation (2.4):

$$E = \frac{\int \Psi^* \hat{H} \Psi d\tau}{\int \Psi^* \Psi d\tau} \tag{2.4}$$

For a normalized wave function, $\int \Psi^* \Psi d\tau = 1$ and $E = \int \Psi^* \hat{H} \Psi d\tau$.

According to the variation theorem, the energy, *E*, of a system, obtained by the minimization process is always greater than or equal to the exact energy, E_0, of the system, that is, $\int \Psi^* \hat{H} \Psi d\tau \geq E_0$. The variation principle allows the calculation of an upper bound for a system's ground-state energy.

2.2.3 Pauli Exclusion Principle[21]

The Pauli exclusion principle states that a many-electron wave function must be antisymmetric with respect to the interchange of the coordinates of any two electrons (Equation (2.5)):

$$\Psi\left[x_1,...,x_i,...,x_j,...,x_N\right] = -\Psi\left[x_1,...,x_j,...,x_i,...,x_N\right] \tag{2.5}$$

in which *x* denotes both the spatial and spin coordinates of the electron.

2.2.4 Hartree–Fock Approximation[22]

The electronic Hamiltonian of a molecule under the Born–Oppenheimer approximation is given by Equation (2.2). The electron–electron repulsion term in Equation (2.2) makes the

Schrödinger equation nonseparable. To overcome this problem, one-electron functions, ϕ, are used to describe the many-electron wave function, called the Hartree product (Equation (2.6)):

$$\Psi(r_1, r_2, ..., r_n) = \phi(r_1)\phi(r_2)...\phi(r_n) \tag{2.6}$$

In the Hartree product, the wave function Ψ does not obey the Pauli exclusion principle. Hence, an antisymmetric wave function is defined by using the Slater determinant (Equation (2.7)).[23] The best possible description of an antisymmetric wave function Ψ, with Hamiltonian $\hat{H}$, is obtained by means of the variation principle by using the self-consistence field (SCF) procedure.

$$\Psi = (n!)^{-1/2}\begin{vmatrix} \phi_1(r_1)\alpha(1) & \phi_1(r_1)\beta(1) & \phi_2(r_1)\alpha(1) & ... & \phi_{n/2}(r_1)\beta(1) \\ \phi_1(r_2)\alpha(2) & \phi_1(r_2)\beta(2) & \phi_2(r_2)\alpha(2) & ... & \phi_{n/2}(r_2)\beta(2) \\ \phi_1(r_3)\alpha(3) & \phi_1(r_3)\beta(3) & \phi_2(r_3)\alpha(3) & ... & \phi_{n/2}(r_3)\beta(3) \\ ... & ... & .... & ... & .... \\ ... & ... & .... & ... & .... \\ \phi_1(r_n)\alpha(n) & \phi_1(r_n)\beta(n) & \phi_2(r_n)\alpha(n) & ... & \phi_{n/2}(r_n)\beta(n) \end{vmatrix} \tag{2.7}$$

The SCF calculation that gives the antisymmetrized spin orbitals is called the Hartree–Fock method and the differential equation for the Hartree–Fock orbital is given by Equation (2.8):

$$\hat{F}_i(1)\phi_i(1) = \varepsilon_i(1)\phi_i(1) \tag{2.8}$$

in which $\hat{F}$ is the Fock operator and ε_i is the eigenvalue or energy of the orbitals. The Fock operator has the form shown in Equation (2.9):

$$\hat{F}(1) = \mathbf{h}^{\text{core}}(1) + \sum_i 2\mathbf{J}_i(1) - \mathbf{K}_i(1) \tag{2.9}$$

in which $\mathbf{h}^{\text{core}}$ is the one-electron operator (Equation (2.10)), $\mathbf{J}_i$ is the coulomb (Equation (2.11)), and $\mathbf{K}_i$ is the exchange operator (Equation (2.12)).

$$\mathbf{h}^{\text{core}}(1) = -\frac{1}{2}\nabla_1^2 - \sum_A \frac{Z_A}{|r_{1A}|} \tag{2.10}$$

$$\mathbf{J}_i(1) = \int \phi_i^*(2)\phi_i(2)\frac{1}{r_{12}}d\tau_2 \tag{2.11}$$

$$\mathbf{K}_i(1) = \int \phi_i^*(2)\phi_i(1)\mathbf{P}_{12}\frac{1}{r_{12}}d\tau_2 \tag{2.12}$$

The coulomb integral corresponds to the potential energy of the interaction between a given electron and the rest of the electrons. The exchange integral takes care of the antisymmetric behavior of the wave function with respect to electron exchange.

2.2.5 LCAO-MO Approximation

Roothaan and Hall[24] suggested that the linear combination of a finite number of atomic orbitals (LCAO) could be used to represent the molecular orbitals (MOs) (Equation (2.13)):

$$\phi_i = \sum_{\mu=1} c_{\mu i} \chi_\mu \tag{2.13}$$

in which $c_{\mu i}$ is the MO expansion coefficients. From Equations (2.8) and (2.13), Equation (2.14) is obtained:

$$\hat{F} \sum_{\mu} c_{\mu i} \chi_\mu = \varepsilon_i \sum_{\mu} c_{\mu i} \chi_\mu \tag{2.14}$$

Equation (2.14) is called the Hartree–Fock–Roothan equation, which leads to the secular equation, Equation (2.15):

$$\sum_{\nu=1} \left(F_{\mu\nu} - \varepsilon_i S_{\mu\nu} \right) c_{\nu i} = 0 \tag{2.15}$$

The solution then becomes Equation (2.16):

$$\mathbf{FC}=\mathbf{SC}\varepsilon \tag{2.16}$$

in which **F** is the Fock matrix, **S** is the overlap matrix in the atomic orbital basis, **C** are the eigenvectors, and ε is the diagonal matrix containing the orbital eigenvalues. The elements of the Fock matrix are given by Equation (2.17):

$$F_{\mu\nu} = H_{\mu\nu}^{\text{core}} + \sum_{\lambda=1}^{N} \sum_{\sigma=1}^{N} P_{\lambda\sigma} \left[(\mu\nu \mid \lambda\sigma) - \frac{1}{2} (\mu\lambda \mid \nu\sigma) \right] \tag{2.17}$$

The $H_{\mu\nu}^{\text{core}}$ matrix represents the kinetic energy of an electron in a field of bare nuclei (Equation (2.18)):

$$H_{\mu\nu}^{\text{core}} = \left\langle \chi_\mu(1) \mid \hat{H}^{\text{core}}(1) \mid \chi_\nu(1) \right\rangle \tag{2.18}$$

$(\mu\nu \mid \lambda\sigma)$ are the two-electron integrals given by Equation (2.19):

$$(\mu\nu \mid \lambda\sigma) \equiv \int\int \frac{\chi_\mu^*(1) \chi_\nu(1) \chi_\lambda^*(2) \chi_\sigma(2)}{r_{12}} \tag{2.19}$$

$P_{\lambda\sigma}$ is the element of the one-electron density matrix given by Equation (2.20):

$$P_{\lambda\sigma} = 2\sum_{i=1}^{occ} c_{\lambda i}^{*} c_{\sigma i} \tag{2.20}$$

In the Hartree–Fock model, the antisymmetric nature of the wave function is incorporated by using the Slater determinant of one-electron orbitals. According to the Pauli principle, electrons with the same spin do not occupy the same point in space at the same time; however, the probability of finding two electrons of opposite spin in the same point in space is not zero. Therefore, the correlation between electrons of opposite spin is neglected in the Hartree–Fock method. The energy difference between the exact and the Hartree–Fock wave function gives the correlation energy, E_c, given by Equation (2.21):

$$E_c = E_{exact} - E_{HF} \tag{2.21}$$

There are a number of ways to account for electron correlation; some of them are described below in brief.

2.2.6 Configuration Interaction (CI)

Configuration interaction (CI) is one of the post-Hartree–Fock methods for solving the nonrelativistic Schrödinger equation, which includes electron correlation to the Hartree–Fock wave function. The wave function in CI is expressed as a linear combination of a finite number of higher order Slater determinants called the configuration state functions (CSFs) given by Equation (2.22):

$$\Psi_{CI} = \sum_{I}^{CI} C_I \Phi_I = a_0 \Phi_{HF} + \sum_{I>0} a_I \Phi_I \tag{2.22}$$

in which C_I is the CI expansion coefficient and Φ_I is the CSF. The CI wave function is determined by using the variational principle. In Equation (2.22), the first term corresponds to the Hartree–Fock determinant. If the CI expansion includes all possible configurations with all possible electronic excitations of the appropriate symmetry then the procedure is called a full CI (FCI). FCI is the best possible variational treatment. The energy difference between the Hartree–Fock and FCI wave functions of the chosen basis gives the electron correlation energy, E_c, within that basis set. However, FCI calculations are highly demanding and the number of determinants increases as the size of the molecules and basis sets used increase. Therefore, most calculations are limited to CISD (single and double CI), which includes all possible single- and double-excitations terms. The CID (double-excitation CI) is also available; single excitations (CIS) do not mix with the Hartree–Fock determinant and cannot be applied to the ground state of the molecules. However, CIS is useful for excited states.

2.2.7 Møller–Plesset Perturbation Methods[25]

In 1934, Møller and Plesset developed a perturbation theory for treating a system of *n* electrons in which the Hartree–Fock solution appears as the zero-order approximation. The difference between the exact Hamiltonian and the Hartree–Fock Hamiltonian is considered to be a small perturbation, $\lambda\hat{V}$, in which λ is a dimensionless parameter (Equation (2.23)):

$$\hat{H}_\lambda = \hat{H}_0 + \lambda\hat{V} \tag{2.23}$$

In the Møller–Plesset perturbation theory, an unperturbed Hamiltonian, $\hat{H}_0$, is taken as the sum of one-electron Fock operators Equation (2.24):

$$\hat{H}_0 = \sum_i F_i \rightarrow \left(\Phi_0 \middle| \hat{H}_0 \middle| \Phi_0\right) = \sum_i \varepsilon_i \tag{2.24}$$

And the perturbation is given by Equation (2.25):

$$\hat{V} = \hat{H} - H_0 = \sum_i \sum_j \frac{1}{r} - 2\langle V_{ee} \rangle \tag{2.25}$$

According to the Rayleigh–Schrödinger perturbation theory, Ψ_i and E_i could be expanded in a Taylor series (Equation (2.26)).

$$\begin{aligned} \Psi_i &= \Psi^{(0)} + \lambda\Psi^{(1)} + \lambda^2\Psi^{(2)} + \lambda^3\Psi^{(3)} + \ldots \\ E_i &= E^{(0)} + \lambda E^{(1)} + \lambda^2 E^{(2)} + \lambda^3 E^{(3)} + \ldots \end{aligned} \tag{2.26}$$

The energy correction in Møller–Plesset perturbation theory can be taken in various orders by setting the parameter λ=1 and truncating the series to MP1, MP2, MP3, and so forth. The first-order correction (MP1) to an unperturbed wave function accounts for only electron–electron repulsion and does not advance beyond the Hartree–Fock level. The electron correlation energy starts only at order 2, that is, MP2. The second-order Møller–Plesset contribution to the energy expression is given by Equation (2.27). MP2 has the scaling order of about N^5.

$$E^{(\mathrm{MP2})} = -\sum_{i}^{\mathrm{occ}} \sum_{j>i}^{\mathrm{occ}} \sum_{a}^{\mathrm{vir}} \sum_{b>a}^{\mathrm{vir}} \left(\varepsilon_a + \varepsilon_b - \varepsilon_i - \varepsilon_j\right)^{-1} \left|(ij \mid ab)\right|^2 \tag{2.27}$$

2.2.8 Coupled-Cluster (CC) methods[26]

The coupled-cluster (CC) method is one of the most reliable ab initio methods available for treating electron correlation in quantum mechanical calculations of molecules. In CC theory, the full CI (FCI) wave function is expressed by Equation (2.28):

$$\Psi_{CC} = e^{\hat{T}} \Phi \tag{2.28}$$

in which Φ is a CSF and $\hat{T}$ is the excitation operator defined as $\hat{T} = \hat{T}_1 + \hat{T}_2 + \hat{T}_3 + ... + \hat{T}_n$, in which n is the total number of electrons. When the operator $\hat{T}$ acts on the reference wave function, Φ_0, it produces single, double, …, n excitations (Equations (2.29) and (2.30)):

$$\hat{T}_1 \Phi_0 = \sum_{i}^{occ} \sum_{a}^{vir} t_i^a \Phi_i^a \tag{2.29}$$

$$\hat{T}_2 \Phi_0 = \sum_{i<j}^{occ} \sum_{a<b}^{vir} t_{ij}^{ab} \Phi_{ij}^{ab} \tag{2.30}$$

in which i and j are the occupied MOs and a and b are the virtual MOs in the reference wave function Φ_0. The summation terms on the right-hand side of Equations (2.29) and (2.30) show the excitation of an electron from an occupied orbital indicated by the subscript into the virtual orbital indicated by the superscript.

If only the double excitation is considered then it is called coupled-cluster double excitation (CCD), in which the CC wave function is approximated by limiting $\hat{T} = \hat{T}_2$ (Equation (2.31)):

$$\Psi_{CCD} = e^{\hat{T}_2} \Phi \tag{2.31}$$

Expanding $e^{\hat{T}_2}$ in Taylor series gives Equation (2.32):

$$\Psi_{\mathrm{CCD}} = \left(1 + \hat{T}_2 + \frac{\hat{T}_2^2}{2!} + \frac{\hat{T}_2^3}{3!} + ...\right)\Phi \tag{2.32}$$

Similarly, CCSD uses both single and double excitations ($\hat{T} = \hat{T}_1 + \hat{T}_2$). CCSDT invokes the single, double, and triple excitations ($\hat{T} = \hat{T}_1 + \hat{T}_2 + \hat{T}_3$) and when all cluster operators up to $\hat{T}_n$ are included then $\Psi_{\mathrm{CC}} = \Psi_{\mathrm{CI}}$. CCSD(T), in which single and double excitations are treated fully and triple excitations are treated by using the perturbation method, is an approximation to the CCSDT to reduce computational time. CCSDT scales to the order N^8 (N is the number of basis functions), CCSD scales to about N^6, and CCSD(T) has a scaling order in between CCSDT and CCSD.

2.3 Density Functional Theory

Although ab initio methods are considered to be more reliable, solving the Schrödinger equation of larger systems becomes more expensive and computational time increases with increasing the number of the basis functions. Density functional theory (DFT) is a method parallel to ab initio

methods and is computationally less demanding with almost the same accuracy as other computational methods. In DFT the electronic energy E is regarded as a function of electron density ρ. Since it is integrated over all space, the electron density, ρ, gives the total number of electrons, n, that is, $n = \int \rho(r)\, dr$. The advantage of DFT over pure wave function based methods is that the wave function of a system, with n number of electrons depends on $3n$ coordinates, whereas electron density depends only on three coordinates independent of the number of electrons.

The concept of DFT dates back to the late 1920s when Fermi[27] and Thomas[28] introduced the idea of expressing the energy of a system as a function of the total electron density. However, formal proof of the above notion was put forward by Hohenberg and Kohn, called the Hohenberg–Kohn theorem.[29] The Hohenberg–Kohn theorem states that the ground-state energy of a nondegenerate electronic system and the corresponding electronic properties are uniquely defined by the electron density.

The application of DFT to real systems was possible only after the publication of the Kohn–Sham equation in 1965[30]. The Kohn–Sham equation was derived from the Hohenberg–Kohn theorem. Under the Kohn–Sham approach, the contribution to the total energy can be divided into two main parts, as shown in Equation (2.33). The first part contains the terms for the kinetic energies, potential energies, and the classical coulomb energies of the noninteracting electrons. The second part contains a small correction term that incorporates the electron–electron interaction term, called the exchange-correlation energy.

$$E[\rho] = -\frac{1}{2}\sum_{i=1}^{n}\Psi_i^*(r_1)\nabla_i^2\Psi_i(r_1)dr_1 - \sum_{X=1}^{N}\int\frac{Z_X}{r_{Xi}}\rho(r_1)dr_1 + \frac{1}{2}\int\int\frac{\rho(r_1)\rho(r_2)}{r_{12}}dr_1dr_2 + E^{XC}[\rho] \quad (2.33)$$

In Equation (2.33), Ψ_i (i = 1, 2, …, n) are the Kohn–Sham orbitals, determined by solving the Kohn-Sham equations, by applying the variation principle to the electronic energy, $E[\rho]$, Equation (2.34):

$$\hat{h}_i\Psi_i(r_i) = \varepsilon_i\Psi_i(r_i) \quad (2.34)$$

in which $\hat{h}_i$ is the Kohn–Sham Hamiltonian and ε_i are the energies of the Kohn–Sham orbitals. The Kohn–Sham Hamiltonian is given by the Equation (2.35):

$$\hat{h}_i = -\frac{1}{2}\nabla_i^2 - \sum_{X=1}^{N}\frac{Z_X}{r_{Xi}} + \int\frac{\rho(r)}{r_{12}}dr_2 + V^{XC}(r_1) \quad (2.35)$$

$V^{XC}[\rho] = \dfrac{\delta E^{XC}[\rho]}{\delta\rho}$ is the functional derivative of the exchange-correlation energy.

Moreover, the ground-state electron density ρ(r), at a location r, can be expressed in terms of a set of one-electron orbitals (the Kohn–Sham orbitals) Equation (2.36):

$$\rho(\mathrm{r}) = \sum_{i=1}^{n} \left|\Psi_i(\mathrm{r})\right|^2 \tag{2.36}$$

The exchange-correlation energy, E^{XC}, is generally divided into an exchange term, E^{X}, and the correlation term, E^{C}. The exchange term is associated with the interaction between electrons of the same spin, whereas the correlation term corresponds to the interaction between electrons of opposite spin.

$$E^{XC}[\rho] = E^{X}[\rho] + E^{C}[\rho] \tag{2.37}$$

$E^{X}[\rho]$ and $E^{C}[\rho]$ are also functionals of the electron density and the corresponding functionals are known as the exchange and correlation functionals, respectively. Once E^{XC} is known, the Kohn–Sham equation is solved by means of the SCF procedure. During SCF calculations, the Kohn–Sham orbitals in each iteration are expressed in terms of the linear combination of the basis function, similar to that of Hartree–Fock calculations. The exchange and correlation functionals could be of two distinct types: local functionals, depending only on the electron density, ρ, and gradient-corrected functionals, which depend on both the electron density, ρ, and the gradient, $\Delta\rho$. The following approximation methods are used in DFT calculations.

Local Density Approximation (LDA): LDA assumes the model of a homogeneous electron gas and the exchange-correlation energy at any point in space is a function of the electron density at that point in space. In the homogeneous electron gas model, electrons move in a field of uniformly distributed positive charge. The exchange energy in the Thomas–Fermi–Dirac[31] method is given by Equation (2.38)

$$E_{\mathrm{LDA}}^{\mathrm{X,Dirac}}[\rho] = -C_{\mathrm{X}} \int \rho^{4/3}(\mathrm{r})\mathrm{dr} \tag{2.38}$$

$$C_{\mathrm{X}} = -\frac{3}{4} \cdot \left(\frac{3}{\pi}\right)^{1/3} \tag{2.39}$$

Improvements in the results of LDA were made after the introduction of a local spin density approximation[32] (LSDA). In the LSDA model, the exchange functional is given as the function of both α and β spin electron densities (ρ^{α} and ρ^{β}) (Equation (2.40)):

$$E_{\mathrm{LDA}}^{\mathrm{X}}[\rho] = -2^{1/3} C_{\mathrm{X}} \int (\rho^{4/3} + \rho^{4/3})\mathrm{dr} \tag{2.40}$$

In LDA the correlation energy E^{C} is generally obtained by using a suitable interpolation formula from a set of values calculated for different densities in a homogeneous electron gas. The correlation energy could be treated by using the Vosko–Wilk–Nusair (VWN)[33] functional or the local correlation functional of Perdew[34] (PL). It was stated in a review article, "General Performance of Density

Functionals", that "LDA typically underestimates E^X but overestimates E^C resulting in unexpectedly good E^{XC} values". However, LDA is in general, worse for small molecules and tends to underestimate atomic ground-state energies, whereas ionization and binding energies are overestimated.[35]

Generalized Gradient Approximation (GGA): The GGA method takes into account that real systems are spatially inhomogeneous (with spatially varying density); hence, the exchange-correlation energy in GGA methods depends not only on the density, ρ, but also on the gradient of the density, $\Delta\rho$. Most of the gradient-corrected functionals are constructed with a correction term being added to the LDA functional (Equation (2.41)).

$$E_{GGA}^{X/C} = E_{LDA}^{X/C}[\rho(r)] + \Delta E^{X/C}\left[\frac{|\nabla\rho(r)|}{\rho^{4/3}(r)}\right] \tag{2.41}$$

The correction term depends on the dimensionless reduced gradient and not on the absolute gradient. Examples of GGA exchange functionals are Becke88 (B),[36] Perdew–Wang (PW),[37] modified-Perdew–Wang (mPW),[37-38] Becke86 (B86),[39] Perdew 86 (P),[40] Perdew–Burke–Ernzerhof (PBE),[41] and modified-Perdew–Burke–Ernzerhof (m-PBE).[41-42] Examples of GGA correlation functionals include Becke 88 (B88),[43] Perdew 86,[40] and Lee–Yang–Parr (LYP).[44] GGA methods are good for the calculation of covalent, ionic, metallic, and hydrogen-bridge bonds and fail in case of the van der Waals interactions.[35] The next levels of approximation towards the divine level of DFT, that is, the complete nonlocal level of chemical accuracy in Jacob's ladder (according to the vision of Perdew) include the following approximations:

Meta-GGA, which depends on the higher order density gradients or the kinetic energy density. Examples of meta-GGA include B95,[45] TPSS,[46] and VSXC.[47]

Hybrid Density Functional (H-GGA),[35] which combines the exchange correlation of conventional GGA methods with a percentage of Hartree–Fock (or exact) exchange. Examples of H-GGA include B3LYP,[36, 44-45] B3P86,[36, 45] B3PW91,[36, 45] MPW1K,[38] B97-1, B97-2, and X3LYP.

Hybrid Meta-GGA (HM-GGA)[35] methods are similar to H-GGA, but start from M-GGA and mix with the Hartree–Fock exchange. Hybrid-meta GGA depends on the Hartree–Fock exchange, the electron density and its gradients, and the kinetic energy density. B1B95, BB1K, MPW1B95, TPSSh, BMK, MPWB1K, PWB6K, M05,[48] M05-2X,[48] M06,[49] and M06-2X[49] are examples of HM-GGA.

2.4 Basis sets

In quantum chemical calculations of molecules, the MOs are usually expressed as LCAO. Atomic orbitals (AOs) are obtained from a set of mathematical functions called basis sets. Two types of basis functions used to calculate LCAO-MO are Slater-type orbitals (STOs)[50] and Gaussian-type orbitals (GTOs).[51] The functional form of STO is given by Equation (2.42):

$$\chi_{\xi,n,l,m}(r,\theta,\varphi) = NY_{l,m}(\theta,\varphi)r^{n-1}\exp(-\xi r) \tag{2.42}$$

in which N is the normalization constant; ξ is the exponent; (r, θ, φ) are the spherical constants; $Y_{l,m}$ is the angular momentum part describing the shape; and n, l, and m are the quantum numbers. GTO has the functional form given by Equation (2.43):

$$\chi_{\xi,n,l,m}(r,\theta,\varphi) = NY_{l,m}(\theta,\varphi)r^{(2n-2-l)}\exp(-\xi r^2) \tag{2.43}$$

Calculations using STOs are time consuming, in the case of the molecules with significant size, due to the unavailability of an analytical solution to four-index integrals. To overcome the above problem, STOs are approximated by summing up a number of GTOs with different exponents and coefficients. Defining a basis function as a linear combination of Gaussians is known as basis set contraction and the final basis function is called the contracted basis function. The individual Gaussians from which the contracted basis set is formed are called primitive Gaussians.

$$\chi^{\mathrm{CGTO}}(\mathrm{r}) = \sum_{i=1}^{M} d_i \chi_i^{\mathrm{GTO}}(\alpha_i,\mathrm{r}) \tag{2.44}$$

In Equation (2.44) M is the length of contraction and d_i is the contraction coefficient. As a result of the linear combination of primitive Gaussians, the improper functional behavior of GTOs at the origin is also removed. Hehre, Stewart, and Pople constructed basis sets called STO-MG[52] (STOs approximated by M number of Gaussians), in which M = 2 to 6. STO-MG is called a minimal basis set. A minimal basis set is one in which there is only one basis function for each atomic orbital. The molecular properties calculated by using minimal basis sets are not accurate; the improvements in the performance of these basis sets were achieved after introducing more flexible basis functions, such as polarization function, diffuse function, and split-valence basis set. Additional polarization function indicates the presence of higher angular momentum orbitals than the actual number of valence orbitals present in the atomic ground state. Adding a diffuse function allows the orbital to occupy more space and is necessary for the correct description of anions, molecules with lone pairs, weak bonds, and so forth. A split-valence basis set is one in which the valence atomic orbitals are represented by two or more basis functions (for example, 3-21G). A multiple-ξ basis set is one in which each AO is represented by more than one basis function, for example, DZ (a double-ξ) and TZ (a triple-ξ) basis sets are also available.

2.5 Effective Core Potential[53]

The effective core potential (ECP) or pseudopotential is another set of approximations used commonly in electronic structure calculations. The core electrons are chemically inert and their contribution to the total electronic energy does not change in a chemical environment. The pseudopotential or frozen-core approximation replaces the effects of the motion of core electrons in an

atom. The advantage of using pseudopotential is that it reduces computational time greatly in comparison to all electron calculations and pseudopotential incorporates relativistic effects of core electrons in heavy elements. A 'large-core' ECP includes everything except the valence-shell electrons, whereas a 'small-core' ECP scales back to the next lower shell. When ECP is used, valence basis sets are needed for the description of the remaining valence electrons. It was Hellmann[54] who first proposed the concept of treating the core and valence electrons separately. The semi-local pseudopotential[55] used in molecular calculations is given by Equation (2.45)

$$V_{\mathrm{PP}}(i) = -\frac{Q}{r_i} + \sum_{l=0}^{l_{max}} \sum_{k} A_{lk} \exp(-\alpha_{lk} r_i^2) P_l$$
$$P_l = \sum_{m=-l}^{l} |Y_{lm}\rangle\langle Y_{lm}| \tag{2.45}$$

in which Q is the core charge of the atom and P_l is the projection operator onto the Hilbert subspace of angular symmetry l. The coefficient A_{lk} and the exponential parameter α_{lk} could be adjusted to an all-electron atomic Hartree–Fock valence spectrum by a least-squares fit (Stuttgart pseudopotential)[56] to give an 'energy-consistent' pseudopotential. If the parameters are adjusted such that valence orbitals of specific symmetry from Hartree–Fock calculations are reproduced to high accuracy, above a certain cutoff radius r_c, they are called 'shape-consistent' pseudopotentials. Below r_c a smooth polynomial fit is chosen. The energy-consistent pseudopotentials are shape consistent, but the reverse is not true.[57]

2.6 Geometry Optimization

Geometry optimization involves locating stationary points on the potential energy surface (PES). Stationary points are characteristic geometries of a molecule on the PES where the force on each atom is zero. For example, local minima on the PES are equilibrium geometries and the transition states are first-order saddle points. The PES of an N-atom molecule depends on the $3N$ Cartesian coordinates or $3N$-6 internal coordinates (Z matrix) of a nonlinear molecule. The electronic energy $E(x)$ at an arbitrary point obtained by a small displacement, x from the reference geometry, x_0 is given by the Taylor series given in Equations (2.46) and (2.47):

$$E(x) = E_0 + \sum_i \frac{\partial E}{\partial x_i} x_i + \frac{1}{2} \sum_{ij} \frac{\partial^2 E}{\partial x_i \partial x_j} x_i x_j + \ldots \tag{2.46}$$

$$E(x) = E_0 + g_0^T x + \frac{1}{2} x^T F_0 x \tag{2.47}$$

in which the first derivative, $g_i = \left.\frac{\partial E}{\partial x_i}\right|_0$, is called the gradient and the second derivative, $F_{i,j} = \left.\frac{\partial^2 E}{\partial x_i \partial x_j}\right|_0$, is called the Hessian.

Taking the derivative of $E(x)$ gives Equation (2.48):

$$\left.\frac{\partial E}{\partial x}\right|_x = g_0 + F_0 x \tag{2.48}$$

At a stationary point, $x = -F_0^{-1} g_0 = -H_0 g_0$, in which H_0 can be the exact or an approximate inverse Hessian matrix F_0^{-1}. H_0 is improved in subsequent steps to give a new H_0. This type of optimization is called the variable metric or quasi-Newton method.[58] Once optimization is completed, the structure is tested for a minimum by calculating the second-derivative matrix or the vibrational frequencies. The number of negative eigenvalues of the Hessian or the number of imaginary frequencies (index i) at the stationary point determines if the structure is a minimum ($i = 0$) or a saddle-point ($i > 0$) geometry.

2.7 Natural Bond Orbital Analysis (NBO)[59]

Natural orbitals[60] $\{\theta_k\}$ are defined as eigenfunctions of the first-order reduced density operator, $\hat{\Gamma}$, $\hat{\Gamma}\theta_k = q_k\theta_k$, in which q_k represents the occupancy. Natural orbitals could also be characterized as maximum-occupancy orbitals, $q_\phi = \langle\phi|\Gamma|\phi\rangle$, in which q_ϕ is the electronic occupancy of the normalized trial function ϕ. The optimal population, q_k, and orbitals, $\{\theta_k\}$, are obtained by variational maximization. The natural orbitals are intrinsic and unique to the wave function, Ψ, and are independent of the basis function, $\{\chi_i\}$, satisfying the Pauli exclusion principle (i.e., $0 \le q_k \le 2$). NBO analysis involves a series of transformations from the input basis set, $\{\chi_i\}$, to different localized orbitals.

$$\{\chi_i\} \rightarrow \text{pre-NAOs} \rightarrow \text{NAOs} \rightarrow \text{NHOs} \rightarrow \text{NBOs} \rightarrow \text{NLMOs} \tag{2.49}$$

The localized orbitals may be subsequently transformed to delocalized natural orbitals or canonical molecular orbitals. Natural atomic orbitals (NAOs), $\{\phi_i\}$, are constructed based on the occupancy-weighted symmetric orthogonalization (OWSO) procedure from nonorthogonal basis atomic orbitals $\{\tilde{\phi}_i\}$ or pre-NAOs. The subsequent formation of natural hybrid orbitals (NHOs) and natural bond orbitals (NBOs) involves unitary transformation. NAOs are distinguished from pre-NAOs due to the

lack of 'orthogonalization tails' at the positions of other nuclei. The natural population $q_i^{(A)}$ of orbital $\phi_i^{(A)}$ on atom A is given by the diagonal density matrix element in the NAO basis (Equation (2.50)):

$$q_i^{(A)} = \left\langle \phi_i^{(A)} \middle| \hat{\Gamma} \middle| \phi_i^{(A)} \right\rangle \tag{2.50}$$

Since the population $q_i^{(A)}$ satisfies the Pauli principle, the atomic population $q^{(A)}$ sums to the total number of electrons N_{elec} (Equation (2.51)):

$$q^{(A)} = \sum_i q_i^{(A)}, \qquad N_{elec} = \sum_A^{atoms} q^{(A)} \tag{2.51}$$

Once NAOs are formed, the next step in NBO analysis is the identification of the optimal Lewis structure by locating lone-pair eigenvectors, n_A, bond vectors, σ_{AB}, and so forth. Each σ_{AB} is decomposed into its normalized hybrid contributions, h_A and h_B, from each atom. Natural localized molecular orbitals (NLMOs) are obtained from the NBO basis density matrix by carrying out a successive 2 × 2 Jacobi rotation, as a result of which the off-diagonal coupling elements $\Gamma_{\sigma\sigma^*}$ are removed.

The Wiberg bond[61] index is a measure of MO bond order and is given by the summation of the squared off-diagonal elements in the density matrix between the atoms (Equation (2.52)).

$$P(A,B) = \sum_{i \in A} \sum_{j \in B} b_{ij}^2 \tag{2.52}$$

2.8 Energy Decomposition Analysis (EDA)

Energy decomposition analysis (EDA) gives a quantitative description of the chemical bonds in molecules.[62] In the EDA or the extended transition-state method (ETS), developed independently by Morokuma,[63] and Zieglar and Rauk,[64] the bond dissociation energy, D_e, of a molecule AB, formed from the two fragments A^0 and B^0, is given by Equation (2.53).

$$\Delta E = E_{AB} - E_A^0 - E_B^0 = -D_e = \Delta E_{prep} + \Delta E_{elstat} + \Delta E_{Pauli} + \Delta E_{orb} \tag{2.53}$$

ΔE_{prep} is the preparation energy required to distort fragments A^0 and B^0 from their equilibrium geometries to the geometries and electronic states (frozen geometry) of A and B in the composite molecule (Equation (2.54)).

$$\Delta E_{prep} = E_A + E_B - E_A^0 - E_B^0 \tag{2.54}$$

Once the fragments are distorted to the geometry and electronic state they will have in the combined molecule, the second step is to bring the frozen fragments from infinite separation to their final

positions in the combined molecule without changing their densities, ρ_A and ρ_B. During this process, superposition of the fragment densities ($\rho_A+\rho_B$) takes place and the energy change associated with this step is given by ΔE_{elstat}, which is the electrostatic attractive interaction energy term. This classical coulomb interaction term is usually attractive in case of neutral fragments.

In the third step, ρ_A and ρ_B undergo antisymmetrization to fulfill the Pauli exclusion principle without going through any other relaxation. The energy change associated with this step is called ΔE_{Pauli}; the destabilizing interaction between the fragments (Equation (2.55)):

$$\Delta E_{\text{Pauli}} = E^0\left[\rho^0\right] - E^A\left[\rho^A\right] - E^B\left[\rho^B\right] + \Delta E^0_{XC} \tag{2.55}$$

in which ρ^0 is the density corresponding to the normalized antisymmetric wave function, $\Psi^0 = N\hat{A}\{\Psi^A\Psi^B\}$, and ΔE^0_{XC} corresponds to the change in Kohn–Sham exchange-correlation energy, which comes from the previous step along with $\Delta E_{elstat.}$ The ΔE_{elstat} and ΔE_{Pauli} interaction terms can be combined to give the steric interaction energy, $\Delta E_{steric} = \Delta E_{elstat} + \Delta E_{Pauli}$.

The final step of EDA is the relaxation of Ψ^0 to the final ground-state wave function, Ψ, of the molecule. The associated energy change during this step is called ΔE_{orb}. The orbital interaction term, ΔE_{orb}, is obtained by the interaction between the occupied orbitals on one fragment and the unoccupied orbitals of the other fragment, as well as by mixing the occupied and virtual orbitals within the same fragment. The orbital interaction term can be further partitioned into the contributions of the orbitals belonging to different irreducible representations of the point group of the interacting system, as shown in Equations (2.56) and (2.57):

$$\Delta E_{orb}\,(C_{\infty v}) = \Delta E_\sigma\,(A_1) + \Delta E_\pi\,(E_1) + \Delta E_\delta\,(E_2) \tag{2.56}$$

$$\Delta E_{orb}\,(C_s) = \Delta E_\sigma\,(A') + \Delta E_\pi\,(A'') \tag{2.57}$$

Most of the molecules investigated in this thesis are C_s symmetric, with a triple bond, that is, a σ and two π bonds ($\pi_{||}$ and $\pi\perp$), therefore, Equations (2.56) and (2.57) could be rewritten as Equations (2.58) and (2.59):

$$\Delta E_{orb}\,(C_{\infty v}) = \Delta E_\sigma\,(A_1) + [\Delta E_{\pi||}\,(E_1) + \Delta E_{\pi\perp}\,(E_1)] + \Delta E_\delta\,(E_2) \tag{2.58}$$

$$\Delta E_{orb}\,(C_s) = [\Delta E_\sigma\,(A') + \Delta E_{\pi||}\,(A')] + \Delta E_{\pi\perp}\,(A'') \tag{2.59}$$

In the energy decomposition analysis of the $C_{\infty v}$ symmetric molecules, the $\Delta E_{\pi||}$ and $\Delta E_{\pi\perp}$ contributions are summed under $\Delta E_\pi\,(E_1)$. Similarly, the $\Delta E_{\pi||}$ contribution of C_s symmetric molecules comes under the irreducible representation A′ and cannot be separated from $\Delta E_\sigma\,(A')$. ETS-NOCV,[65] which is a combined charge and energy decomposition scheme, was used to get the $\Delta E_{\pi||}$ contribution of C_s

symmetric molecules. Brief descriptions of NOCV[66] and ETS-NOCV[65] are given in the following sections.

2.9 Natural Orbitals for Chemical Valence (NOCV)

Mitoraj and Michalak introduced NOCV as descriptors of chemical bonds in transition-metal complexes.[66c] NOCV decomposes the deformation density, ($\Delta\rho$), into a diagonal matrix. NOCV is defined as the eigenvector of the valence operator, $\hat{V}$, given by Equation (2.60):

$$\hat{V}\psi_i = \upsilon_i\psi_i \tag{2.60}$$

in which i =1, 2, ..., N and the eigenvalue, υ_i, is the contribution from the ith NOCV to the global valence, V, given by Equation (2.61):

$$V = \frac{1}{2}\sum_{i=1}^{N}\upsilon_i^2 \tag{2.61}$$

The differential density, $\Delta\rho$, is expressed in terms of NOCV as shown in Equation (2.62):

$$\Delta\rho(\mathrm{r}) = \sum_{i=1}^{N}\upsilon_i\left|\psi_i(\mathrm{r})\right|^2 \tag{2.62}$$

From the normalization conditions: $\int \rho(r)\mathrm{d}r = 0$ and $\int \left|\psi_{\mathrm{i}}(r)\right|^2 \mathrm{d}r = 1$ (Equation (2.63)):

$$\sum_{i=1}^{N}\upsilon_i = 0 \tag{2.63}$$

From Equation (2.63), it is evident that at least two orbitals with nonzero eigenvalues are required to satisfy the normalization condition. In contrast to the other orbital-based approaches, NOCV defines a chemical bond (deformation density) in terms of two complementary orbitals with the same eigenvalues and opposite sign (Equations (2.64) and (2.65)).

$$\hat{V}\psi_{-k} = -\upsilon_k\psi_{-k} \qquad \hat{V}\psi_k = \upsilon_k\psi_k \qquad k=1, 2, \ldots, N/2 \tag{2.64}$$

$$\Delta\rho(\mathrm{r}) = \sum_{k=1}^{N/2}\upsilon_k\left[-\psi_{-k}^2(\mathrm{r}) + \psi_k^2(\mathrm{r})\right] = \sum_{k=1}^{N/2}\Delta\rho_k(\mathrm{r}) \tag{2.65}$$

The eigenvalue, υ_k, is the fraction of electron density transferred from the donor NOCV, ψ_{-k}, to the acceptor ψ_k orbital, during the formation of a molecule from the frozen geometry of the fragments. If the molecule is formed between two unrestricted fragments, the final deformation density is given separately in terms of alpha and beta electrons, $\Delta\rho^{\alpha}$ and $\Delta\rho^{\beta}$.

2.10 ETS-NOCV

ETS-NOCV[65] combines the charge (NOCV) and energy decomposition (ETS or EDA) schemes to decompose the deformation density, $\Delta\rho$, into different components (σ, π, δ, etc.) of the chemical bond and provides the corresponding energy contributions to the total bond energy. In the ETS-NOCV scheme the orbital interaction term, ΔE_{orb}, is given by Equation (2.66):

$$\Delta E_{\text{orb}} = \sum_{k=1}^{N/2} \Delta E_k^{\text{orb}} = \sum_{k=1}^{N/2} \upsilon_k \left[-F_{-k,-k}^{\text{TS}} + F_{k,k}^{\text{TS}} \right] \tag{2.66}$$

in which $F_{-k,-k}^{\text{TS}}$ and $F_{k,k}^{\text{TS}}$ are diagonal transition-state Kohn–Sham matrix elements corresponding to NOCV with the eigenvalues $-\upsilon_k$ and υ_k, respectively. The ΔE_k^{orb} term of a particular type of bond, σ, $\pi_{\parallel}$, $\pi_{\perp}$, δ, and so forth, are assigned by looking at the shape of the deformation density, $\Delta\rho_k$. The ETS-NOCV scheme provides both qualitative ($\Delta\rho_{\text{orb}}$) and quantitative (ΔE_{orb}) pictures of chemical bonds, even in molecules with C_1 point-group symmetry.

2.11 Topological Analysis of Electron Densities [67]

Electron density, ρ(r), is a measurable quantity (both experimentally and theoretically). The topological properties of electron density provide information about chemical bonds and charge distributions between atoms in a molecule. Saddle points in electron density distribution where the first derivative of density vanishes are called critical points. The critical points are named according to their rank and signature (ω, σ), where the rank ω is the number of nonzero eigenvalues and the signature σ is sum of the signs of eigenvalues. (3, -3) is the nuclear critical point (NCP) where the electron density has a local maximum. (3, -1) is the bond critical point (BCP) where the density is a minimum. BCP connects two points of maximum density (atom center). The plane separating the atom centers is called the zero-flux surface. (3, +1) is the ring critical point (RCP) and (3, +3) is the cage critical point (CCP). The Laplacian of electron density, $\nabla^2\rho(\text{r})$, and the energy density, H(r), are the other important parameters in describing the nature of the chemical bond. A large negative Laplacian, with significant electron density at BCP indicates the presence of a covalent bond and charge concentration due to the sharing of an electron between two atoms. A small density and a positive value for the Laplacian indicate an ionic bond, where there is charge depletion because of the closed-shell interaction. The connection between the nature of the chemical bond and the value of the Laplacian is also understood from Equation (2.67), which is the local-virial theorem expression:

$$(\hbar^2/4m)\nabla^2\rho(\text{r}) = 2G(\text{r}) + V(\text{r}) \tag{2.67}$$

in which G(r) and V(r) are the kinetic and potential energy densities. A negative Laplacian is indicative of a lowering of potential energy (covalent character) and a positive Laplacian is associated with

excess kinetic energy (ionic character). The energy density, $H(\mathrm{r})$, at a BCP is given by the summation of the kinetic, $G(\mathrm{r})$, and potential, $V(\mathrm{r})$, energy densities at that BCP (Equation (2.68)).

$$H(\mathrm{r}) = G(\mathrm{r}) + V(\mathrm{r}) \tag{2.68}$$

The energy density at BCP also indicates the type of interaction, for example, a covalent bond has a strong negative energy density value. The closed-shell interaction between ions or van der Waals complexes has zero or even positive energy density.

3. Heavier Homologues of HCN–HNC

3.1 Introduction

Hydrogen cyanide (HCN) is a linear molecule with a CN triple bond. Both HCN and its isomer hydrogen isocyanide (HNC) are astronomically interesting molecules.[3] Some of the heavier homologues of HCN and HNC known are HSiN–HNSi,[4] HCP,[5] and HPSi.[6] Previous quantum chemical calculations on the HSiN–HNSi system suggest that the isomer HNSi is more stable than HSiN, in contrast to the HCN–HNC system. The barrier height for the isomerization of HSiN → HNSi was predicted to be about 9.7 kcal/mol, with a reverse barrier height of about 74.4 kcal/mol.[68] Both of the isomers were characterized spectroscopically. The formation of HCP as a stable compound with a CP triple bond was first reported by Gier in 1961.[5a] The spectroscopically measured CP triple-bond length was 1.5421 Å.[5b] Later a number of compounds of the type R–C≡P, (R = *t*-Bu, Ph_3C, Ph, Me, F, CF_3) were synthesized.[69] The existence of the species HPSi was recently confirmed by Lattanzi et al., by using a rotational spectroscopic technique.[6] Quantum chemical calculations suggest that HPSi has a bent geometry with a PSi double bond, a PH single bond, and a donor–acceptor interaction between the PH bond and the empty p orbital on Si.[6] Bent HPSi is more stable than the linear isomer HSiP. The barrier height for HSiP → HPSi isomerization was calculated to be about 13 kcal/mol.[7]

Compounds of the heavier main-group elements are known to exhibit unusual structures from the first row compounds, for example, the heavy-atom analogues of acetylene. The heavier analogues of the HCN–HNC system are also not an exception; HPSi has a bent geometry, in contrast to the linear isovalent first-row compounds HCN, HNSi, and HCP. The HCN–HNC system and the heavier analogues are potential targets to be detected in interstellar space and are experimentally interesting compounds to synthesize and characterize spectroscopically. In this chapter, the potential energy surface (PES) of a system involving the atoms H, X, and E—hereafter called the (H, X, E) system, in which X = Group 14 elements and E = Group 15 elements—are studied. Charge and energy decomposition analyses of the systems are also presented.

3.2 Methods

Geometries of the system, involving the atoms H, X, and E (X = N to Bi and E = C to Pb), were optimized at the CCSD(T) level with a split-valance basis set of doubly polarized triple-ζ-quality (def2-TZVPP).[70] Effective core potential (ECP) was used for the nonvalence-shell electrons of the heavier elements (Sn, Pb, Sb, and Bi). This level of theory is denoted as CCSD(T)/TZVPP. The geometries were also optimized at the nonlocal DFT level of theory by using Becke's exchange functional in conjunction with Perdew's correlation functional (BP86).[36, 40] The triple-ζ-quality basis set augmented by two sets of polarization function with a frozen-core approximation for the core electrons was employed. Uncontracted Slater-type orbitals (STOs) were used as a basis function for the SCF calculation.[71] An auxiliary set of s, p, d, f, and g STOs were used to fit the molecular

densities and to represent the Coulomb and exchange potentials accurately in each SCF cycle.[72] Scalar relativistic effects were incorporated by applying the zeroth-order regular approximation (ZORA)[73] and the level of theory is denoted as BP86/TZ2P+. The stationary points were characterized as minima (i = 0) or saddle points (i > 0) (for transition states, i = 1) on the PES by computing the Hessian matrix. CCSD(T) calculations were done by using the program package MOLPRO 2009.1.[74] BP86/TZ2P+ calculations were carried out by using the ADF 2009.01[75] program package. NBO[59] analysis was done at the BP86/TZVPP level on the BP86/TZ2P+ optimized geometries by using Gaussian NBO version 3.1 as implemented in the Gaussian 09 program package.[76] The topological analysis of the electron density (AIM analysis)[77] was performed by using the AIMPAC program package.[78] The wave function for Bader's AIM analysis was obtained at the BP86/TZVPP//BP86/TZ2P+ level by using the program package Gaussian 09. EDA[63-64] and ETS-NOCV[65, 66c] analyses were carried out at the BP86/TZ2P+ level of theory by using the ADF 2009.01 program package. For technical reasons, the EDAs involving open-shell fragments neglect the spin polarization in the fragments and thus yield slightly too stable bonds (on the order of a few kcal/mol per unpaired electron). The bond energies were corrected for the spin-polarization error ΔE_{corr}, which is given in the tables.

The singlet PES of the system (H, X, E) is scanned for all of the possible geometrical arrangements between the atoms H, X, and E at the CCSD(T)/TZVPP and BP86/TZ2P+ levels of theory. Scheme 3.1 shows the stationary points located on the PES of (H, X, E) and the nomenclature that will be followed throughout this discussion. The linear geometries with $C_{\infty v}$ symmetry are prefixed with *lin*- and the planar bent structures with C_s symmetry are prefixed with *bent*-, except for the transition-state (TS) geometries. The BP86/TZ2P+ level performs as well as CCSD(T), but it fails when predicting the global minimum of the system (H, Bi, Si) as *lin*-HSiBi. Discussions in the Geometries and Energies section are based on the results obtained at the CCSD(T)/TZVPP level of theory, unless otherwise mentioned.

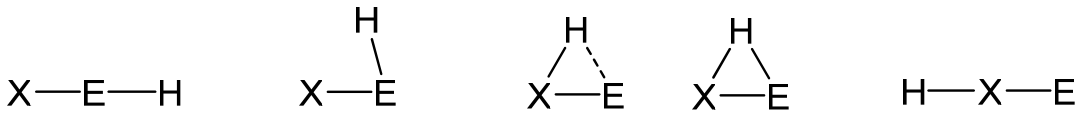

Scheme 3.1: Geometry of the stationary points on the PES of (H, X, E) where X = N to Bi and E = C to Pb. The lines connecting the atoms indicate the connections between them and not the bond multiplicity.

3.3 (H, N, E) System

3.3.1 Geometries and Energies

The stationary points characterized on the PES of the (H, N, E) system are shown in Figure 3.1. All of the minima located on the PES of the (H, N, E) system have linear geometry. The bent

structures located are first-order saddle points, that is, the TS of the 1,2-H-shift isomerization reaction, (*lin*-HEN → *lin*-HNE). *lin*-HNE (E = Si to Pb) is the global minimum and *lin*-HEN is the local minimum, lying 67.5, 64.8, 69.7, and 71.5 kcal/mol higher in energy for E = Si, Ge, Sn, and Pb, respectively. The 1,2-H-shift isomerization reaction (*lin*-HEN → *lin*-HNE) is exothermic with energy barriers of 11.4, 15.6, 19.9, and 21.7 kcal/mol for E = Si, Ge, Sn, and Pb, respectively, and the reverse reaction (*lin*-HNE → *lin*-HEN) has barrier heights of 78.9 (Si), 80.4 (Ge), 87.6 (Sn), and 93.2 kcal/mol (Pb). The TS is closer in energy to *lin*-HEN and the barrier height increases with E = Si to Pb. The (H, N, C) system behaves differently from rest of the homologues. *lin*-HCN is -14.9 kcal/mol lower in energy than *lin*-HNC. The energy barrier for the isomerization reaction (*lin*-HCN → *lin*-HNC) is 47.8 kcal/mol and the reaction is endothermic, with a reverse barrier height of 32.9 kcal/mol. The TS is closer in energy to the isomer *lin*-HNC (Figure 3.1b).

In Figure 3.1, the HN bond length in *lin*-HNE is almost same for E = C to Sn and slightly longer in *lin*-HNPb. The TS of the isomerization reaction, *lin*-HEN → *lin*-HNE, has a planar bent geometry, with N-E-H bond angles of 71.8 (C), 84.1 (Si), 82.2 (Ge), 79.8 (Sn), and 86.4° (Pb) and H attached to E. On going from *lin*-HEN to TS, the HE bond length increases by 0.118 (C), 0.029 (Si), 0.056 (Ge), 0.068 (Sn), and 0.102 Å (Pb). The increase in the HE bond length increases from Si to Pb, due to poor orbital overlap between H and heavier elements of Group 14. The HN bond length in the TS of the (H, N, C) system is only 0.398 Å longer than the HN bond length in *lin*-HNC, compared with a 1.103 Å longer HN bond length between the TS of (H, N, Si) and in *lin*-HNSi. The NE bond length increases by 0.033 (C), 0.137 (Si), 0.062 (Ge), 0.085 (Sn), and 0.174 Å (Pb) from *lin*-HEN to TS and then decreases by 0.018 (C), 0.045 (Si), 0.064 (Ge), 0.080 (Sn), and 0.110 Å (Pb) from TS to *lin*-HNE.

3.3.2 Natural Bond Orbital Analysis

Table 3.1 shows NBO data of the system (H, N, E). H has a positive natural partial atomic (NPA) charge, which increases from *lin*-HCN (0.23) to TS (0.35) and then to *lin*-HNC (0.44). The negative NPA charge on N increases from -0.29 in *lin*-HCN to -0.34 in TS and then to -0.69 in *lin*-HNC. C has almost a neutral charge in *lin*-HCN and TS and a positive charge of 0.26 in *lin*-HNC. The Wiberg bond index of the HN bond, *P*(HN), increases; however, *P*(CH) and *P*(NC) decrease first and then increase during the isomerization reaction (*lin*-HCN → TS → *lin*-HNC). In *lin*-HCN, there are three NC bond pair orbitals, one lone pair on N, and one CH bond pair. In TS there are two NC bond pairs, one three-centre two-electron (3C 2e) bonding orbital between H, C, and N and a lone pair on C. This shows that, during the isomerization reaction, one of the CN bonds and the HC bond in *lin*-HCN weakens and C retains its electrons as a lone pair and the octet rule is fulfilled by forming a 3C 2e bond between H, C, and N in the TS. In the product (*lin*-HNC), there are three NC bonds, one HN bond, and a lone pair on C with more s character (71.6%).

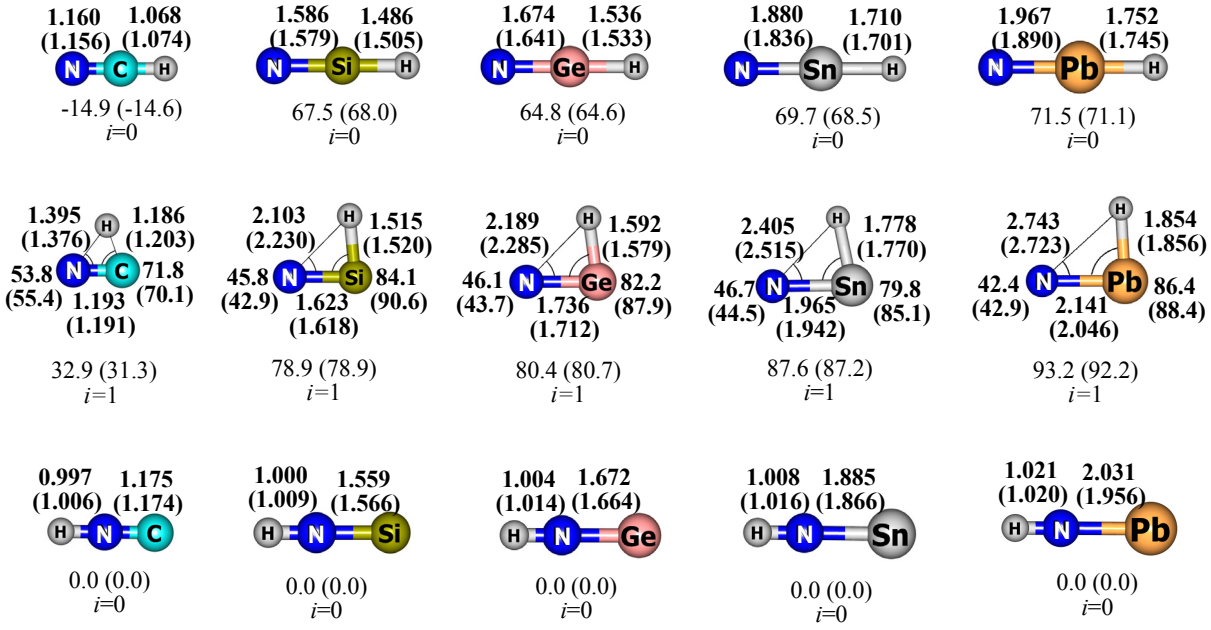

(a)

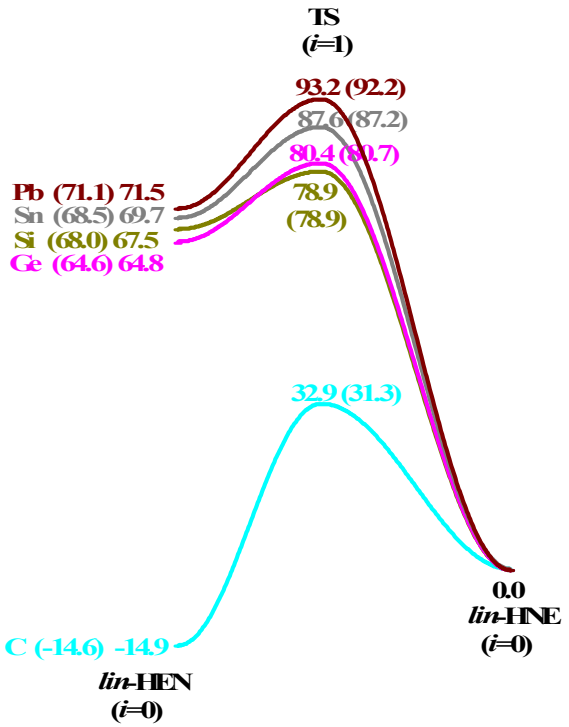

(b)

Figure 3.1: **(a)** Optimized geometries of the stationary points on the PES of the (H, N, E) system (E = C to Pb) at the CCSDT/TZVPP level. Relative energies in kcal/mol, bond distances in Å, and bond angles in degrees. BP86/TZ2P+ values are given in parentheses. Number of imaginary frequency is given by (*i*). **(b)** Energy profile diagram (reaction coordinate versus relative energy) of the (H, N, E) system.

H has a negative NPA charge of -0.12 in *lin*-HSiN and -0.04 in TS and a positive NPA charge of 0.40 in *lin*-HNSi. The negative partial charge on N decreases from *lin*-HSiN to TS and then increases from TS to *lin*-HNSi. There is a large negative partial charge of -1.36 on N in *lin*-HNSi relative to that of only -0.69 in *lin*-HNC. In *lin*-HSiN, Si has a positive charge of 1.10, which decreases to 0.83 in the TS and then increases to 0.96 in *lin*-HNSi. The NPA charges of the (H, N, C) and (H, N, Si) systems are different due to the difference in the electronegativity of the atoms involved in the systems.

Table 3.1: NBO analysis of (H, N, E) (E = C to Pb) at BP86/def2-TZVPP//BP86/TZ2P+.

	q(H)	q(N)	q(E)	*P*(HN)	*P*(NE)	*P*(HE)	LP(N)	LP(E)	LP(H)	BP(HN)	BP(NE)	BP(HE)	3C 2e
lin-HCN	0.23	-0.29	0.06	0.022	3.001	0.929	1				3	1	
TS	0.35	-0.34	-0.01	0.264	1.747	0.507	1	1			2		1
lin-HNC	0.44	-0.69	0.26	0.779	2.495	0.034		1		1	3		
lin-HSiN	-0.12	-0.99	1.10	0.095	2.673	0.893	1				3	1	
TS	-0.04	-0.78	0.83	0.218	2.234	0.792	1				3	1	
lin-HNSi	0.40	-1.36	0.96	0.820	1.755	-0.005		1		1	3		
lin-HGeN	-0.10	-0.94	1.04	0.143	2.642	0.850	1				3	1	
TS	-0.04	-0.73	0.77	0.269	2.146	0.743	1				3	1	
lin-HNGe	0.39	-1.33	0.94	0.818	1.788	0.032		1		1	3		
lin-HSnN	-0.17	-0.96	1.13	0.213	2.524	0.762	1				3	1	
TS	-0.12	-0.73	0.85	0.294	1.934	0.701	1	1			2		1
lin-HNSn	0.38	-1.36	0.98	0.835	1.723	0.027		1		1	3		
lin-HPbN	-0.15	-0.93	1.08	0.299	2.401	0.684	1				3	1	
TS	-0.13	-0.67	0.80	0.321	1.768	0.669	1	1			2		1
lin-HNPb	0.37	-1.33	0.96	0.836	1.750	0.032		1		1	3		

q-partial charge, *P*-Wiberg bond index, LP-number of lone pair orbitals, BP-number of bond pair orbitals and 3C 2e- number of 3center 2electron orbitals.

The Wiberg bond index *P*(HN) increases, whereas *P*(SiH) and *P*(NSi) decrease during the isomerization reaction (*lin*-HSiN → TS → *lin*-HNSi). The observed trend in Wiberg bond index of the (H, N, Si) system is almost same as that in the (H, N, C) system, except for *P*(NSi) due to the more polar NSi bond than that of the NC bond. In *lin*-HSiN and TS, there are three NSi bond pairs, one SiH bond pair, and one lone pair orbital on N. In the product, *lin*-HNSi, there are three NSi bonds, one HN bond, and one lone pair on Si. The bonding between the atoms is not altered much in *lin*-HSiN and TS (in contrast to the (H, N, C) system). In addition, NBO data are consistent with the observed energy barrier and structural changes of the system. The trend observed in NBO data of the other systems (H, N, E) E = Ge, Sn, and Pb are almost same as that in the (H, N, Si) system. The NBO analysis of the TS of (H, N, Sn) and (H, N, Pb) systems show a 3C 2e bond instead of HSn and HPb bonds. This might be due to poor overlap between the 1s orbital of H and the more diffuse valence sp hybrid orbital of the metal atoms Sn and Pb.

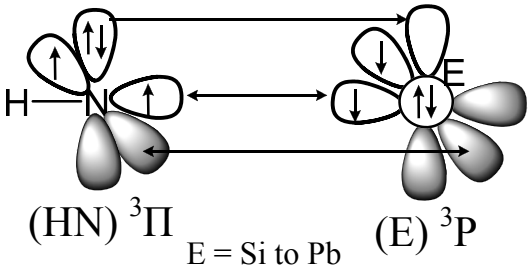

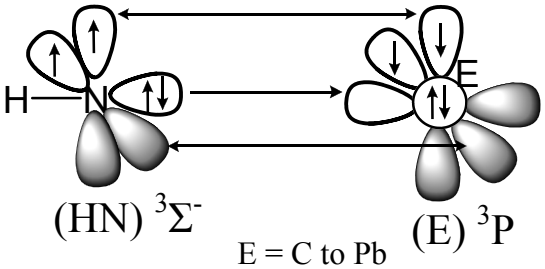

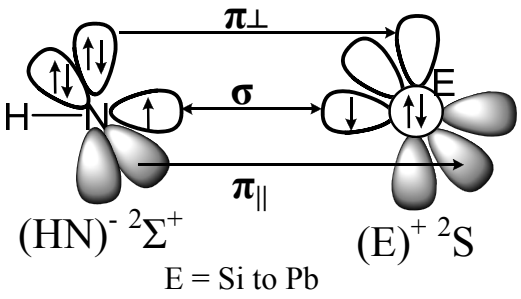

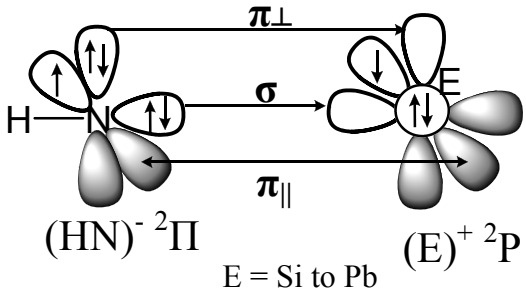

lin-HNE

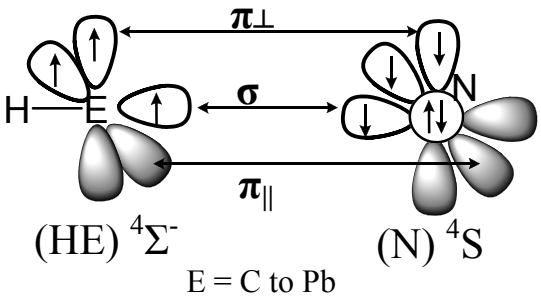

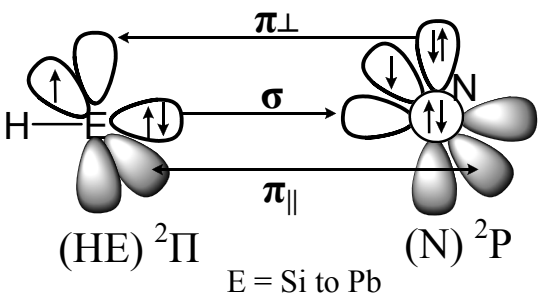

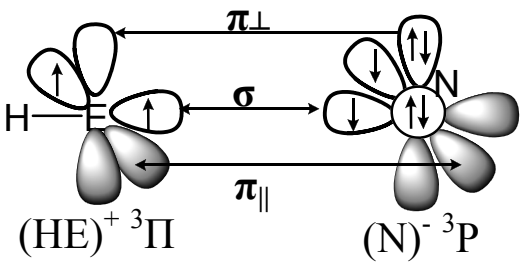

E = Si to Pb

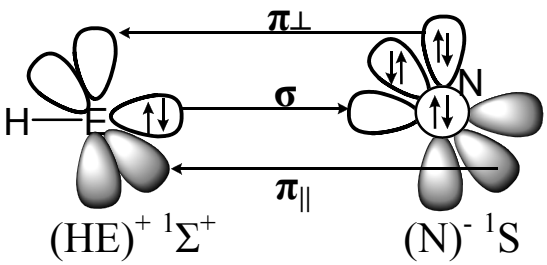

E = Si to Pb

lin-HEN

Scheme 3.2: Valence orbital interaction between the fragments HN or $(HN)^-$ and E or E^+ in *lin*-HNE and the valence orbital interaction between the fragments HE or $(HE)^+$ and N or N^- in lin-HEN.

3.3.3 Energy Decomposition Analysis

The nature of the bonding between E and N in the minima of the (H, N, E) system, E = Si to Pb, could be viewed as shown in Scheme 3.2. In *lin*-HNC, the fragment HN in the $^3\Sigma^-$ electronic state interacts with (^{3}P) C to form a σ-donor bond and two π-electron-sharing bonds. In *lin*-HCN, HC in the $^4\Sigma^-$ electronic state interacts with the ground-state N(^{4}S) to form a CN triple bond. Unlike the (H, N, C) system, both the neutral and charged fragments are considered for the (H, N, E) system, E = Si to Pb (Scheme 3.2), due to the larger NPA charge on the atoms involved in the system (Table 3.1).

Table 3.2: EDA of *lin*-HNSi and *lin*-HSiN at BP86/TZ2P+

lin-HNSi				
Inter.frags	HN($^3\Pi$) ; Si (^{3}P)	HN($^3\Sigma^-$) ; Si(^{3}P)	HN$^-$($^2\Sigma^+$) ; Si$^+$(^{2}S)	HN$^-$($^2\Pi$) ; Si$^+$(^{2}P)
Symmetry	C_{2v}	C_{2v}	C_{2v}	C_{2v}
ΔE_{int}	-240.3	-158.4	-423.6	-343.0
ΔE_{Pauli}	283.6	268.9	269.7	299.7
ΔE_{elstat}[a]	-161.2 (34.5)	-147.4 (34.5)	-351.3 (50.7)	-376.9 (58.6)
ΔE_{orb}[a]	-362.6 (65.5)	-280.0 (65.5)	-342.0 (49.3)	-265.9 (41.4)
ΔE(A1)[b]	-243.0 (67.0)	-96.6 (34.5)	-224.8 (65.7)	-139.2 (52.4)
ΔE(A2)[b]	0.0	0.0	0.0	0.0
ΔE(B1)[b]	-85.3 (23.5)	-91.7 (32.7)	-58.6 (17.1)	-71.5 (26.9)
ΔE(B2)[b]	-34.3 (9.5)	-91.7 (32.7)	-58.6 (17.1)	-55.2 (20.8)
ΔE_{prep}(HN)or (HN)$^-$	82.1	0.8	81.0	0.9
ΔE_{prep} Si or Si$^+$	0.0	0.0	0.0	0.0
ΔE_{corr}[d]	4.1	3.5	2.7	2.1
ΔE(= -D_e)	-154.1	-154.1	-339.9	-339.9
lin-HSiN				
Inter.frags	N(^{4}S) ; HSi ($^4\Sigma^-$)	N(^{2}P) ; HSi($^2\Pi$)	N$^-$(^{3}P) ;HSi$^+$($^3\Pi$)	N$^-$(^{1}S) ; HSi$^+$($^1\Sigma^+$)
Symmetry	C_{2v}	C_{2v}	C_{2v}	C_{2v}
ΔE_{int}	-144.8	-170.7	-342.9	-337.4
ΔE_{Pauli}	244.7	296.3	255.5	262.3
ΔE_{elstat}[a]	-121.8 (31.3)	-97.5 (20.9)	-336.3 (56.2)	-262.0 (43.7)
ΔE_{orb}[a]	-267.7 (68.7)	-369.5 (79.1)	-262.1 (43.8)	-337.8 (56.3)
ΔE(A1)[b]	-135.9 (50.8)	-257.3 (69.6)	-135.1 (51.6)	-186.7 (55.3)
ΔE(A2)[b]	0.0	0.0	0.0	0.0
ΔE(B1)[b]	-65.9 (24.6)	-75.6 (20.5)	-57.0 (21.7)	-75.5 (22.4)
ΔE(B2)[b]	-65.9 (24.6)	-36.7 (9.9)	-70.0 (26.7)	-75.5 (22.4)
ΔE_{prep} N or N$^-$	0.0	66.6	0.0	46.5
ΔE_{prep} HSior(HSi)$^+$	39.5	0.3	48.7	0.1
ΔE_{corr}[d]	3.7	2.2	3.3	0.0
ΔE(= -D_e)	-101.6	-101.6	-290.8	-290.8

[a] The values in parentheses are the percentage contributions to the total attractive interaction ΔE_{elstat} + ΔE_{orb}. [b] The values in parentheses are the percentage contributions to the total orbital interactions ΔE_{orb}. [d] Correction for spin polarization. Energy values in kcal/mol.

Table 3.2 shows the EDA results of *lin*-HNSi and *lin*-HSiN. Among the different schemes of interaction, one with the smallest orbital interaction (ΔE_{orb}) value is the best choice for describing bonding between the fragments being considered. In *lin*-HNSi, the charged fragments, HN$^-$($^2\Pi$) and Si$^+$(^{2}P), interacting in the doublet electronic state have the smallest ΔE_{orb} value (-265.9) and the preparation energy of the fragments is almost zero. However, the interaction between the neutral fragments, HN($^3\Sigma^-$) and Si(^{3}P), has only a slightly higher ΔE_{orb} value (-280.0), with zero preparation

energy for the fragments. In *lin*-HSiN, the charged fragments, $N^-(^3P)$ and $(HSi)^+(^3\Pi)$, interacting in the triplet electronic state have the smallest ΔE_{orb} value (-262.1), with a preparation energy of 48.7 kcal/mol for the fragment $(HSi)^+$. The interaction between the neutral fragments, $N(^4S)$ and HSi ($^4\Sigma^-$), has only a slightly higher ΔE_{orb} value (-267.7), with a preparation energy of 39.5 kcal/mol. The preparation energy of the fragment, $(HSi)^+$ is higher than that of HSi. The EDA results of the systems (H, N, E), E = Ge to Pb, are not expected to deviate much from the (H, N, Si) system due to the similarity in the NBO data.

In *lin*-HNE, the fragments interact in their ground state. In *lin*-HEN, the fragment HE or $(HE)^+$ needs an excitation energy of ($^2\Pi \rightarrow {}^4\Sigma^-$) or ($^1\Sigma^+ \rightarrow {}^3\Pi$) to interact with the ground state, $N(^4S)$ or N^- (^3P), and this excitation energy increases on going from HC to HPb (Table 3.3). During the isomerization reaction (*lin*-HEN → *lin*-HNE), the fragment HE transfers H to N and goes to the electronic ground state of E (in *lin*-HNE). Therefore, the reaction is exothermic for E = Si to Pb, in addition to the influence of the reaction energy profile by the charge, size, electronegativity, and the geometrical parameters. However, the excitation energy required for the HC fragment is only 15 kcal/mol at the BP86/TZ2P+ level (Table 3.3).

Table 3.3: Excitation energy (kcal/mol) of X ($^4S \rightarrow {}^2P$), HX ($^3\Sigma^- \rightarrow {}^3\Pi$), and HE ($^2\Pi \rightarrow {}^4\Sigma^-$) at BP86/TZ2P+. X = N to Bi and E = C to Pb.

	^4S g^1	^2P e^1		$^3\Sigma^-$ g^1	$^3\Pi$ e^1		$^2\Pi$ g^1	$^4\Sigma^-$ e^1
N	0.0	66.6 (*82.5*)	HN	0.0	81.5 (*85.2*)	HC	0.0	15.1 (*16.7*)
P	0.0	41.3 (*53.5*)	HP	0.0	83.1 (*84.3*)	HSi	0.0	39.5 (*36.4*)
As	0.0	39.3 (*52.0*)	HAs	0.0	85.5	HGe	0.0	46.9 (*47.8*)
Sb	0.0	34.4 (*46.9*)	HSb	0.0	79.5 (*76.9*)	HSn	0.0	45.2 (*44.5*)
Bi	0.0	32.8 (*61.9*)	HBi	0.0	81.7	HPb	0.0	51.9 (*50.3*)

[1] g – ground state and e –excited state

Experimental values are given in parenthesis (taken from NIST database, http://www.nist.gov/pml/data/). The experimental excitation values of atom X are given with respect to the excitation $^4S \rightarrow {}^2P_{3/2}$.

3.4 (H, P, E) System

3.4.1 Geometries and Energies

The stationary points characterized on the PES of the (H, P, E) system are shown in Figure 3.2a. For the (H, P, C) system, only two structures are characterized. One is the minimum, *lin*-HCP, and the other a second-order saddle-point geometry, *lin*-HPC, located 78.5 kcal/mol from the minimum. The (H, P, E) system, in which E = Si to Pb, has *bent*-HPE as the global minimum, *lin*-HEP as a local minimum, and TS structure connecting the two minima. *lin*-HPE is a second-order saddle-point geometry. *lin*-HPE (i = 2) is lower in energy than the TS (i = 1) and the local minimum, *lin*-HEP. However, *lin*-HSiP is 1.4 kcal/mol lower in energy at the CCSDT/TZVPP level of theory and almost equal in energy with *lin*-HPSi at the BP86/TZ2P+ level of theory.

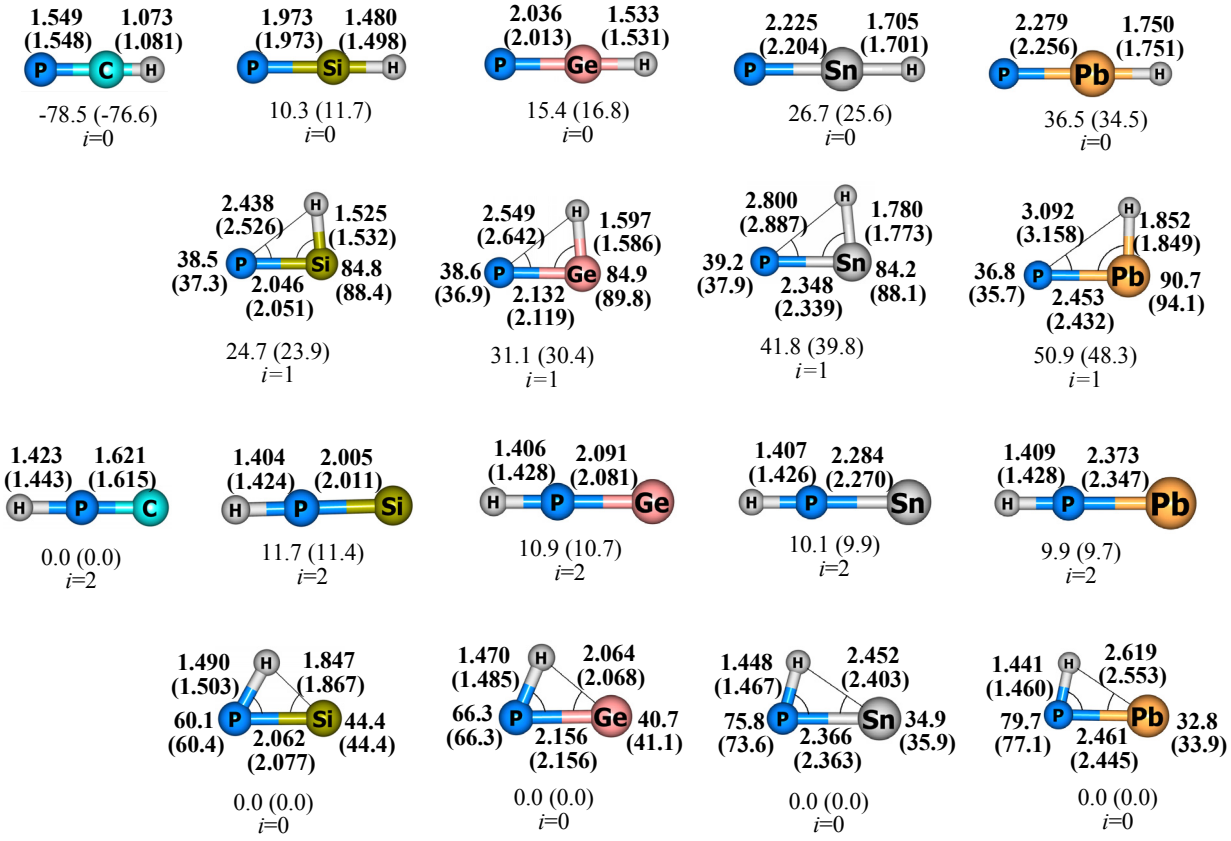

Figure 3.2: (a) Optimized geometries of the stationary points on the PES of the (H, P, E) system (E = C to Pb) at the CCSDT/TZVPP level. Relative energies in kcal/mol, bond distances in Å, and bond angles in degrees. BP86/TZ2P+ values are given in parentheses. Number of imaginary frequencies is given by (*i*). **(b)** Energy profile diagram (reaction coordinate versus relative energy) of the (H, P, E) system.

The reaction energy profile for the isomerization of *lin*-HEP → *bent*-HPE is shown in Figure 3.2b. The reaction is exothermic. The energy difference between the global minimum (*bent*-HPE) and the local minimum (*lin*-HEP) (the reverse-reaction energy) increases as the size of E increases: 10.3 (Si), 15.4 (Ge), 26.7 (Sn), and 36.5 kcal/mol (Pb). Also, the energy difference between *bent*-HPE and TS (the reverse-reaction barrier) increases as the size of E increases: 24.7 (Si), 31.1 (Ge), 41.8 (Sn), and 50.9 kcal/mol (Pb). However, the energy difference between *lin*-HEP and the TS (the forward-reaction barrier) remains almost constant in relation to the size of E: 14.4 (Si), 15.9 (Ge), 15.1 (Sn), and 14.4 kcal/mol (Pb). The TS is closer in energy to *lin*-HEP.

During the isomerization of *lin*-HEP to *bent*-HPE, the HE and PE bonds elongate, the P-E-H bond angle decreases, and the HP bond forms. In *bent*-HPE, the HP bond length decreases and the H-P-E bond angle increases from Si to Pb. The HP and PE bond lengths in *lin*-HPE are shorter than the HP and PE bond lengths in *bent*-HPE. The HP bond lengths in *lin*-HPE are same for E = Si to Pb and slightly longer in *lin*-HPC. The HE bond lengths in *lin*-HEN and *lin*-HEP are almost same for E = C to Pb, also the HE distances in the TS of the (H, N, E) and (H, P, E) systems are almost the same for E = Si to Pb.

Table 3.4: NBO analysis of (H, P, E) (E = C to Pb) at BP86/def2-TZVPP//BP86/TZ2P+.

	q(H)	q(P)	q(E)	*P*(HP)	*P*(PE)	*P*(HE)	LP(P)	LP(E)	LP(H)	BP(HP)	BP(PE)	BP(HE)	3C 2e
lin-HCP	0.22	0.50	-0.72	0.031	2.926	0.925	1				3	1	
lin-HPC	0.09	0.28	-0.37	0.852	2.976	0.146	1			1	3		
lin-HSiP	-0.09	-0.29	0.38	0.076	2.960	0.919	1				3	1	
TS	-0.07	-0.11	0.18	0.183	2.448	0.826	1				3	1	
bent-HPSi	-0.03	-0.37	0.40	0.797	1.995	0.235	1	1			2		1
lin-HPSi	0.10	-0.53	0.43	0.907	2.422	0.086		1		1	3		
lin-HGeP	-0.07	-0.29	0.36	0.116	2.907	0.883	1				3	1	
TS	-0.06	-0.13	0.19	0.201	2.370	0.810	1				3	1	
bent-HPGe	-0.01	-0.44	0.45	0.858	1.973	0.170	1	1			2		1
lin-HPGe	0.10	-0.53	0.43	0.905	2.412	0.089		1		1	3		
lin-HSnP	-0.13	-0.44	0.57	0.157	2.784	0.829	1				3	1	
TS	-0.13	-0.22	0.35	0.224	2.179	0.769	1				3	1	
bent-HPSn	-0.01	-0.57	0.59	0.921	1.886	0.094	1	1		1	2		
lin-HPSn	0.09	-0.66	0.57	0.914	2.251	0.083		1		1	3		
lin-HPbP	-0.12	-0.43	0.55	0.231	2.643	0.761	1		1		3		
TS	-0.13	-0.22	0.36	0.235	2.024	0.235	1	1			2		1
bent-HPPb	-0.01	-0.59	0.60	0.941	1.877	0.073	1	1		1	2		
lin-HPPb	0.08	-0.66	0.58	0.916	2.224	0.082		1		1	3		

q-partial charge, *P*-Wiberg bond index, LP-number of lone pair orbitals, BP-number of bond pair orbitals and 3C 2e- number of 3center 2electron orbitals.

3.4.2 Natural Bond Orbital Analysis

Table 3.4 shows the NBO data of the system (H, P, E). During the isomerization of *lin*-HEP to *bent*-HPE (for E = Si to Pb), the smaller negative charge on H decreases, both the negative charge on P and the positive charge on E decrease first from *lin*-HEP to TS and then increase from TS to *bent*-HPE. On going from *bent*-HPE to *lin*-HPE, H becomes positively charged; the negative charge on P increases and the charge on E do not change significantly. The NPA charges of the systems (H, P, Si)

and (H, P, Ge) are almost the same and increase in the systems (H, P, Sn) and (H, P, Pb). The Wiberg bond indices, *P*(HP) increases and *P*(HE) and *P*(PE) decrease from *lin*-HEP to TS and from TS to *bent*-HPE. *P*(HP) and *P*(PE) increase from *bent*-HPE to *lin*-HPE. The Wiberg bond index *P*(HP) increases, and the *P*(PE) and *P*(EH) decrease in the (H, P, E) system on moving from Si to Pb. The number of bond pairs, lone pairs, and 3C 2e bonding orbitals in the (H, P, E) systems are shown in Table 3.4. P has a lone pair in each of the structures *lin*-HEP, TS, and *bent*-HPE. Both *bent*-HPE and *lin*-HPE have a lone pair orbital on E. There are three PE bonds in *lin*-HEP, TS, and *lin*-HPE; two PE bonds and a 3C 2e orbital between H, P, and E in *bent*-HPE. *lin*-HEP and TS have an HE bonding pair and *lin*-HPE has an HP bonding orbital.

3.4.3 Energy Decomposition Analysis

Scheme 3.3 shows the orbital interactions between the atoms X and E in *lin*-HXE, *lin*-HEX, and *bent*-HXE. The EDA results of *lin*-HEP, *bent*-HPE, and *lin*-HPE are given in Table 3.5. The EDA of *lin*-HEP and *lin*-HPE are performed with C_{2v} symmetry and the EDA of *bent*-HPE is performed with C_s symmetry. The ETS-NOCV analysis of *bent*-HPE is performed to separate the ΔE_{σ} and $\Delta E_{\pi\|}$ contributions, since both contributions come under the same irreducible representation, A′ in EDA.

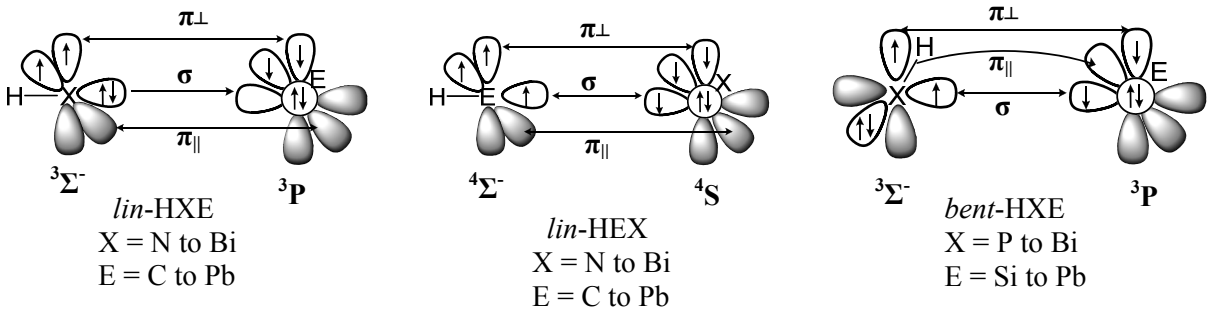

Scheme 3.3: Valence orbital interactions between the atoms X and E in *lin*-HXE, *lin*-HEX, and *bent*-HXE.

In *lin*-HEP, ($^4\Sigma^-$) HE and (^{4}S) P interact to form the PE triple bond (Scheme 3.3). The instantaneous interaction energy (ΔE_{int}) between fragments HE and P is same for *lin*-HSiP and *lin*-HGeP and decreases in *lin*-HSnP and *lin*-HPbP. The Pauli repulsion of the PE bond in *lin*-HEP increases from Si to Ge, then it decreases in Sn and then increases again from Sn to Pb. The ΔE_{elstat} term increases and the ΔE_{orb} term decreases on going from Si to Pb. The dissociation energy, D_e, of *lin*-HEP decreases from Si to Pb. The preparation energy (ΔE_{prep}) for P is 0.0 kcal/mol, because P interacts in its ground state. The preparation energy of HE, which is the excitation energy ($^2\Pi \rightarrow {}^4\Sigma^-$), increases on going down the group (Si to Pb). EDA and ETS-NOCV analyses of *bent*-HPE are performed between the fragments HP ($^3\Sigma^-$) and E (^{3}P) (Scheme 3.3). Figure 3.3 shows the most important deformation densities and the energies of the valence orbital interactions between the fragments HP and E in *bent*-HPE. The deformation densities, $\Delta\rho_{\sigma}^{\alpha}$ and $\Delta\rho_{\sigma}^{\beta}$, indicate the charge flow of α and β electrons in the σ-type orbital of one fragment to the other. Similarly, $\Delta\rho_{\pi\|}^{\alpha}$ and $\Delta\rho_{\pi\|}^{\beta}$

indicate the $\pi_{\|}$-type orbital (in-plane π orbital) and $\Delta\rho^{\alpha}_{\pi\perp}$ and $\Delta\rho^{\beta}_{\pi\perp}$ indicate the $\pi_{\perp}$-type orbital (out-of-plane π orbital). The $\Delta E_{\pi\|}$ contribution of *bent*-HPE in Table 3.4 was taken from the energy of the deformation densities, $\Delta\rho^{\alpha}_{\pi\|}$ and $\Delta\rho^{\beta}_{\pi\|}$ (Figure 3.3), and the ΔE_{σ} contribution was given by the equation $\Delta E_{\sigma} = \Delta E_{orb} - \Delta E_{\pi\|} - \Delta E_{\pi\perp}$. The ΔE_{int} and ΔE_{Pauli} terms decrease from Si to Pb. The percentage electrostatic contribution increases from Si to Pb. In *bent*-HPE, there is one σ and one π bond between P and E and their contribution to the total orbital interaction is given under ΔE_{σ} and $\Delta E_{\pi\perp}$, respectively.

Table 3.5: EDA and ETSNOCV analyses of (H, P, E) for E = Si, Ge, Sn, and Pb at BP86/TZ2P+.

lin-HEP				
Inter.frags	HSi($^4\Sigma^-$) ; P (^{4}S)	HGe($^4\Sigma^-$) ; P (^{4}S)	HSn($^4\Sigma^-$) ; P (^{4}S)	HPb($^4\Sigma^-$) ; P (^{4}S)
Symmetry	C_{2v}	C_{2v}	C_{2v}	C_{2v}
ΔE_{int}	-127.8	-127.0	-110.4	-108.7
ΔE_{Pauli}	181.0	196.7	174.2	184.7
ΔE_{elstat}[a]	-114.9 (37.2)	-131.9 (40.7)	-123.1 (43.3)	-125.8 (42.9)
ΔE_{orb}[a]	-193.8 (62.8)	-191.9 (59.3)	-161.5 (56.7)	-167.6 (57.1)
ΔE (A1)	-102.6 (52.9)	-103.6 (54.0)	-83.9 (51.9)	-88.7 (52.9)
ΔE (A2)	0.0 (0.0)	0.0 (0.0)	0.1 (-0.1)	0.1 (-0.1)
ΔE (B1)	-45.6 (23.6)	-44.2 (23.0)	-38.9 (24.1)	-39.6 (23.6)
ΔE (B2)	-45.6 (23.6)	-44.2 (23.0)	-38.9 (24.1)	-39.6 (23.6)
ΔE_{prep} (P)	0.0	0.0	0.0	0.0
ΔE_{prep} (HE)	39.6	47.4	45.8	54.4
ΔE_{corr}[d]	2.1	1.8	1.7	2.2
ΔE(= $-D_e$)	-86.1	-77.8	-62.9	-52.1
bent-HPE				
Inter. frags	HP($^3\Sigma^-$) ; Si (^{3}P)	HP($^3\Sigma^-$) ; Ge (^{3}P)	HP($^3\Sigma^-$) ; Sn (^{3}P)	HP($^3\Sigma^-$) ; Pb (^{3}P)
Symmetry	C_s	C_s	C_s	C_s
ΔE_{int}	-98.0	-89.7	-77.4	-72.0
ΔE_{Pauli}	280.0	244.0	200.2	184.7
ΔE_{elstat}[a]	-165.5 (43.8)	-154.1 (46.2)	-134.6 (48.5)	-126.0 (49.1)
ΔE_{orb}[a]	-212.5 (56.2)	-179.6 (53.8)	-143.1 (51.5)	-130.7 (50.9)
ΔE_{σ}[b]	-136.8 (64.4)	-118.3 (65.9)	-96.3 (67.3)	-89.7 (68.6)
$\Delta E_{\pi\|}$[b]	-26.3 (12.4)	-17.6 (9.8)	-10.2 (7.1)	-7.6 (5.9)
$\Delta E_{\pi\perp}$[b]	-49.5 (23.3)	-43.7 (24.3)	-36.6 (25.6)	-33.4 (25.5)
ΔE_{prep} (HP)	0.7	0.4	0.1	0.1
ΔE_{prep} (E)	0.0	0.0	0.0	0.0
ΔE_{corr}[d]	2.4	2.3	2.2	2.2
ΔE(= $-D_e$)	-94.9	-86.9	-75.1	-69.7
lin-HPE				
Inter.frags	HP($^3\Sigma^-$) ; Si (^{3}P)	HP($^3\Sigma^-$) ; Ge (^{3}P)	HP($^3\Sigma^-$) ; Sn (^{3}P)	HP($^3\Sigma^-$) ; Pb (^{3}P)
Symmetry	C_{2v}	C_{2v}	C_{2v}	C_{2v}
ΔE_{int}	-85.9	-78.6	-67.4	-62.2
ΔE_{Pauli}	165.7	157.9	137.5	127.1
ΔE_{elstat}[a]	-73.5 (29.2)	-79.2 (33.5)	-74.6 (36.4)	-69.8 (36.9)
ΔE_{orb}[a]	-178.0 (70.8)	-157.3 (66.5)	-130.3 (63.6)	-119.5 (63.1)
ΔE(A1)[b]	-72.6 (40.8)	-61.9 (39.4)	-44.0 (33.8)	-40.0 (33.5)
ΔE(A2)[b]	0.0 (0.0)	0.0 (0.0)	0.0 (0.0)	0.0 (0.0)
ΔE(B1)[b]	-52.7 (29.6)	-47.7 (30.3)	-43.1 (33.1)	-39.8 (33.3)
ΔE(B2)[b]	-52.7 (29.6)	-47.7 (30.3)	-43.1 (33.1)	-39.8 (33.3)
ΔE_{prep} (HP)	0.1	0.1	0.1	0.1
ΔE_{prep} (E)	0.0	0.0	0.0	0.0
ΔE_{corr}[d]	2.4	2.3	2.2	2.1
ΔE(= $-D_e$)	-83.4	-76.2	-65.1	-60.0

Table 3.5 continued:		*lin*-HPE		
Inter.frags	HP($^3\Pi$) ; Si (^{3}P)	HP($^3\Pi$) ; Ge (^{3}P)	HP($^3\Pi$) ; Sn (^{3}P)	HP($^3\Pi$) ; Pb (^{3}P)
Symmetry	C_{2v}	C_{2v}	C_{2v}	C_{2v}
ΔE_{int}	-169.4	-162.1	-150.9	-145.8
ΔE_{Pauli}	185.3	170.6	148.7	138.0
ΔE_{elstat} [a]	-129.1 (36.4)	-122.5 (36.8)	-109.7 (36.6)	-101.8 (35.9)
ΔE_{orb} [a]	-225.6 (63.6)	-210.2 (63.2)	-189.9 (63.4)	-182.0 (64.1)
$\Delta E(A1)$ [b]	-133.3 (59.1)	-127.5 (60.6)	-121.7 (64.1)	-120.7 (66.3)
$\Delta E(A2)$ [b]	0.0 (0.0)	0.0 (0.0)	0.0 (0.0)	0.0 (0.0)
$\Delta E(B1)$ [b]	-49.7 (22.0)	-45.0 (21.4)	-40.1 (21.1)	-37.3 (20.5)
$\Delta E(B2)$ [b]	-42.7 (18.9)	-37.8 (18.0)	-28.1 (14.9)	-23.9 (13.2)
ΔE_{prep} (E)	0.0	0.0	0.0	0.0
ΔE_{prep} (HP)	83.4	83.3	83.4	83.3
ΔE_{corr} [d]	2.6	2.5	2.4	2.4
$\Delta E(= -D_e)$	-83.4	-76.2	-65.1	-60.0

[a] The values in parentheses are the percentage contributions to the total attractive interaction $\Delta E_{elstat} + \Delta E_{orb}$. [b] The values in parentheses are the percentage contributions to the total orbital interactions ΔE_{orb}. [d] Correction for spin polarization. Energy values in kcal/mol.

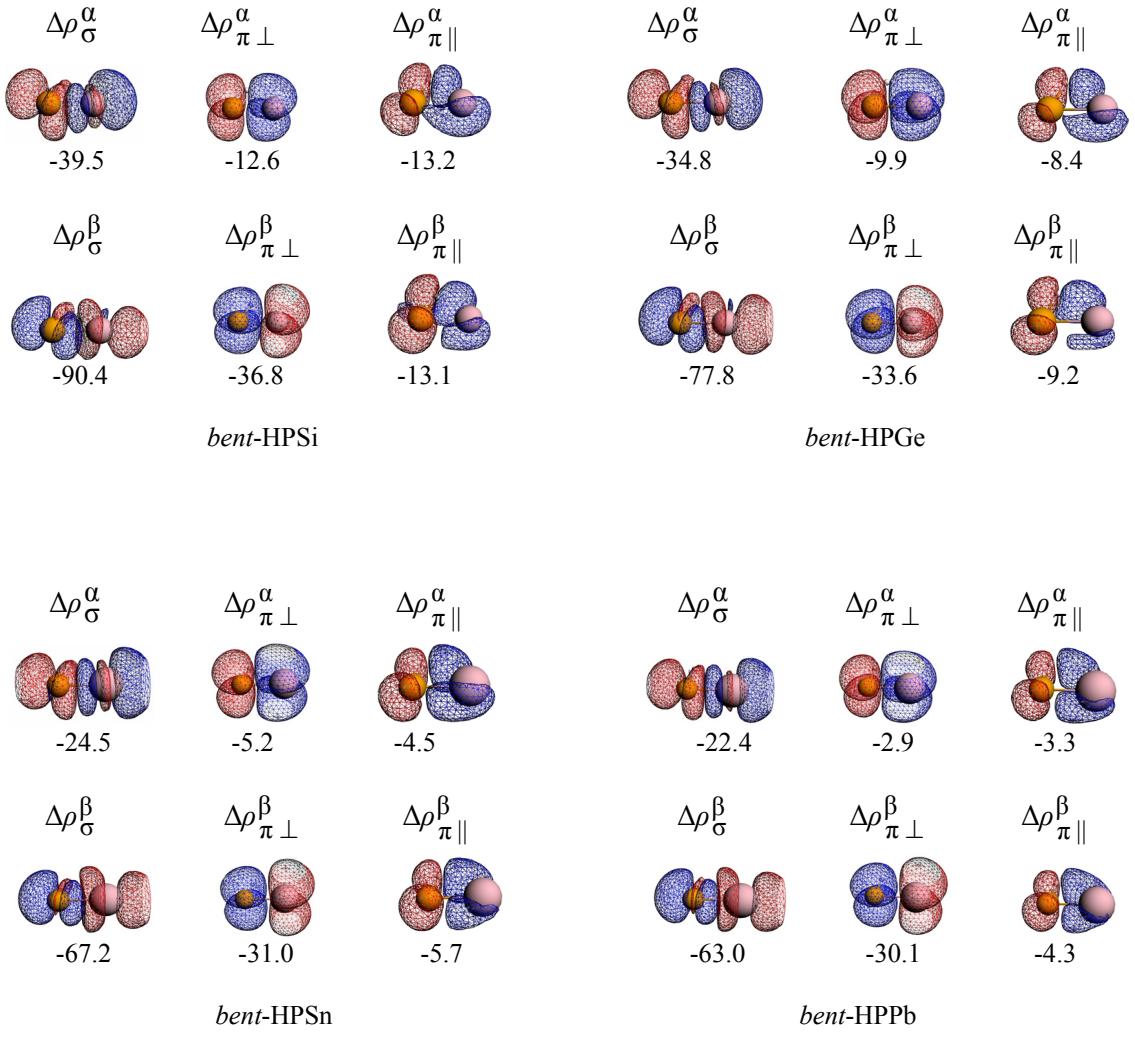

Figure 3.3

Figure 3.3: The most important deformation densities and the energies (kcal/mol) of the valance orbital interaction between the fragments HP and E in *bent*-HPE at BP86/TZ2P+.
The deformation densities $\Delta\rho_{\sigma}^{\alpha}$ and $\Delta\rho_{\sigma}^{\beta}$ indicates the charge flow of α and β electrons in the σ-type orbital of one fragment to the other (direction of charge flow: red to blue). Similarly $\Delta\rho_{\pi||}^{\alpha}$ and $\Delta\rho_{\pi||}^{\beta}$ for $\pi_{||}$ type orbital (in plane π orbital) and $\Delta\rho_{\pi\perp}^{\alpha}$ and $\Delta\rho_{\pi\perp}^{\beta}$ for $\pi_{\perp}$ type orbital (out of plane π orbital). $\Delta\rho_{\pi||}^{\alpha}$ and $\Delta\rho_{\pi||}^{\beta}$ looks similar due to the dative bond: HP bond pair electron donation in to the empty $p_{\pi||}$ orbital on E.

NBO analysis showed a lone pair on each of the P and E (Table 3.4). The octet electron configuration on E is attained by the HP bond-pair electron donation to the empty p_{π} orbital of E and this contribution is given by $\Delta E_{\pi||}$. The $\Delta E_{\pi||}$ contribution decreases with increasing the size of E, and hence, the HP bond length decreases as the size of E increases. Moreover, the Wiberg bond index of the HP bond, *P*(HP), in *bent*-HPE increases, whereas *P*(HE) decreases from Si to Pb (Table 3.4). The dissociation energy decreases from *bent*-HPSi to *bent*-HPPb. In *bent*-HPE, both fragments interact in their ground state. During the isomerization of *lin*-HEP to *bent*-HPE, the fragment HE in *lin*-HEP relaxes to the ground state of E in *bent*-HPE by transferring H to P, and hence, the reaction is exothermic.

In *lin*-HPE, the fragments HP and E interact in their ground state, as shown in Scheme 3.3. The trend observed in ΔE_{int}, ΔE_{Pauli}, and dissociation energy is almost the same as that in *bent*-HPE on going from Si to Pb. However, the percentage electrostatic contribution (ΔE_{elstat}) to the total interaction (ΔE_{int}) in *bent*-HPE is relatively higher than that of *lin*-HPE and is the driving force for the molecule (*lin*-HPE) to bend. The dissociation energies of *lin*-HEP and *lin*-HPE are almost the same (Table 3.5).

3.5 (H, As, E) System

3.5.1 Geometries and Energies

The stationary points characterized on the PES of the (H, As, E) system are shown in Figure 3.4a. For the (H, As, C) system, only linear structures are characterized; one is the minimum, *lin*-HCAs, and the other a second-order saddle-point geometry, *lin*-HAsC, which is located 77.3 kcal/mol higher than the minimum. The (H, As, E) system, in which E = Si to Pb, has a global minimum (*bent*-HAsE), a local minimum (*lin*-HEAs), and a TS structure connecting the two minima. *lin*-HAsE is a second-order saddle-point geometry. *lin*-HAsE (E = Si and Ge) is higher in energy than *lin*-HEAs (E = Si and Ge); however, for E = Sn and Pb, *lin*-HAsE is lower in energy than *lin*-HEAs. The reaction energy profile for the isomerization of *lin*-HEAs → *bent*-HAsE is shown in Figure 3.4b. The reaction is exothermic and the energy difference between the global minimum (*bent*-HAsE) and the local minimum (*lin*-HEAs) (the reverse-reaction energy) increases with increasing the size of E: 4.7 (Si), 9.5 (Ge), 19.7 (Sn), and 29.7 kcal/mol (Pb). In addition, the energy difference between *bent*-HAsE and TS (the reverse-reaction barrier) increases with increasing the size of E: 17.9 (Si), 23.6 (Ge), 33.2 (Sn), and 41.9 kcal/mol (Pb).

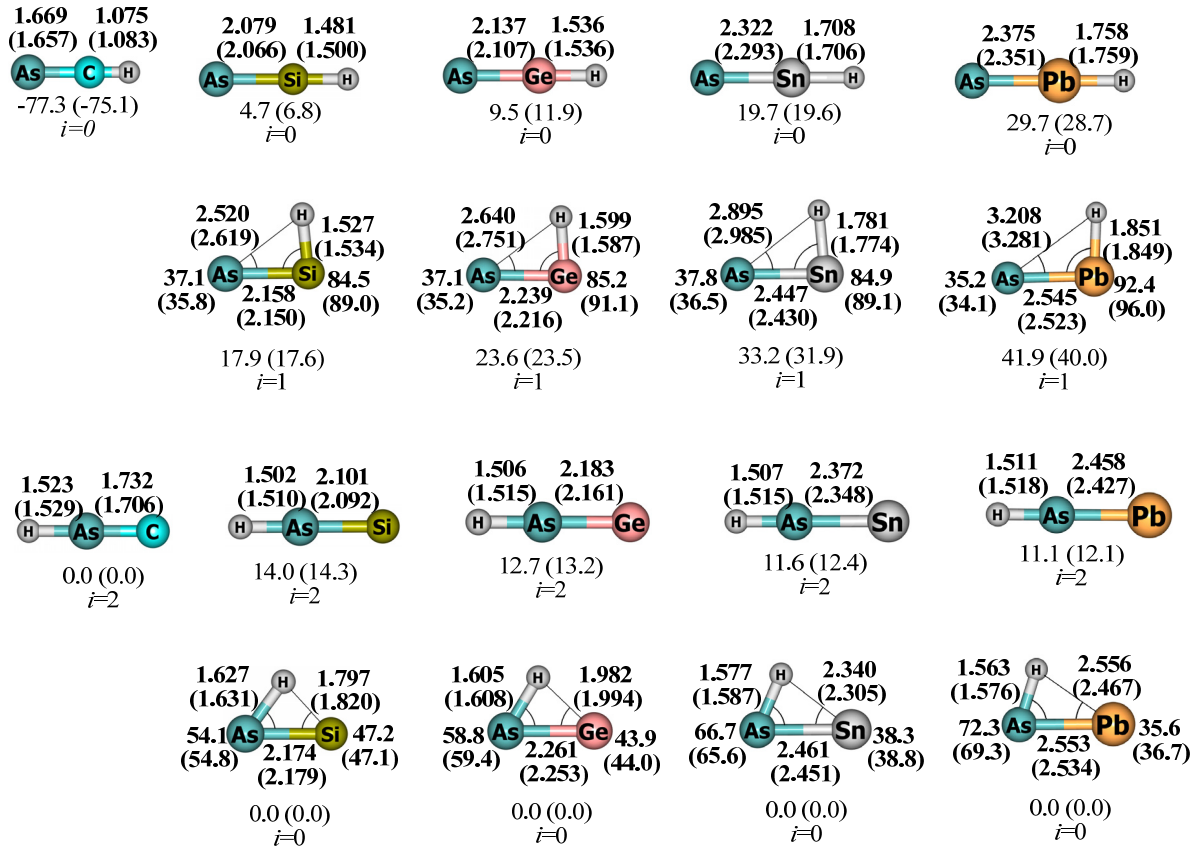

(a)

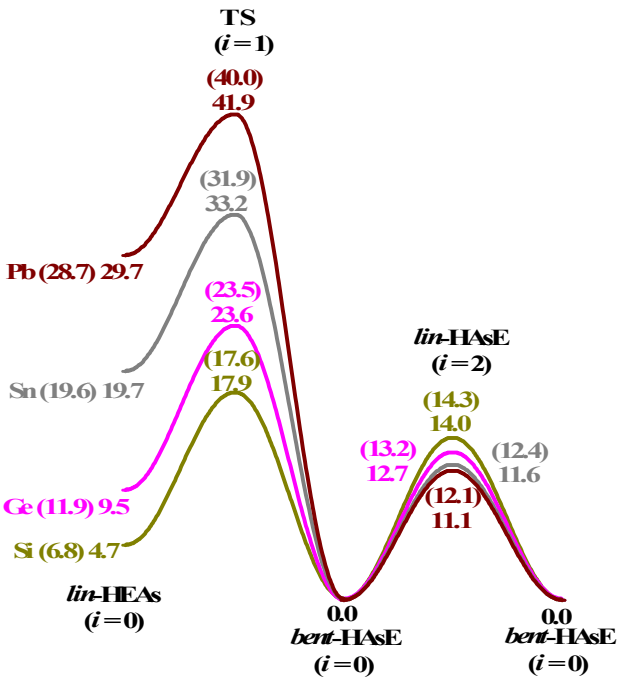

(b)

Figure 3.4: (a) Optimized geometry of the stationary points on the PES of the (H, As, E) system (E = C to Pb) at the CCSDT/TZVPP level. Relative energies in kcal/mol, bond distances in Å, and bond angles in degrees. BP86/TZ2P+ values are given in parentheses. Number of imaginary frequencies is given by (*i*). **(b)** Energy profile diagram (reaction coordinate versus relative energy) of the (H, As, E) system.

However, the energy difference between *lin*-HEAs and TS (the forward-reaction barrier) remains almost constant with respect to E: 13.2 (Si), 14.1 (Ge), 13.5 (Sn), and 12.2 kcal/mol (Pb). The TS is closer in energy to *lin*-HEAs.

During the isomerization of *lin*-HEAs to *bent*-HAsE, the AsE and HE bonds elongate, the P-E-H bond angle decreases, and the HAs bond forms. In *bent*-HAsE, the HAs bond length decreases and the H-As-E bond angle increases with increasing the size of E (Si to Pb). The HAs and AsE bond lengths in *lin*-HAsE are shorter than the HAs and AsE bond lengths in *bent*-HAsE. The HAs bond length in *lin*-HAsE is same for E = Si to Pb and slightly longer in *lin*-HAsC. Another interesting observation is that the HE bond in *bent*-HAsE gets shorter than the HE bond in *bent*-HPE. The HE bond lengths in *lin*-HEN and *lin*-HEP are almost same for each of E = C to Pb. Also, the HE bond lengths in the TS of the (H, N, E) and (H, P, E) systems are almost the same for E = Si to Pb.

3.5.2 Natural Bond Orbital Analysis

Table 3.6 shows the NBO data of the system (H, As, E). The trend observed in the NPA charges and the Wiberg bond index are same as those of the (H, P, E) system with small changes in the absolute values, due to the more electropositive character of As compared with P. The Wiberg bond index of the HE bond in *bent*-HAsE is increased relative to that of the HE bond in *bent*-HPE. The number of lone pairs, bond pairs, and 3C 2e pair orbitals in the (H, As, E) system are almost the same as those of the (H, P, E) system.

Table 3.6: NBO analysis of (H, As, E) (E = C to Pb) at BP86/def2-TZVPP//BP86/TZ2P+.

	q(H)	q(As)	q(E)	*P*(HAs)	*P*(AsE)	*P*(HE)	LP(As)	LP(E)	LP(H)	BP(HAs)	BP(AsE)	BP(HE)	3C 2e
lin-HCAs	0.21	0.54	-0.76	0.035	2.910	0.924	1				3	1	
lin-HAsC	0.06	0.36	-0.42	0.821	2.972	0.181		1		1	3		
lin-HSiAs	-0.10	-0.19	0.29	0.083	2.964	0.911	1				3	1	
TS	-0.08	-0.02	0.10	0.170	2.439	0.836	1				3	1	
bent-HAsSi	-0.07	-0.23	0.30	0.727	2.035	0.306	1	1			2		1
lin-HAsSi	0.09	-0.44	0.35	0.889	2.481	0.108		1		1	3		
lin-HGeAs	-0.07	-0.18	0.26	0.122	2.908	0.876	1				3	1	
TS	-0.07	-0.03	0.10	0.184	2.369	0.824	1				3	1	
bent-HAsGe	-0.05	-0.30	0.36	0.794	2.013	0.236	1	1			2		1
lin-HAsGe	0.08	-0.44	0.36	0.887	2.462	0.111		1		1	3		
lin-HSnAs	-0.14	-0.33	0.46	0.163	2.798	0.822	1				3	1	
TS	-0.14	-0.14	0.28	0.208	2.182	0.781	1				3	1	
bent-HAsSn	-0.05	-0.46	0.51	0.874	1.922	0.142	1	1			2		1
lin-HAsSn	0.07	-0.57	0.50	0.900	2.304	0.099		1		1	3		
lin-HPbAs	-0.12	-0.32	0.45	0.235	2.652	0.755	1				3	1	
TS	-0.14	-0.15	0.29	0.216	2.037	0.770	1	1			2		1
bent-HAsPb	-0.05	-0.48	0.53	0.905	1.908	0.108	1	1		1	2		
lin-HAsPb	0.07	-0.57	0.51	0.904	2.271	0.096		1		1	3		

q-partial charge, *P*-Wiberg bond index, LP-number of lone pair orbitals, BP-number of bond pair orbitals, and 3C 2e- number of 3center 2electron orbitals.

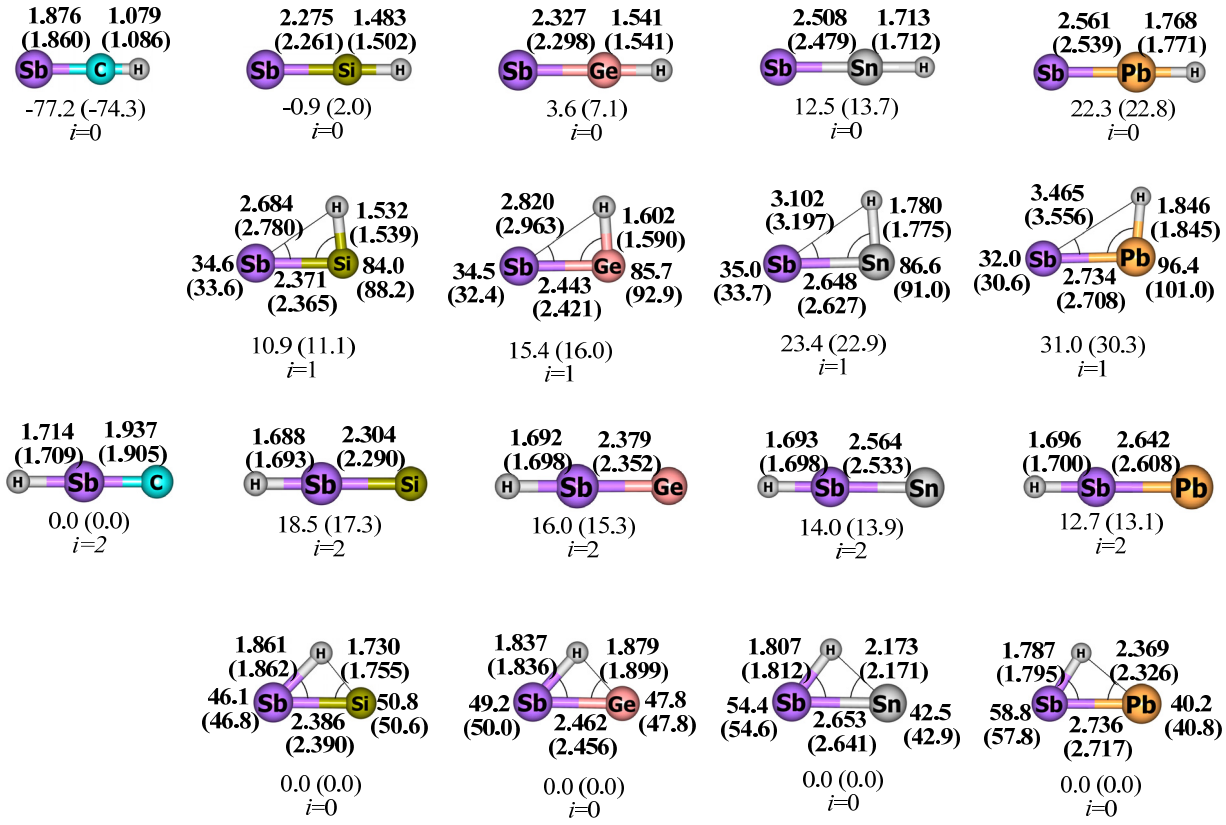

(a)

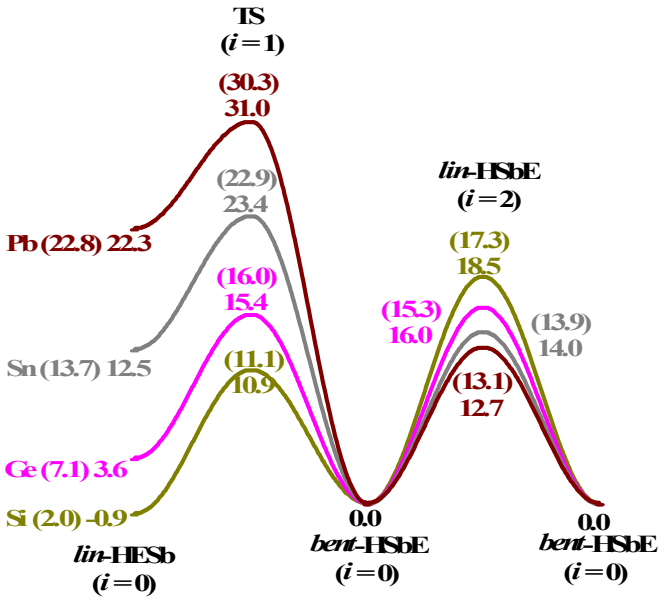

(b)

Figure 3.5: (a) Optimized geometry of the stationary points on the PES of (H, Sb, E) system (E = C to Pb) at the CCSDT/TZVPP level. Relative energies in kcal/mol, bond distances in Å, and bond angles in degrees. BP86/TZ2P+ values are given in parentheses. Number of imaginary frequencies is given by (*i*). **(b)** Energy profile diagram (reaction coordinate versus relative energy) of the (H, Sb, E) system.

3.6 (H, Sb, E) System

3.6.1 Geometries and Energies

The stationary points characterized on the PES of the (H, Sb, E) system are shown in Figure 3.5a. Similar to the (H, P, C) and (H, As, C) systems, (H, Sb, C) has only linear structures. One is the minimum, *lin*-HCSb, and the other is a second-order saddle-point geometry, *lin*-HSbC, located 77.2 kcal/mol higher than the minimum. (H, Sb, E), in which E = Ge to Pb, has a global minimum (*bent*-HSbE), a local minimum (*lin*-HESb), and a TS structure connecting the two minima. In the (H, Sb, Si) system, *lin*-HSiSb is -0.9 kcal/mol lower in energy than *bent*-HSbSi at the CCSD(T)/TZVPP level and 2.0 kcal/mol higher in energy at the BP86/TZ2P+ level of theory. *lin*-HSbE is a second-order saddle point. For E = Si to Sn, the energy of *lin*-HSbE is higher than that of *lin*-HESb. *lin*-HSbPb is lower in energy than *lin*-HPbSb. The reaction energy profile for the isomerization of *lin*-HESb → *bent*-HSbE is shown in Figure 3.5b. The reaction is exothermic except for E = Si. The energy difference between the global minimum (*bent*-HSbE) and the local minimum (*lin*-HESb) (the reverse-reaction energy) increases with increasing the size of E, -0.9 (Si), 3.6 (Ge), 12.5 (Sn), and 22.3 kcal/mol (Pb), and becomes smaller compared with the (H, P, E) and (H, As, E) systems, as a result of which, *lin*-HSiSb and *bent*-HSbSi become almost degenerate. The energy difference between *bent*-HSbE and TS (the reverse-reaction barrier) increases with increasing the size of E: 10.9 (Si), 15.4 (Ge), 23.4 (Sn), and 31.0 kcal/mol (Pb). The energy difference between *lin*-HESb and the TS (the forward-reaction barrier) decreases with the size of E: 12.8 (Si), 11.8 (Ge), 10.9 (Sn), and 8.7 kcal/mol (Pb). The TS is closer in energy to *lin*-HESb, except for *lin*-HSiSb.

The structural changes during the isomerization of *lin*-HESb to *bent*-HSbE are almost the same as those in the (H, P, E) and (H, As, E) systems. The HSb and SbE bond lengths in *lin*-HSbE are shorter than the HSb and SbE bond lengths in *bent*-HSbE. The HSb bond length in *lin*-HSbE is almost the same for E = Si to Pb and a little longer in *lin*-HSbC. The HE bond in *bent*-HSbE is shorter than the HE bond in *bent*-HPE and *bent*-HAsE. The EH bond lengths in *lin*-HEN, *lin*-HEP, *lin*-HEAs, and *lin*-HESb are almost the same for E = C to Pb. Also, the HE bond length in the TSs of (H, N, E), (H, P, E), (H, As, E), and (H, Sb, E) are almost the same for E = Si to Pb.

3.6.2 Natural Bond Orbital Analysis

Table 3.7 shows the NBO data of the system (H, Sb, E). The trend in the change in the Wiberg bond index of the (H, Sb, E) system is the same as that in the (H, P, E) and (H, As, E) systems with small changes in the absolute values. This is due to the increase in the electropositive character of Sb. In the (H, Sb, E) system, the positive charge on E decreases compared with (H, P, E) and (H, As, E) and Sb has neutral, positive, or negative charges compared with only a negative charge on P and As in the (H, P, E) and (H, As, E) systems. The Wiberg bond index of the HE bond in *bent*-HSbE is increased and the *P*(HSb) are decreased relative to those of *P*(HE) and *P*(XE) (X = P and As) in *bent*-

HPE and *bent*-HAsE. The number of lone pairs, bond pairs, and 3C 2e pair orbitals are the same as those of the (H, P, E) and (H, As, E) systems.

Table 3.7: NBO analysis of (H, Sb, E) (E = C to Pb) at BP86/def2-TZVPP//BP86/TZ2P+.

	q(H)	q(Sb)	q(E)	*P*(HSb)	*P*(SbE)	*P*(HE)	LP(Sb)	LP(E)	LP(H)	BP(HSb)	BP(SbE)	BP(HE)	3C 2e
lin-HCSb	0.19	0.66	-0.85	0.037	2.840	0.931	1				3	1	
lin-HSbC	-0.04	0.58	-0.54	0.783	2.962	0.221		1		1	3		
lin-HSiSb	-0.11	0.01	0.10	0.087	2.940	0.906	1				3	1	
TS	-0.11	0.16	-0.05	0.155	2.376	0.847	1				3	1	
bent-HSbSi	-0.15	0.03	0.12	0.588	2.079	0.426	1	1			2		1
lin-HSbSi	0.00	-0.16	0.16	0.864	2.610	0.140		1		1	3		
lin-HGeSb	-0.08	0.01	0.07	0.116	2.873	0.881	1				3	1	
TS	-0.09	0.14	-0.05	0.157	2.339	0.850	1				3	1	
bent-HSbGe	-0.14	-0.02	0.16	0.656	2.067	0.358	1	1			2		1
lin-HSbGe	-0.01	-0.18	0.19	0.857	2.574	0.146		1		1	3		
lin-HSnSb	-0.14	-0.17	0.31	0.149	2.786	0.834	1				3	1	
TS	-0.16	0.01	0.15	0.179	2.174	0.807	1				3	1	
bent-HSbSn	-0.16	-0.19	0.35	0.754	1.982	0.243	1	1			2		1
lin-HSbSn	-0.02	-0.33	0.35	0.875	2.424	0.128		1		1	3		
lin-HPbSb	-0.13	-0.18	0.30	0.212	2.631	0.776	1				3	1	
TS	-0.15	-0.02	0.17	0.183	2.066	0.800	1	1			2	1	
bent-HSbPb	-0.16	-0.23	0.39	0.802	1.967	0.194	1	1			2		1
lin-HSbPb	-0.03	-0.35	0.38	0.881	2.374	0.122		1		1	3		

q-partial charges, *P*-Wiberg bond index, LP-number of lone pair orbitals, BP-number of bond pair orbitals and 3C 2e- number of 3center 2electron orbitals.

3.7 (H, Bi, E) System

3.7.1 Geometries and Energies

The stationary points characterized on the PES of the (H, Bi, E) system are shown in Figure 3.6a. For the (H, Bi, C) system, only the linear structures (*lin*-HCBi and *lin*-HCBi) are characterized on the PES. *lin*-HBiC is 78.5 kcal/mol higher in energy than *lin*-HCBi. Although *lin*-HBiC has $i = 0$ (Figure 3.6), no TS was found that connected *lin*-HBiC with *lin*-HCBi. The (H, Bi, E) system, in which E = Ge to Pb has a global minimum (*bent*-HBiE), a local minimum (*lin*-HEBi), and a TS structure connecting the two minima. *lin*-HSiBi is 3.1 kcal/mol lower in energy than *bent*-HBiSi at the CCSD(T)/TZVPP level and is almost equal in energy at BP86/TZ2P+ level of theory. *lin*-HBiE is a second-order saddle point. *lin*-HBiPb is 1.2 kcal/mol lower in energy than *lin*-HPbBi, however, for E = Si to Sn, *lin*-HEBi is more stable than *lin*-HBiE. The reaction energy profile for the isomerization of *lin*-HEBi → *bent*-HBiE is shown in Figure 3.6b. The reaction is exothermic except for E = Si. The energy difference between *bent*-HBiE and *lin*-HEBi (the reverse-reaction energy) increases with increasing the size of E: -3.1 (Si), 1.1 (Ge), 9.0 (Sn), and 18.3 kcal/mol (Pb). The energy difference between *bent*-HBiE and TS (the reverse-reaction barrier) increases with increasing the size of E: 7.8 (Si), 11.8 (Ge), 18.9 (Sn), and 25.8 kcal/mol (Pb).

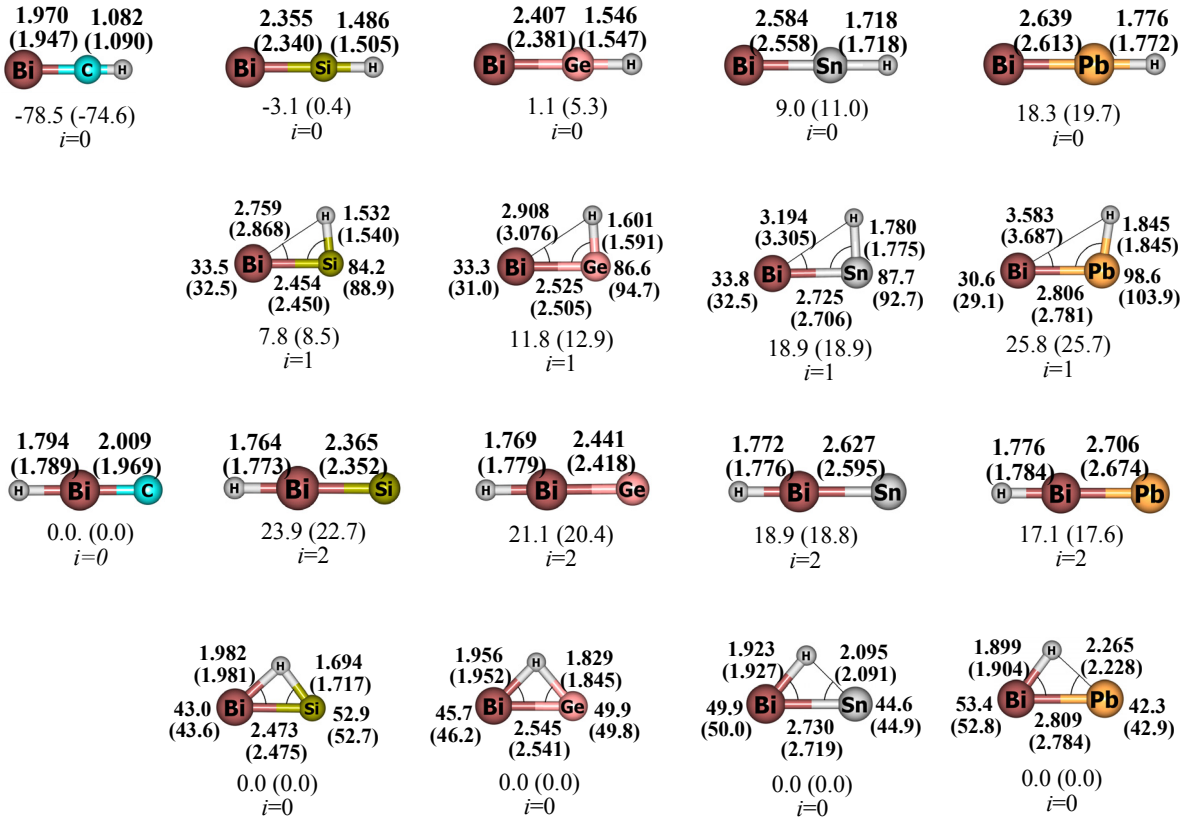

(a)

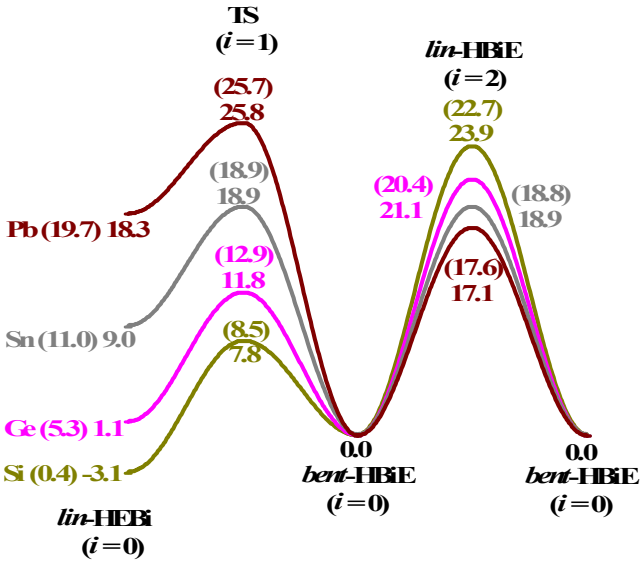

(b)

Figure 3.6: (a) Optimized geometry of the stationary points on the PES of (H, Bi, E) system (E = C to Pb) at the CCSDT/TZVPP level. Relative energies in kcal/mol, bond distances in Å, and bond angles in degrees. BP86/TZ2P+ values are given in parentheses. Number of imaginary frequencies is given by (*i*). **(b)** Energy profile diagram (reaction coordinate versus relative energy) of the (H, Bi, E) system.

The energy difference between *lin*-HEBi and the TS (the forward-reaction barrier) decreases with E: 10.9 (Si), 10.7 (Ge), 9.9 (Sn), and 7.5 kcal/mol (Pb). The TS is closer in energy to *lin*-HEP, except for E = Si.

The structural changes during the isomerization of *lin*-HEBi to *bent*-HBiE are the same as that of the structural changes in the (H, P, E), (H, As, E), and (H, Sb, E) systems. The HBi and BiE bond lengths in *lin*-HBiE are shorter than the HBi and BiE bond lengths in *bent*-HBiE. The HBi bond length in *lin*-HBiE is almost the same for E = Si to Pb and slightly longer in *lin*-HBiC. The HE bond in *bent*-HBiE becomes shorter than the HE bond in *bent*-HPE, *bent*-HAsE, and *bent*-HSbE. AIM analysis shows the EH, HBi, and BiE bond critical points and a ring critical point in *bent*-HBiSi and *bent*-HBiGe (Figure 3.7). With increasing the size of the atom X (P to Bi), H prefers to bond with the relatively smaller Si and Ge in *bent*-HBiSi and *bent*-HBiGe. The EH bond lengths in *lin*-HEX (X = N to Bi) are almost same for each of E = C to Pb, also the EH bond lengths in the TS of the (H, X, E) (X = N to Bi) system are almost the same for E = Si to Pb.

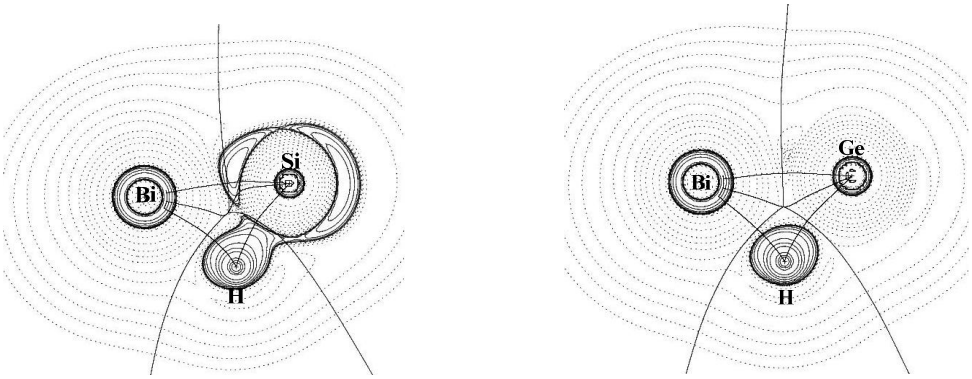

Figure 3.7: Contour line plot of $\nabla^2\rho(r)$ of *bent*-HBiSi and *bent*-HBiGe in the molecular plane. The thick solid lines connecting the atomic nuclei are the bond paths. The thick solid lines separating the atomic basins indicate the zero-flux surfaces.

3.7.2 Natural Bond Orbital Analysis

Table 3.8 shows the NBO data of the system (H, Bi, E). The trend observed in the NPA charges and the Wiberg bond indices are same as that of the (H, Sb, E) system with small changes in the absolute values, due to an increase in the electropositive character of Bi. The Wiberg bond indices *P*(EH) increases and *P*(HBi) decreases in *bent*-HBiE relative to that of the HE and HX bonds in *bent*-HXE (X = P to Sb); these results are in agreement with the observed structural changes (decrease in HE bond length) of *bent*-HXE on going from P to Bi. The numbers of bond pairs, lone pairs, and 3C 2e pair orbitals are same as those of the (H, Sb, E) system.

Table 3.8: NBO analysis of (H, Bi, E) (E = C to Pb) at BP86/def2-TZVPP//BP86/TZ2P+.

	q(H)	q(Bi)	q(E)	*P*(HBi)	*P*(BiE)	*P*(HE)	LP(Bi)	LP(E)	LP(H)	BP(HBi)	BP(BiE)	BP(HE)	3C 2e
lin-HCBi	0.18	0.65	-0.84	0.042	2.838	0.928	1				3	1	
lin-HBiC	-0.05	0.60	-0.54	0.716	2.873	0.287		1		1	3		
lin-HSiBi	-0.12	0.05	0.07	0.091	2.913	0.899	1				3	1	
TS	-0.13	0.19	-0.06	0.147	2.342	0.854	1				3	1	
bent-HBiSi	-0.17	0.10	0.07	0.515	2.085	0.491	1	1			2		1
lin-HBiSi	-0.01	-0.11	0.12	0.817	2.579	0.187		1		1	3		
lin-HGeBi	-0.09	0.04	0.05	0.118	2.838	0.877	1				3	1	
TS	-0.11	0.18	-0.07	0.144	2.314	0.859	1				3	1	
bent-HBiGe	-0.16	0.05	0.11	0.581	2.072	0.426	1	1			2		1
lin-HBiGe	-0.02	-0.14	0.16	0.811	2.537	0.192		1		1	3		
lin-HSnBi	-0.15	-0.12	0.27	0.150	2.757	0.830	1				3	1	
TS	-0.17	0.05	0.12	0.165	2.156	0.816	1				3	1	
bent-HBiSn	-0.19	-0.11	0.30	0.679	1.995	0.310	1	1			2		1
lin-HBiSn	-0.02	-0.29	0.31	0.839	2.403	0.164		1		1	3		
lin-HPbBi	-0.14	-0.13	0.27	0.209	2.604	0.776	1				3	1	
TS	-0.16	0.01	0.15	0.170	2.065	0.810	1	1			2	1	
bent-HBiPb	-0.18	-0.16	0.34	0.731	1.980	0.256	1	1			2		1
lin-HBiPb	-0.03	-0.31	0.34	0.849	2.347	0.154		1		1	3		

q-partial charge, *P*-Wiberg bond index, LP-number of lone pair orbitals, BP-number of bond pair orbitals and 3C 2e- number of 3center 2electron orbitals.

3.7.3 Energy Decomposition Analysis

The results of the EDA of *lin*-HEBi, *bent*-HBiE, and *lin*-HBiE are given in Table 3.9. The fragments and their electronic states being considered for the EDA are same as those of the fragments considered for the EDA of the (H, P, E) system (Scheme 3.3). The instantaneous interaction energy (ΔE_{int}) and the dissociation energy (D_e) are lower in the (H, Bi, E) system than in the (H, P, E) system. The percentage contribution of $\Delta E_{\pi|}$ (obtained from ETS-NOCV analysis) is higher in *bent*-HBiE than in *bent*-HPE, which is consistent with the Wiberg bond index values and structural changes. Otherwise the trend observed in the EDA results of the (H, Bi, E) system is the same as in the (H, P, E) system on moving from Si to Pb.

In addition to the quartet electronic state interaction between the fragments in *lin*-HEBi (Scheme 3.3), the EDA of *lin*-HEBi was also performed between the doublet electronic state (like the neutral doublet electronic state fragments in *lin*-HEN, Scheme 3.2) of the fragments HE ($^2\Pi$) and Bi (^{2}P) and the results are given in Table 3.10. The fragment HE interacts in its ground state and Bi needs 32.8 kcal/mol of energy ($^4S \rightarrow {}^2P$) to interact with HE at the BP86/TZ2P+ level. Among the two schemes (quartet and doublet), the one with the smallest orbital interaction (ΔE_{orb}) value is the best choice to describe the bonding. In *lin*-HSiBi, the quartet state interaction has the smallest orbital interaction value. On going from Si to Pb, the ΔE_{orb} interaction values of the two schemes (quartet and doublet) approach each other and, for *lin*-HPbBi, the doublet electronic state interaction gets the smallest ΔE_{orb} interaction value. This is also evident from the longer HPb bond length in *lin*-HPbBi than the HPb bond length in *lin*-HPbX (X = N to Sb). This change in bonding picture is due to the

increase in the excitation energy ($^2\Pi \rightarrow {}^4\Sigma^-$) of the HE fragment on going down the group from Si to Pb.

Table 3.9: EDA and ETSNOCV analyses of the (H, Bi, E) system (E = Si to Pb) at BP86/TZ2P+

lin-HEBi				
Inter. frags	Bi(^{4}S) ; HSi ($^4\Sigma^-$)	Bi(^{4}S) ; HGe ($^4\Sigma^-$)	Bi(^{4}S) ; HSn ($^4\Sigma^-$)	Bi(^{4}S) ; HPb ($^4\Sigma^-$)
Symmetry	C_{2v}	C_{2v}	C_{2v}	C_{2v}
ΔE_{int}	-102.0	-104.2	-94.6	-94.6
ΔE_{Pauli}	143.6	149.2	137.3	141.2
ΔE_{Elstat}[a]	-104.0 (42.3)	-109.9 (43.3)	-106.9 (46.1)	-104.6 (44.3)
ΔE_{orb}[a]	-141.7 (57.7)	-143.6 (56.7)	-125.1 (53.9)	-131.2 (55.7)
ΔE(A1)[b]	-85.0 (60.0)	-87.7 (61.1)	-73.5 (58.7)	-78.4 (59.7)
ΔE(A2)[b]	0.0	0.0	0.0	0.0
ΔE(B1)[b]	-28.3 (20.0)	-27.9 (19.4)	-25.8 (20.6)	-26.4 (20.2)
ΔE(B2)[b]	-28.3 (20.0)	-27.9 (19.4)	-25.8 (20.6)	-26.4 (20.2)
ΔE_{prep} (Bi)	0.0	0.0	0.0	0.0
ΔE_{prep} (HE)	39.5	47.2	45.6	53.9
ΔE_{corr}[d]	2.5	2.1	2.0	2.5
ΔE(= -D_e)	-60.0	-54.9	-47.0	-38.2

bent-HBiE				
Inter. frags	HBi($^3\Sigma^-$) ; Si (^{3}P)	HBi($^3\Sigma^-$) ; Ge (^{3}P)	HBi($^3\Sigma^-$) ; Sn (^{3}P)	HBi($^3\Sigma^-$) ; Pb (^{3}P)
Symmetry	C_s	C_s	C_s	C_s
ΔE_{int}	-79.6	-73.7	-65.1	-60.9
ΔE_{Pauli}	288.9	256.6	223.0	204.6
ΔE_{elstat}[a]	-179.5 (48.7)	-168.5 (51.0)	-155.2 (53.9)	-146.6 (55.2)
ΔE_{orb}[a]	-188.9 (51.3)	-161.8 (49.0)	-132.9 (46.1)	-118.9 (44.8)
ΔE_{σ}[b]	-118.6 (62.8)	-102.8 (63.5)	-86.2 (64.9)	-78.2 (65.8)
$\Delta E_{\pi\parallel}$[b]	-38.5 (20.4)	-29.5 (18.2)	-19.7 (14.8)	-15.2 (12.8)
$\Delta E_{\pi\perp}$[b]	-31.9 (16.8)	-29.5 (18.2)	-27.0 (20.3)	-25.5 (21.5)
ΔE_{prep} (HBi)	2.8	1.9	1.3	0.9
ΔE_{prep} (E)	0.0	0.0	0.0	0.0
ΔE_{corr}[d]	1.9	1.8	1.7	1.6
ΔE(= -D_e)	-74.9	-70.0	-62.1	-58.4

lin-HBiE				
Inter. frags	HBi($^3\Sigma^-$) ; Si (^{3}P)	HBi($^3\Sigma^-$) ; Ge (^{3}P)	HBi($^3\Sigma^-$) ; Sn (^{3}P)	HBi($^3\Sigma^-$) ; Pb (^{3}P)
Symmetry	C_{2v}	C_{2v}	C_{2v}	C_{2v}
ΔE_{int}	-54.3	-51.5	-45.1	-42.5
ΔE_{Pauli}	121.6	110.4	100.1	112.8
ΔE_{elstat}[a]	-55.5 (31.6)	-54.4 (33.6)	-53.0 (36.5)	-46.7 (30.1)
ΔE_{orb}[a]	-120.3 (68.4)	-107.6 (66.4)	-92.1 (63.5)	-108.6 (69.9)
ΔE(A1)[b]	-52.1 (43.3)	-44.9 (41.8)	-33.8 (36.7)	-30.0 (27.6)
ΔE(A2)[b]	0.0	0.0	0.0	0.0
ΔE(B1)[b]	-34.1 (28.3)	-31.3 (29.1)	-29.2 (31.7)	-39.3 (36.2)
ΔE(B2)[b]	-34.1 (28.3)	-31.3 (29.1)	-29.2 (31.7)	-39.3 (36.2)
ΔE_{prep} (HBi)	0.3	0.2	0.2	0.1
ΔE_{prep} (E)	0.0	0.0	0.0	0.0
ΔE_{corr}[d]	1.8	1.7	1.6	1.6
ΔE(= -D_e)	-52.3	-49.6	-43.3	-40.8

[a] The values in parentheses are the percentage contributions to the total attractive interaction $\Delta E_{elstat} + \Delta E_{orb}$. [b] The values in parentheses are the percentage contributions to the total orbital interactions ΔE_{orb}. [d] Correction for spin polarization. Energy values in kcal/mol.

Table 3.10: EDA of *lin*-HEBi in the doublet electronic state of the fragments HE and Bi at BP86/TZ2P+, E = Si to Pb

Inter. frags	Bi(^{2}P) ; HSi ($^2\Pi$)	Bi(^{2}P) ; HGe ($^2\Pi$)	Bi(^{2}P) ; HSn ($^2\Pi$)	Bi(^{2}P) ; HPb ($^2\Pi$)
Symmetry	C_{2v}	C_{2v}	C_{2v}	C_{2v}
ΔE_{int}	-94.4	-89.5	-81.6	-73.0
ΔE_{Pauli}	169.2	153.4	133.7	121.0
ΔE_{elstat}[a]	-110.3 (41.9)	-98.6 (40.6)	-86.4 (40.2)	-77.0 (39.7)
ΔE_{orb}[a]	-153.3 (58.2)	-144.3 (59.4)	-128.8 (59.8)	-117.0 (60.3)
ΔE(A1)[b]	-67.2 (43.9)	-63.2 (43.8)	-60.5 (47.0)	-53.6 (45.9)
ΔE(A2)[b]	0.0	0.0	0.0	0.0
ΔE(B1)[b]	-35.1 (22.9)	-34.2 (23.7)	-31.4 (24.4)	-31.3 (26.8)
ΔE(B2)[b]	-51.0 (33.2)	-46.8 (32.4)	-36.9 (28.7)	-32.0 (27.4)
ΔE_{prep}(Bi)	32.8	32.8	32.8	32.8
ΔE_{prep}(HE)	0.3	0.6	0.8	1.2
ΔE_{corr}[d]	1.3	1.2	1.0	0.8
ΔE(= -D_e)	-60.0	-54.9	-47.0	-38.2

[a] The values in parentheses are the percentage contributions to the total attractive interaction $\Delta E_{elstat} + \Delta E_{orb}$. [b] The values in parentheses are the percentage contributions to the total orbital interactions ΔE_{orb}. [d] Correction for spin polarization. Energy values in kcal/mol.

3.8 (H, P, Si) versus (H, Bi, Si)

The PESs of the two systems are different. The relative energy between *bent*-HXE and *lin*-HEX and the relative energy between *bent*-HXE and TS decreases and the relative energy between *bent*-HXE and *lin*-HXE increases on going from X = P to Bi. As a result, the shape of the reaction profile becomes symmetric on going down the group from P to Bi (Figure 3.2b and 3.6b). EDA of *lin*-HSiX, TS, *bent*-HXSi, and *lin*-HXSi (X = P and Bi) was performed and the results are given in Table 3.11. The ETS-NOCV analysis of TS and *bent*-HXSi (X = P and Bi) was carried out to get the $\Delta E_{\pi||}$ contribution and the deformation densities are shown in Figures 3.8 and 3.9. In *lin*-HSiX and TS the fragments (HSi and X) were considered to interact in the doublet (HSi ($^2\Pi$) ; X (^{2}P)) and the quartet (HSi ($^4\Sigma^-$) ; X (^{4}S)) electronic states (Scheme 3.4). In *bent*-HXE, two fragmentation schemes were considered: one in which H is attached to X (HX ($^3\Sigma^-$) and Si (^{3}P)) and in the other H is attached to Si (X (^{2}P) and HSi ($^2\Pi$)) (Scheme 3.4). The EDA results of the (H, P, Si) system suggest that in *lin*-HSiP and TS the fragments are interacting in the quartet electronic state and not in the doublet state. In *bent*-HPSi, H attached to P, that is, the fragment HP interacts with Si. In the (H, Bi, Si) system both the quartet and doublet state interactions are valid for *lin*-HSiBi and TS. In *bent*-HBiSi the fragmentation scheme in which H attached to Si (HSi) interacting with Bi has the smallest orbital interaction value and larger preparation energy than the other fragmentation scheme involving the interaction between HBi and Si. Scheme 3.4 shows the bonding situation and the changes in the electronic state of the interacting fragments during the isomerization reaction in the systems (H, P, Si) and (H, Bi, Si). The ΔE is the energy change associated with the change in the electronic state of the interacting fragment during a reaction (equivalent to ΔE_{prep} in EDA). For example, when two fragments, one in the ground state (g) and the other in excited state (e), interact in the reactant and changes to the product in which one of the fragments in the ground state (g) interacts with the other in the excited state (e), the ΔE

value will be approximately zero, as in Equation (3.1) and further situations are given in Equations (3.2) to (3.5):

$g + e \rightarrow g + e$ (or) $e + g \rightarrow e + g$ $\Delta E \approx 0$ (3.1)

$g + e \rightarrow e + g$ (or) $e + g \rightarrow g + e$ $\Delta E \approx 0$ (3.2)

$g + e \rightarrow g + g$ (or) $e + g \rightarrow g + g$ $\Delta E < 0$ (exothermic) (3.3)

$g + e \rightarrow e + e$ (or) $e + g \rightarrow e + e$ $\Delta E > 0$ (endothermic) (3.4)

$g + g \rightarrow g + g$ (or) $e + e \rightarrow e + e$ $\Delta E = 0$ (3.5)

The observed change in the energy profile of the systems (H, P, Si) and (H, Bi, Si) could be explained qualitatively based on the ΔE value. In Scheme 3.4, the (H, P, Si) system is in the blue colored box and (H, Bi, Si) is in the pink colored box. As mentioned earlier, during the isomerization of *lin*-HSiP to *bent*-HPSi, the fragment HE in *lin*-HEP relaxes to the ground state of E in *bent*-HPE by transferring H to P, and hence, the reaction is exothermic. The conversion of *lin*-HSiBi to *bent*-HBiSi follow Equations (3.1) or (3.2). For the conversion of *lin*-HSiX to TS, $\Delta E \approx 0$ for both P and Bi and the forward-reaction barrier for the isomerization of *lin*-HSiX to *bent*-HXSi involves only structural changes, and hence, it is small and almost the same for the P (14.4 kcal/mol) and Bi (10.9 kcal/mol) systems at the CCSD(T)/TZVPP level of theory.

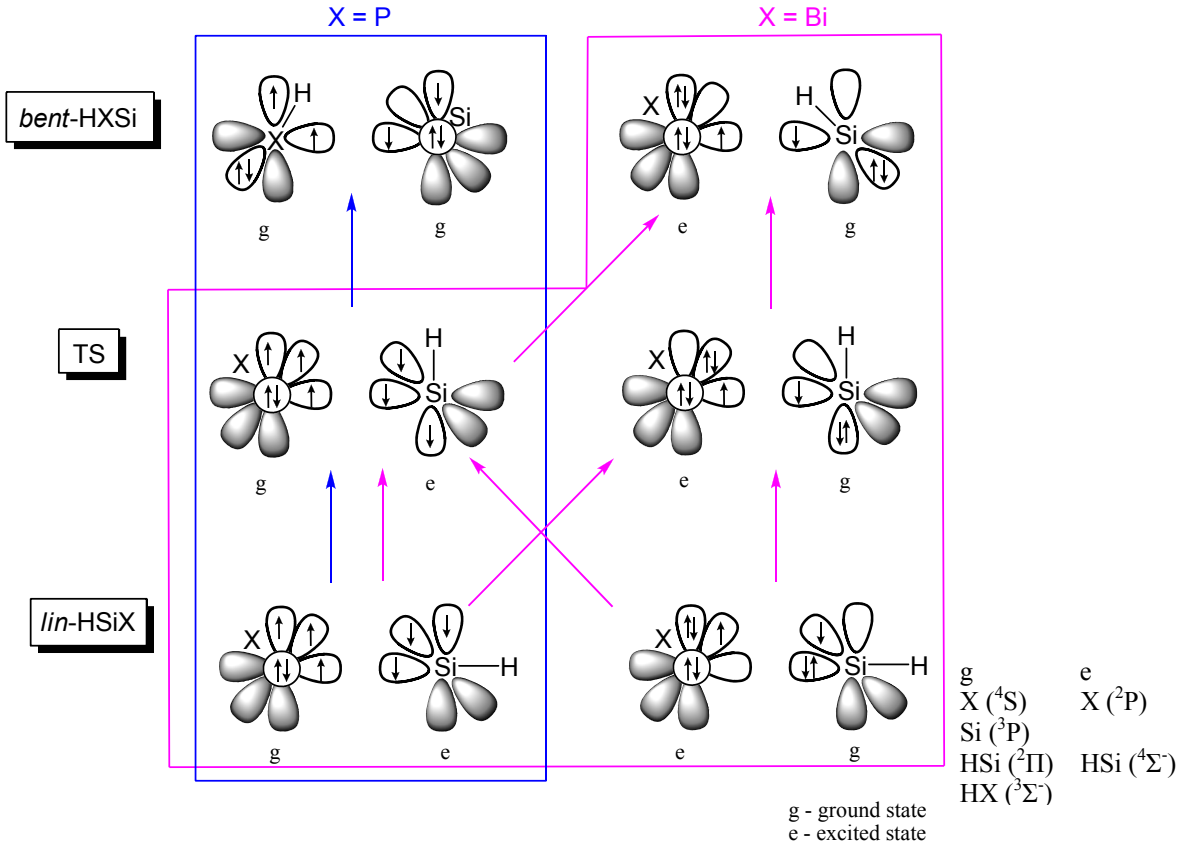

Scheme 3.4: Bonding situation and the changes in the electronic state of the interacting fragments during the isomerization reaction (*lin*-HSiX → *bent*-HXE) in the systems (H, P, Si) and (H, Bi, Si).

Table 3.11: EDA and ETSNOCV analyses of (H, P, Si) and (H, Bi, Si) system at BP86/TZ2P+

	lin-HSiBi		TS		*bent*-HBiSi		*lin*-HBiSi
Inter. frags	Bi(^{4}S) ; SiH($^4\Sigma^-$)	Bi(^{2}P) ; SiH($^2\Pi$)	Bi(^{4}S) ; SiH($^4\Sigma^-$)	Bi(^{2}P) ; SiH($^2\Pi$)	HBi($^3\Sigma^-$) ; Si(^{3}P)	Bi(^{2}P) ; HSi($^2\Pi$)	HBi($^3\Sigma^-$) ; Si(^{3}S)
Symmetry	C_{2v}	C_{2v}	C_s	C_s	C_s	C_s	C_{2v}
ΔE_{int}	-102.0	-94.4	-93.9	-86.0	-79.6	-98.0	-54.3
ΔE_{Pauli}	143.6	169.2	197.2	201.2	288.9	247.6	121.6
ΔE_{elstat}[a]	-104.0 (42.3)	-110.3 (41.9)	-149.9 (51.5)	-148.6 (51.7)	-179.5 (48.7)	-166.8 (48.3)	-55.5 (31.6)
ΔE_{orb}[a]	-141.7 (57.7)	-153.3 (58.2)	-141.2 (48.5)	-138.7 (48.3)	-188.9 (51.3)	-178.9 (51.7)	-120.3 (68.4)
ΔE(A1) or ΔE_σ [b]	-85.0 (60.0)	-67.2 (43.9)	-78.1 (55.3)	-81.1 (58.5)	-118.6 (62.8)	-104.3 (58.3)	-52.1 (43.3)
ΔE(A2)[b]	0.0	0.0	-	-	-	-	0.00
ΔE(B1) or $\Delta E_{\pi\parallel}$ [b]	-28.3 (20.0)	-35.1 (22.9)	-38.5 (27.3)	-20.1 (14.5)	-38.5 (20.4)	-33.0 (18.4)	-34.1 (28.3)
ΔE(B2) or $\Delta E_{\pi\perp}$ [b]	-28.3 (20.0)	-51.0 (33.2)	-24.6 (17.4)	-37.5 (27.1)	-31.9 (16.8)	-41.6 (23.2)	-34.1 (28.3)
ΔE_{prep} (Bi)	0.0	32.8	0.0	32.8	2.8	32.8	0.3
ΔE_{prep} (HE)	39.5	0.3	39.6	0.0	0.0	3.5	0.0
ΔE_{corr}[d]	2.5	1.3	2.4	1.3	1.9	1.3	1.8
ΔE(= -D_e)	-60.0	-60.0	-51.9	-51.9	-74.9	-60.4	-52.2

	lin-HSiP		TS		*bent*-HPSi		*lin*-HPSi
	P(^{4}S) ; SiH($^4\Sigma^-$)	P(^{2}P) ; SiH($^2\Pi$)	P(^{4}S) ; SiH($^4\Sigma^-$)	P(^{2}P) ; SiH($^2\Pi$)	HP($^3\Sigma^-$) ; Si(^{3}P)	P(^{2}P) ; HSi($^2\Pi$)	HP($^3\Sigma^-$) ; Si (^{3}S)
Symmetry	C_{2v}	C_{2v}	C_s	C_s	C_s	C_s	C_{2v}
ΔE_{int}	-127.8	-129.6	-115.6	-117.1	-98.0	-151.2	-85.9
ΔE_{Pauli}	181.0	204.4	239.3	264.7	280.0	360.6	165.7
ΔE_{elstat}[a]	-114.9 (37.2)	-99.7 (29.8)	-156.6 (44.1)	-170.1 (44.6)	-165.5 (43.8)	-201.3 (39.3)	-73.5 (29.2)
ΔE_{orb}[a]	-193.8 (62.8)	-234.3 (70.2)	-198.4 (55.9)	-211.7 (55.4)	-212.5 (56.2)	-310.5 (60.7)	-178.0 (70.8)
ΔE(A1) or ΔE_σ [b]	-102.6 (52.9)	-127.4 (54.4)	-117.7 (59.3)	-128.6 (60.7)	-136.8 (64.4)	-186.6 (60.1)	-72.6 (40.8)
ΔE(A2)[b]	0.0 (0.0)	0.0	-	-	-	-	0.0 (0.0)
ΔE(B1) or $\Delta E_{\pi\parallel}$ [b]	-45.6 (23.6)	-53.1 (22.7)	-37.0 (18.6)	-41.7 (19.7)	-26.3 (12.4)	-75.3 (24.3)	-52.7 (29.6)
ΔE(B2) or $\Delta E_{\pi\perp}$ [b]	-45.6 (23.6)	-53.8 (23.0)	-43.7 (22.0)	-41.4 (19.5)	-49.5 (23.3)	-48.5 (15.6)	-52.7 (29.6)
ΔE_{prep} (P)	0.0	41.3	0.0	41.3	0.7	41.3	0.1
ΔE_{prep} (HE)	39.6	0.4	39.5	0.0	0.0	10.2	0.0
ΔE_{corr}[d]	2.1	1.8	2.2	1.9	2.4	1.9	2.4
ΔE(= -D_e)	-86.1	-86.1	-73.9	-73.9	-94.9	-97.8	-83.4

[a] The values in parentheses are the percentage contributions to the total attractive interaction $\Delta E_{elstat} + \Delta E_{orb}$. [b] The values in parentheses are the percentage contributions to the total orbital interactions ΔE_{orb}. [d] Correction for spin polarization.

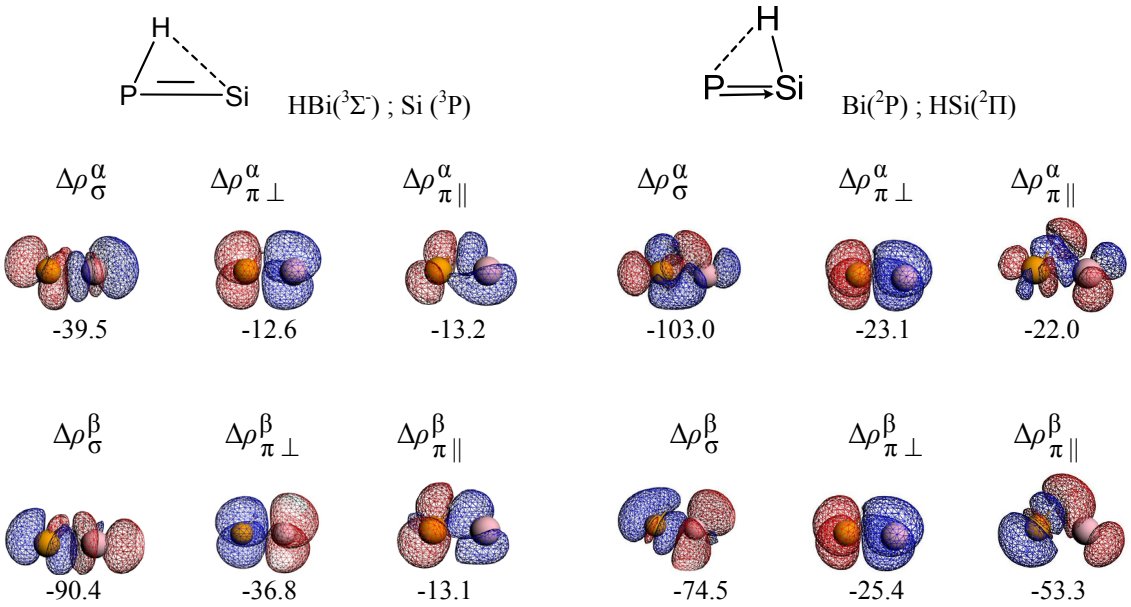

bent-HPSi

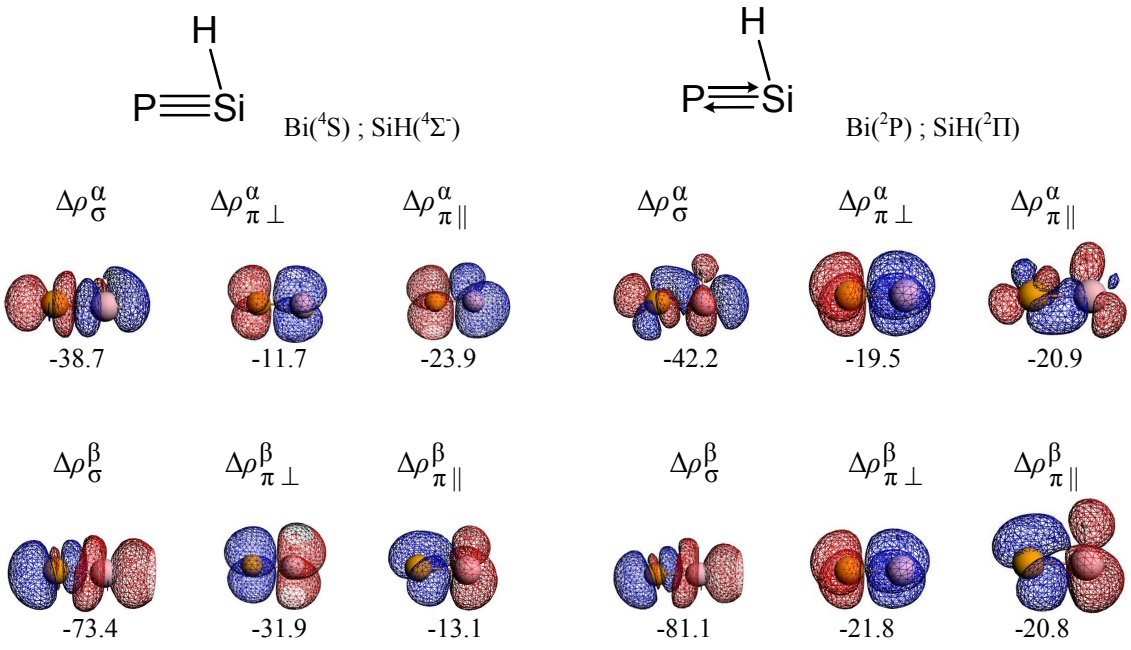

TS

Figure 3.8: The most important deformation densities and the energy (kcal/mol) of the valance orbital interaction between the fragments in *bent*-HPSi and TS at BP86/TZ2P+. The deformation densities $\Delta\rho_{\sigma}^{\alpha}$ and $\Delta\rho_{\sigma}^{\beta}$ indicates the charge flow of α and β electrons in the σ-type orbital of one fragment to the other. Similarly $\Delta\rho_{\pi\,||}^{\alpha}$ and $\Delta\rho_{\pi\,||}^{\beta}$ for $\pi_{||}$ type orbital (in plane π orbital) and $\Delta\rho_{\pi\,\perp}^{\alpha}$ and $\Delta\rho_{\pi\,\perp}^{\beta}$ for $\pi_{\perp}$ type orbital (out of plane π orbital). Direction of charge flow: red to blue. The deformation densities $\Delta\rho^{\alpha}$ and $\Delta\rho^{\beta}$ of a bond looks similar if it involves donor-acceptor interaction between the fragments. The solid lines and arrows between the atoms indicate the electron-sharing and dative bonds, respectively, and the dotted lines shows the bond-pair donation.

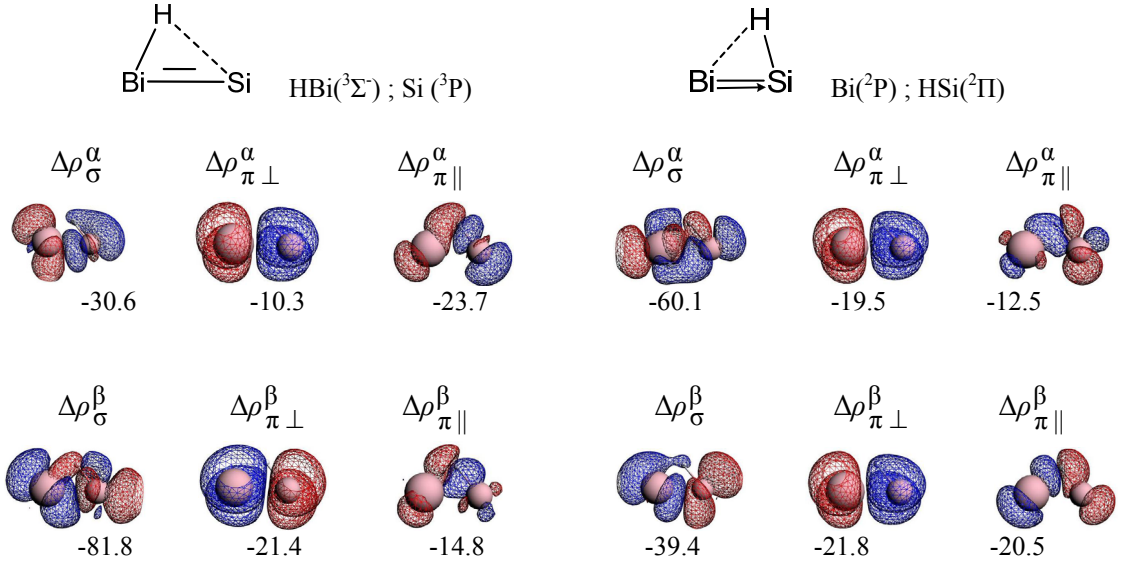

bent-HBiSi

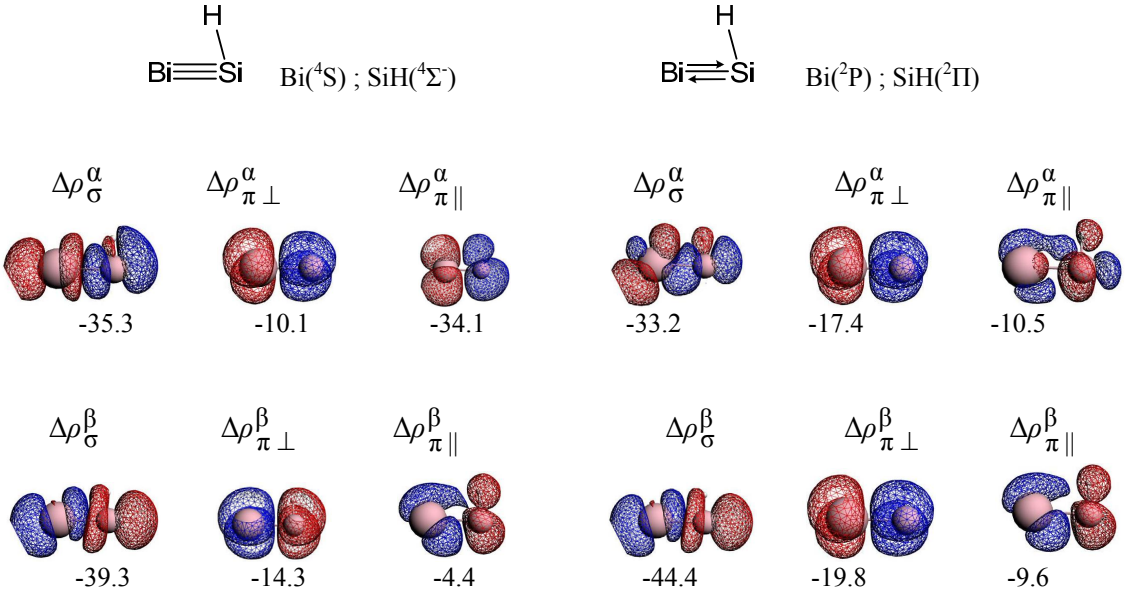

TS

Figure 3.9: The most important deformation densities and the energy of the valance orbital interaction between the fragments in *bent*-HBiSi and TS at BP86/TZ2P+. The deformation densities $\Delta\rho_{\sigma}^{\alpha}$ and $\Delta\rho_{\sigma}^{\beta}$ indicates the charge flow of α and β electrons in the σ-type orbital of one fragment to the other. Similarly $\Delta\rho_{\pi\parallel}^{\alpha}$ and $\Delta\rho_{\pi\parallel}^{\beta}$ for $\pi_{\parallel}$ type orbital (in plane π orbital) and $\Delta\rho_{\pi\perp}^{\alpha}$ and $\Delta\rho_{\pi\perp}^{\beta}$ for $\pi_{\perp}$ type orbital (out of plane π orbital). Direction of charge flow: red to blue. The deformation densities $\Delta\rho^{\alpha}$ and $\Delta\rho^{\beta}$ of a bond looks similar if it involves the donor-acceptor interaction between the fragments. The solid lines and arrows between the atoms indicate the electrons-sharing and dative bonds, respectively, and the dotted lines shows the bond-pair donation.

3.9 Summary

The PES of the system (H, X, E) in which X = N to Bi and E = C to Pb, involving the singlet electronic structures was explored at the CCSD(T)/TZVPP and BP86/TZ2P+ levels of theory. The BP86 level performs as well as CCSD(T), but it fails to predict *lin*-HSiBi as the global minimum of the (H, Bi, Si) system. The PES of the (H, N, E) system is different from the rest of (H, X, E) (X = P to Bi). *lin*-HNE is the global minimum and *lin*-HEN is the local minimum for E = Si to Pb. In contrast, *lin*-HCN is lower in energy than *lin*-HNC. Planar TS connects the two minima. No bent structures were observed as minima on the PES of the (H, N, E) system, whereas *bent*-HXE and *lin*-HEX are minima and *lin*-HXE is a second-order saddle point in the case of (H, X, E) for X = P to Bi and E = Si to Pb. *bent*-HXE is the global minimum and *lin*-HEX is the local minimum, except *bent*-HBiSi, which is 3.1 kcal/mol higher in energy than *lin*-HSiBi. The relative energy between *bent*-HXE and TS and the relative energy between *bent*-HXE and *lin*-HEX decreases and the relative energy between *bent*-HXE and *lin*-HXE increases on going from X = P to Bi. As a result, the shape of the reaction profile of the systems (H, X, E) becomes symmetric on going down the group from P to Bi. Planar TS connects the two minima. The systems involving C, that is, (H, X, C) in which X = P to Bi behaves differently. Only two structures were observed: one is the minimum, *lin*-HCX, and the other, *lin*-HXC, is a second-order saddle point. However, both *lin*-HCN and *lin*-HNC are minima on the PES of the (H, N, C) system.

Some of the common structural features observed on the PES of the (H, X, E) are i) All of the TSs connecting the minima have a planar bent geometry with H being attached to E. The bending angle X-E-H ranges from 80 to 90° except for (H, N, C) and (H, Bi, Pb). ii) In *lin*-HXE, for X = N to Bi the HX bond length is nearly the same on moving from Si to Pb, however, the HX bond length in *lin*-HXC is a little longer. iii) The HE bond length is almost the same in *lin*-HEX for E = C to Pb on going from X = N to Bi. However, the HC and HPb bond lengths increase from N to Bi. This trend in the HE bond lengths also observed in the TSs of the system (H, X, E), X = N to Bi, for E = Si to Pb. iv) In *bent*-HXE on going from X = P to Bi the HE bond gets shorter and for *bent*-HBiSi and *bent*-HBiGe the AIM analysis finds a ring critical point. This is because with increasing the size of X (from P to Bi) H prefers to overlap with the smaller E atom. In *bent*-HXE, the HX bond length decreases on going from E = Si to Pb for X = P to Bi.

The NPA charges on the atoms, of the (H, X, E) system follow the periodic trend and they fall into the following groups: i) (H, N, C); ii) (H, N, E), E = Si to Pb; iii) (H, X, E), X = P and As and E = Si and Ge; iv) (H, X, E), X = Sb and Bi and E = Si and Ge; v) (H, X, E), X = P and As and E = Sn and Pb; vi) (H, X, E), X = Sb and Bi and E = Sn and Pb; and vii) (H, X, C) X = P to Bi. The changes in the Wiberg bond index values are consistent with the structural changes of the system (H, X, E).

The nature of the EX in *lin*-HEX involves one σ- and two π-electron-sharing bonds. However, for X=Bi, the fragment HE interacting in the ($^2\Pi$) electronic ground state, with the (^{2}P) Bi, also becomes valid. In *bent*-HXE, there is one σ- and one π-electron-sharing bond between X and E and a

donor–acceptor interaction between the HX bond pair and the empty p orbital on E and the donor–acceptor interaction increases from P to Bi.

Apart from the size, charge, and electronegativity differences between the atoms involved in the system (H, X, E), the electronic state of the interacting fragments in the stationary points also influence the nature of the PES of the system. For example, the stationary points where the fragments interacting in their electronic ground state are global minima. In *lin*-HNE (E = Si to Pb), the fragments HN and E interact in their ground electronic state. The fragments HX and E in *bent*-HXE (X = P to Bi and E = Si to Pb) also interact in their ground state. The interaction between the fragments HX and E in *bent*-HXE has the larger electrostatic interaction than that in *lin*-HXE. In the (H, P, Si) system, *bent*-HPSi is the global minimum and *lin*-HSiP is the local minimum, however, in the (H, Bi, Si) system, *lin*-HSiBi is 3.1 kcal/mol lower in energy. This change in relative energy between the minima of the (H, P, Si) and (H, Bi, Si) systems is due of the more diffuse nature of the valence 5p orbital of Bi, H prefers to overlap with the relatively smaller 2p orbital of Si. Therefore, *bent*-HBiSi could be rather viewed as the HSi fragment interacting with Bi instead of the HBi interacting with Si.

4. Compounds with Triple Bonds to Sulfur

4.1 Introduction

The element sulfur exists in different forms and bond with other elements, such as halogens, oxygen, nitrogen, and metals. Sulfur can extend its valency from two to six. Compounds containing a hypervalent sulfur atom and compounds with multiple bonds to sulfur have attracted special attention. For example, CS_2, $H_2C{=}SF_4$, $F_3C\text{-}CH{=}SF_4$, $HN{=}SPh_2$, CS, $F_3C\text{-}C{\equiv}SF_3$, $F_5S\text{-}C{\equiv}SF_3$, $HC{\equiv}SOH$, $N{\equiv}SF_3$, $N{\equiv}SF$, $N{\equiv}SOH$, and $N{\equiv}SAr_2F$ are some of the compounds with a hypervalent sulfur atom or with multiple bonds to sulfur.[8-11, 79] This chapter focuses on compounds with a triple bond to sulfur. Compounds with a CS triple bond are called sulfaalkynes and those with an NS triple bond are called sulfanenitrile or thiazynes. Other than carbon and nitrogen, there have been no other elements reported so far, forming a triple bond with sulfur. The CS bond length in $F_3C\text{-}C{\equiv}SF_3$[9a, 9b] and $F_5S\text{-}C{\equiv}SF_3$[10a, 79c] is 1.420 and 1.390 Å, respectively, with the varying bending angles of about 155–171° at the triply bonded carbon center. Despite the smaller CS bond lengths, these compounds were suspected to have a hidden carbene character[9c, 12] because the bending potential was very flat and the barrier to linearity has been predicted to be only 0.35 kcal/mol in the case of $F_3C\text{-}C{\equiv}SF_3$ at the MP2/6-31G*//HF/6-31G* level. The molecule HCSOH was reported by Schreiner et al.[11] and was considered to have a weak CS triple bond or a strong CS double-bond character. The calculated CS bond length of 1.547 Å in HCSOH is in agreement with the sum of the triple-bond covalent radii for carbon (0.60 Å) and sulfur (0.95 Å), giving a CS triple-bond length of 1.55 Å (as suggested by Pyykkö et al.), which is slightly longer than the distance in CS (1.535 Å).

The NS bond lengths in these compounds range from approximately 1.410 to 1.470 Å.[79h] NSOH, an isoelectronic compound of HCSOH, was reported by Tchir and Spratley in 1975.[79e, 79f] Bharatam et al. suggested that the NS interaction in NSF, NSH, NSF_3, and NSH_3 is a hybrid of the NS triple bond and the $S^+\text{-}N^-$ single bond. The balance between these two resonating structures shifts towards the NS triple-bonded arrangement with an increase in the electronegativity of the substituents on sulfur.[79h] Rzepa showed that the CS bond in HCSR (R = F, Cl, OH, OTf, H_2N, CN, H_2B) is highly tuneable from having a CS triple bond character at one end to being almost a CS single bond at the other, depending on the nature of the substituent, R, on S.[80] The thioxophosphanes, R-P=S, in which R = F, Cl, Br, and H, were stable in the gas phase and were characterised by using IR and photoelectron spectroscopic techniques. The simple thioxophosphane, H-P=S, and its tautomer, P-S-H, were characterised to be stable in the gas phase by Wong et al. in 1992.[81] PSH was the first example of a molecule in which the atom P does not take the central position.

This chapter gives a detailed investigation of the nature of the CS and NS triple bonds in the molecules HCSF and NSF. The possibility of the existence of SiS and the PS triple bonding character in HSiSF and PSF was also explored. The nature of the CS, NS, SiS, and PS bonds in HCSH, HCSOH, $F_5S\text{-}C{\equiv}SF_3$, NSH, NSOH, HSiSH, PSOH, and PSH is also be discussed.

4.2 Methods

Geometries were optimized at the CCSD(T) level with a split-valance basis set of doubly polarized triple-ζ-quality (def2-TZVPP).[70] This level of theory is denoted as CCSD(T)/TZVPP. The geometries were also optimized at the non-local DFT level of theory by using Becke's exchange functional in conjunction with Perdew's correlation functional (BP86)[36, 40] with the def2-TZVPP basis set and the level of theory is denoted as BP86/TZVPP. The stationary points were characterized as minima (i=0) or saddle points (i > 0) on the potential energy surface (PES) by computing the Hessian matrix. CCSD(T) calculations were done by using the program package MOLPRO 2009.1.[74] BP86 calculations were carried out by using Gaussian 09 program package.[76] The NBO analysis[59] was done at BP86/TZVPP level by using Gaussian NBO version 3.1 as implemented in the Gaussian 09 program package. The EDA[63-64] and ETS-NOCV[65, 66b, 66c] analyses were carried out at the BP86 level on the BP86/TZVPP optimized geometries by using the program package ADF 2009.01.[75] A triple-ζ-quality basis set augmented by two sets of polarization functions with frozen core approximations for the core electrons was employed. Uncontracted Slater-type orbitals (STOs) were used as the basis function for the SCF calculation.[71] An auxiliary set of s, p, d, f, and g STOs was used to fit the molecular densities and to represent the Coulomb and exchange potentials accurately in each SCF cycle.[72] Scalar relativistic effects were incorporated by applying the zeroth-order regular approximation (ZORA)[73] and the level of theory is denoted as BP86/TZ2P+. Topological analysis of the electron density was performed by using AIMPAC program package.[78] The wave function for the Bader's AIM analysis[77] was obtained at the BP86/TZVPP level by using the program package Gaussian 09. The ETS-NOCV analysis was done to separate the ΔE_{σ} and $\Delta E_{\pi\|}$ contributions, since both contributions come under the same irreducible representation A′ in the EDA of C_s symmetric geometries. The $\Delta E_{\pi\|}$ contribution was taken from the energy of deformation density of $\pi_{\|}$-type orbitals and finally the ΔE_{σ} contribution was given by the equation $\Delta E_{\sigma} = \Delta E_{orb} - \Delta E_{\pi\|} - \Delta E_{\pi\perp}$. For technical reasons, the EDAs involving open-shell fragments neglect the spin polarization in the fragments and thus yield slightly too stable bonds (on the order of a few kcal/mol per unpaired electron). The bond energies were corrected for the spin-polarization error ΔE_{corr}, which is given in the tables.

For clarity, the results and discussion of this chapter is divided as follows:

4.3 Nature of the CS bond in HCSF, HCSH, HCSOH, and F_5SCSF_3

4.4 Nature of the SiS bond in HSiSF and HSiSH

4.5 Nature of the NS bond in NSF, NSH, and NSOH

4.6 Nature of the PS bond in PSF, PSH, and PSOH

4.3 Nature of the CS bond in HCSF, HCSH, HCSOH, and F_5SCSF_3

The nature of the CS bond in the model systems HCSF and HCSH was studied and compared with the experimentally known systems HCSOH and F_5SCSF_3. The geometries of HCSF and HCSH in their singlet electronic states were optimized at the CCSD(T)/TZVPP level of theory (Figure 4.3.1). HCSF has the planar bent geometry with *cis* orientation of the F atom with respect to the HC bond (*cis*-HCSF). *trans*-HCSF is not minimum on the PES. The linear geometry (*lin*-HCSF) is a second-order saddle point and is 28.3 kcal/mol higher in energy than *cis*-HCSF. The HC and CS bond lengths in *cis*-HCSF and *lin*-HCSF are almost similar. The SF bond length in *lin*-HCSF is 0.185 Å longer than the SF bond length in *cis*-HCSF. HCSH has planar bent geometries with *cis* and *trans* orientations of the SH bond with respect to the HC bond (*cis*-HCSH and *trans*-HCSH). *cis*-HCSH is 1.7 kcal/mol higher in energy than *trans*-HCSH. *lin*-HCSH is a second-order saddle point geometry on the PES. The CS bond length in *trans*-HCSH is 0.144 Å longer than the CS bond length in *cis*-HCSF. The SH distance in *lin*-HCSH is 0.550 Å longer than the SH distance in *trans*-HCSH. The relative energies and the geometric parameters optimized at BP86/TZVPP level are given in parentheses in Figure 4.3.1. BP86/TZVPP level overestimate the HSi and SF bond lengths and underestimate the relative energy of the linear structures.

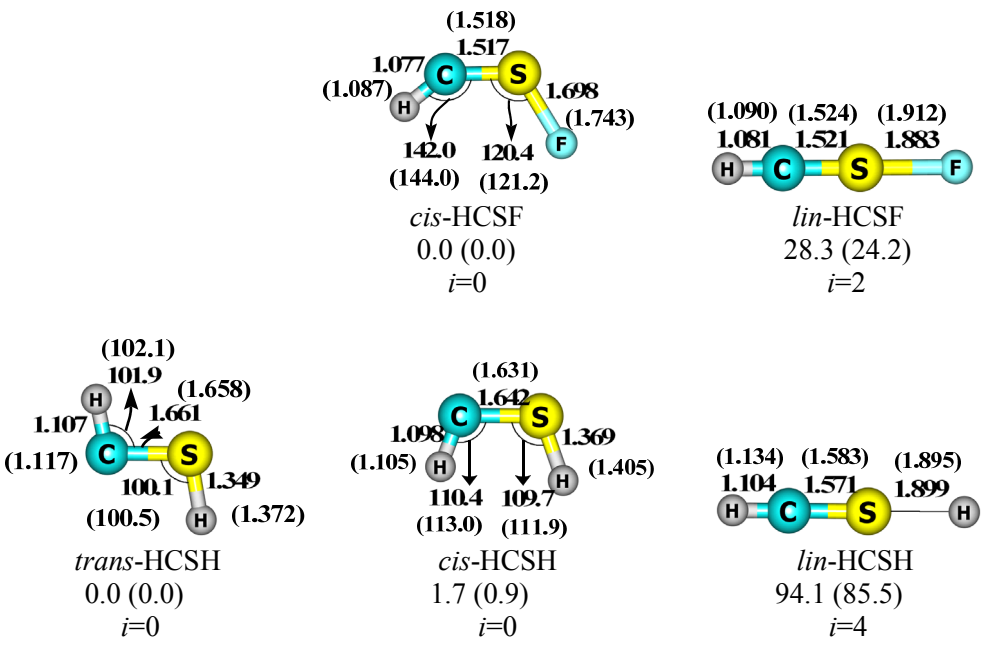

Figure 4.3.1: Optimized geometries at the CCSD(T)/TZVPP. Bond lengths in angstrom, angles in degrees, and relative energies in kcal/mol. Values in parentheses correspond to BP86/TZVPP level. All of the molecules are in the singlet electronic state. The index, *i,* shows the number of imaginary frequencies.

4.3.1 HCSF

The nature of the CS bond in *cis*-HCSF could be viewed as shown in Scheme 4.3.1: triple bond (**a**), double bond (**b**), and single bond (**c**) between C and S. The EDA and ETS-NOCV analyses were performed by considering the fragments HC and SF interacting in different electronic states, as shown in Scheme 4.3.2. The fragments HC and SF interact in the $^4\Sigma^-$ state to form a CS triple bond in

a. The fragment $(HC)^-$ in the $^3\Pi$ or $^3\Sigma^-$ electronic states interact with the $^3\Sigma^-$ $(SF)^+$ fragment in **b1** or **b2** to form CS double bond. In **c1** and **c2**, HC is in the $^2\Sigma^+$ electronic state and SF is in the $^2\Pi$ electronic state and together forms the CS single bond with the C lone-pair electrons residing in the $\pi_{\|}$ and $\pi_{\perp}$ orbitals, respectively. In **c3** the fragments HC and SF interact in the $^2\Pi$ electronic state and form a CS single bond. $^2\Pi$ (HC) and $^2\Pi$ (SF) interact as in **d** to form a dative σ bond and an electron-sharing π bond between C and S. This type of interaction was also previously reported in the literature: a dative carbon-to-metal σ bond and a covalent metal–carbon π bond in the high-valent transition-metal alkylidene complexes.[82]

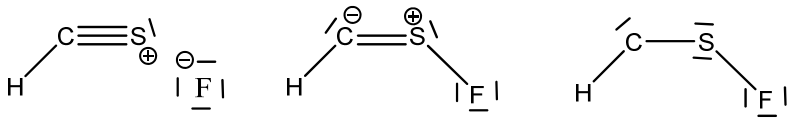

a **b** **c**

Scheme 4.3.1: Resonance structures of *cis*-HCSF. In the Lewis structures **a**, and **b** all of the atoms have the octet electronic configuration, however, the C atom in the structure **c** has only the sextet electronic configuration.

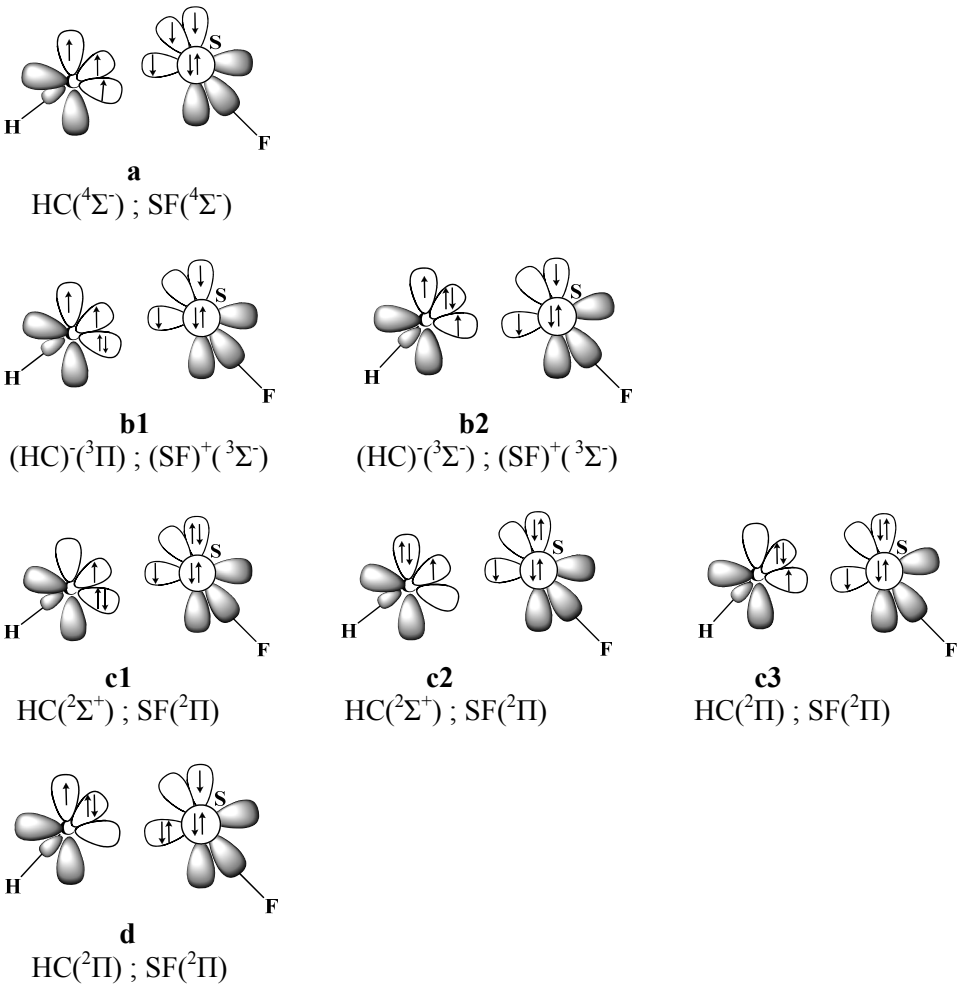

Scheme 4.3.2: Possible valance orbital interactions between C and S in *cis*-HCSF.

Table 4.3.1: Energy decomposition and ETS-NOCV analyses of the CS bond in *cis*-HCSF at BP86/TZ2P+

Interacting Fragments	$HC(^4\Sigma^-)$; $SF(^4\Sigma^-)$		$(HC)^-(^3\Pi)$; $(SF)^+(^3\Sigma^-)$		$(HC)^-(^3\Sigma^-)$; $(SF)^+(^3\Sigma^-)$		$HC(^2\Sigma^+)$; $SF(^2\Pi)$	
	a		**b1**		**b2**		**c1**	
	EDA	ETS-NOCV	EDA	ETS-NOCV	EDA	ETS-NOCV	EDA	ETS-NOCV
Symmetry	C_s	C_s	C_s	C_s	C_s	C_s	C_s	C_s
ΔE_{int}	-210.1	-210.1	-426.1	-426.1	-363.6	-363.6	-221.9	-221.9
ΔE_{Pauli}	390.4	390.4	527.3	527.3	677.3	677.3	473.6	473.6
ΔE_{elstat} [a]	-209.7 (34.9)	-209.7 (34.9)	-434.7 (45.6)	-434.7 (45.6)	-516.5 (49.6)	-516.5 (49.6)	-249.9 (35.9)	-249.9 (35.9)
ΔE_{orb} [a]	-390.9 (65.1)	-390.9 (65.1)	-518.7 (54.4)	-518.7 (54.4)	-524.3 (50.4)	-524.3 (50.4)	-445.6 (64.1)	-445.6 (64.1)
ΔE_{σ} [b]	-318.6 (81.5)	-220.6 (56.4)	-420.4 (81.0)	-368.8 (71.1)	-424.9 (81.0)	-373.7 (71.3)	-356.8 (80.1)	-323.0 (72.5)
ΔE_{π} [b][c]	-72.2 (18.4)	-170.2 (43.6)	-98.3 (19.0)	-149.9 (28.9)	-99.5 (19.0)	-150.7 (28.7)	-88.8 (19.9)	-122.6 (27.5)
$\Delta E_{\pi\parallel}$ [b][c]	-	-98.0 (25.2)	-	-51.6 (9.9)	-	-51.2 (9.7)	-	-33.8 (7.6)
$\Delta E_{\pi\perp}$ [b][c]	-72.2 (18.4)	-72.2 (18.4)	-72.2 (18.4)	-98.3 (19.0)	-99.5 (19.0)	-99.5 (19.0)	-72.2 (18.4)	-88.8 (19.9)
ΔE_{prep} HC or $(HC)^-$	15.2	15.2	62.7	62.7	1.3	1.3	72.3	72.3
ΔE_{prep} SF or $(SF)^+$	45.7	45.7	13.8	13.8	13.8	13.8	3.4	3.4
ΔE_{corr} [d]	6.0	6.0	5.0	5.0	3.9	3.9	3.0	3.0
$\Delta E(= -D_e)$	-143.2	-143.2	-344.6	-344.6	-344.6	-344.6	-143.2	-143.2

[a] The values in parentheses are the percentage contributions to the total attractive interaction $\Delta E_{elstat} + \Delta E_{orb}$. [b] The values in parentheses are the percentage contributions to the total orbital interactions ΔE_{orb}. [c] The ΔE_{π} interaction is further divided into $\Delta E_{\pi\parallel}$ (in plane) and $\Delta E_{\pi\perp}$ (out of plane) interactions. [d] Correction for spin polarization.

Note: The electronic ground state of the fragments are: $HC(^2\Pi)$; $SF(^2\Pi)$; $(HC)^-(^3\Sigma^-)$ and $(SF)^+(^3\Sigma^-)$. Energy values in kcal/mol.

Table 4.3.1 continued. Energy decomposition and ETS-NOCV analyses of the CS bond in *cis*-HCSF at BP86/TZ2P+

Interacting Fragments	HC($^2\Sigma^+$) ; SF($^2\Pi$)	HC($^2\Pi$) ; SF($^2\Pi$)		HC($^2\Pi$) ; SF($^2\Pi$)
	c2	**c3**		**d**
	EDA	EDA	ETS-NOCV	EDA
Symmetry	C_s	C_s	C_s	C_s
ΔE_{int}	-221.8	-150.0	-150.0	-150.0
ΔE_{Pauli}	387.3	614.8	614.8	686.9
ΔE_{elstat} [a]	-134.4	-310.2 (40.6)	-310.2 (40.6)	-326.8 (39.0)
ΔE_{orb} [a]	-474.8	-454.6 (59.4)	-454.6 (59.4)	-510.2 (61.0)
ΔE_{σ} [b]	-622.2 (131.1)	-361.4 (79.5)	-313.6 (69.0)	-428.5 (84.0)
ΔE_{π} [b][c]	147.4 (-31.0)	-93.2 (20.5)	-141.0 (31.0)	-81.7 (16.0)
$\Delta E_{\pi\parallel}$ [b][c]	-	-	-47.8 (10.5)	-
$\Delta E_{\pi\perp}$ [b][c]	147.4 (-31.0)	-93.2 (20.5)	-93.2 (20.5)	-81.7 (16.0)
ΔE_{prep} (HC)	72.3	0.8	0.8	0.8
ΔE_{prep} (SF)	3.4	3.4	3.4	3.4
ΔE_{corr} [d]	3.0	2.6	2.6	2.6
$\Delta E(= -D_e)$	-143.2	-143.2	-143.2	-143.2

[a] The values in parentheses are the percentage contributions to the total attractive interaction $\Delta E_{elstat} + \Delta E_{orb}$. [b] The values in parentheses are the percentage contributions to the total orbital interactions ΔE_{orb}. [c] The ΔE_{π} interaction is further divided into $\Delta E_{\pi\parallel}$ (in plane) and $\Delta E_{\pi\perp}$ (out of plane) interactions. [d] Correction for spin polarization.
Note: The electronic ground state of the fragments are: HC($^2\Pi$) ; SF($^2\Pi$) ; $(HC)^-(^3\Sigma^-)$ and $(SF)^+(^3\Sigma^-)$. Energy values in kcal/mol.

The EDA and ETS-NOCV results are given in Table 4.3.1. Among the different interaction schemes, **a** has the smallest magnitude for the orbital interaction term, ΔE_{orb}. Hence, **a** is the best choice to describe the nature of the CS bond in *cis*-HCSF. The CS bond in *cis*-HCSF has 34.9% electrostatic and 65.1% orbital contributions according to interaction scheme **a**. The total orbital contribution is divided into 56.4% σ, 25.2% $\pi_{\parallel}$, and 18.4% $\pi_{\perp}$ contributions. Figure 4.3.2 shows the valance orbital interaction between the frozen geometry of the fragments HC ($^4\Sigma^-$) and SF ($^4\Sigma^-$) in *cis*-HC≡SF. The orbitals HOMO (7A′), HOMO-1 (2A″), and HOMO-5 (4A′) are the $\pi_{\parallel}$, $\pi_{\perp}$, and σ type orbitals, respectively, of the CS bond in *cis*-HCSF. HOMO-7 (2A′) has a major contribution (56.7%) from the valance s orbital of S (2A′) of the SF fragment. NBO analysis (Table 4.3.2) shows three CS bond-pair orbitals, one lone-pair orbital on S (with 69.8% s character), and four lone-pair orbitals on F. The Wiberg bond index of the CS bond is 2.506. The NOCV pairs and the deformation densities of the σ- and π-type contributions to the CS triple bond in *cis*-HCSF are shown in Figure 4.3.3. The σ NOCV pairs of the CS bond resemble the molecular orbitals 2A′ of the HC fragment and 5A′ of the SF fragment in Figure 4.3.2; the $\pi_{\parallel}$ NOCV pairs resemble 3A′ of HC and 6A′ of the SF fragments and the $\pi_{\perp}$ NOCV pairs are 1A″ of HC and 2A″ of the SF fragment.

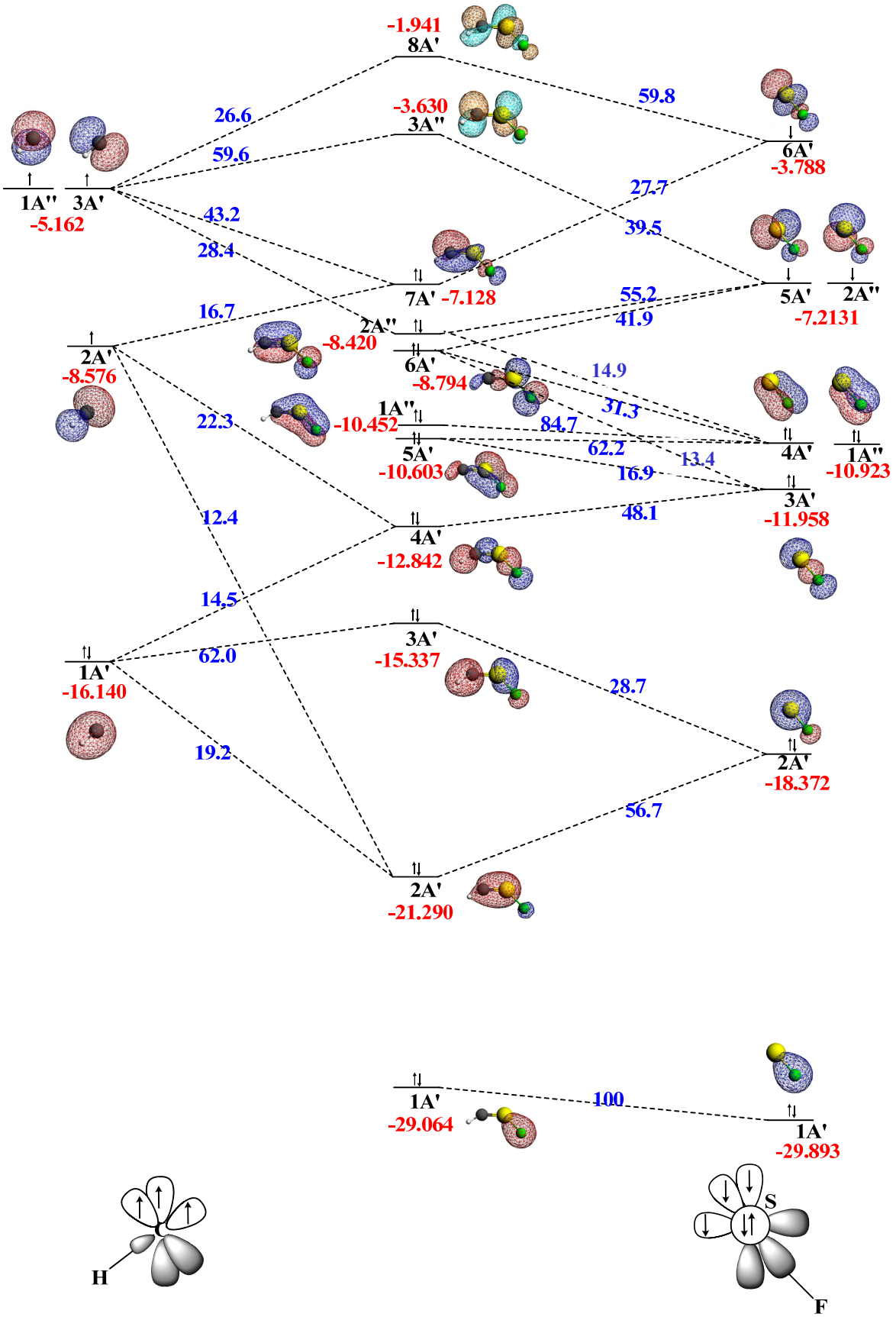

Figure 4.3.2: Plot of the valence orbital interaction between the frozen geometry of the fragments HC and SF in HC≡SF at BP86/TZ2P. The percentage contributions are shown in blue colour and the orbital energies (eV) are shown in red colour. The percentage contributions less than 5% are not shown.

Alpha electrons				
k	Orbital type	NOCVS		Deformation Density $\Delta\rho_k$
		ψ_{-k}	ψ_k	
		(υ_{-k})	(υ_k)	ΔE (kcal/mol)
1	σ	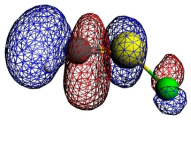	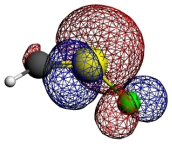	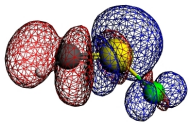
		-0.61	0.61	-111.4
2	$\pi_{\|\|}$	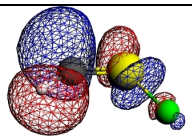	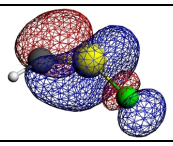	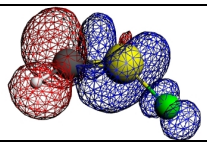
		-0.43	0.43	-26.0
3	$\pi_\perp$	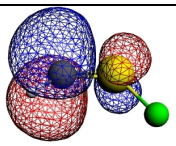	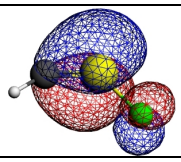	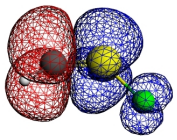
		-0.69	0.69	-42.7

Figure 4.3.3a

Beta electrons				
k	Orbital type	NOCVS		Deformation Density $\Delta\rho_k$
		ψ_{-k}	ψ_k	
		(υ_{-k})	(υ_k)	ΔE (kcal/mol)
1	σ	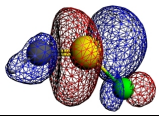	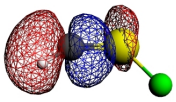	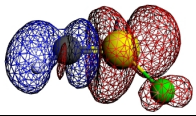
		-0.49	0.49	-92.4
2	$\pi_{\|\|}$	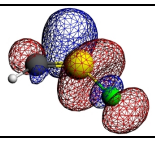	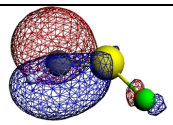	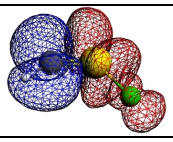
		-0.72	0.72	-72.0
3	$\pi_\perp$	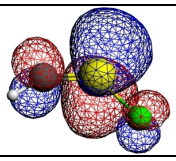	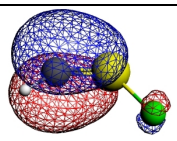	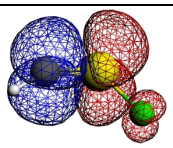
		-0.50	0.50	-28.7

Figure 4.3.3b

Figure 4.3.3: (a) Contours of the most important NOCV pairs (ψ_{-k}, ψ_k) and their eigenvalues (υ_{-k}, υ_k) of alpha electrons, representing electron donation from HC to the SF fragment and corresponding deformation density ($\Delta\rho_k$) with the orbital stabilization energy (ΔE); **(b)** Contours of the most important NOCV pairs (ψ_{-k}, ψ_k) and their eigenvalues (υ_{-k}, υ_k) of beta electrons representing electron donation from SF to HC fragment and corresponding deformation density ($\Delta\rho_k$) with the orbital stabilization energy (ΔE); in *cis*-HCSF, corresponding to interaction **a** (Scheme 4.3.2).

Table 4.3.2: NBO partial charges (q), Wiberg bond indices (P), and the number of bond-pair (BP) and lone-pair (LP) orbitals at BP86/TZVPP

	Partial charges (q)				P(CS)	LP			BP		
	H	C	S	F(H)		C (%s and p)	S (% s and p)	F(H)	HC	CS	SF or SH
cis-HCSF	0.23	-0.56	0.85	-0.52	2.506	0	1 s(69.8) p(30.0)	4[1]	1	3	0
lin-HCSF	0.23	-0.40	0.78	-0.59	2.678	0	1 s(88.4) p(11.2)	4[2]	1	3	0
trans-HCSH	0.14	-0.47	0.23	0.10	1.847	1 s(59.9) p(39.7)	1 s(65.5) p(34.5)	0	1	2	1
cis-HCSH	0.16	-0.48	0.28	0.04	1.913	1 s(51.6) p(47.9)	1 s(62.7) p(37.3)	0	1	2	1

[1] Electron occupancy in the lone pair orbitals on F in *trans*-HCSF (1.99, 1.97, 1.93, 1.63)
[2] Electron occupancy in the lone pair orbitals on F in *lin*-HCSF (1.99, 1.87, 1.87, 1.84)

lin-HCSF is a second-order saddle-point structure, which is 28.3 kcal/mol higher in energy than the bent structure at the CCSD(T)/TZVPP level and 24.2 kcal/mol at the BP86/TZVPP level of theory. The HC and the CS bond lengths are almost same in both the linear and bent structures. The SF bond length in the linear structure is 0.185 Å longer than the SF bond in the bent structure at the CCSD(T)/TZVPP level and 0.169 Å longer at the BP86/TZVPP level. Table 4.3.3 shows the results of the EDA and ETS-NOCV analyses of the CS and SF bonds in *lin*- and *cis*-HCSF. The EDA and ETS-NOCV results of the CS bond in *lin*- and *cis*-HCSF are almost same, except the $\Delta E_{\pi\|}$ contribution of *cis*-HCSF (25.2%) is higher than the $\Delta E_{\pi\|}$ contribution of *lin*-HCSF (19.6%). This is because in the bent structure the $\pi_{\|}$ orbital of one fragment can interact not only with the $\pi_{\|}$ orbital but also with the σ orbital of the other fragment.

The nature of the SF bond was analysed by considering the interaction between the charged species $(HCS)^+$ and F^-. In both *lin*- and *cis*-HCSF, the SF bond has larger electrostatic contribution than the orbital contribution. The electrostatic contribution is larger in *lin*-HCSF (67.3%) than in *cis*-HCSF (62.7%) and the reverse is true for the total orbital contribution. *cis*-HCSF has 82.2% σ contribution to the total orbital contribution of the SF bond, whereas *lin*-HCSF has only 55.1% σ contribution. NBO analysis showed four lone pair orbitals on F with almost the same occupancy on *lin*-HCSF (Table 4.3.2). *cis*-HCSF also has four lone pair orbitals on F: three of them with the similar occupancy and the fourth lone pair orbital on F has a smaller occupancy of only 1.63 electrons (Table 4.3.2). The SH bond in *lin*-HCSH is 0.550 Å longer than the SH bond in *trans*-HCSH at the CCSD(T)/TZVPP level and 0.523 Å longer at the BP86/TZVPP level of theory (Figure 4.3.1). In addition, *lin*-HCSH in the triplet electronic state has two imaginary frequencies (i = 2); with H being dissociated from the rest of the HCS fragment at the BP86/TZVPP level. These results suggest that the

SF bond in *cis*-HCSF and the SH bond in *cis*- and *trans*-HCSH are more polarised (with good orbital overlapping) with the shorter bonds than in the linear structures.

Table 4.3.3: ETS-NOCV analysis at BP86/TZ2P+ between the fragments $(HCS)^+$ and F^- and between the fragments HC and SF in *lin*- and *cis*-HCSF.

Interacting fragments	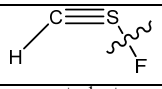	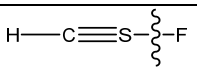	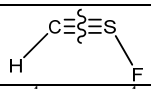	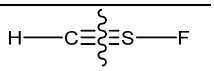
	$(HCS)^+(^1\Sigma^+)$; F^- $(^1\Sigma^+)$	$(HCS)^+(^1\Sigma^+)$; F^- $(^1\Sigma^+)$	$HC(^4\Sigma^-)$; $SF(^4\Sigma^-)$	$HC(^4\Sigma^-)$; $SF(^4\Sigma^-)$
Symmetry	C_s	$C_{\infty v}$	C_s	$C_{\infty v}$
ΔE_{int}	-200.4	-168.3	-210.1	-181.3
ΔE_{Pauli}	228.7	136.6	390.4	396.5
ΔE_{elstat} [a]	-268.9 (62.7)	-205.2 (67.3)	-209.7 (34.9)	-208.4 (36.1)
ΔE_{orb} [a]	-160.1 (37.3)	-99.8 (32.7)	-390.9 (65.1)	-369.3 (63.9)
ΔE_{σ} [b]	-131.6 (82.2)	-55.0 (55.1)	-220.6 (56.4)	-224.6 (60.8)
ΔE_{π} [b][c]	-28.6 (17.8)	-44.8 (44.9)	-170.2 (43.6)	-144.6 (39.2)
$\Delta E_{\pi\parallel}$ [b][c]	-11.4 (7.1)	-22.4 (22.4)	-98.0 (25.2)	-72.3 (19.6)
$\Delta E_{\pi\perp}$ [b][c]	-17.2 (10.7)	-22.4 (22.4)	-72.2 (18.4)	-72.3 (19.6)
$\Delta E_{prep}(HCS)^+$ or (HC)	9.8	1.2	15.2	15.2
$\Delta E_{prep}(F^-)$ or (SF)	0.0	0.0	45.7	40.3
$\Delta E(= -D_e)$	-190.6	-167.1	-149.2	-125.8

[a] The values in parentheses are the percentage contributions to the total attractive interaction $\Delta E_{elstat} + \Delta E_{orb}$. [b] The values in parentheses are the percentage contributions to the total orbital interactions ΔE_{orb}. [c] The ΔE_{π} interaction is further divided into $\Delta E_{\pi\parallel}$ (in plane) and $\Delta E_{\pi\perp}$ (out of plane) interactions.

4.3.2 HCSH

trans-HCSH is global minimum at both levels of theory (Figure 4.3.1). The CS bond in *trans*-HCSH is 0.019 Å longer than the CS bond in *cis*-HCSH at the CCSD(T)/TZVPP level and 0.027 Å longer at the BP86/TZVPP level of theory. The SH bond in *cis*-HCSH is 0.020 Å longer than the SH bond in *trans*-HCSH at the CCSD(T)/TZVPP level and 0.027 Å longer at the BP86/TZVPP level of theory. The positive charge on S and the Wiberg bond index of the CS bond, *P*(CS), in *cis*- and *trans*-HCSH are smaller than that of *cis*-HCSF (Table 4.3.2). The nature of the CS bond in *cis*-HCSH was not expected to deviate much from that of *trans*-HCSH. The nature of the CS bond in *trans*-HCSH could be viewed as shown in Scheme 4.3.3. In Scheme 4.3.3, the fragments HC and SH interact in different electronic states to form triple bonds (**a**), double bonds (**b**), single bonds (**c**), and dative σ bonds and a π-electron-sharing covalent bond (**d**) between the atoms C and S in *trans*-HCSH.

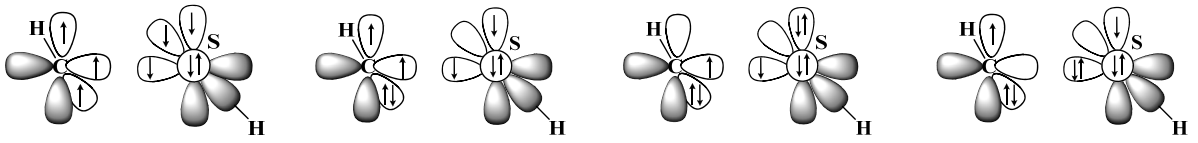

a $HC(^4\Sigma^-)$; $SH(^4\Sigma^-)$ **b** $(HC)^-(^3\Sigma^-)$; $(SH)^+(^3\Sigma^-)$ **c** $HC(^2\Pi)$; $SH(^2\Pi)$ **d** $HC(^2\Pi)$; $SH(^2\Pi)$

Scheme 4.3.3: Valence orbital interactions between C and S in *trans*-HCSH.

Table 4.3.4: Energy decomposition and ETS-NOCV analyses of the CS bond in *trans*-HCSH at BP86/TZ2P+

Interacting Fragments	$HC(^4\Sigma^-)$; $SH(^4\Sigma^-)$		$(HC)^-(^3\Sigma^-)$; $(SH)^+(^3\Sigma^-)$		$HC(^2\Pi)$; $SH(^2\Pi)$			
	a		**b**		**c**		**d**	
	EDA	ETS-NOCV	EDA	ETS-NOCV	EDA	ETS-NOCV	EDA	ETS-NOCV
Symmetry	C_s	C_s	C_s	C_s	C_s	C_s	C_s	C_s
ΔE_{int}	-252.2	-252.2	-324.1	-324.1	-113.5	-113.5	-113.5	-113.5
ΔE_{Pauli}	294.1	294.1	405.3	405.3	362.5	362.5	347.2	347.2
ΔE_{elstat} [a]	-168.4 (30.8)	-168.4 (30.8)	-377.9 (51.8)	-377.9 (51.8)	-198.1 (41.6)	-198.1 (41.6)	-153.7 (33.4)	-153.7 (33.4)
ΔE_{orb} [a]	-377.8 (69.2)	-377.8 (69.2)	-351.5 (48.2)	-351.5 (48.2)	-277.9 (58.4)	-277.9 (58.4)	-307.0 (66.6)	-307.0 (66.6)
ΔE_{σ} [b]	-314.1 (83.1)	-190.2 (50.3)	-254.6 (72.4)	-222.5 (63.3)	-224.4 (80.7)	-203.2 (73.1)	-235.1 (76.6)	-208.8 (68.0)
ΔE_{π} [b][c]	-63.7 (16.9)	-187.6 (49.7)	-96.9 (27.6)	-129.0 (36.7)	-53.5 (19.3)	-74.7 (26.9)	-71.9 (23.4)	-98.2 (32.0)
$\Delta E_{\pi\parallel}$ [b][c]	-	-123.9 (32.8)	-	-32.1 (9.1)	-	-21.2 (7.6)	-	-26.3 (8.6)
$\Delta E_{\pi\perp}$ [b][c]	-63.7 (16.9)	-63.7 (16.9)	-96.9 (27.6)	-96.9 (27.6)	-53.5 (19.3)	-53.5 (19.3)	-71.9 (23.4)	-71.9 (23.4)
ΔE_{prep} (HC)	15.2	15.2	0.4	0.4	0.0	0.0	0.0	0.0
ΔE_{prep} (SH)	120.2	120.2	0.0	0.0	0.0	0.0	0.0	0.0
ΔE_{corr} [d]	6.1	6.1	3.6	3.6	2.8	2.8	2.8	2.8
$\Delta E(= -D_e)$	-110.7	-110.7	-320.1	-320.1	-110.7	-110.7	-110.7	-110.7

[a] The values in parentheses are the percentage contributions to the total attractive interaction $\Delta E_{elstat} + \Delta E_{orb}$. [b] The values in parentheses are the percentage contributions to the total orbital interactions ΔE_{orb}. [c] The ΔE_{π} interaction is further divided into $\Delta E_{\pi\parallel}$ (in plane) and $\Delta E_{\pi\perp}$ (out of plane) interactions. [d] Correction for spin polarization.

Note: The electronic ground state of the fragments are: $HC(^2\Pi)$; $SH(^2\Pi)$; $(HC)^-(^3\Pi)$ and $(SH)^+(^3\Pi)$. Energy values in kcal/mol.

Alpha electrons				
k	Orbital type	NOCVS		Deformation Density
		ψ_{-k}	ψ_k	$\Delta\rho_k$
		(υ_{-k})	(υ_k)	ΔE (kcal/mol)
1	σ	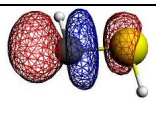	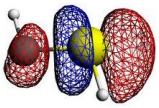	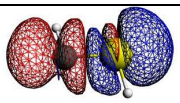
		-0.62	0.62	-104.4
2	$\pi_{\|\|}$	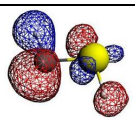	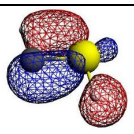	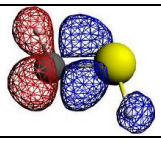
		-0.19	0.19	-8.4
3	$\pi_\perp$	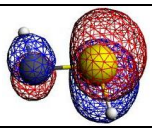	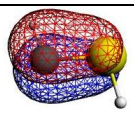	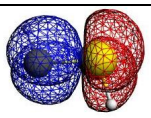
		-0.38	0.38	-27.8

Figure 4.3.4a

Beta electrons				
k	Orbital type	NOCVS		Deformation Density
		ψ_{-k}	ψ_k	$\Delta\rho_k$
		(υ_{-k})	(υ_k)	ΔE (kcal/mol)
1	σ	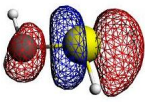	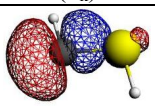	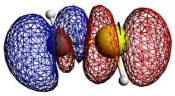
		-0.58	0.58	-89.1
2	$\pi_{\|\|}$	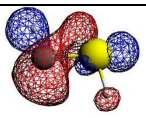	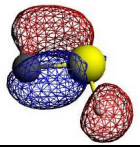	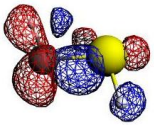
		-0.20	0.20	-12.8
3	$\pi_\perp$	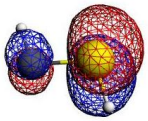	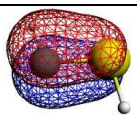	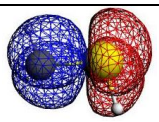
		-0.38	0.38	-25.7

Figure 4.3.4b

Figure 4.3.4: **(a)** Contours of the most important NOCV pairs (ψ_{-k}, ψ_k) and their eigenvalues (υ_{-k}, υ_k) of alpha electrons representing electron donation from HC to the SH fragment and corresponding deformation density ($\Delta\rho_k$) with the orbital stabilization energy (ΔE); **(b)** Contours of the most important NOCV pairs (ψ_{-k}, ψ_k) and their eigenvalues (υ_{-k}, υ_k) of beta electrons representing electron donation from SH to the HC fragment and corresponding deformation density ($\Delta\rho_k$) with the orbital stabilization energy (ΔE); in *trans*-HCSH corresponding to **c** (Scheme 4.3.3).

The bonding nature of the CS bond in *trans*-HCSH was analysed by using the EDA and ETS-NOCV methods and the results are given in Table 4.3.4, where the interaction scheme **c** has the smallest orbital interaction (ΔE_{orb}) value. In the interaction scheme **c**, the fragments HC and SH interact in the $^2\Pi$ electronic state to form a CS single bond (Scheme 4.3.3). The lone pair electrons in the $p_{\pi\perp}$ orbital of S (**c** in scheme 3) are delocalized to the empty $p_{\pi\perp}$ orbital of C, resulting in 19.3% of the $\Delta E_{\pi\perp}$ contribution to the total orbital contribution of the CS bond. This is consistent with the Wiberg bond index value, *P*(CS), of 1.847. In addition, NBO analysis shows a lone pair each on C and S (Table 4.3.2). The CS bond in HCSH has an electron-sharing σ bond with a sp hybrid lone pair on C and the lone-pair electrons in the $p_{\pi\perp}$ orbital of S are shared with the $p_{\pi\perp}$ orbital of C. This is also evident from the NOCV and deformation density pictures of the CS bond in Figure 4.3.4. The NOCV pairs and the deformation density of the σ-type orbitals in Figure 4.3.4a indicates charge transfer of an alpha electron from the fragment HC to the fragment SH and the reverse for the beta electron in Figure 4.3.4b. The NOCV pairs and deformation densities of the $\pi_{||}$- and $\pi\perp$-type orbitals in Figure 4.3.4a and 4.3.4b look similar due to lone-pair electron donation from one fragment to the other.

The σ-bond pair electrons of the SF bond in *cis*-HCSF are delocalized towards the F atom and remain as a lone pair (presence of 4th lone pair on F with slightly smaller electron occupation from the NBO data given in Table 4.3.2), leaving the p orbital on S (the orbital 6A′ of the SF fragment in Figure 4.3.2) available for bonding with the $p_{\pi||}$ orbital of C. However, in *trans*-HCSH, the p orbital on S is not available for bonding with the $p_{\pi||}$ orbital of C because of the SH covalent bond. Moreover the fragment SH has larger preparation energy than the fragment SF in interaction scheme **a (**Tables 4.3.4 and 4.3.1).

4.3.3 HCSOH

Figure 4.3.5 shows the geometries of the molecule HCSOH optimized at the BP86/TZVPP level of theory. HCSOH has four different conformers, *cis,cis, cis,trans, trans,cis*, and *trans,trans*, based on the orientation of the O atom relative to HCS and that of the H atom relative to the CSO moiety. *cis,cis*-HCSOH is the most stable conformation (also reported in the literature).[11] The Wiberg bond index of the CS bond in *cis,cis*-HCSOH is 2.345, which is slightly smaller than that in *cis*-HCSF. Table 4.3.5 shows the EDA and ETS-NOCV results of the CS bond in *cis,cis*-HCSOH between the fragments HC and SOH (only the most important valance orbital interaction schemes between C and S were considered). Similar to *cis*-HCSF, interaction scheme **a** in *cis,cis*-HCSOH has a smaller value for the orbital contribution. However, the difference in orbital contribution values between interaction schemes **a** and **c3** in *cis,cis*-HCSOH is smaller than that in *cis*-HCSF, which implies that the CS triple-bond character in *cis,cis*-HCSOH is weaker than that in *cis*-HCSF.

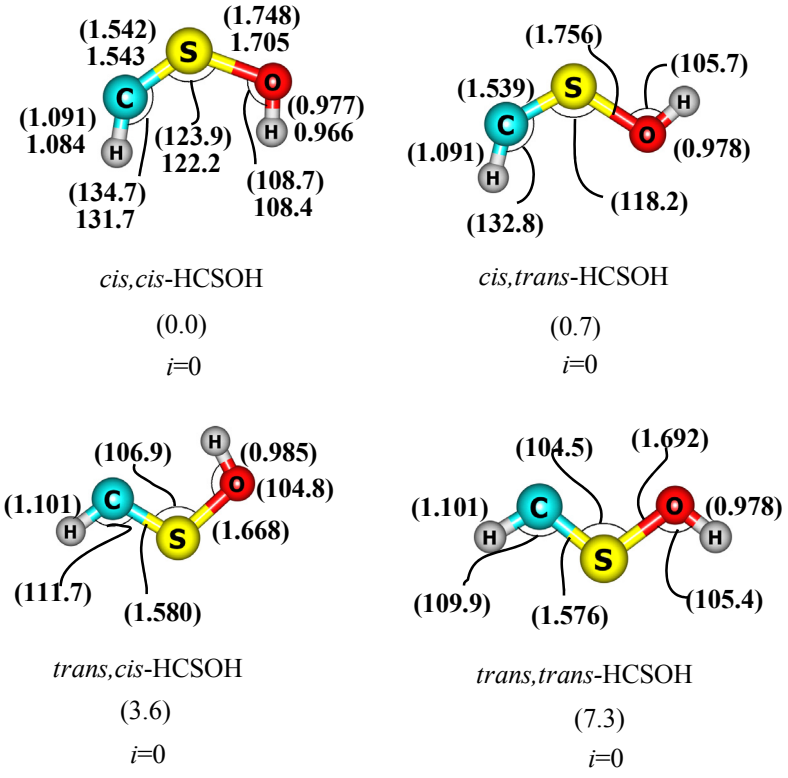

cis,cis-HCSOH
(0.0)
i=0

cis,trans-HCSOH
(0.7)
i=0

trans,cis-HCSOH
(3.6)
i=0

trans,trans-HCSOH
(7.3)
i=0

Figure 4.3.5: Optimized geometries of the singlet HCSOH in different conformations at BP86/TZVPP level. For, *cis,cis*-HCSOH geometrical parameters are also given at the CCSD(T)/TZVPP level. Bond lengths in angstrom, angles in degrees, and relative energies in kcal/mol. The index, *i,* shows the number of imaginary frequencies.

Table 4.3.5. Energy decomposition and ETS-NOCV analyses of the CS bond in *cis,cis*-HCSOH at BP86/TZ2P+

Inter. frags	$HC(^4\Sigma^-)$; $SOH(^4\Sigma^-)$		$(HC)^-(^3\Sigma^-)$; $(SOH)^+(^3\Sigma^-)$		$HC(^2\Pi)$; $SOH(^2\Pi)$	
	a		**b2**		**c3**	
	EDA	ETS-NOCV	EDA	ETS-NOCV	EDA	ETS-NOCV
Symmetry	C_s	C_s	C_s	C_s	C_s	C_s
ΔE_{int}	-213.9	-213.9	-329.1	-329.1	-144.1	-144.1
ΔE_{Pauli}	374.2	374.2	618.1	618.1	559.8	559.8
ΔE_{elstat} [a]	-207.6 (35.3)	-207.6 (35.3)	-480.8 (50.8)	-480.8 (50.8)	-289.7 (41.2)	-289.7 (41.2)
ΔE_{orb} [a]	-380.6 (64.7)	-380.6 (64.7)	-466.5 (49.2)	-466.5 (49.2)	-414.2 (58.8)	-414.2 (58.8)
ΔE_{σ} [b]	-313.8 (82.5)	-215.2 (56.5)	-373.2 (80)	-336.1 (72)	-321.3 (77.6)	-298.7 (72.1)
ΔE_{π} [b][c]	-66.8 (17.6)	-165.0 (43.4)	-93.3 (20)	-130.4 (27.9)	-92.8 (22.4)	-115.5 (27.9)
$\Delta E_{\pi\parallel}$ [b][c]	-	-99.9 (26.2)	-	-39.2 (8.4)	-	-24.1 (5.8)
$\Delta E_{\pi\perp}$ [b][c]	-66.8 (17.6)	-65.5 (17.2)	-93.3 (20)	-91.1 (19.5)	-92.8 (22.4)	-91.4 (22.1)
ΔE_{prep}	81.2	81.2	11.9	11.9	14.8	14.8
ΔE_{corr} [d]	6.1	6.1	3.7	3.7	2.3	2.3
$\Delta E(= -D_e)$	-126.6	-126.6	-313.5	-313.5	-126.6	-126.6

[a] The values in parentheses are the percentage contributions to the total attractive interaction $\Delta E_{elstat} + \Delta E_{orb}$. [b] The values in parentheses are the percentage contributions to the total orbital interactions ΔE_{orb}. [c] The ΔE_{π} interaction is further divided into $\Delta E_{\pi\parallel}$ (in plane) and $\Delta E_{\pi\perp}$ (out of plane) interactions. [d] Correction for spin polarization.
Note: The electronic ground state of the fragments are: $HC(^2\Pi)$, $SOH(^2\Pi)$, $(HC)^-(^3\Sigma^-)$ and $(SOH)^+(^3\Sigma^-)$. Energy values in kcal/mol.

4.3.4 F_5SCSF_3

Figure 4.3.6 shows the geometries of F_5SCSF_3 optimized at the BP86/TZVPP level of theory. The structure with the S-C-S bending angle of 152.0° is slightly lower in energy than the structure with the S-C-S angle of 179.8°. The second structure has two imaginary frequencies of smaller magnitude. The nature of the CS^1 bond in F_5SCSF_3 could be viewed as shown in Scheme 4.3.4.

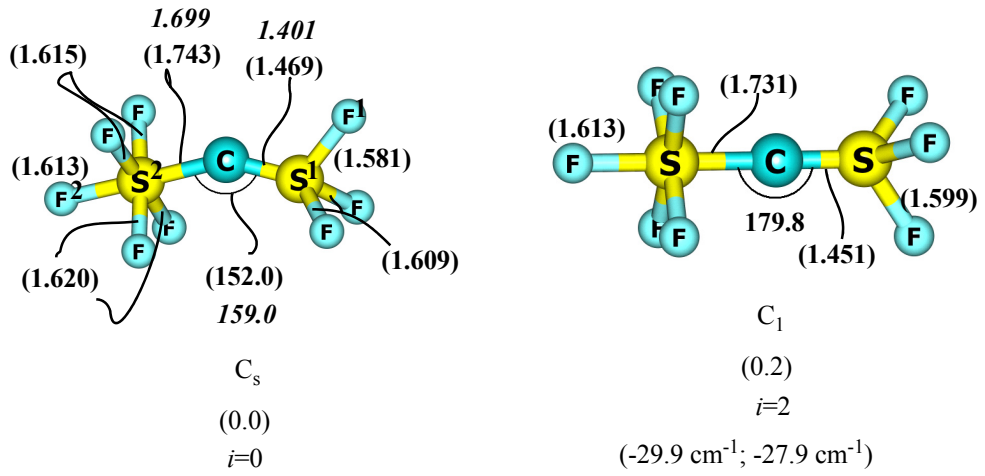

C_s (0.0) i=0 C_1 (0.2) i=2 (-29.9 cm^{-1}; -27.9 cm^{-1})

Figure 4.3.6: Optimized geometries of the singlet F_5SCSF_3 in two different S-C-S bond angles, at BP86/TZVPP level. Bond lengths in angstrom, angles in degrees, and relative energies in kcal/mol. Experimental[79c] (gas phase electron diffraction) values in italics. The index, *i,* shows the number of imaginary frequencies.

EDA and ETS-NOCV analyses of F_5SCSF_3 were performed by considering fragments F_5SC and SF_3 interacting in different electronic states and forming CS triple (**a**), double (**b**), and single (**c**) bonds (Scheme 4.3.4). Similar to *cis*-HCSF, interaction scheme **a** (CS triple bond) in Table 4.3.6 has the smallest orbital interaction value relative to the other schemes **b** and **c**. The interaction scheme **a** of F_5SCSF_3 has a slightly larger ΔE_{int} value and slightly smaller Pauli repulsion, ΔE_{Pauli}, than that in interaction scheme **a** of *cis*-HCSF (Table 4.3.1). The smaller Pauli repulsion in F_5SCSF_3 is due to the presence of more electronegative F atoms than in *cis*-HCSF. Moreover, the Pauli repulsion in **c** is smaller than that in **a** in case of F_5SCSF_3 and *cis*-HCSF has the opposite trend. This trend in Pauli repulsion could be explained by the electronic state of the interacting fragments in the respective interaction schemes **a** and **c3** (**c3** has the second smallest orbital interaction value in Table 4.3.1) in Scheme 4.3.2 and the interaction schemes **a** and **c** in Scheme 4.3.4. The lone-pair electrons on C in scheme **c** (of F_5SCSF_3) are in the out-of-plane $p_{\pi\perp}$ orbital, reducing the lone pair–bond pair repulsion. However, in interaction scheme **c3** (of *cis*-HCSF), the lone-pair electrons are in the sp-hybrid (in-plane) orbital of C. Having the lone-pair electrons in the $p_{\pi\parallel}$ orbital of C increases the ΔE_{Pauli} value of the CS bond in F_5SCSF_3. The very high preparation energy of the SF_3 fragment comes from the structural deformation (from planar T-shaped to trigonal pyramidal geometry) and the electronic excitation energy. Though the bonding descriptions in interaction schemes **b** and **c** are double and

single, the CS bond in these resonance schemes has significant $\Delta E_{\pi\|}$ contribution, similar to **a** (Table 4.3.6). The Wiberg bond index of the CS^1 bond in F_5SCSF_3 is 2.231; C has the charges -0.94 and 2.00 on S^1. NBO analysis does not show any lone-pair orbitals on C and S (which indicates that all of the valance electrons of C and S are involved in bonding). Figure 4.3.7 shows the NOCV pairs and the deformation densities of the CS triple bond in F_5SCSF_3. The NOCV pairs corresponding to the σ-type orbital of the SF_3 fragment comes mainly from the s orbital of S and the p orbital of the three F atoms. The proton affinities (at C center) of F_5SCSF_3, *cis*-HCSF, *cis,cis*-HCSOH, and *cis*-HCSH are -190.4, -201.3, -220.3, and -234.5 kcal/mol, respectively, at the BP86/TZVPP level.

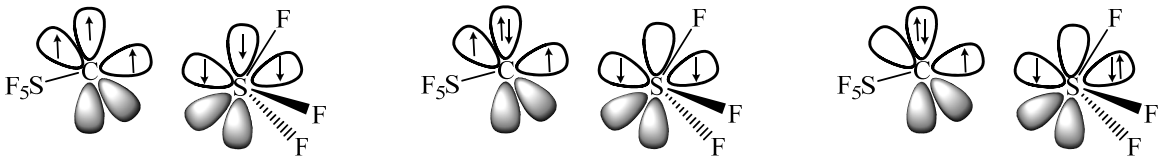

a $(F_5S\text{-}C)(^4\Sigma^-)$; $(SF_3)(^4\Sigma^-)$

b $(F_5S\text{-}C)^-(^3\Pi)$; $(SF_3)^+(^3\Pi)$

c $(F_5S\text{-}C)(^2\Sigma^+)$; $(SF_3)(^2\Sigma^+)$

Scheme 4.3.4: Valence orbital interactions between C and S in F_5SCSF_3.

Table 4.3.6: EDA and ETS-NOCV analyses of the CS bond in F_5SCSF_3 at BP86/TZ2P+

Interacting Fragments	$(F_5S\text{-}C)(^4\Sigma^-)$; $(SF_3)(^4\Sigma^-)$		$(F_5S\text{-}C)^-(^3\Pi)$; $(SF_3)^+(^3\Sigma^-)$		$(F_5S\text{-}C)(^2\Sigma^+)$; $(SF_3)(^2\Sigma^+)$	
	a		**b**		**c**	
	EDA	ETS-NOCV	EDA	ETS-NOCV	EDA	ETS-NOCV
Symmetry	C_s	C_s	C_s	C_s	C_s	C_s
ΔE_{int}	-259.4	-259.4	-427.8	427.8	-348.9	-348.9
ΔE_{Pauli}	367.4	367.4	409.4	409.4	349.6	349.6
ΔE_{elstat} [a]	-175.7 (28.0)	-175.7 (28.0)	-314.0 (37.5)	-314.0 (37.5)	-153.4 (22.0)	-153.4 (22.0)
ΔE_{orb} [a]	-451.1 (72.0)	-451.1 (72.0)	-523.2 (62.5)	-523.2 (62.5)	-545.1 (78.0)	-545.1 (78.0)
ΔE_{σ} [b]	-343.2 (76.1)	-227.9 (50.5)	-376.5 (72.0)	-267.9 (51.2)	-449.9 (82.5)	-292.0 (53.6)
ΔE_{π} [b][c]	-107.9 (23.9)	-223.2 (49.5)	-146.7 (28.0)	-255.3 (48.8)	-95.2 (17.5)	-253.1 (46.4)
$\Delta E_{\pi\|}$ [b][c]	-	-115.3 (25.6)	-	-108.6 (20.8)	-	-157.9 (28.9)
$\Delta E_{\pi\perp}$ [b][c]	-107.9 (23.9)	-107.9 (23.9)	-146.7 (28.0)	-146.7 (28.0)	-95.2 (17.5)	-95.2 (17.5)
ΔE_{prep} (Frag1)	28.3	28.3	92.1	92.1	80.7	80.7
ΔE_{prep} (Frag2)	155.8	155.8	238.7	238.7	201.5	201.5
ΔE_{corr} [d]	11.6	11.6	6.7	6.7	3.1	3.1
$\Delta E(= -D_e)$	-63.7	-63.7	-182.4	-182.4	-63.7	-63.7

[a] The values in parentheses are the percentage contributions to the total attractive interaction $\Delta E_{elstat} + \Delta E_{orb}$. [b] The values in parentheses are the percentage contributions to the total orbital interactions ΔE_{orb}. [c] The ΔE_{π} interaction is further divided into $\Delta E_{\pi\|}$ (in plane) and $\Delta E_{\pi\perp}$ (out of plane) interactions. [d] Correction for spin polarization. Frag1: $(F_5S\text{-}C)$ or $(F_5S\text{-}C)^-$, and Frag2: (SF_3) or $(SF_3)^+$.

Note: Equilibrium geometries and the electronic states of the fragments to which F_5SCSF_3 dissociated are: Octahedral $-(F_5S\text{-}C)(^2\Pi)$; T-shaped $-(SF_3)(^2\Pi)$; Octahedral $-(F_5S\text{-}C)^-(^3\Sigma^-)$ and Trigonal pyramidal $-(SF_3)^+(^1\Sigma^+)$. In **b** and **c** the lone pair electrons of carbon are in $p_{\pi\perp}$ orbital, the ΔE_{Pauli} value increases, when the lone pair electrons are in $p_{\pi\|}$ orbital. Energy values in kcal/mol.

Alpha electrons				
k	Orbital type	NOCVS ψ_{-k} (υ_{-k})	NOCVS ψ_k (υ_k)	Deformation Density $\Delta\rho_k$ ΔE (kcal/mol)
1	σ	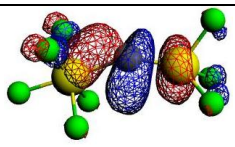	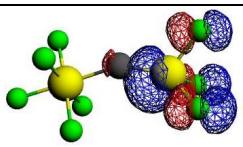	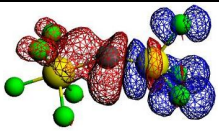
		-0.62	0.62	-116.3
2	σ	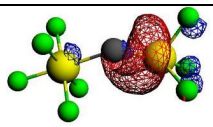	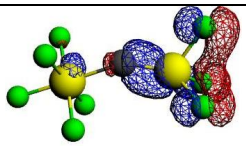	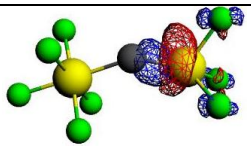
		-0.12	0.12	-11.4
3	$\pi_{\parallel}$	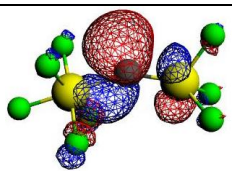	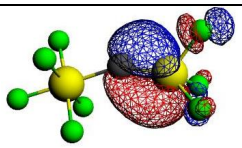	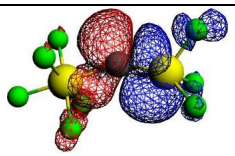
		-0.50	0.50	-32.8
4	$\pi_{\perp}$	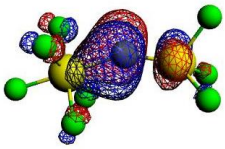	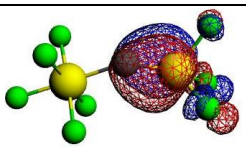	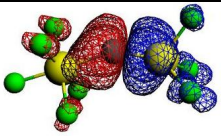
		-0.51	0.51	-32.6

Figure 4.3.7: (a) Contours of the most important NOCV pairs (ψ_{-k}, ψ_k) and their eigenvalues (υ_{-k}, υ_k) of alpha electrons representing electron donation from F_5S-C to the SF_3 fragment and corresponding deformation density ($\Delta\rho_k$) with the orbital stabilization energy (ΔE) in F_5SCSF_3, corresponding to **a** (Scheme 4.3.4).

Beta electrons				
k	Orbital type	NOCVS		Deformation Density
		ψ_{-k}	ψ_k	$\Delta\rho_k$
		(υ_{-k})	(υ_k)	ΔE (kcal/mol)
1	σ	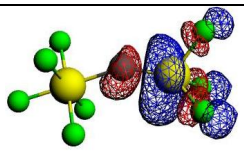	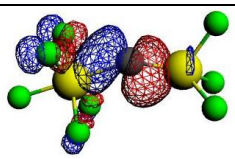	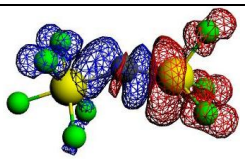
		-0.48	0.48	-85.9
2	σ	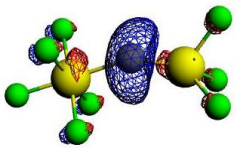	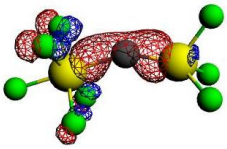	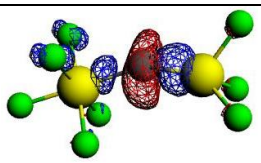
		-0.13	0.13	-9.9
3	$\pi_{\parallel}$	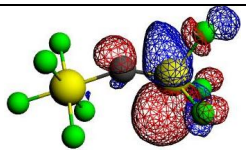	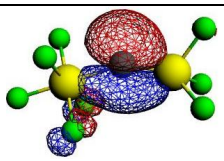	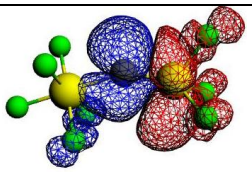
		-0.68	0.68	-82.5
4	$\pi_{\perp}$	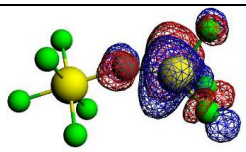	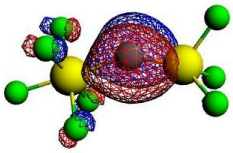	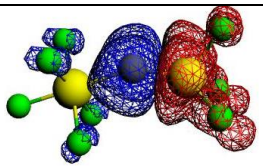
		-0.63	0.63	-73.4

Figure 4.3.7: (b) Contours of most important NOCV pairs (ψ_{-k}, ψ_k) and their eigenvalues (υ_{-k}, υ_k) of beta electrons representing electron donation from SF_3 to F_5S-C fragment and the corresponding deformation density ($\Delta\rho_k$) with the orbital stabilization energy (ΔE) in F_5SCSF_3, corresponding to **a** (Scheme 4.3.4).

4.3.5 Topological analysis

In the topological analysis of electron density, a large negative Laplacian, $\nabla^2\rho(r)$ with significant electron density, $\rho(r)$, at the bond critical point indicates the presence of a covalent bond, whereas a small density and a positive value for the Laplacian indicates an ionic bond. The results of the topological analysis of the electron density distribution in selected species are given in Table 4.3.7 and Figure 4.3.8. The electron density at the CS bond critical point decreases in the order F_5SCSF_3 >

cis-HCSF > *cis,cis*-HCSOH > *lin*-HCSF > *trans*-HCSH. The Laplacian at the CS bond critical point decreases (i.e., from a positive to a negative Laplacian value) in the order *lin*-HCSF >> *cis*-HCSF > F_5SCSF_3 > *cis,cis*-HCSOH >> *trans*-HCSH. The Laplacian of the SF bond in *lin*-HCSF is more positive than that in *cis*-HCSF, where the Laplacian of the SH bond in *trans*-HCSH is highly negative, indicating the ionic and covalent nature of the SF and SH bonds, respectively. The energy density, $H(r)$, of the CS bond decreases in the order F_5SCSF_3 > *cis*-HCSF > *cis,cis*-HCSOH > *lin*-HCSF > *trans*-HCSH.

Table 4.3.7: Topological analysis of the electron density distribution at BP86/TZVPP

	cis-HCSF	*lin*-HCSF	*trans*-HCSH	*cis,cis*-HCSOH	$F_5S^2CS^1F_3$	
Bond	CS	CS	CS	CS	CS^1	CS^2
$\rho(r)$	1.915	1.830	1.607	1.870	2.009	1.487
$\nabla^2\rho(r)$	-0.394	7.228	-12.040	-5.501	-1.538	-12.048
$H(r)$	-2.534	-2.300	-1.486	-2.473	-2.753	-1.227
d	1.518	1.524	1.658	1.542	1.469	1.743
Bond	SF	SF	SH	SO	S^1F^1	S^2F^2 (axial)
$\rho(r)$	1.066	0.745	1.442	1.165	1.457	1.450
$\nabla^2\rho(r)$	-0.969	4.721	-15.637	-3.534	1.156	-4.063
$H(r)$	-0.821	-0.317	-1.368	-0.954	-1.657	-1.714
d	1.743	1.912	1.372	1.748	1.581	1.613

$\rho(r)$- electron density in (eÅ^{-3}) at bond critical points, $\nabla^2\rho(r)$ - laplacian of the electron density in (Å^{-5}) at bond critical points, $H(r)$ – electron energy density in (Hartree Å^{-3}) and d – the bond distance in (Å). Geometries - C_s symmetric except *lin*-HCSF ($C_{\infty v}$ symmetry).

The CS bond in *cis*-HCSF has a negative Laplacian value of -0.394 at BP86/TZVPP (this work), and a positive Laplacian value of 3.621 at CCSD/cc-pVTZ // CCSD(T)/cc-pVTZ (from the literature)[80] levels of theory. This is also understood from the slight changes in the Laplacian distribution of electron density plot (Figure 4.3.9) compared with both the levels of theory. The visual inspection of the Laplacian distribution of electron density of *cis*-HCSF at CCSD/cc-pVTZ // CCSD(T)/cc-pVTZ level of theory shows that there is slight charge depletion at the atom center S relative to BP86/TZVPP level of theory.

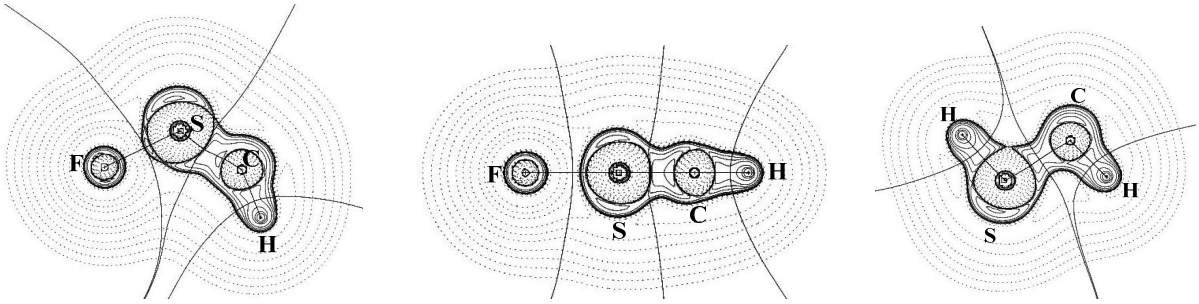

cis-HCSF *lin*-HCSF *trans*-HCSH

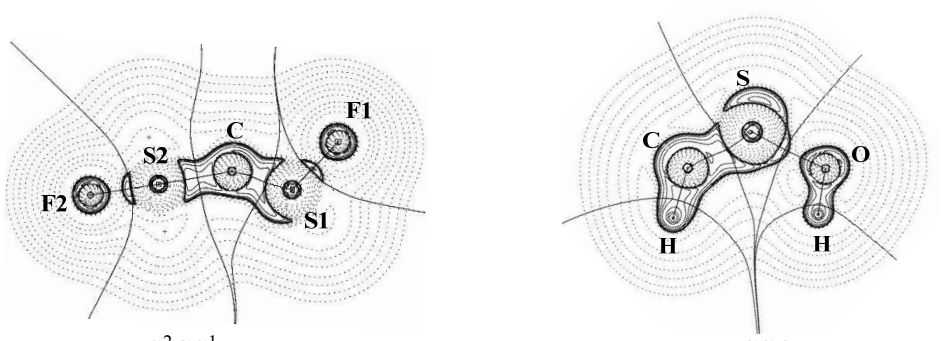

$F_5S^2CS^1F_3$ *cis,cis*-HCSOH

Figure 4.3.8: Contour line plot of $\nabla^2\rho(r)$ at BP86/TZVPP level of theory. The thick solid lines connecting the atomic nuclei are the bond paths and the thick solid lines separating the atomic basins indicate the zero-flux surfaces.

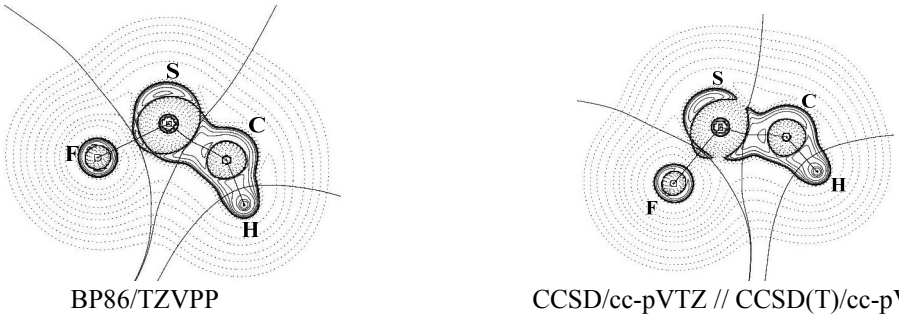

BP86/TZVPP CCSD/cc-pVTZ // CCSD(T)/cc-pVTZ[80]

Figure 4.3.9: Contour line plot of $\nabla^2\rho(r)$ at the BP86/TZVPP, and CCSD/cc-pVTZ // CCSD(T)/cc-pVTZ[80] levels of theory. The thick solid lines connecting the atomic nuclei are the bond paths and the thick solid lines separating the atomic basins indicate the zero-flux surfaces.

4.4 Nature of the SiS bond in HSiSF and HSiSH

4.4.1 HSiSF

Figure 4.4.1 shows the optimized geometries of HSiSF and HSiSH in the singlet electronic state at the CCSD(T)/TZVPP level. Both HSiSF and HSiSH have planar, bent (*cis*- and *trans*-) geometries. *lin*-HSiSF and *lin*-HSiSH are the second-order saddle-point geometries. *cis*-HSiSF is 3.8 kcal/mol higher in energy than *trans*-HSiSF; *lin*-HSiSF is 45.3 kcal/mol higher in energy than *trans*-HSiSF. The SF bond in *lin*-HSiSF is 0.121 Å longer than the SF bond in *trans*-HSiSF. *cis*-HSiSH is 2.5 kcal/mol higher in energy than *trans*-HSiSH; *lin*-HSiSH is 76.3 kcal/mol higher in energy than *trans*-HSiSH. The SiS bond in *trans*-HSiSH is 0.060 Å longer than the SiS bond in *trans*-HSiSF. Results at the BP86/TZVPP level of theory are given in parentheses in Figure 4.4.1.

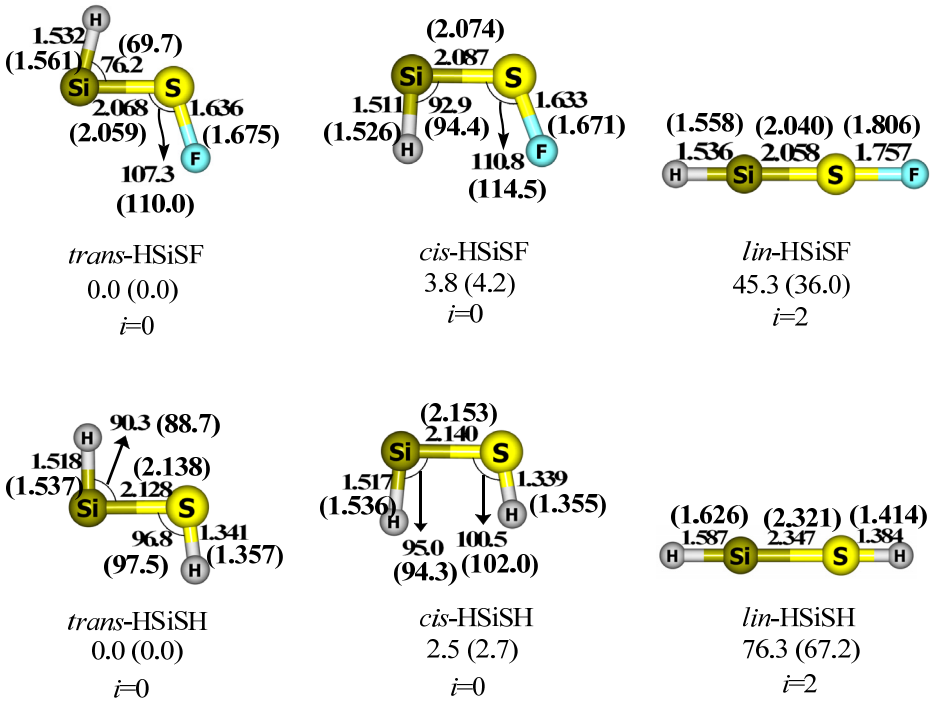

trans-HSiSF
0.0 (0.0)
i=0

cis-HSiSF
3.8 (4.2)
i=0

lin-HSiSF
45.3 (36.0)
i=2

trans-HSiSH
0.0 (0.0)
i=0

cis-HSiSH
2.5 (2.7)
i=0

lin-HSiSH
76.3 (67.2)
i=2

Figure 4.4.1: Optimized geometries at the CCSD(T)/TZVPP. Bond lengths in angstrom, angles in degrees, and relative energies in kcal/mol. Values in parentheses correspond to BP86/TZVPP level. All the molecules are in singlet electronic state. The index, i, shows the number of imaginary frequencies.

trans-HSiSF

The SiS bond in *trans*-HSiSF could be viewed as in Scheme 4.4.1: triple bond (**a**), double bond (**b**), and single bond (**c**). EDA and ETS-NOCV analyses between the HSi and SF fragments in different electronic states were performed as shown in Scheme 4.4.2. The types of interaction between the fragments in Scheme 4.4.2 are similar to those of the CS bond discussed in Scheme 4.3.2. Additionally, an interaction **e** is considered between the fragments $(HSi)^+$ and $(SF)^-$ in the $(^1\Sigma^+)$ electronic state.

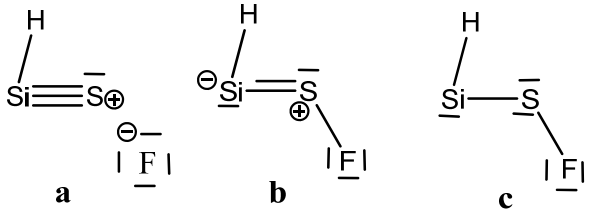

Scheme 4.4.1: Resonance structures of *trans*-HSiSF. In the Lewis structures **a** and **b** all the atoms have the octet electronic configuration, however, the Si atom in the structure **c** has only sextet electronic configuration.

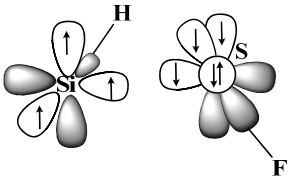

a

$HSi(^4\Sigma^-)$; $SF(^4\Sigma^-)$

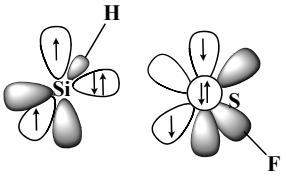

b1

$(HSi)^-(^3\Pi)$; $(SF)^+(^3\Sigma^-)$

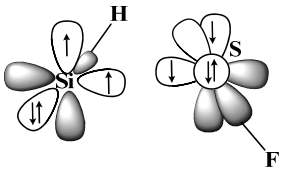

b2

$(HSi)^-(^3\Sigma^-)$; $(SF)^+(^3\Sigma^-)$

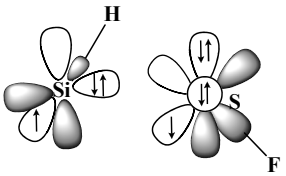

c1

$HSi(^2\Sigma^+)$; $SF(^2\Pi)$

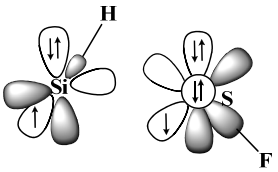

c2

$HSi(^2\Sigma^+)$; $SF(^2\Pi)$

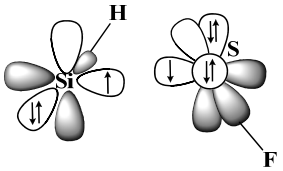

c3

$HSi(^2\Pi)$; $SF(^2\Pi)$

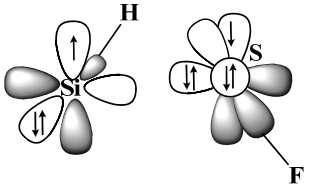

d

$HSi(^2\Pi)$; $SF(^2\Pi)$

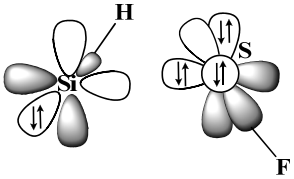

e

$(HSi)^+(^1\Sigma^+)$; $(SF)^-(^1\Sigma^+)$

Scheme 4.4.2: Possible valance orbital interactions between Si and S in *trans*-HSiSF.

Table 4.4.1: EDA and ETS-NOCV analyses of the SiS bond in *trans*-HSiSF at BP86/TZ2P+

Interacting Fragments	$HSi(^4\Sigma^-)$; $SF(^4\Sigma^-)$		$(HSi)^-(^3\Pi)$; $(SF)^+(^3\Sigma^-)$		$(HSi)^-(^3\Sigma^-)$; $(SF)^+(^3\Sigma^-)$		$HSi(^2\Sigma^+)$; $SF(^2\Pi)$	
	a		**b1**		**b2**		**c1**	
	EDA	ETS-NOCV	EDA	ETS-NOCV	EDA	ETS-NOCV	EDA	ETS-NOCV
Symmetry	C_s	*Cs*	*Cs*	*Cs*	*Cs*	*Cs*	*Cs*	*Cs*
ΔE_{int}	-186.1	-186.1	-369.6	-369.6	-303.4	-303.4	-171.7	-171.7
ΔE_{Pauli}	253.0	253.0	431.5	431.5	276.0	276.0	397.1	397.1
ΔE_{elstat} [a]	-143.1 (32.6)	-143.1 (32.6)	-345.9 (43.2)	-345.9 (43.2)	-252.3 (43.6)	-252.3 (43.6)	-218.6 (38.4)	-218.6 (38.4)
ΔE_{orb} [a]	-295.9 (67.4)	-295.9 (67.4)	-455.3 (56.8)	-455.3 (56.8)	-327.1 (56.5)	-327.1 (56.5)	-350.1 (61.6)	-350.1 (61.6)
ΔE_{σ} [b]	-236.1 (79.8)	-142.9 (48.3)	-355.0 (78.0)	-339.2 (74.5)	-221.2 (67.6)	-182.4 (55.8)	-318.3 (90.9)	-309.3 (88.3)
ΔE_{π} [b][c]	-59.9 (20.2)	-153.1 (51.7)	-100.3 (22.0)	-116.1 (25.5)	-105.8 (32.4)	-144.6 (44.2)	-31.9 (9.1)	-40.9 (11.7)
$\Delta E_{\pi\parallel}$ [b][c]	-	-93.2 (31.5)	-	-15.8 (3.5)	-	-38.8 (11.8)	-	-9.0 (2.6)
$\Delta E_{\pi\perp}$ [b][c]	-59.9 (20.2)	-59.9 (20.2)	-100.3 (22.0)	-100.3 (22.0)	-105.8 (32.4)	-105.8 (32.4)	-31.9 (9.1)	-31.9 (9.1)
ΔE_{prep} HSi or $(HSi)^-$	39.7	39.7	65.6	65.6	0.0	0.0	76.3	76.3
ΔE_{prep} SF or $(SF)^+$	50.9	50.9	7.0	7.0	7.0	7.0	0.6	0.6
ΔE_{corr} [d]	3.2	3.2	3.6	3.6	3.0	3.0	2.5	2.5
$\Delta E(= -D_e)$	-92.3	-92.3	-288.7	-288.7	-288.7	-288.7	-92.3	-92.3

[a] The values in parentheses are the percentage contributions to the total attractive interaction $\Delta E_{elstat} + \Delta E_{orb}$. [b] The values in parentheses are the percentage contributions to the total orbital interactions ΔE_{orb}. [c] The ΔE_{π} interaction is further divided into $\Delta E_{\pi\parallel}$ (in plane) and $\Delta E_{\pi\perp}$ (out of plane) interactions. [d] Correction for spin polarization.

Note: The electronic ground state of the fragments are: $HSi(^2\Pi)$; $SF(^2\Pi)$; $(HSi)^-(^3\Sigma^-)$ and $(SF)^+(^3\Sigma^-)$. Energy values in kcal/mol.

Table 4.4.1 continued. EDA and ETS-NOCV analysis of the SiS bond in *trans*-HSiSF at BP86/TZ2P+

Interacting Fragments	$HSi(^2\Sigma^+)$; $SF(^2\Pi)$	$HSi(^2\Pi)$; $SF(^2\Pi)$		$HSi(^2\Pi)$; $SF(^2\Pi)$		$(HSi)^+(^1\Sigma^+)$; $(SF)^-(^1\Sigma^+)$	
	c2	**c3**		**d**		**e**	
	EDA	EDA	ETS-NOCV	EDA	ETS-NOCV	EDA	ETS-NOCV
Symmetry	C_s	C_s	C_s	C_s	C_s	C_s	C_s
ΔE_{int}	-171.6	-95.0	-95.0	-95.0	-95.0	-229.8	-229.8
ΔE_{Pauli}	153.1	248.1	248.1	181.3	181.3	220.6	220.6
ΔE_{elstat} [a]	-42.8 (13.2)	-141.7 (41.3)	-141.7 (41.3)	-100.1 (36.2)	-100.1 (36.2)	-259.3 (57.6)	-259.3 (57.6)
ΔE_{orb} [a]	-281.9 (86.8)	-201.4 (58.7)	-201.4 (58.7)	-176.2 (63.8)	-176.2 (63.8)	-191.1 (42.4)	-191.1 (42.4)
ΔE_{σ} [b]	-440.1 (156.1)	-172.6 (85.7)	-149.2 (74.1)	-104.8 (59.5)	-80.8 (45.9)	-141.1 (73.8)	-127.1 (66.5)
ΔE_{π} [b][c]	158.1 (-56.1)	-28.8 (14.3)	-52.2 (25.9)	-71.4 (40.5)	-95.4 (54.1)	-50.0 (26.2)	-64.0 (33.5)
$\Delta E_{\pi\parallel}$ [b][c]	-	-	-23.4 (11.6)	-	-24.0 (13.6)	-	-14.0 (7.3)
$\Delta E_{\pi\perp}$ [b][c]	158.1 (-56.1)	-28.8 (14.3)	-28.8 (14.3)	-71.4 (40.5)	-71.4 (40.5)	-50.0 (26.2)	-50.0 (26.2)
ΔE_{prep} HSi or $(HSi)^+$	76.3	0.0	0.0	0.0	0.0	0.1	0.1
ΔE_{prep} SF or $(SF)^-$	0.6	0.6	0.6	0.6	0.6	1.4	1.4
ΔE_{corr} [d]	2.4	2.1	2.1	2.1	2.1	-	-
$\Delta E(= -D_e)$	-92.3	-92.3	-92.3	-92.3	-92.3	-228.3	-228.3

[a] The values in parentheses are the percentage contributions to the total attractive interaction $\Delta E_{elstat} + \Delta E_{orb}$. [b] The values in parentheses are the percentage contributions to the total orbital interactions ΔE_{orb}. [c] The ΔE_{π} interaction is further divided into $\Delta E_{\pi\parallel}$ (in plane) and $\Delta E_{\pi\perp}$ (out of plane) interactions. [d] Correction for spin polarization.

Note: The electronic ground state of the fragments are: $(HSi)^-(^3\Sigma^-)$; $(SF)^+(^3\Sigma^-)$; $HSi(^2\Pi)$; $SF(^2\Pi)$; $(HSi)^+(^1\Sigma^+)$ and $(SF)^-(^1\Sigma^+)$. Energy values in kcal/mol.

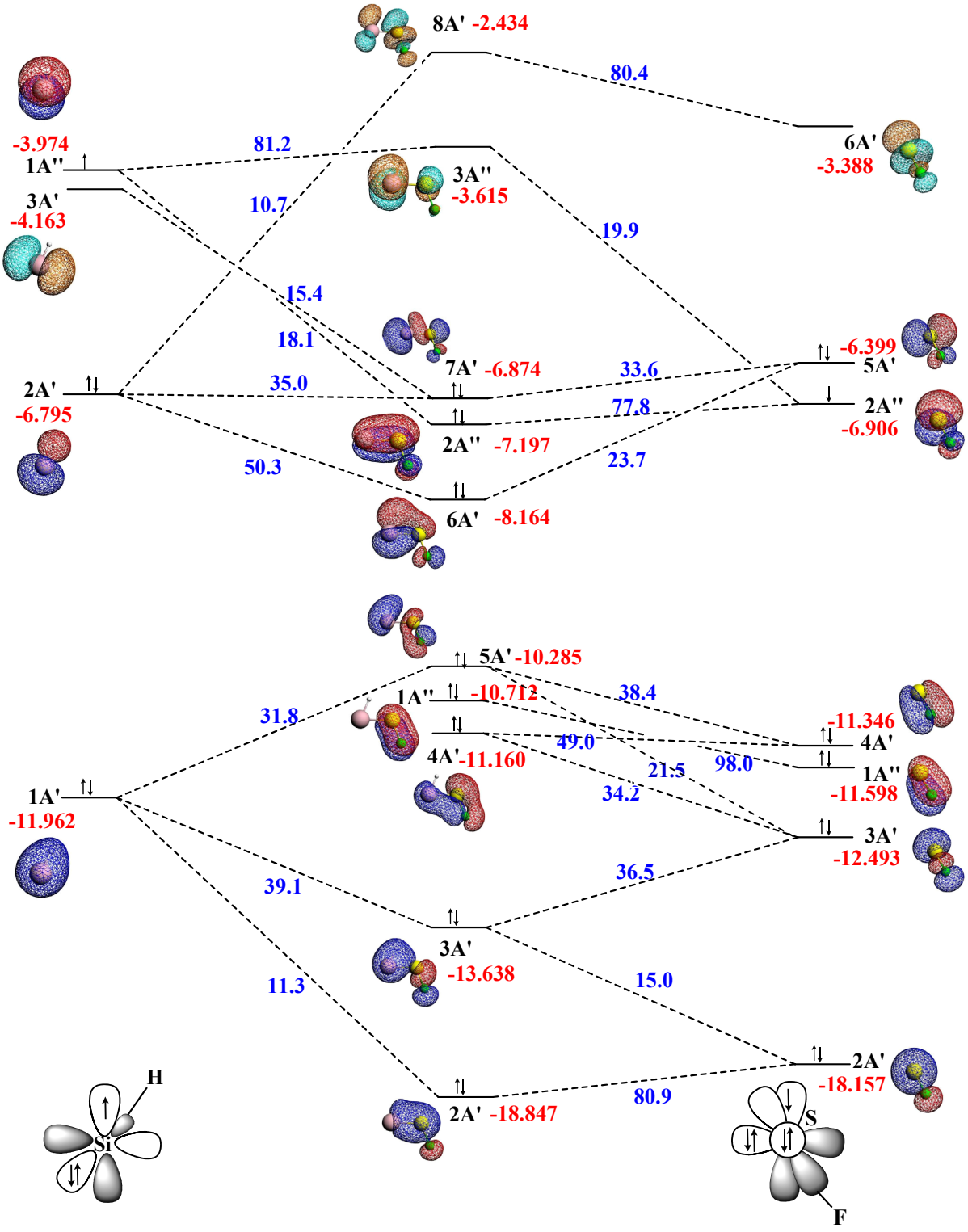

Figure 4.4.2: Plot of the valance orbital interaction between the frozen geometry of the fragments HSi and SF in *trans*-HSiSF at BP86/TZ2P+. The percentage contributions are shown in blue colour and the orbital energies (eV) in red colour. The percentage contributions less than 5% are not shown.

Table 4.4.1 shows the EDA and ETS-NOCV results of the SiS bond in *trans*-HSiSF. Interaction **d** has the smallest magnitude (-176.2 kcal/mol) for the orbital contribution, ΔE_{orb}, followed by **e** (-191.1 kcal/mol), **c3** (-201.4 kcal/mol), and **a** (-295.9 kcal/mol). Interaction scheme **d** also has the smallest Pauli repulsion. In **d**, fragments HSi and SH interact in their $^2\Pi$ electronic ground states, forming a dative σ bond and a covalent π bond between Si and S (Scheme 4.4.2). The SiS bond in **d** has 36.2% electrostatic and 63.8% orbital contributions. The total orbital contribution is divided into 45.9% σ, 13.6% $\pi_{\parallel}$, and 40.5% $\pi_{\perp}$ contributions.

The plot of valance orbital interaction between the frozen geometry of the fragments HSi($^2\Pi$) and SF($^2\Pi$) in *trans*-HSiSF is shown in Figure 4.4.2. The molecular orbitals 7A′ and 2A″ are σ- and $\pi_{\perp}$-type orbitals, respectively, of the SiS bond in *trans*-HSiSF. Unlike *cis*-HCSF (Figure 4.3.2), the $\pi_{\parallel}$ orbital of the SiS bond (6A′) in *trans*-HSiSF has a major contribution (50.3%) from 2A′ of the HSi fragment and 23.7% from 5A′ of the SF fragment and has no contribution from 6A′ of the SF fragment. Figure 4.4.3 shows the σ- and π-type NOCV pairs and deformation densities of the SiS bond in interaction **d**. The σ-type NOCV pairs and deformation densities of both alpha and beta electrons indicate the charge flow of electrons from SF to HSi (S→Si σ bond). The $\pi_{\perp}$ NOCV pairs and deformation density shows the electron-sharing covalent bond between the singly occupied $p_{\pi\perp}$ orbitals on Si and S. The $\pi_{\parallel}$ NOCV pairs come from the delocalization of the HSi bond-pair electrons to the empty $\pi_{\parallel}$-type orbital on S in the SF fragment and they look similar for the alpha and beta electrons. NBO analysis (Table 4.4.2) indicates a lone pair on Si and S and three lone pairs on F, one SF bond, one HSi bond, and two SiS bonds. The lone-pair orbital on Si has 83% s character and the lone-pair orbital on S has 73.6% s character. The Wiberg bond index of the SiS bond in *trans*-HSiSF is 1.493.

Table 4.4.2: NBO partial charges (*q*), Wiberg bond indices (*P*), and the number of bond-pair (BP) and lone-pair (LP) orbitals at BP86/TZVPP

	Partial charges *(q)*				*P*(SiS)	LP		BP			
	H	Si	S	F(H)		Si (% s and p)	S (% s and p)	F(H)	HSi	SiS	SF or SH
trans-HSiSF	-0.18	0.46	0.19	-0.47	1.493	1 s(83.0) p(16.9)	1 s(73.6) p(26.3)	3	1	2	1
cis-HSiSF	-0.17	0.42	0.19	-0.45	1.543	1 s(77.1) p(22.8)	1 s(69.9) p(30.1)	3	1	2	1
lin-HSiSF	-0.21	0.74	-0.02	-0.52	2.160	0	1 s(99.7) p(0.3)	4	1	3	0
trans-HSiSH	-0.24	0.49	-0.40	0.15	1.246	1 s(80.5) p(19.4)	1 s(67.8) p(32.1)	0	1	2	1
cis-HSiSH	-0.24	0.50	-0.42	0.16	1.221	1 s(79.3) p(20.7)	1 s(65.2) p(34.7)	0	1	2	1

Alpha electrons				
k	Orbital type	NOCVS ψ_{-k}	NOCVS ψ_k	Deformation Density, $\Delta\rho_k$
		(υ_{-k})	(υ_k)	ΔE (kcal/mol)
1	σ	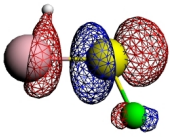	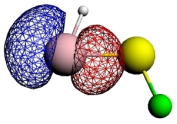	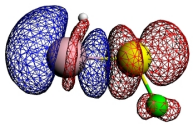
		-0.40	0.40	-38.0
2	$\pi_{\|\|}$	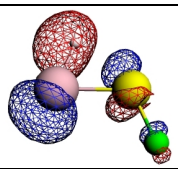	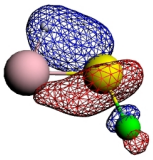	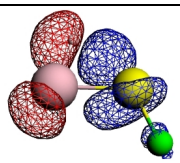
		-0.24	0.24	-11.6
3	$\pi_\perp$	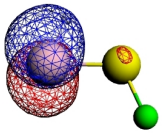	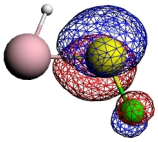	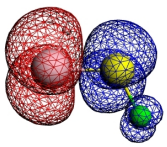
		-0.83	0.83	-63.1

Figure 4.4.3a

Beta electrons				
k	Orbital type	NOCVS ψ_{-k}	NOCVS ψ_k	Deformation Density, $\Delta\rho_k$
		(υ_{-k})	(υ_k)	ΔE (kcal/mol)
1	σ	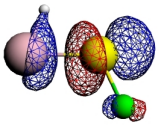	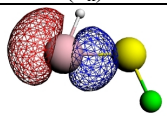	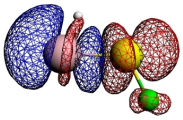
		-0.40	0.40	-35.4
2	$\pi_{\|\|}$	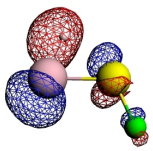	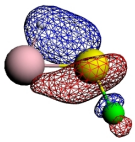	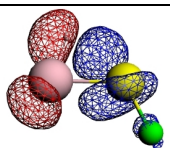
		-0.24	0.24	-12.4
3	$\pi_\perp$	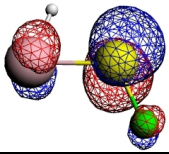	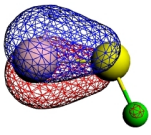	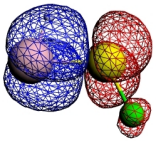
		-0.36	0.36	-8.1

Figure 4.4.3b

Figure 4.4.3: (a) Contours of the most important NOCV pairs (ψ_{-k}, ψ_k) and their eigenvalues (υ_{-k}, υ_k) of alpha electrons, representing the electron donation from HSi to the SF fragment and the corresponding deformation density ($\Delta\rho_k$) with the orbital stabilization energy (ΔE); **(b)** Contours of the most important NOCV pairs (ψ_{-k}, ψ_k) and their eigenvalues (υ_{-k}, υ_k) of beta electrons representing electron donation from SF to the HSi fragment and the corresponding deformation density ($\Delta\rho_k$) with the orbital stabilization energy (ΔE); in *trans*-HSiSF, corresponding to **d** (Scheme 4.4.2).

Table 4.4.3: EDA and ETS-NOCV analyses of the SiS bond in *cis*-HSiSF at BP86/TZ2P+

Interacting Fragments	$HSi(^4\Sigma^-)$; $SF(^4\Sigma^-)$		$(HSi)^-(^3\Pi)$; $(SF)^+(^3\Sigma^-)$		$(HSi)^-(^3\Sigma^-)$; $(SF)^+(^3\Sigma^-)$		$HSi(^2\Sigma^+)$; $SF(^2\Pi)$	
	a		**b1**		**b2**		**c1**	
	EDA	ETS-NOCV	EDA	ETS-NOCV	EDA	ETS-NOCV	EDA	ETS-NOCV
Symmetry	C_s	C_s	C_s	C_s	C_s	C_s	C_s	C_s
ΔE_{int}	-181.6	-181.6	-364.4	-364.4	-298.7	-298.7	-166.9	-166.9
ΔE_{Pauli}	226.0	226.0	424.9	424.9	284.6	284.6	381.3	381.3
ΔE_{elstat} [a]	-138.8 (34.1)	-138.8 (34.1)	-349.4 (44.3)	-349.4 (44.3)	-259.7 (44.5)	-259.7 (44.5)	-218.5 (39.9)	-218.5 (39.9)
ΔE_{orb} [a]	-268.8 (65.9)	-268.8 (65.9)	-439.9 (55.7)	-439.9 (55.7)	-323.5 (55.5)	-323.5 (55.5)	-329.7 (60.2)	-329.7 (60.2)
ΔE_{σ} [b]	-209.6 (78.0)	-143.3 (53.3)	-338.7 (77.0)	-325.3 (73.9)	-217.0 (67.1)	-202.2 (62.5)	-299.9 (90.9)	292.4 (88.7)
ΔE_{π} [b][c]	-59.2 (22.0)	-125.5 (46.7)	-101.2 (23.0)	-114.6 (26.1)	-106.5 (32.9)	-121.3 (37.5)	-29.9 (9.1)	-37.4 (11.3)
$\Delta E_{\pi\parallel}$ [b][c]	-	-66.3 (24.7)	-	-13.4 (3.1)	-	-14.8 (4.6)	-	-7.5 (2.2)
$\Delta E_{\pi\perp}$ [b][c]	-59.2 (22.0)	-59.2 (22.0)	-101.2 (23.0)	-101.2 (23.0)	-106.5 (32.9)	-106.5 (32.9)	-29.9 (9.1)	-29.9 (9.1)
ΔE_{prep} HSi or $(HSi)^-$	39.5	39.5	65.4	65.4	0.4	0.4	76.3	76.3
ΔE_{prep} SF or $(SF)^+$	51.2	51.2	6.7	6.7	6.7	6.7	0.5	0.5
ΔE_{corr} [d]	3.2	3.2	3.5	3.5	2.8	2.8	2.4	2.4
$\Delta E(= -D_e)$	-87.7	-87.7	-292.3	-292.3	-291.6	-291.6	-87.7	-87.7

[a] The values in parentheses are the percentage contributions to the total attractive interaction $\Delta E_{elstat} + \Delta E_{orb}$. [b] The values in parentheses are the percentage contributions to the total orbital interactions ΔE_{orb}. [c] The ΔE_{π} interaction is further divided into $\Delta E_{\pi\parallel}$ (in plane) and $\Delta E_{\pi\perp}$ (out of plane) interactions. [d] Correction for spin polarization.

Note: The electronic ground state of the fragments are: $HSi(^2\Pi)$; $SF(^2\Pi)$; $(HSi)^-(^3\Sigma^-)$ and $(SF)^+(^3\Sigma^-)$. Energy values in kcal/mol.

Table 4.4.3 continued. EDA and ETS-NOCV analyses of the SiS bond in *cis*-HSiSF at BP86/TZ2P+

Interacting Fragments	$HSi(^2\Sigma^+)$; $SF(^2\Pi)$	$HSi(^2\Pi)$; $SF(^2\Pi)$		$HSi(^2\Pi)$; $SF(^2\Pi)$		$(HSi)^+(^1\Sigma^+)$; $(SF)^-(^1\Sigma^+)$	
	c2	**c3**		**d**		**e**	
	EDA	EDA	ETS-NOCV	EDA	ETS-NOCV	EDA	ETS-NOCV
Symmetry	C_s	C_s	C_s	C_s	C_s	C_s	C_s
ΔE_{int}	-166.9	-90.3	-90.3	-90.3	-90.3	-225.2	-225.2
ΔE_{Pauli}	381.3	250.0	250.0	173.6	173.6	205.4	205.4
ΔE_{elstat} [a]	-218.5 (39.9)	-145.2 (42.6)	-145.2 (42.6)	-96.7 (36.6)	-96.7 (36.6)	-251.3 (58.4)	-251.3 (58.4)
ΔE_{orb} [a]	-329.7 (60.2)	-195.2 (57.4)	-195.2 (57.4)	-167.2 (63.4)	-167.2 (63.4)	-179.3 (41.6)	-179.3 (41.6)
ΔE_{σ} [b]	292.4 (88.7)	-168.3 (86.3)	-159.6 (81.8)	-95.7 (57.3)	-74.5 (44.6)	-132.0 (73.6)	-117.6 (65.6)
ΔE_{π} [b][c]	-37.4 (11.3)	-26.8 (13.7)	-35.5 (18.2)	-71.5 (42.7)	-92.7 (55.4)	-47.3 (26.4)	-61.7 (34.4)
$\Delta E_{\pi\parallel}$ [b][c]	-7.5 (2.2)	-	-8.7 (4.5)	-	-21.2 (12.7)	-	-14.4 (8.0)
$\Delta E_{\pi\perp}$ [b][c]	-29.9 (9.1)	-26.8 (13.7)	-26.8 (13.7)	-71.5 (42.7)	-71.5 (42.7)	-47.3 (26.4)	-47.3 (26.4)
ΔE_{prep} HSi or $(HSi)^+$	76.3	0.1	0.1	0.1	0.1	0.0	0.0
ΔE_{prep} SF or $(SF)^-$	0.5	0.5	0.5	0.5	0.5	1.6	1.6
ΔE_{corr} [d]	2.4	2.0	2.0	2.0	2.0	-	-
$\Delta E(= -D_e)$	-87.7	-87.7	-87.7	-87.7	-87.7	-223.6	-223.6

[a] The values in parentheses are the percentage contributions to the total attractive interaction $\Delta E_{elstat} + \Delta E_{orb}$. [b] The values in parentheses are the percentage contributions to the total orbital interactions ΔE_{orb}. [c] The ΔE_{π} interaction is further divided into $\Delta E_{\pi\parallel}$ (in plane) and $\Delta E_{\pi\perp}$ (out of plane) interactions. [d] Correction for spin polarization.

Note: The electronic ground state of the fragments are: $(HSi)^-(^3\Sigma^-)$; $(SF)^+(^3\Sigma^-)$; $HSi(^2\Pi)$; $SF(^2\Pi)$; $(HSi)^+(^1\Sigma^+)$ and $(SF)^-(^1\Sigma^+)$. Energy values in kcal/mol.

Alpha electrons				
k	Orbital type	NOCVS ψ_{-k}	NOCVS ψ_k	Deformation Density $\Delta\rho_k$
		(υ_{-k})	(υ_k)	ΔE (kcal/mol)
1	σ	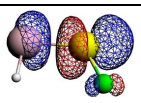	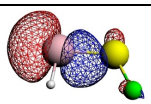	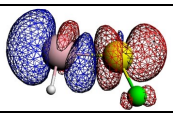
		-0.40	0.40	-36.2
2	$\pi_{\parallel}$	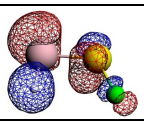	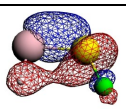	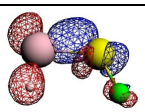
		-0.20	0.20	-10.3
3	$\pi_{\perp}$	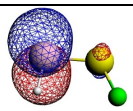	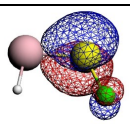	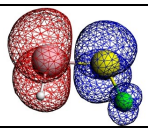
		-0.80	0.80	-64.0

Figure 4.4.4a

Beta electrons				
k	Orbital type	NOCVS ψ_{-k}	NOCVS ψ_k	Deformation Density $\Delta\rho_k$
		(υ_{-k})	(υ_k)	ΔE (kcal/mol)
1	σ	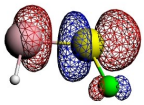	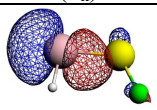	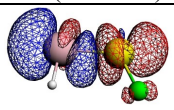
		-0.40	0.40	-33.9
2	$\pi_{\parallel}$	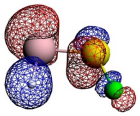	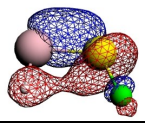	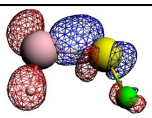
		-0.20	0.20	-10.9
3	$\pi_{\perp}$	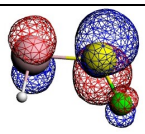	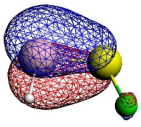	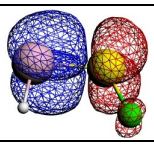
		-0.35	0.35	-7.3

Figure 4.4.4b

Figure 4.4.4: (a) Contours of the most important NOCV pairs ($\psi_{-k,}$ ψ_k) and their eigenvalues ($\upsilon_{-k,}$ υ_k) of alpha electrons representing electron donation from HSi to SF fragment and the corresponding deformation density ($\Delta\rho_k$) with the orbital stabilization energy (ΔE); **(b)** Contours of the most important NOCV pairs ($\psi_{-k,}$ ψ_k) and their eigenvalues ($\upsilon_{-k,}$ υ_k) of beta electrons representing electron donation from SF to HSi fragment and the corresponding deformation density ($\Delta\rho_k$) with the orbital stabilization energy (ΔE); in *cis*-HSiSF corresponding to **d** (Scheme 4.4.2).

***cis*-HSiSF**

The EDA and ETSNOCV results of different types of interaction between the HSi and SF fragments in *cis*-HSiSF are shown in Table 4.4.3. The SiS bond in *cis*-HSiSF has a dative σ bond and a π-electron-sharing bond (**d**), similar to that of *trans*-HSiSF. The percentage contributions of σ and π bonds in *cis*-HSiSF are similar to that of *trans*-HSiSF. Figure 4.4.4 shows the NOCV pairs and deformation densities of the SiS bond, as in interaction scheme **d** in *cis*-HSiSF. The only difference between *cis*- and *trans*-HSiSF is that the $\pi_{\|}$-acceptor NOCV (ψ_k) of *cis*-HSiSF lies mainly in the SiS bonding region (Figure 4.4.4), whereas it lies mainly on S in the case of *trans*-HSiSF (Figure 4.4.3). In addition, the percentage s character of the lone-pair orbital on Si (77.1) and S (69.9) in *cis*-HSiSF is less than that of *trans*-HSiSF (Table 4.4.2). These results suggest that the bond-pair electrons donated by the HSi bond are better accepted by S in the *trans* orientation than in *cis*, which is also reflected through the slightly longer (0.021 Å) HSi bond in *trans*-HSiSF than that of *cis*-HSiSF.

***lin*-HSiSF**

lin-HSiSF is not a minimum on the PES. The HSi and SiS bond lengths in *lin*-HSiSF are almost the same as that of *trans*-HSiSF, but the SF bond in *lin*-HSiSF is 0.121 Å longer than in *trans*-HSiSF at the CCSD(T)/TZVPP level and 0.131 Å longer at the BP86/TZVPP level (similar to the HCSF system). The Wiberg bond index of the SiS bond in *lin*-HSiSF is 2.160, which is higher than that of the SiS bond in *trans*-HSiSF. There are no lone pairs found on Si, however, F has four lone pairs in *lin*-HSiSF (Table 4.4.2). These results suggest that the SiS bond in *lin*-HSiSF (Scheme 4.4.3) is different from that of *trans*-HSiSF.

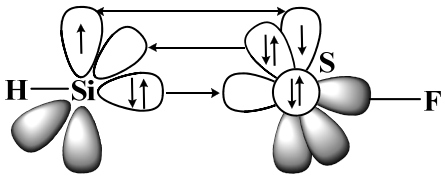

Scheme 4.4.3: Valence orbital interaction between Si and S in *lin*-HSiSF

4.4.2 HSiSH

Previous quantum chemical calculations[83-84] on HSiSH show some double-bond character between silicon and sulfur. Silicon is divalent with a lone pair (silylene). The double-bond character of SiS in HSiSH was supported in studies reported by Veszpremi et al. on the stability (singlet–triplet energy gap), dimerization nucleophilicity, and electrophilicity characteristics of substituted silylenes.

Table 4.4.4: EDA and ETS-NOCV analyses of the SiS bond in *trans*-HSiSH at BP86/TZ2P+

Interacting Fragments	$HSi(^4\Sigma^-)$; $SH(^4\Sigma^-)$	$(HSi)^-(^3\Sigma^-)$; $(SH)^+(^3\Sigma^-)$	$HSi(^2\Pi)$; $SH(^2\Pi)$

	a		**b**		**c**		**d**	
	EDA	ETS-NOCV	EDA	ETS-NOCV	EDA	ETS-NOCV	EDA	ETS-NOCV
Symmetry	C_s	C_s	C_s	C_s	C_s	C_s	C_s	C_s
ΔE_{int}	-254.9	-254.9	-302.2	-302.2	-92.1	-92.1	-92.1	-92.1
ΔE_{Pauli}	177.7	177.7	224.3	224.3	194.1	194.1	150.0	150.0
ΔE_{elstat} [a]	-110.8 (25.6)	-110.8 (25.6)	-234.8 (44.6)	-234.8 (44.6)	-122.3 (42.8)	-122.3 (42.8)	-87.0 (35.9)	-87.0 (35.9)
ΔE_{orb} [a]	-321.8 (74.4)	-321.8 (74.4)	-291.7 (55.4)	-291.7 (55.4)	-163.8 (57.2)	-163.8 (57.2)	-155.1 (64.1)	-155.1 (64.1)
ΔE_{σ} [b]	-252.1 (78.4)	-132.2 (41.1)	-180.9 (62.0)	-167.5 (57.4)	-143.3 (87.4)	-132.5 (80.9)	-81.0 (52.3)	-72.7 (46.9)
ΔE_{π} [b][c]	-69.7 (21.6)	-189.5 (58.9)	-110.8 (38.0)	-124.2 (42.6)	-20.6 (12.6)	-31.5 (19.1)	-74.0 (47.7)	-82.3 (53.1)
$\Delta E_{\pi\parallel}$ [b][c]	-	-119.8 (37.2)	-	-13.4 (4.6)	-	-10.9 (6.6)	-	-8.3 (5.4)
$\Delta E_{\pi\perp}$ [b][c]	-69.7 (21.6)	-69.7 (21.7)	-110.8 (38.0)	-110.8 (38.0)	-20.6 (12.6)	-20.6 (12.5)	-74.0 (47.7)	-74.0 (47.7)
ΔE_{prep} (HSi) or $(HSi)^-$	39.5	39.5	0.2	0.2	0.0	0.0	0.0	0.0
ΔE_{prep} (SH) or $(SH)^+$	122.1	122.1	0.0	0.0	0.0	0.0	0.0	0.0
ΔE_{corr} [d]	3.3	3.3	2.9	2.9	2.1	2.1	2.1	2.1
$\Delta E(= -D_e)$	-90.0	-90.0	-299.1	-299.1	-90.0	-90.0	-90.0	-90.0

[a] The values in parentheses are the percentage contributions to the total attractive interaction $\Delta E_{elstat} + \Delta E_{orb}$. [b] The values in parentheses are the percentage contributions to the total orbital interactions ΔE_{orb}. [c] The ΔE_{π} interaction is further divided into $\Delta E_{\pi\parallel}$ (in plane) and $\Delta E_{\pi\perp}$ (out of plane) interactions. [d] Correction for spin polarization.

Note: The electronic ground state of the fragments are: $HSi(^2\Pi)$; $SH(^2\Pi)$, $(HSi)^-(^3\Sigma^-)$ and $(SH)^+(^3\Sigma^-)$. Energy values in kcal/mol.

The singlet–triplet energy gap in HSiSH was predicted to be 30.4 kcal/mol at the MP2/6-31G* // MP2/6-31G* + ZPE level of theory.[83b] Being a π donor, the SH group stabilizes the ground singlet state of HSiSH. The dimerization energy of HSiSH forming disilene with *trans*-bent geometry (a Fischer-type donor–acceptor Si=Si bond) is -29.0 kcal/mol and to form bridged structure (with SH at the bridging position) is -25.2 kcal/mol at MP2/6-311+G(2D).[84a] These characteristics depend on the interaction between the empty p orbital on the silyl center with the lone-pair electrons on the neighbouring group forming a dative π bond.

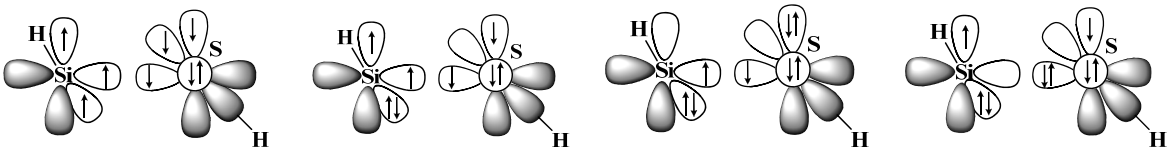

Scheme 4.4.4: Valence orbital interaction between Si and S in *trans*-HSiSH

trans-HSiSH is global minima at both levels of theory (Figure 4.4.1). The Wiberg bond index of the SiS bond in *cis*- and *trans*-HSiSH is slightly smaller than those of *cis*- and *trans*-HSiSF. S has a negative charge in HSiSH, whereas in HSiSF S is positively charged (Table 4.4.2). However, the number of lone pairs on Si and S and the number of HSi, SiS, and SH(SF) bond-pair orbitals in HSiSH and HSiSF are the same (from the NBO data in Table 4.4.2). In addition, EDA and ETS-NOCV analyses suggest that there is a dative σ bond and a covalent π bond (**d** in Scheme 4.4.4 and Table 4.4.4) between Si and S in *trans*-HSiSH, however, interaction **c** is not negligible. The selected molecular orbitals of *trans*-HSiSH are shown in Figure 4.4.5. The HOMO-2, and HOMO-1 are the σ-, and $\pi_\perp$-type orbitals of the SiS bond. The HOMO is the non-bonding lone-pair orbital of Si and LUMO is the anti-bonding $\pi_\perp^*$ orbital.

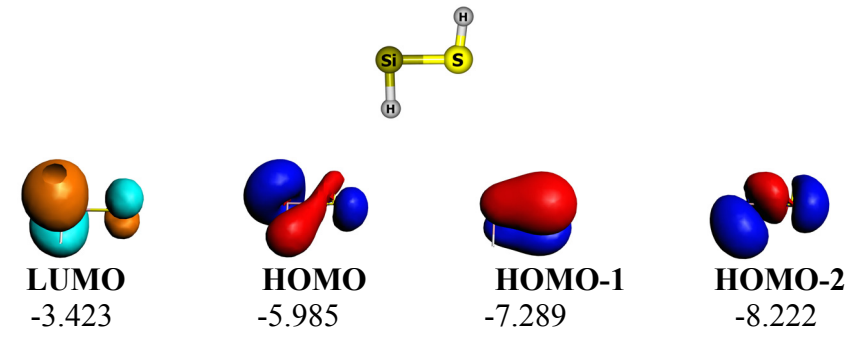

Figure 4.4.5: Important molecular orbitals of *trans*-HSiSH, (in the singlet electronic state) at BP86/TZ2P+. Orbital energies are given in (eV).

4.4.3 Topological analysis

The results of topological analysis of selected molecules are given in Table 4.4.5 and Figure 4.4.6. The SiS bond has a positive Laplacian value, indicating the ionic nature of the bond. H_3SiSF, which has an SiS single bond, is used as reference. The electron density of the SiS bond in HSiSF is slightly larger than that in H_3SiSF.

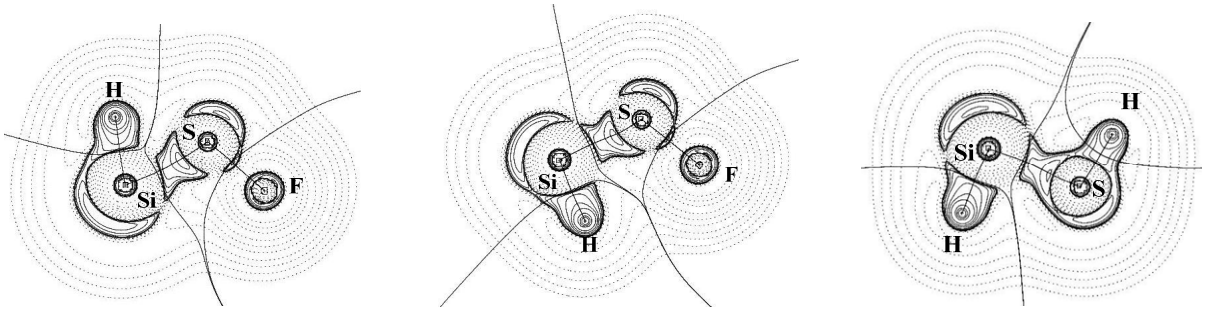

trans-HSiSF *cis*-HSiSF *trans*-HSiSH

Figure 4.4.6: Contour line plot of $\nabla^2\rho(r)$. The thick solid lines connecting the atomic nuclei are the bond paths and the thick solid lines separating the atomic basins indicate the zero-flux surfaces.

Table 4.4.5: Topological analysis of the electron density distribution at BP86/TZVPP

	cis-HSiSF	*trans*-HSiSF	*lin*-HSiSF	*trans*-HSiSH	H_3SiSF
Bond	SiS	SiS	SiS	SiS	SiS
$\rho(r)$	0.709	0.719	0.718	0.644	0.668
$\nabla^2\rho(r)$	4.196	4.902	1.533	2.430	1.665
$H(r)$	-0.413	-0.414	-0.460	-0.373	-0.406
d	2.074	2.059	2.040	2.138	2.157
Bond	SF	SF	SF	SH	SF
$\rho(r)$	1.178	1.167	0.929	1.432	1.174
$\nabla^2\rho(r)$	-1.722	-1.690	1.742	-15.018	-0.358
$H(r)$	-1.171	-1.158	-0.572	-1.392	-1.188
d	1.671	1.675	1.757	1.357	1.664

$\rho(r)$- electron density in (eÅ^{-3}) at bond critical points, $\nabla^2\rho(r)$ - laplacian of the electron density in (Å^{-5}) at bond critical points, $H(r)$ – electron energy density in (Hartree Å^{-3}) and d – the bond distance in (Å). Geometries in C_s symmetry except *lin*-HSiSF in $C_{\infty v}$ symmetry.

4.5 Nature of the NS bond in NSF, NSH, and NSOH

4.5.1 NSF

Geometries of NSF and NSH optimized at the CCSD(T)/TZVPP and BP86/TZVPP levels of theory are shown in Figure 4.5.1. Both NSF and NSH have the planar (C_s symmetric) bent geometry with a singlet electronic ground state. The triplet NSF is 51.8 kcal/mol higher in energy than the singlet NSF at the BP86/TZVPP level. *lin*-NSF ($C_{\infty v}$ symmetry) is a second-order saddle-point geometry. The SF bond in *lin*-NSF is longer than the SF bond in the planar geometry of NSF. The triplet NSH is 7.1 and 7.8 kcal/mol higher in energy than the singlet NSH at the CCSD(T)/TZVPP and BP86/TZVPP levels, respectively. The NS bond in the triplet NSH is longer than that of the singlet NSH and the reverse is true for the SH bond. The NS bond in NSH is longer than in NSF. The BP86/TZVPP level overestimates the SF and SH bond lengths and underestimates the relative energy of the linear structures. Otherwise, the BP86/TZVPP level performs as well as the CCSD(T)/TZVPP level of theory.

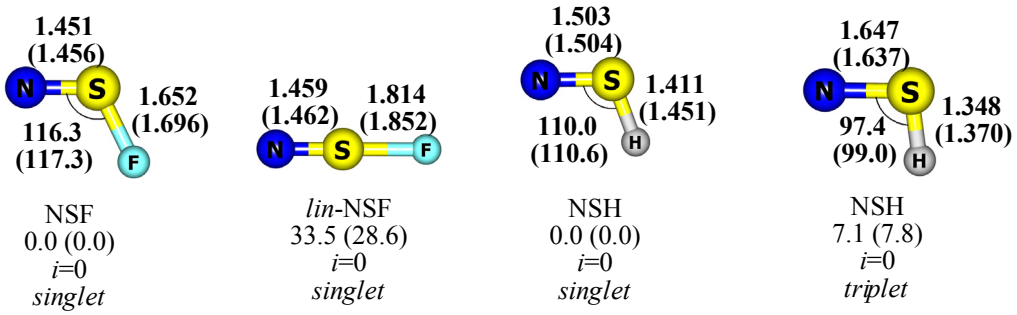

Figure 4.5.1: Optimized geometries at the CCSD(T)/TZVPP. Bond lengths in angstrom, angles in degrees, and relative energies in kcal/mol. Values in parenthesis correspond to BP86/TZVPP level. The index *i,* shows the number imaginary frequencies.

The NS bond in NSF could be viewed as shown in Scheme 4.5.1: triple bond (**a**), double bond (**b**), and single bond (**c**). EDA and ETS-NOCV analyses were performed by considering the N and SF fragments interacting in different electronic states as shown in Scheme 4.5.2. N in the ^4S electronic state interacts with ($^4\Sigma^-$) SF to form an NS triple bond in **a**. In **b1**, (^3P) N^- and ($^3\Sigma^-$) $(SF)^+$ interact to form an NS double bond. In **b2**, (^3S) N^- interacts with ($^3\Pi$) $(SF)^+$ to form a dative σ bond and two covalent π bonds. (^2S) N and ($^2\Pi$) SF interacts in **c** to form an NS single bond. A dative σ bond and a π-electron-sharing covalent bond in **d** is formed by the interaction between (^2P) N and ($^2\Pi$) SF fragments.

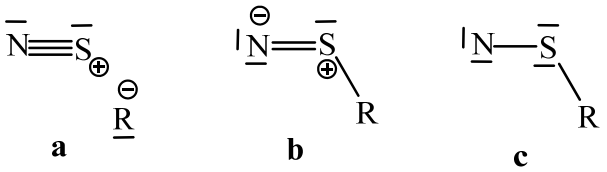

Scheme 4.5.1: Resonance structures of NSR, R = F, OH and H. In the Lewis structures **a**, and **b** all of the atoms have the octet electronic configuration, however, the atom N in the structure **c** has only the sextet electronic configuration.

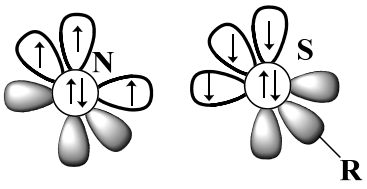

a

$N(^4S)$; $SR(^4\Sigma^-)$

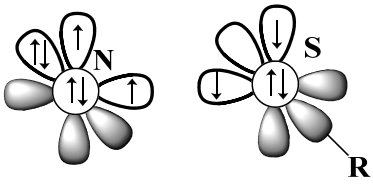

b1

$(N)^-(^3P)$; $(SR)^+(^3\Sigma^-)$

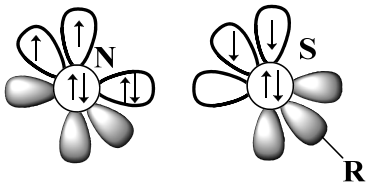

b2

$(N)^-(^3S)$; $(SR)^+(^3\Pi)$

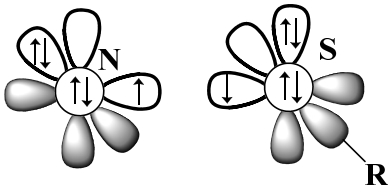

c

$N(^2S)$; $SR(^2\Pi)$

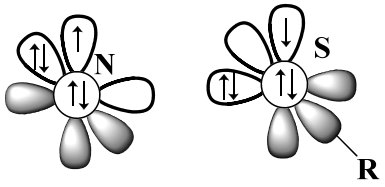

d

$(N)(^2P)$; $(SR)(^2\Pi)$

Scheme 4.5.2: Valence orbital interactions between N and S in NSR, R = F, OH and H.

Table 4.5.1: EDA and ETS-NOCV analyses of the NS bond in NSF at BP86/TZ2P+ level

Interacting Fragments	$N(^4S)$; $SF(^4\Sigma^-)$		$(N)^-(^3P)$; $(SF)^+(^3\Sigma^-)$		$N^-(^3S)$; $(SF)^+(^3\Pi)$	
	a		**b1**		**b2**	
	EDA	ETS-NOCV	EDA	ETS-NOCV	EDA	ETS-NOCV
Symmetry	C_s	C_s	C_s	C_s	C_s	C_s
ΔE_{int}	-178.5	-178.5	-374.4	-374.4	-464.2	-464.2
ΔE_{Pauli}	543.5	543.5	577.9	577.9	674.7	674.7
ΔE_{elstat} [a]	-243.2 (33.7)	-243.2 (33.7)	-463.9 (48.7)	-463.9 (48.7)	-570.6 (50.1)	-570.6 (50.1)
ΔE_{orb} [a]	-478.8 (66.3)	-478.8 (66.3)	-488.4 (51.3)	-488.4 (51.3)	-568.3 (49.9)	-568.3 (49.9)
ΔE_{σ} [b]	-400.9 (83.7)	-263.5 (55.0)	-395.4 (81.0)	-282.6 (57.9)	-475.7 (83.7)	-366.6 (64.5)
ΔE_{π} [b][c]	-77.8 (16.3)	-215.2 (45.0)	-92.9 (19.0)	-205.7 (42.1)	-92.6 (16.3)	-201.7 (35.5)
$\Delta E_{\pi\|}$ [b][c]	-	-137.4 (28.7)	-	-112.8 (23.1)	-	-109.1 (19.2)
$\Delta E_{\pi\perp}$ [b][c]	-77.8 (16.3)	-77.8 (16.3)	-92.9 (19.0)	-92.9 (19.0)	-92.6 (16.3)	-92.6 (16.3)
ΔE_{prep} (N) or $(N)^-$	0.0	0.0	0.0	0.0	0.0	0.0
ΔE_{prep} (SF) or $(SF)^+$	49.0	49.0	9.0	9.0	98.8	98.8
ΔE_{corr} [d]	3.8	3.8	3.9	3.9	3.9	3.9
$\Delta E(= -D_e)$	-125.7	-125.7	-361.5	-361.5	-361.5	-361.5

[a] The values in parentheses are the percentage contributions to the total attractive interaction $\Delta E_{elstat} + \Delta E_{orb}$. [b] The values in parentheses are the percentage contributions to the total orbital interactions ΔE_{orb}. [c] The ΔE_{π} interaction is further divided into $\Delta E_{\pi\|}$ (in plane) and $\Delta E_{\pi\perp}$ (out of plane) interactions. [d] Correction for spin polarization.

Note: The electronic ground state of the fragments are: $N(^4S)$; $SF(^2\Pi)$; $N^-(^3P)$ and $(SF)^+(^3\Sigma^-)$. Energy values in kcal/mol.

Table 4.5.1 continued. EDA and ETS-NOCV analyses of the NS bond in NSF at BP86/TZ2P+ level

Interacting Fragments	$N(^2S)$; $SF(^2\Pi)$		$(N)(^2P)$; $(SF)(^2\Pi)$	
	c		**d**	
	EDA	ETS-NOCV	EDA	ETS-NOCV
Symmetry	C_s	C_s	C_s	C_s
ΔE_{int}	-196.2	-196.2	-196.2	-196.2
ΔE_{Pauli}	537.6	537.6	515.3	515.3
ΔE_{elstat} [a]	-246.4 (33.6)	-246.4 (33.6)	-192.2 (27.0)	-192.2 (27.0)
ΔE_{orb} [a]	-487.3 (66.4)	-487.3 (66.4)	-519.3 (73.0)	-519.3 (73.0)
ΔE_{σ} [b]	-350.1 (71.8)	-279.8 (57.4)	-430.0 (82.8)	-353.2 (68.0)
ΔE_{π} [b][c]	-137.3 (28.2)	-207.6 (42.6)	-89.3 (17.2)	-166.1 (32.0)
$\Delta E_{\pi\|}$ [b][c]	-	-70.3 (14.4)	-	-76.8 (14.8)
$\Delta E_{\pi\perp}$ [b][c]	-137.3 (28.2)	-137.3 (28.2)	-89.3 (17.2)	-89.3 (17.2)
ΔE_{prep} (N) or $(N)^-$	66.6	66.6	66.6	66.6
ΔE_{prep} (SF) or $(SF)^+$	1.3	1.3	1.3	1.3
ΔE_{corr} [d]	2.6	2.6	2.6	2.6
$\Delta E(= -D_e)$	-125.7	-125.7	-125.7	-125.7

[a] The values in parentheses are the percentage contributions to the total attractive interaction $\Delta E_{elstat} + \Delta E_{orb}$. [b] The values in parentheses are the percentage contributions to the total orbital interactions ΔE_{orb}. [c] The ΔE_{π} interaction is further divided into $\Delta E_{\pi\|}$ (in plane) and $\Delta E_{\pi\perp}$ (out of plane) interactions. [d] Correction for spin polarization.

Note: The electronic ground state of the fragments are: $N(^4S)$; $SF(^2\Pi)$; $N^-(^3P)$ and $(SF)^+(^3\Sigma^-)$. Energy values in kcal/mol.

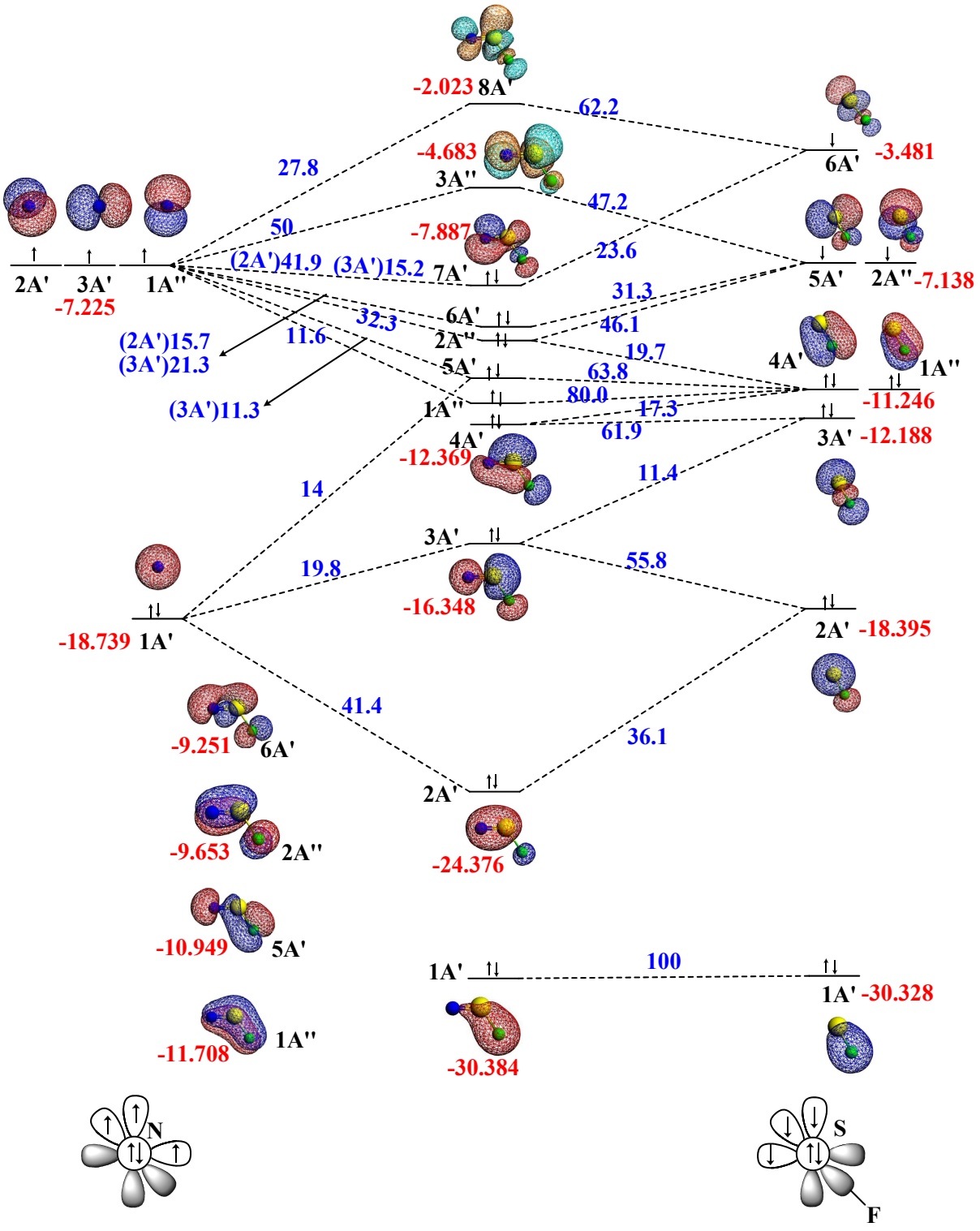

Figure 4.5.2: Plot of the valance orbital interaction between the frozen geometry of the fragments N and SF in N≡SF at BP86/TZ2P+. The percentage contributions are shown in blue colour and the orbital energies (eV) in red colour. The percentage contributions less than 5% are not shown.

The EDA and ETS-NOCV results are given in Table 4.5.1. Of the different interaction schemes, **a** has the smallest orbital interaction value, ΔE_{orb} (-478.8), followed by **c** (-487.3) and **b1** (-488.4). The NS bond in the resonance structure **a** has 33.7% electrostatic contribution (ΔE_{elstat}) and 66.3% orbital contribution (ΔE_{orb}). The total orbital contribution is divided into 55.0% σ, 25.2% $\pi_{||}$, and 18.4% $\pi_{\perp}$ contributions. Although the bonding descriptions in **b1** and **c** are not triple bonds, they have significant in-plane ($\Delta E_{\pi||}$) and out-of-plane ($\Delta E_{\pi\perp}$) π contributions to the total orbital contribution (Table 4.5.1).

The NBO data in Table 4.5.2 show three NS bond-pair orbitals, one SF bond-pair orbital, and a lone pair (with larger s character) on N and S in NSF and *lin*-NSF. Sulfur has a positive charge of about one. The Wiberg bond indices of the NS bond in NSF and *lin*-NSF are 2.499 and 2.624, respectively. Thus, the NS bond in NSF has significant triple-bond character. Figure 4.5.2 shows the valence orbital interaction between the frozen geometry of the fragments N (^{4}S) and SF ($^4\Sigma^-$) in N≡SF. The HOMO (7A′), HOMO-1 (6A′), and the HOMO-2 (2A″) are the $\pi_{||}$, σ, and $\pi_{\perp}$ orbitals, respectively, of the NS bond in NSF. The NOCV pairs and deformation densities of the σ- and π-type contributions to the NS triple bond in NSF are shown in Figure 4.5.3. Because of the electronegativity difference between N and S, ΔE_{orb} has a larger contribution from the SF fragment (i.e., electron sharing between the N and SF fragments is not symmetric). In particular, $\Delta\rho_{\pi||}$ of the beta electron (from the SF fragment) has a larger contribution to $\Delta E_{\pi||}$ of the NS bond (Figure 4.5.3b).

Table 4.5.2: NBO partial charges (*q*), Wiberg bond indices (*P*), and the number of bond-pair (BP) and lone-pair (LP) orbitals at BP86/TZVPP

	Partial charges (*q*)			*P*(NS)	LP			BP	
	N	S	F(H)		N (% s and p)	S (% s and p)	F(H)	NS	SF or SH
NSF	-0.63	1.12	-0.49	2.499	1 s(74.0) p(26.0)	1 s(73.8) p(26.0)	3	3	1
lin-NSF	-0.49	1.04	-0.55	2.624	1 s(69.4) p(30.5)	1 s(90.6) p(8.9)	3	3	1
NSH	-0.62	0.67	-0.04	2.199	2 s(76.9) p(23.0) s(0.9) p(98.3)	1 s(69.7) p(31.3)	0	2	1

		(a) Alpha electrons			**(b) Beta electrons**		
		NOCVS		Deformation Density	NOCVS		Deformation Density
k	Orbital type	ψ_{-k} (υ_{-k})	ψ_k (υ_k)	$\Delta\rho_k$ ΔE (kcal/mol)	ψ_{-k} (υ_{-k})	ψ_k (υ_k)	$\Delta\rho_k$ ΔE (kcal/mol)
1	σ	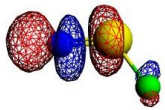	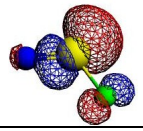	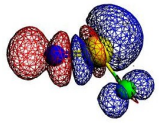	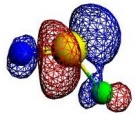	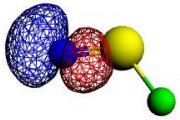	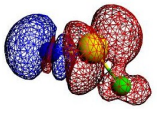
		-0.58	0.58	-105.9	-0.64	0.64	-137.0
2	σ	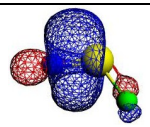	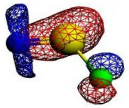	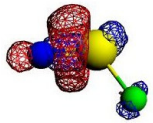	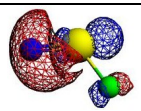	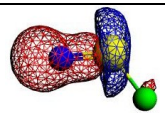	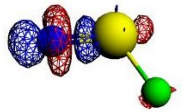
		-0.12	0.12	-10.5	-0.09	0.09	-7.1
3	$\pi_{\|\|}$	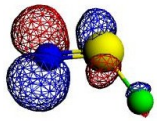	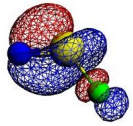	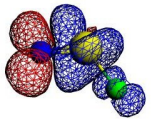	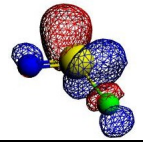	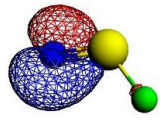	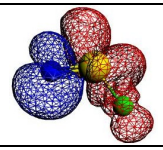
		-0.43	0.43	-22.6	-0.76	0.76	-114.8
4	$\pi_{\perp}$	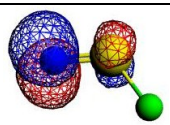	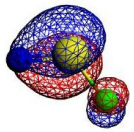	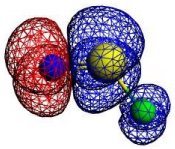	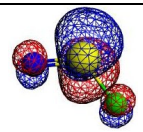	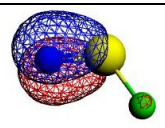	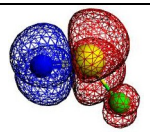
		-0.64	0.64	-29.1	-0.57	0.57	-48.2

Figure 4.5.3: (a) Contours of the most important NOCV pairs (ψ_{-k}, ψ_k) and their eigenvalues (υ_{-k}, υ_k) of alpha electrons representing electron donation from N to SF fragment and the corresponding deformation density ($\Delta\rho_k$) with the orbital stabilization energy (ΔE); **(b)** Contours of the most important NOCV pairs (ψ_{-k}, ψ_k) and their eigenvalues (υ_{-k}, υ_k) of beta electrons representing electron donation from SF to N fragment and the corresponding deformation density ($\Delta\rho_k$) with the orbital stabilization energy (ΔE); in NSF, corresponding to the interaction **a** in Scheme 4.5.2.

Table 4.5.3: EDA and ETS-NOCV analyses of the NS bond in NSH at BP86/TZ2P+ level

Interacting Fragments	$N(^4S)$; $SH(^4\Sigma^-)$		$(N)^-(^3P)$; $(SH)^+(^3\Sigma^-)$		$N^-(^3S)$; $(SH)^+(^3\Pi)$	
	a		**b1**		**b2**	
	EDA	ETS-NOCV	EDA	ETS-NOCV	EDA	ETS-NOCV
Symmetry	C_s	C_s	C_s	C_s	C_s	C_s
ΔE_{int}	-196.7	-196.7	-329.3	-329.3	-522.2	-522.2
ΔE_{Pauli}	447.7	447.7	490.2	490.2	545.5	545.5
ΔE_{elstat} [a]	-199.8 (31.0)	-199.8 (31.0)	-410.9 (50.1)	-410.9 (50.1)	-525.2 (49.2)	-525.2 (49.2)
ΔE_{orb} [a]	-444.6 (69.0)	-444.6 (69.0)	-408.6 (49.9)	-408.6 (49.9)	-542.5 (50.8)	-542.5 (50.8)
ΔE_{σ} [b]	-377.9 (85.0)	-244.7 (55.0)	-321.4 (78.6)	-253.5 (62.0)	-453.7 (83.6)	-344.0 (63.4)
ΔE_{π} [b][c]	-66.7 (15.0)	-199.9 (45.0)	-87.3 (21.4)	-155.2 (38.0)	-88.9 (16.4)	-198.6 (36.6)
$\Delta E_{\pi\parallel}$ [b][c]	-	-133.2 (30.0)	-	-67.9 (16.6)	-	-109.7 (20.2)
$\Delta E_{\pi\perp}$ [b][c]	-66.7 (15.0)	-66.7 (15.0)	-87.3 (21.4)	-87.3 (21.4)	-88.9 (16.4)	-88.9 (16.4)
ΔE_{prep} (N) or $(N)^-$	0.0	0.0	0.0	0.0	0.0	0.0
ΔE_{prep} (SH) or $(SH)^+$	111.9	111.9	0.8	0.8	193.5	193.5
ΔE_{corr} [d]	3.8	3.8	3.8	3.8	4.0	4.0
$\Delta E(= -D_e)$	-81.0	-81.0	-324.7	-324.7	-324.7	-324.7

[a] The values in parentheses are the percentage contributions to the total attractive interaction $\Delta E_{elstat} + \Delta E_{orb}$. [b] The values in parentheses are the percentage contributions to the total orbital interactions ΔE_{orb}. [c] The ΔE_{π} interaction is further divided into $\Delta E_{\pi\parallel}$ (in plane) and $\Delta E_{\pi\perp}$ (out of plane) interactions. [d] Correction for spin polarization.

Note: The electronic ground state of the fragments are $N(^4S)$; $SF(^2\Pi)$; $N^-(^3P)$ and $(SF)^+(^3\Sigma^-)$. Energy values in kcal/mol.

Table 4.5.3 continued. EDA and ETS-NOCV analyses of the NS bond in NSH at BP86/TZ2P+ level

Interacting Fragments	$N(^2S)$; $SH(^2\Pi)$		$(N)(^2P)$; $(SH)(^2\Pi)$	
	c		**d**	
	EDA	ETS-NOCV	EDA	ETS-NOCV
Symmetry	C_s	C_s	C_s	C_s
ΔE_{int}	-152.2	-152.2	-152.2	-152.2
ΔE_{Pauli}	459.5	459.5	455.7	455.7
ΔE_{elstat} [a]	-208.8 (34.1)	-208.8 (34.1)	-161.3 (26.5)	-161.3 (26.5)
ΔE_{orb} [a]	-402.9 (65.9)	-402.9 (65.9)	-446.6 (73.5)	-446.6 (73.5)
ΔE_{σ} [b]	-297.6 (73.9)	-257.4 (63.9)	-369.1 (82.7)	-326.8 (73.2)
ΔE_{π} [b][c]	-105.3 (26.1)	-145.5 (36.1)	-77.5 (17.4)	-119.8 (26.8)
$\Delta E_{\pi\parallel}$ [b][c]	-	-40.2 (10.0)	-	-42.3 (9.5)
$\Delta E_{\pi\perp}$ [b][c]	-105.3 (26.1)	-105.3 (26.1)	-77.5 (17.4)	-77.5 (17.4)
ΔE_{prep} (N)	66.6	66.6	66.6	66.6
ΔE_{prep} (SH)	2.0	2.0	2.0	2.0
ΔE_{corr} [d]	2.6	2.6	2.6	2.6
$\Delta E(= -D_e)$	-81.0	-81.0	-81.0	-81.0

[a] The values in parentheses are the percentage contributions to the total attractive interaction $\Delta E_{elstat} + \Delta E_{orb}$. [b] The values in parentheses are the percentage contributions to the total orbital interactions ΔE_{orb}. [c] The ΔE_{π} interaction is further divided into $\Delta E_{\pi\parallel}$ (in plane) and $\Delta E_{\pi\perp}$ (out of plane) interactions. [d] Correction for spin polarization.

Note: The electronic ground state of the fragments are $N(^4S)$; $SF(^2\Pi)$; $N^-(^3P)$ and $(SF)^+(^3\Sigma^-)$. Energy values in kcal/mol.

4.5.2 NSH

EDA and ETS-NOCV analyses of the NS bond in NSH were performed by considering the N and SH fragments interacting in different electronic states, as shown in Scheme 4.5.2 (similar to NSF). Interaction scheme **c** in Table 4.5.3 has the smallest orbital interaction followed by **b1**. Although the bonding description in **b1** and **c** are double and single bonds, respectively, they have significant ΔE_{π} contribution. Interaction scheme **c** has 26.1% π contribution due to lone-pair electron donation from the $p_{\pi\perp}$ orbital of S to the $p_{\pi\perp}$ orbital on N and 10.0% of the contribution comes from the donation of lone-pair electrons in the $p_{\pi\parallel}$ orbital of N to the $p_{\pi\parallel}$ orbital on S. NBO analysis finds two lone-pair orbitals on N: one with 76.9% s character and the other with 98.3% p character (Table 4.5.2). The Wiberg bond index of the NS bond in NSH is 2.199.

4.5.3 NSOH

The optimized geometries of NSOH are shown in Figure 4.5.4. NSOH has two conformations: *cis* and *trans*. *trans*-NSOH is 3.5 kcal/mol higher in energy than *cis*-NSOH; the NS bond in NSOH is slightly longer than in NSF. Table 4.5.4 shows the EDA and ETS-NOCV results of the NS bond in *cis*-NSOH. Interaction scheme **b1** has the smallest orbital interaction followed by **a** and **c**. Although the bonding description in **b1** is not a triple bond, the NS bond in **b1** has 20.7% $\Delta E_{\pi\parallel}$ and 18.9% $\Delta E_{\pi\perp}$ contributions to the total orbital interaction term. The Wiberg bond index of the NS bond in *cis*-NSOH is 2.366.

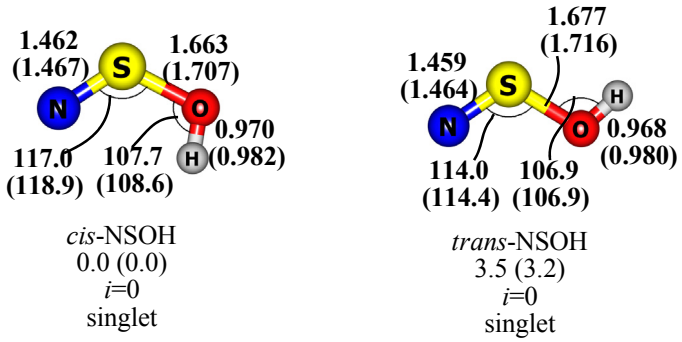

Figure 4.5.4: Optimized geometries of *cis*- and *trans*-NSOH in the singlet electronic state at the CCSD(T)/TZVPP level. Values in parenthesis correspond to BP86/TZVPP level. Bond lengths in angstrom, angles in degrees, and relative energies in kcal/mol. The index, *i,* shows the number of imaginary frequencies.

4.5.4 Topological analysis

Table 4.5.5 shows the results of the topological analysis of electron density in the singlet ground electronic state of selected species. The NS bond in NSF and NSOH has a highly positive Laplacian value with significant electron density. The NS bond in NSH also has a positive Laplacian, but smaller than that in NSF. However, the energy densities are significantly negative. The large positive Laplacian of the NS bond is due to the electronegativity difference between N and S. Unlike *cis*-HCSF, the SF bond in NSF has a negative Laplacian value.

Table 4.5.4. Energy decomposition and ETS-NOCV analyses of NS bond in *cis*-NSOH at BP86/TZ2P+

Interacting Fragments	$N(^4S)$; $SOH(^4\Sigma^-)$		$N^-(^3P)$; $(SOH)^+$ $(^3\Sigma^-)$		$N(^2P)$; $SOH(^2\Pi)$	
	a		**b1**		**c**	
	EDA	ETS-NOCV	EDA	ETS-NOCV	EDA	ETS-NOCV
Symmetry	C_s	C_s	C_s	C_s	C_s	C_s
ΔE_{int}	-185.4	-185.4	-344.8	-344.8	-195.1	-195.1
ΔE_{Pauli}	517.0	517.0	566.2	566.2	526.7	526.7
ΔE_{elstat} [a]	-232.9 (33.2)	-232.9 (33.2)	-451.8 (49.6)	-451.8 (49.6)	-245.4 (34.0)	-245.4 (34.0)
ΔE_{orb} [a]	-469.5 (66.8)	-469.5 (66.8)	-459.2 (50.4)	-459.2 (50.4)	-476.4 (66.0)	-476.4 (66.0)
ΔE_{σ} [b]	-394.2 (83.9)	-263.2 (56.1)	-370.4 (80.7)	-277.5 (60.4)	-334.3 (70.2)	-277.4 (58.2)
ΔE_{π} [b][c]	-75.4 (16.1)	-206.3 (43.9)	-88.8 (19.3)	-181.7 (39.6)	-142.2 (29.8)	-199.0 (41.8)
$\Delta E_{\pi\parallel}$ [b][c]	-	-132.2 (28.1)	-	-94.9 (20.7)	-	-57.4 (12.0)
$\Delta E_{\pi\perp}$ [b][c]	-75.4 (16.1)	-74.1 (15.8)	-88.8 (19.3)	-86.8 (18.9)	-142.2 (29.8)	-141.6 (29.8)
ΔE_{prep}	69.0	69.0	7.3	7.3	79.8	79.8
ΔE_{corr} [d]	3.4	3.4	3.8	3.8	2.7	2.7
$\Delta E(= -D_e)$	-112.6	-112.6	-333.7	-333.7	-112.6	-112.6

[a] The values in parentheses are the percentage contributions to the total attractive interaction $\Delta E_{elstat} + \Delta E_{orb}$. [b] The values in parentheses are the percentage contributions to the total orbital interactions ΔE_{orb}. [c] The ΔE_{π} interaction is further divided into $\Delta E_{\pi\parallel}$ (in plane) and $\Delta E_{\pi\perp}$ (out of plane) interactions. [d] Correction for spin polarization.
Note: The electronic ground state of the fragments in $N(^4S)$; $SOH(^2\Pi)$ and $N^-(^3P)$; $(SOH)^+$ $(^3\Sigma^-)$. Energy values in kcal/mol.

Table 4.5.5: Topological analysis of the electron density distribution at BP86/TZVPP

	NSF	NSH	*cis*-NSOH
Bond	NS	NS	NS
$\rho(r)$	2.101	1.933	2.061
$\nabla^2\rho(r)$	18.954	8.888	16.022
$H(r)$	-2.631	-2.419	-2.592
d	1.456	1.504	1.467
Bond	SF	SH	SO
$\rho(r)$	1.163	1.254	1.260
$\nabla^2\rho(r)$	-2.438	-11.432	-5.053
$H(r)$	-1.046	-1.021	-1.195
d	1.696	1.451	1.707

$\rho(r)$- electron density in ($eÅ^{-3}$) at bond critical points, $\nabla^2\rho(r)$ - laplacian of the electron density in ($Å^{-5}$) at bond critical points, $H(r)$ – electron energy density in (Hartree $Å^{-3}$) and d – the bond distance in (Å). Geometries - C_s symmetric except *lin*-HCSF in $C_{\infty v}$ symmetry.

4.6 Nature of the PS bond in PSF, PSH, and PSOH

4.6.1 PSF

Geometries of PSF and PSH optimized at the CCSD(T)/TZVPP and BP86/TZVPP levels of theory are shown in Figure 4.6.1. Both PSF and PSH have a planar (C_s symmetric) bent geometry. Triplet PSF is 26.6 kcal/mol higher in energy than singlet PSF at the BP86/TZVPP level. *lin*-PSF ($C_{\infty v}$ symmetry) is a second-order saddle point. The SF bond in *lin*-PSF is longer than the SF bond in planar PSF. Triplet PSH is -6.2 and -5.1 kcal/mol more stable than singlet PSH at the CCSD(T)/TZVPP and BP86/TZVPP levels, respectively. PSH has the triplet ground state as reported in the literature.[81, 85] The PS bond in the triplet PSH is longer than in the singlet PSH and the reverse is true for the SH bond. The PS bond in PSH is longer than in that PSF. The BP86/TZVPP level overestimates the SF and SH bond lengths and underestimates the relative energy of the linear structures. Otherwise the BP86/TZVPP level performs as well as the CCSD(T)/TZVPP level of theory.

The PS bond in PSF can be viewed as shown in Scheme 4.6.1: triple bond (**a**), double bond (**b**), and single bond (**c**). EDA and ETS-NOCV analyses were performed by considering the P and SF fragments interacting in different electronic states, as shown in Scheme 4.6.2 (similar to NSF).

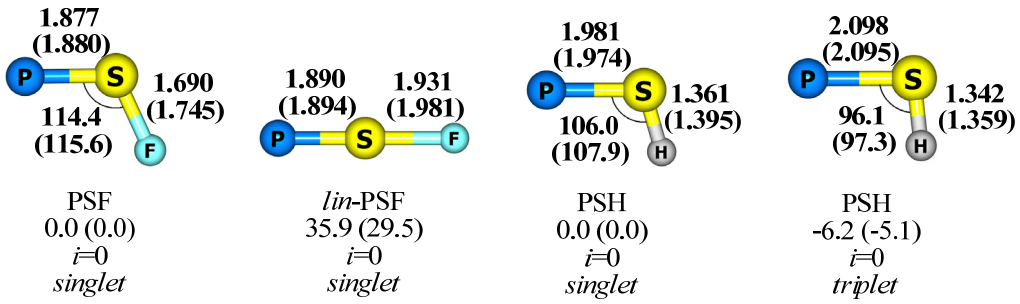

Figure 4.6.1: Optimized geometries at the CCSD(T)/TZVPP. Bond lengths in angstrom, angles in degrees, and relative energies in kcal/mol. Values in parenthesis correspond to BP86/TZVPP level. The index, *i*, shows the number imaginary frequencies.

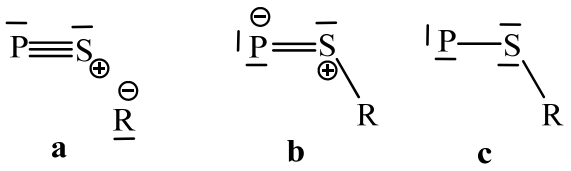

Scheme 4.6.1: Resonance structures of PSR, R = F, OH, and H. In the Lewis structures **a** and **b** all of the atoms have the octet electronic configuration, however, the atom P in the structure **c** has only the sextet electronic configuration.

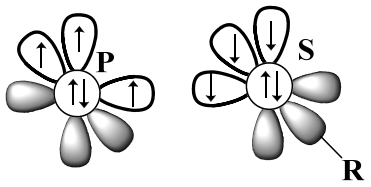

a

$P(^4S)$; $SR(^4\Sigma^-)$

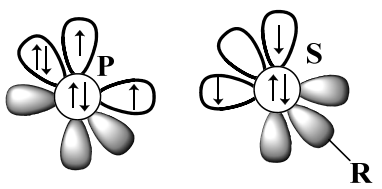

b1

$(P)^-(^3P)$; $(SR)^+(^3\Sigma^-)$

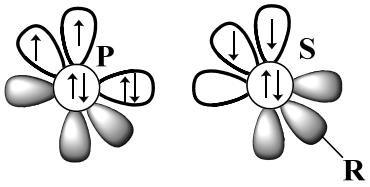

b2

$(P)^-(^3S)$; $(SR)^+(^3\Pi)$

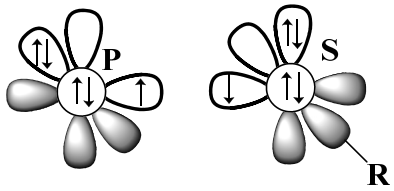

c

$P(^2S)$; $SR(^2\Pi)$

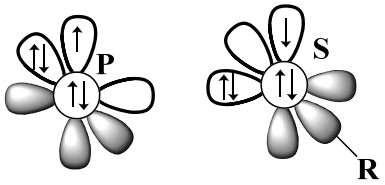

d

$(P)(^2P)$; $(SR)(^2\Pi)$

Scheme 4.6.2: Valence orbital interaction between P and S in PSR, R = F, OH, and H.

The EDA and ETS-NOCV results are given in Table 4.6.1. Of the different interaction schemes, **a** has the smallest orbital interaction value, ΔE_{orb} (-300.5) followed by **c** (-329.3). The PS bond in the resonance structure **a** has 37.9% electrostatic contribution (ΔE_{elstat}) and 62.1% orbital contribution (ΔE_{orb}). The total orbital contribution is divided into 57.3% σ, 22.6% $\pi_{\|}$, and 20.1% $\pi_{\perp}$ contributions. Although the bonding description in **c** is not a triple bond, it has significant in-plane ($\pi_{\|}$) and out-of-plane ($\pi_{\perp}$) π contributions to the total orbital contributions (Table 4.6.1). The NBO data in Table 4.6.2 show three PS bond-pair orbitals, one SF bond-pair orbital, and a lone pair (with larger s-character) on each of the P and S atoms in PSF and in *lin*-PSF. The Wiberg bond indices of the PS bond in PSF and *lin*-PSF are 2.386 and 2.528, respectively. Thus, the PS bond in PSF also has a triple-bond character. Figure 4.6.2 shows the valence orbital interaction between the frozen geometry of the fragments P (^4S) and SF ($^4\Sigma^-$) in P≡SF. The HOMO (7A′), HOMO-1 (2A″), and HOMO-2 (6A′) are the

$\pi_{\parallel}$, $\pi_{\perp}$, and σ orbitals, respectively, of the PS bond in PSF. The NOCV pairs and deformation densities of the σ- and π-type contributions to the PS triple bond in PSF are shown in Figure 4.6.3. Because of nonidentical fragments (P and SF), electron sharing between them is not symmetric.

Table 4.6.1: EDA and ETS-NOCV analyses of the PS bond in PSF at BP86/TZ2P+ level

Interacting Fragments	$P(^4S)$; $SF(^4\Sigma^-)$		$(P)^-(^3P)$; $(SF)^+(^3\Sigma^-)$		$P^-(^3S)$; $(SF)^+(^3\Pi)$	
	a		**b1**		**b2**	
	EDA	ETS-NOCV	EDA	ETS-NOCV	EDA	ETS-NOCV
Symmetry	C_s	C_s	C_s	C_s	C_s	C_s
ΔE_{int}	-137.9	-137.9	-319.2	-319.2	-402.3	-402.3
ΔE_{Pauli}	346.3	346.3	438.8	438.8	384.2	384.2
ΔE_{elstat} [a]	-183.8 (37.9)	-183.8 (37.9)	-337.9 (44.6)	-337.9 (44.6)	-300.2 (38.2)	-300.2 (38.2)
ΔE_{orb} [a]	-300.5 (62.1)	-300.5 (62.1)	-420.1 (55.4)	-420.1 (55.4)	-486.3 (61.8)	-486.3 (61.8)
ΔE_{σ} [b]	-240.0 (79.9)	-172.2 (57.3)	-332.2 (79.1)	-284.6 (67.7)	-398.6 (81.9)	-353.9 (72.8)
ΔE_{π} [b][c]	-60.5 (20.1)	-128.3 (42.7)	-88.0 (20.9)	-135.6 (32.2)	-87.8 (18.1)	-132.5 (27.2)
$\Delta E_{\pi\parallel}$ [b][c]	-	-67.8 (22.6)	-	-47.6 (11.3)	-	-44.7 (9.1)
$\Delta E_{\pi\perp}$ [b][c]	-60.5 (20.1)	-60.5 (20.1)	-88.0 (20.9)	-88.0 (20.9)	-87.8 (18.1)	-87.8 (18.1)
ΔE_{prep} (P) or $(P)^-$	0.0	0.0	0.0	0.0	0.0	0.0
ΔE_{prep} (SF) or $(SF)^+$	45.5	45.5	14.1	14.1	97.2	97.2
ΔE_{corr} [d]	2.4	2.4	3.1	3.1	3.1	3.1
$\Delta E(= -D_e)$	-90.0	-90.0	-302.0	-302.0	-302.0	-302.0

[a] The values in parentheses are the percentage contributions to the total attractive interaction $\Delta E_{elstat} + \Delta E_{orb}$. [b] The values in parentheses are the percentage contributions to the total orbital interactions ΔE_{orb}. [c] The ΔE_{π} interaction is further divided into $\Delta E_{\pi\parallel}$ (in plane) and $\Delta E_{\pi\perp}$ (out of plane) interactions. [d] Correction for spin polarization.
Note: The electronic ground state of the fragments are $P(^4S)$; $SF(^2\Pi)$; $(N)^-(^3P)$ and $(SF)^+(^3\Sigma^-)$. Energy values in kcal/mol.

Table 4.6.1 continued. EDA and ETS-NOCV analyses of PS bond in PSF at BP86/TZ2P+ level

Interacting Fragments	$P(^2S)$; $SF(^2\Pi)$		$(P)(^2P)$; $(SF)(^2\Pi)$
	c		**d**
	EDA	ETS-NOCV	EDA
Symmetry	C_s	C_s	C_s
ΔE_{int}	-137.1	-137.1	-137.1
ΔE_{Pauli}	400.7	400.7	398.5
ΔE_{elstat} [a]	-208.5 (38.8)	-208.5 (38.8)	-192.4 (35.9)
ΔE_{orb} [a]	-329.3 (61.2)	-329.3 (61.2)	-343.2 (64.1)
ΔE_{σ} [b]	-268.7 (81.6)	-241.4 (73.3)	-273.3 (79.6)
ΔE_{π} [b][c]	-60.6 (18.4)	-87.9 (26.7)	-69.9 (20.4)
$\Delta E_{\pi\parallel}$ [b][c]	-	-27.3 (8.3)	-
$\Delta E_{\pi\perp}$ [b][c]	-60.6 (18.4)	-60.6 (18.4)	-69.9 (20.4)
ΔE_{prep} (P) or $(P)^-$	41.3	41.3	41.3
ΔE_{prep} (SF) or $(SF)^+$	3.5	3.5	3.5
ΔE_{corr} [d]	2.3	2.3	2.3
$\Delta E(= -D_e)$	-90.0	-90.0	-90.0

[a] The values in parentheses are the percentage contributions to the total attractive interaction $\Delta E_{elstat} + \Delta E_{orb}$. [b] The values in parentheses are the percentage contributions to the total orbital interactions ΔE_{orb}. [c] The ΔE_{π} interaction is further divided into $\Delta E_{\pi\parallel}$ (in plane) and $\Delta E_{\pi\perp}$ (out of plane) interactions. [d] Correction for spin polarization.
Note: The electronic ground state of the fragments are $P(^4S)$; $SF(^2\Pi)$; $(N)^-(^3P)$ and $(SF)^+(^3\Sigma^-)$. Energy values in kcal/mol

Table 4.6.2: NBO partial charges (*q*), Wiberg bond indices (*P*), and the number of bond-pair (BP) and lone-pair (LP) orbitals at BP86/TZVPP

	Partial charges *(q)*				LP			BP	
	P	S	F(H)	*P*(PS)	P (% s and p)	S (% s and p)	F(H)	PS	SF or SH
PSF	0.15	0.35	-0.50	2.386	1 s(85.3) p(14.7)	1 s(74.2) p(25.7)	4	3	0
lin-PSF	0.35	0.20	-0.55	2.528	1 s(82.5) p(17.4)	1 s(91.7) p(8.0)	4	3	0
PSH	0.03	-0.11	0.08	1.768	2 s(88.4) p(11.6) s(1.0) p(98.9)	1 s(67.1) p(32.8)	0	2	1

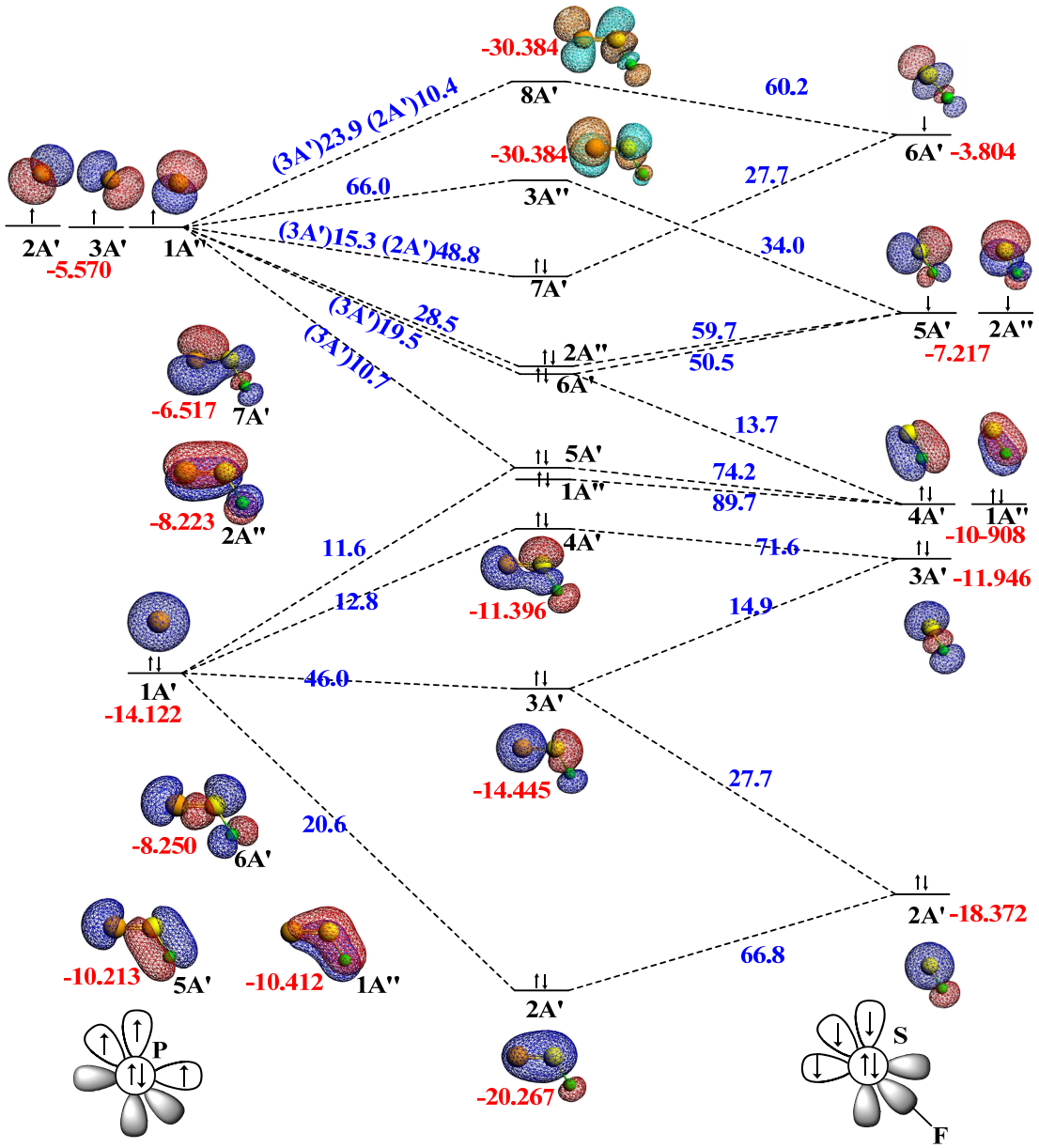

Figure 4.6.2: Plot of the valance orbital interaction between the frozen geometry of the fragments P and SF in P≡SF at BP86/TZ2P+. The percentage contributions are shown in blue colour and the orbital energies (eV) in red colour. The percentage contributions less than 5% are not shown.

		(a) Alpha electrons			**(b)** Beta electrons		
		NOCVS		Deformation Density	NOCVS		Deformation Density
k	Orbital type	ψ_{-k} (υ_{-k})	ψ_k (υ_k)	$\Delta\rho_k$ ΔE (kcal/mol)	ψ_{-k} (υ_{-k})	ψ_k (υ_k)	$\Delta\rho_k$ ΔE (kcal/mol)
1	σ	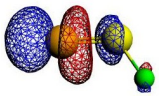	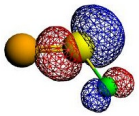	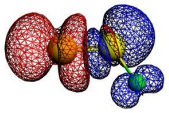	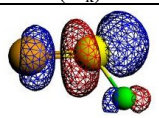	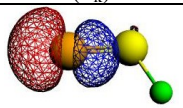	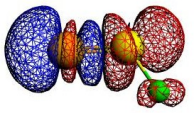
		-0.70	0.70	-106.6	-0.47	0.47	-52.2
2	σ	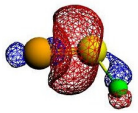	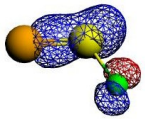	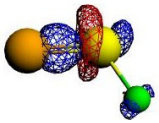	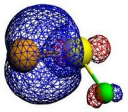	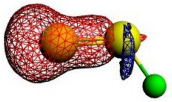	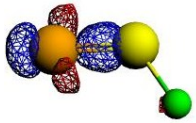
		-0.09	0.09	-5.9	-0.09	0.09	-4.5
3	$\pi_{\|\|}$	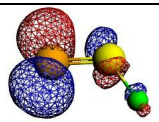	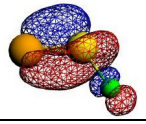		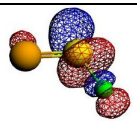	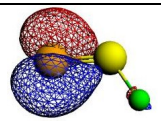	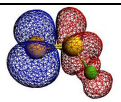
		-0.45	0.45	-21.1	-0.74	0.74	-46.7
4	$\pi_{\perp}$	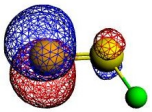	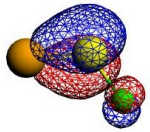	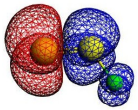	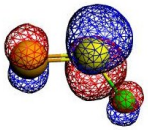	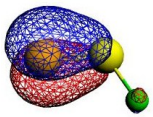	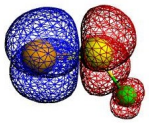
		-0.73	0.73	-42.4	-0.49	0.49	-17.3

Figure 4.6.3: (a) Contours of the most important NOCV pairs (ψ_{-k}, ψ_k) and their eigenvalues (υ_{-k}, υ_k) of alpha electrons representing electron donation from P to SF fragment and the corresponding deformation density ($\Delta\rho_k$) with the orbital stabilization energy (ΔE); **(b)** Contours of the most important NOCV pairs (ψ_{-k}, ψ_k) and their eigenvalues (υ_{-k}, υ_k) of beta electrons representing electron donation from SF to N fragment and the corresponding deformation density ($\Delta\rho_k$) with the orbital stabilization energy (ΔE), in PSF (corresponding to the interaction **a** in Scheme 4.6.2).

4.6.2 PSH

The nature of the PS bond in the singlet PSH molecule could be viewed as shown in Schemes 4.6.1 and 4.6.2. EDA and ETS-NOCV analyses of the PS bond in PSH were performed by considering N and SH fragments interacting in different electronic states, as shown in Scheme 4.6.2 (similar to PSF). Interaction scheme **c** in Table 4.6.3 has the smallest orbital interaction value. It has 19.1% $\Delta E_{\pi\perp}$ contribution due to lone-pair electron donation from the $p_{\pi\perp}$ orbital of S to the $p_{\pi\perp}$ on P and 12.4% $\Delta E_{\pi\parallel}$ contribution due to donation of the lone-pair electrons in the $p_{\pi\parallel}$ orbital of P to the $p_{\pi\parallel}$ orbital on S. NBO analysis shows two lone-pair orbitals on P in singlet PSH (Table 4.6.2). The Wiberg bond index of the PS bond in PSH is 1.768. In Figure 4.6.4, the HOMO-2 and HOMO-1 are the σ and π⊥ orbitals, respectively, of the PS bond in PSH and HOMO is the nonbonding lone-pair orbital on P.

Table 4.6.3. Energy decomposition and ETS-NOCV analyses of PS bond in PSH (singlet) at BP86/TZ2P+

Interacting Fragments	$P(^4S)$; $SH(^4\Sigma^-)$		$P^-(^3P)$; $(SH)^+$ $(^3\Sigma^-)$		$P(^2P)$; $SH(^2\Pi)$	
	a		**b1**		**c**	
	EDA	ETS-NOCV	EDA	ETS-NOCV	EDA	ETS-NOCV
Symmetry	C_s	C_s	C_s	C_s	C_s	C_s
ΔE_{int}	-181.2	-181.2	-284.1	-284.1	-105.1	-105.1
ΔE_{Pauli}	254.6	254.6	283.1	283.1	255.6	255.6
ΔE_{elstat} [a]	-136.6 (31.3)	-136.6 (31.3)	-258.8 (45.6)	-258.8 (45.6)	-142.4 (39.5)	-142.4 (39.5)
ΔE_{orb} [a]	-299.2 (68.7)	-299.2 (68.7)	-308.3 (54.4)	-308.3 (54.4)	-218.3 (60.5)	-218.3 (60.5)
ΔE_{σ} [b]	-237.0 (79.2)	-146.6 (49.0)	-215.7 (70.0)	-179.3 (58.2)	-176.6 (80.9)	-149.5 (68.5)
ΔE_{π} [b][c]	-62.3 (20.8)	-152.7 (51.0)	-92.6 (30.0)	-129.0 (41.8)	-41.8 (19.1)	-68.9 (31.6)
$\Delta E_{\pi\parallel}$ [b][c]	-	-90.4 (30.2)	-	-36.4 (11.8)	-	-27.1 (12.4)
$\Delta E_{\pi\perp}$ [b][c]	-62.3 (20.8)	-62.3 (20.8)	-92.6 (30.0)	-92.6 (30.0)	-41.8 (19.1)	-41.8 (19.1)
ΔE_{prep}	120.0	120.0	2.9	2.9	43.9	43.9
$\Delta E(= -D_e)$	-61.2	-61.2	-281.2	-281.2	-61.2	-61.2

[a] The values in parentheses are the percentage contributions to the total attractive interaction $\Delta E_{elstat} + \Delta E_{orb}$. [b] The values in parentheses are the percentage contributions to the total orbital interactions ΔE_{orb}. [c] The ΔE_{π} interaction is further divided into $\Delta E_{\pi\parallel}$ (in plane) and $\Delta E_{\pi\perp}$ (out of plane) interactions.
Note: The electronic ground state of the fragments are $P(^4S)$; $SH(^2\Pi)$ $P^-(^3P)$; $(SH)^+$ $(^3\Sigma^-)$. Energy values in kcal/mol.

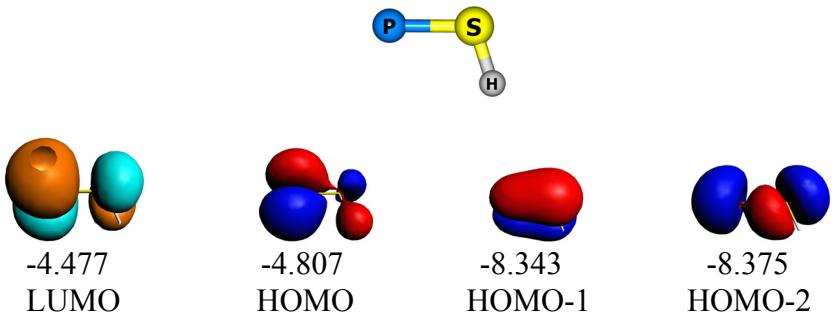

Figure 4.6.4: Important molecular orbitals of the singlet PSH molecule at BP86/TZ2P+. Orbital energies are in eV.

Triplet PSH

The valence orbital interaction between P and SH in triplet PSH is shown in Scheme 4.6.3. (^{4}S) P interacts with ($^2\Pi$) SH to form triplet PSH. The EDA result of the above scheme is shown in Table 4.6.4. In singlet PSH, one of the lone-pair electrons in the nonbonding orbital (HOMO) is promoted to the anti-bonding $\pi_\perp^*$ orbital (LUMO), resulting in triplet PSH. The ΔE_{int} and $\Delta E_{\pi\perp}$ contributions in triplet PSH (Table 4.6.4) are smaller than those in singlet PSH (**c** in Table 4.6.3). The preparation energy for the triplet PSH (1.8 kcal/mol) is smaller than that of singlet PSH (43.9 kcal/mol). The triplet ground state of PSH is due to the fragments interacting in their ground electronic state, which is not the case in singlet PSH.

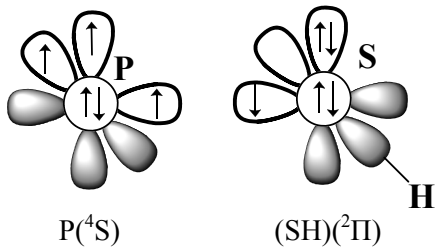

Scheme 4.6.3: Orbital interaction between P and S in triplet PSH.

Table 4.6.4. EDA of PS bond in triplet PSH at BP86/TZ2P+.

Interacting Fragments	P(^{4}S) ; SH($^2\Pi$)
	c
Symmetry	C_s
ΔE_{int}	-69.5
ΔE_{Pauli}	182.8
ΔE_{elstat} [a]	-101.1(40.1)
ΔE_{orb} [a]	-151.2 (59.9)
ΔE_{σ} [b]	-134.2 (88.8)
ΔE_{π} [b]	-17.0 (11.2)
ΔE_{prep}	1.8
$\Delta E(= -D_e)$	-67.7

[a] The values in parentheses are the percentage contributions to the total attractive interaction $\Delta E_{elstat} + \Delta E_{orb}$. [b] The values in parentheses are the percentage contributions to the total orbital interactions ΔE_{orb}. [c] The ΔE_{π} interaction is further divided into $\Delta E_{\pi\|}$ (in plane) and $\Delta E_{\pi\perp}$ (out of plane) interactions. Energy values in kcal/mol

4.6.3 PSOH

Figure 4.6.5 shows the optimized geometries of singlet PSOH. PSOH has two conformations: *cis*- and *trans*-. *trans*-PSOH is 2.1 kcal/mol higher in energy than *cis*-PSOH. The PS bond in PSOH is slightly longer than the PS bond in PSF. Bonding between P and S in PSOH is not expected to deviate much from that of PSF and lies in between PSF and PSH. The Wiberg bond index of the PS bond in *cis*-PSOH is 2.193.

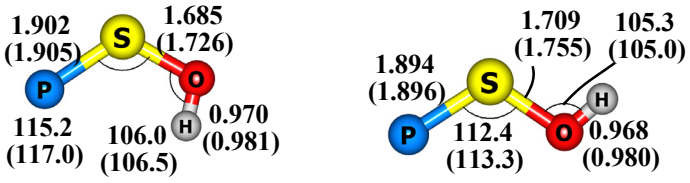

cis-PSOH
(0.0)
i=0
singlet

trans-PSOH
(2.1)
i=0
singlet

Figure 4.6.5: Optimized geometries of PSOH at the CCSD(T)/TZVPP level. Values in parentheses correspond to BP86/TZVPP level.Bond lengths in angstrom, angles in degrees, and relative energies in kcal/mol. The index, *i,* shows the number imaginary frequencies.

4.6.4 Topological analysis

Table 4.6.5 shows the results of the topological analysis of the electron density in selected species. The PS bond in PSF and *cis*-PSOH has a positive Laplacian value, indicating the ionic nature of the bond. The PS bond in the triplet PSH is covalent in nature with a negative Laplacian value.

Table 4.6.5: Topological analysis of the electron density distribution at BP86/TZVPP

	PSF (singlet)	PSH (singlet)	PSH (triplet)	*cis*-PSOH (singlet)
Bond	PS	PS	PS	PS
$\rho(r)$	1.154	0.987	0.867	1.097
$\nabla^2\rho(r)$	3.700	0.139	-4.042	3.175
$H(r)$	-1.054	-0.858	-0.634	-0.981
d	1.880	1.974	2.095	1.905
Bond	SF	SH	SH	SO
$\rho(r)$	1.058	1.361	1.417	1.211
$\nabla^2\rho(r)$	-0.869	-13.607	-14.700	-4.349
$H(r)$	-0.806	-1.225	-1.363	-1.073
d	1.745	1.395	1.359	1.726

$\rho(r)$- electron density in (eÅ^{-3}) at bond critical points, $\nabla^2\rho(r)$ - laplacian of the electron density in (Å^{-5}) at bond critical points, $H(r)$ – electron energy density in (Hartree Å^{-3}) and d – the bond distance in (Å). Geometries in C_s symmetric except *lin*-HCSF in $C_{\infty v}$ symmetry.

4.7 Summary

All of the molecules studied have planar, bent structures. Linear geometries are not minima on the PES. *cis*-HCSF could be a potential target and has a CS triple bond. *trans*-HCSF was not characterized as a stationary point on the PES. The CS triple-bond character in *cis,cis*-HCSOH is weaker than in *cis*-HCSF. HCSH is a carbene with a CS single bond, however, the $p_{\pi\perp}$ lone-pair electrons on S delocalize toward the empty $p_{\pi\perp}$, orbital on C, giving a 19.3% $\Delta E_{\pi\perp}$ contribution to the total orbital contribution of the CS bond. The SF bond in *cis*-HCSF is ionic (the SF bond-pair electrons are localized towards fluorine, leaving the p orbital on S available for bonding with the $p_{\pi\|}$ orbital of C). The SH bond in HCSH is covalent in nature and has higher excitation energy ($^2\Pi \rightarrow {}^4\Sigma^-$) relative to the SF bond in *cis*-HCSF. For F_5SCSF_3, the interaction scheme **a** (CS triple bond) has the smallest orbital interaction value and interaction scheme **c** (CS single bond) has the smallest Pauli repulsion value. The smaller Pauli repulsion in interaction scheme **c** is due to the electronic state of the interacting fragments and the presence of lone-pair electrons in the $p_{\pi\perp}$ orbital of C, reducing the lone pair–bond pair electron repulsion. Although the bonding description in **c** is single, the CS bond in this resonance structure of F_5SCSF_3 has a significant ΔE_π contribution closer to **a** (because of the donor–acceptor interaction between the lone-pair electrons on C and S). The proton affinity, which could be used as a measure of the carbene characteristics, follows the order *cis*-HCSH > *cis,cis*-HCSOH > *cis*-HCSF > F_5SCSF_3.

HSiSF has two conformers: *cis*- and *trans*-HSiSF. *trans*-HSiSF is slightly lower in energy than *cis*-HSiSF. Unlike the CS bond in *cis*-HCSF, the SiS bond in *trans*-HSiSF has a dative σ bond and an electron-sharing covalent π bond (**d**). The instantaneous interaction energy, ΔE_{int}, in **d** and **c3** (covalent σ bond and a dative π bond) are same and the fragments interact in their ground electronic states; however, **d** has the smallest orbital interaction value and the smallest Pauli repulsion. The smallest Pauli repulsion in **d** is because of the presence of an unpaired electron in the $p_{\pi\perp}$ (out-of-plane) orbital of Si in the HSi fragment. In **c3**, the electrons of the HSi fragment are in the in-plane orbitals of Si. The percentage contributions of the σ and π bonds in *cis*-HSiSF are similar to those in *trans*-HSiSF. The bond-pair electrons donated by the HSi bond are better accepted by S in the *trans* orientation than in *cis*-HSiSF; this is also reflected through the slightly longer (0.021 Å) HSi bond lengths in *trans*-HSiSF than in *cis*-HSiSF. The SiS bond in HSiSH also has a dative σ bond and an electron-sharing covalent π bond (**d**), however, interaction **c** (covalent σ bond and a dative π bond) is not negligible.

The NS and PS bonds in NSF and PSF also have triple-bond character. PSF is a potential target to be characterised experimentally, since the molecules NSF, PSH, and FPS were previously characterized by using microwave and IR spectroscopic techniques. NSH and PSH have NS and PS covalent σ bonds with significant ΔE_π contributions due to the donor–acceptor interaction between the filled and empty π-type orbitals of N or P and S. The triplet ground state of PSH is due to the fragments (P and SH) interacting in their ground electronic states. The nature of the NS and PS bonds in the molecules NSOH and PSOH is in between NSF–NSH and PSF–PSH, respectively.

5. Compounds with Triple Bonds to Uranium, Thorium, and Group 4 Metals

5.1 Introduction

The chemistry of uranium is fascinating and challenging. One such example is the unprecedented discovery of $HC{\equiv}UF_3$ by Lyon et al. in 2007,[15] which opened the door to the synthesis of compounds with triple bonds to actinides. Followed by $HC{\equiv}UF_3$, the formation of $N{\equiv}UF_3$, $P{\equiv}UF_3$, and $As{\equiv}UF_3$ have been reported [16] The uranium–imido halide complexes $(C_5Me_5)_2U(=N\text{-}Ar)(X)$ (X = F to I) and (Ar = 2,4,6-*t*-Bu_3-C_6H_2 and 2,6-*i*-Pr_2-C_6H_3) have been synthesized and described to have multiple bonding (one σ and two π interactions) between uranium and imido nitrogen.[86] The UN bond lengths in the uranium–imido halide complexes range from 1.958 to 1.975 Å, with bending angles of 169.6 to 172.2° about the nitrogen center.[86b] Evidence for the presence of terminal UN species was reported by Thomson et al. in 2010.[87] The uranium–aryl oxide complexes $(C_5Me_5)_2U(O\text{-}2,6\text{-}i\text{-}Pr_2\text{-}C_6H_3)(X)$ (X = $-CH_3$, -F, and $-N_3$), with UO bond lengths in the range of 2.11 to 2.126 Å, were reported in 2009.[88] The bending angle around the oxygen center in these complexes is in the range of 163.2 to 165.2°, indicating the possibility of multiple bonding between uranium and oxygen. A year later, terminal uranium(IV) oxo species with UO triple bonds were synthesized by Kraft et al.[89]

The triplet pnictinidene molecules $HC{\div}MF_3$ and $E{\div}MF_3$ (E = N, P, and As; M = Ti, Zr, Hf, and Th) were characterized by using infrared spectroscopy by Andrews et al.[17, 90] DFT calculations showed the presence of smaller electron spin density delocalized over the metal (M) from the unpaired electrons of the atoms E (N, P, and As), leading to a weak π-bonding interaction between the atoms E and M. Therefore, the E÷M bonds in the complexes, $E{\div}MF_3$ are called triplet triple bonds. However, it was reported that, in the case of $E{\div}ThF_3$, degenerate π_α molecular orbitals are entirely from terminal N, P, or As, contrary to that in $HC{\div}ThF_3$, in which the degenerate π_α molecular orbitals has 81% C and 19% Th character.[17b]

This chapter gives a quantitative estimation of the triple bonds and the triplet triple bonds to uranium, thorium, and Group 4 transition metals. Energy decomposition analysis (EDA) of the molecules $HC{\equiv}UF_3$, $E{\equiv}UF_3$, $HC{\div}MF_3$, and $E{\div}MF_3$ (E= N, P, and As; M=Ti, Zr, Hf, and Th) was done. EDA of the model systems $HN{=}UF_3$ and $HO\text{-}UF_3$, imitating the crystal structures $(C_5Me_5)_2U(=N\text{-}Ar)(X)$ and $(C_5Me_5)_2U(O\text{-}2,6\text{-}i\text{-}Pr_2\text{-}C_6H_3)(X)$ is also presented. The performance of the BP86 functional in predicting the geometry of some uranium complexes was also tested.

5.2 Methods

The geometries of uranium complexes were optimized by using Becke's exchange functional and Perdew's correlation functional (BP86),[36, 40] in conjunction with the following basis sets:

(I) A split-valance basis set of doubly polarized triple-ζ-quality[70] (def-TZVPP on uranium and def2-TZVPP on the main group elements) and the quasi-relativistic (small-core ECP 60) pseudopotential on uranium; by using the program package TURBOMOLE 6.1.[91]

(II) A split-valance polarization,[70] def-SV(P), and the quasi-relativistic (small-core ECP 60) pseudopotential on uranium, by using the program package TURBOMOLE 6.1.[91]

(III) A triple-ζ-quality basis augmented by two sets of polarization function with the frozen-core approximation for the core electrons (TZ2P+).[71] Scalar relativistic effects were incorporated by applying the zeroth-order regular approximation (ZORA),[73] by using the program package ADF 2009.01.[75]

And the levels of theory are denoted BP86/TZVPP, BP86/def-SV(P), and BP86/TZ2P+, respectively. The resolution of identity (RI)[92] approximation was used for calculations in the TURBOMOLE program package. Geometries of the Group 4 metal and thorium complexes were optimized at the BP86/TZ2P+ level. The stationary points are characterized as minima (i = 0) on the potential energy surface (PES) by computing a Hessian matrix at the same levels of theory of optimization. EDA[63-64] of uranium, thorium, and Group 4 metal complexes was performed at the BP86/TZ2P+ level of theory.

5.3 Performance of the BP86 Functional

Figure 5.1 shows the crystal structure of the complex PhN=U(MeC_5H_4)$_3$ and the structure of the model complexes PhN=U(C_5H_5)$_3$ and HN=UF_3. The ligand MeC_5H_4 in PhN=U(MeC_5H_4)$_3$ is replaced by C_5H_5 (Cp) in the model complex PhN=U(C_5H_5)$_3$. The ligands PhN and MeC_5H_4 in the complex PhN=U(MeC_5H_4)$_3$ were replaced by HN and F, respectively, in the simple model complex HN=UF_3. The model complex PhN=U(C_5H_5)$_3$ was optimized in the doublet electronic state by using the BP86/TZVPP, BP86/def-SV(P), and B3LYP/def-SV(P)[36, 44-45] levels of theory. The calculated structural parameters of PhN=U(C_5H_5)$_3$ are in good agreement with the experimental data, at all the three levels of theory (Table 5.1). However, the calculated NU bond length in the model complex PhN=U(C_5H_5)$_3$ is slightly smaller than that in the crystal structure. The model system HN=UF_3 in the doublet electronic state was optimized at the BP86/def-SV(P), BP86/TZVPP, and BP86/TZ2P+ levels of theory. The calculated NU bond length in HN=UF_3 is approximately 0.1 Å shorter than that in the crystal structure of PhN=U(MeC_5H_4)$_3$. The BP86/def-SV(P) and BP86/TZVPP levels of theory have almost the same performance in predicting the geometry of the model systems PhN=U(C_5H_5)$_3$ and HN=UF_3, which indicates that the size of the basis set do not play a significant role in predicting the geometry of uranium–imido complexes.

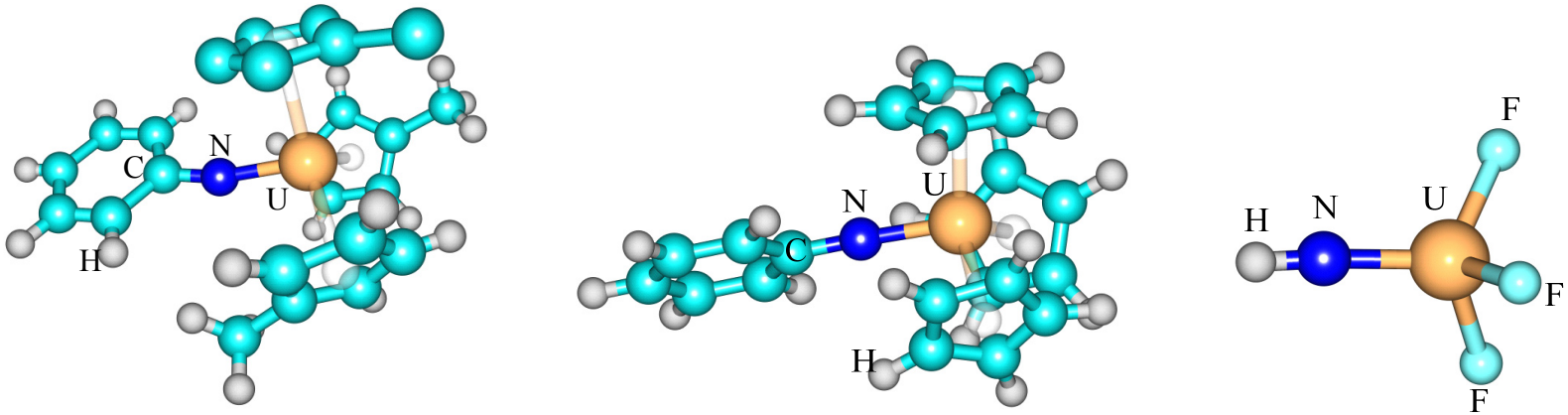

$PhN=U(MeC_5H_4)_3$ $PhN=U(C_5H_5)_3$ $HN=UF_3$

Figure 5.1. X-ray crystal structure of $PhN=U(MeC_5H_4)_3$, taken from the reference [86d], and the structure of the model complexes $PhN=U(C_5H_5)_3$ and $HN=UF_3$. Selected hydrogen atoms are removed for clarity in $PhN=U(MeC_5H_4)_3$.

Table 5.1: Selected structural parameters of the crystal structure and the model structures of uranium–imido complexes. Bond lengths in Å; bond angles in degrees.

	$PhN=U(MeC_5H_4)_3$		$PhN=U(C_5H_5)_3$ (D)		$HN=UF_3$ (D)		
	X-ray structure reference [86d]	BP86/TZVPP	BP86/def-SV(P)	B3LYP/def-SV(P)	BP86/ def-SV(P)	BP86/ TZVPP	BP86/ TZ2P+
Symmetry	C_1	C_1	C_1	C_1	C_s	C_s	C_{3v}
(H or)C-N	1.368	1.373	1.374	1.375	1.033	1.025	1.028
N-U	2.012	1.974	1.975	1.960	1.925	1.922	1.944
U-Cp[1](or F)	2.489, 2.483, 2.466	2.503, 2.508, 2.495	2.482, 2.495, 2.490	2.514, 2.521, 2.528	2.074, 2.074, 2.055	2.078, 2.078, 2.057	2.071
C(or H)-N-U	168.0	176.8	176.3	176.2	175.7	174.9	180.0
N-U-Cp[1](or F)	92.5, 103.4, 101.9	101.9, 104.6, 99.5	99.0, 104.6, 101.5	99.7, 102.0, 104.5	114.2,114.2, 108.5	114.4, 114.4, 107.3	113.6

[1] To the center of the Cp ligand.

Figure 5.2 shows the crystal structural parameters of uranium–imido complex $(C_5Me_5)_2U(=N\text{-}2,6\text{-}^{i}Pr_2\text{-}C_6H_3)(Cl)$ and the structural parameters calculated at the BP86/def-SV(P) level of theory. The calculated structural parameters are in good agreement with the experimental data. Figure 5.3 shows the structure of the complex $(C_5Me_5)_2U(=O\text{-}2,6\text{-}i\text{-}Pr_2\text{-}C_6H_3)(F)$. The complex $(C_5Me_5)_2U(=O\text{-}2,6\text{-}i\text{-}Pr_2\text{-}C_6H_3)(F)$ was optimized at the BP86/def-SV(P) level of theory in the singlet and triplet electronic states. The triplet electronic state is more stable than the singlet electronic state by 22.5 kcal/mol. The OU, OC^1(aryl carbon), and UF bond lengths and the U-O-C^1 bond angle of both the singlet and triplet electronic structures are almost the same and are in agreement with experimental data. There is no large structural difference between singlet and triplet electronic state geometries, which indicates that the two unpaired electrons in the triplet electronic structure of the complex may reside in the nonbonding orbitals of uranium. The geometrical parameters of the triplet electronic state, $Tp^*_2U(O)$ (Tp* = hydrotris(3,5-dimethylpyrazolyl)borate), calculated at the BP86/def-SV(P) level are also in good agreement with the experimental data (Figure 5.4).

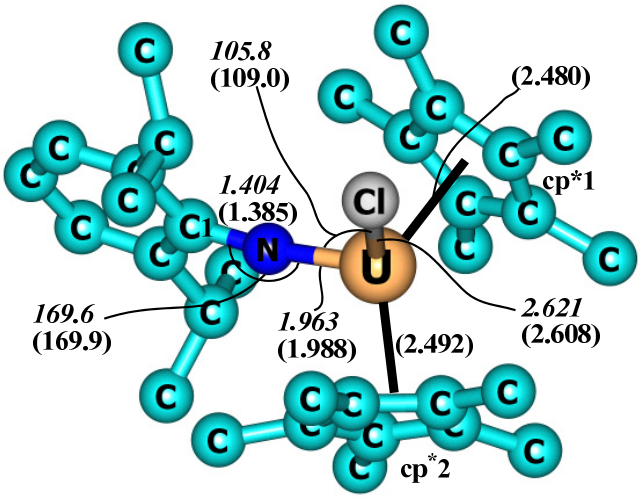

$(C_5Me_5)_2U(=N\text{-}2,6\text{-}i\text{-}Pr_2\text{-}C_6H_3)(Cl)$

Figure 5.2: Structure of $(C_5Me_5)_2U(=N\text{-}2,6\text{-}i\text{-}Pr_2\text{-}C_6H_3)(Cl)$; selected structural parameters at BP86/def-SV(P) level (in the doublet electronic state) are given in parenthesis and the experimental values (reference [86b]) in italics. Bond lengths in Å; bond angles in degrees. Hydrogen atoms are removed for clarity.

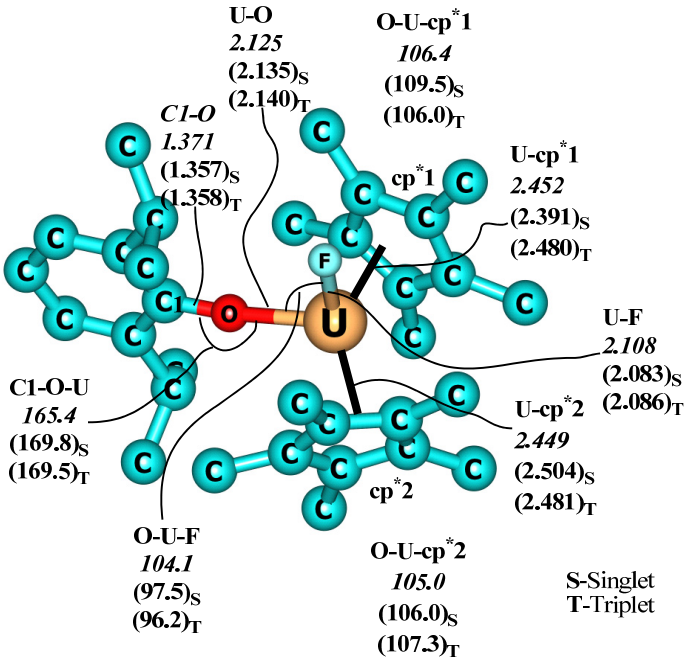

$(C_5Me_5)_2U(=O\text{-}2,6\text{-}i\text{-}Pr_2\text{-}C_6H_3)(F)$

Figure 5.3: Structure of $(C_5Me_5)_2U(=O\text{-}2,6\text{-}i\text{-}Pr_2\text{-}C_6H_3)(F)$; selected structural parameters at the BP86/def-SV(P) level are given in parentheses and the experimental values (reference [88]) in italics. The subscripts S and T correspond to the singlet and triplet electronic states of the structure, respectively. Bond lengths in Å and bond angles in degrees. Hydrogen atoms are removed for clarity.

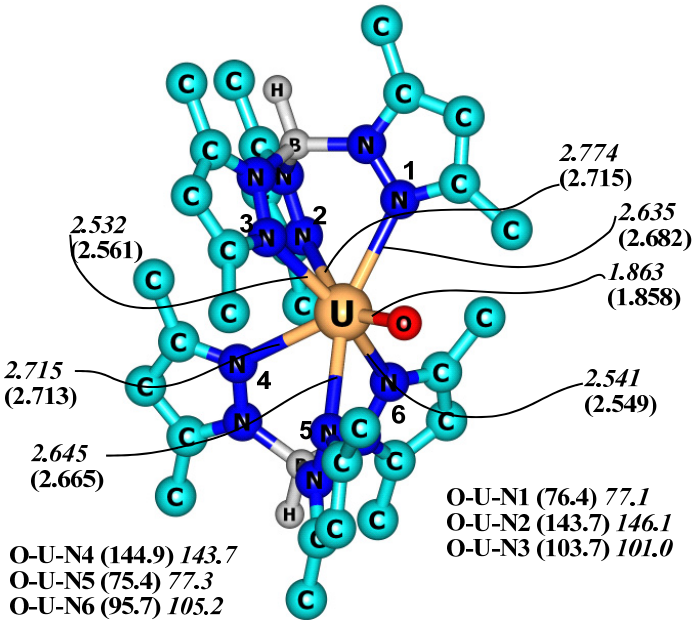

$Tp^*_2U(O)$

Figure 5.4: Structure of $Tp^*_2U(O)$; showing selected structural parameters at the BP86/def-SV(P) level (triplet electronic state) in parentheses and the experimental values (reference [89]) in italics. Bond lengths in Å and bond angles in degrees. Selected hydrogen atoms are removed for clarity.

	BP86/TZ2P+		CASSCF/CASPT2
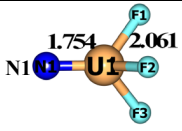 (N1-U1-F1) = 124.7 (F1-U1-F2) = 90.8 C_{3v} (i =2) E_{rel} = 0.1 kcal/mol	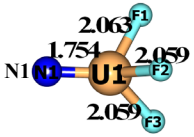 (N1-U1-F1) = 114.9 (F1-U1-F2) = 91.5 (N1-U1-F2) = 129.3 (F1-U1-F3) = 91.5 (N1-U1-F3) = 129.3 (F2-U1-F3) = 89.5 C_s (i= 2) E_{rel} = 0.2 kcal/mol	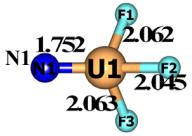 (N1-U1-F1) = 111.2 (F1-U1-F2) = 89.6 (N1-U1-F2) = 148.1 (F1-U1-F3) = 95.0 (N1-U1-F3) = 111.3 (F2-U1-F3) = 89.5 C_1 (i= 0) E_{rel} = 0.0 kcal/mol	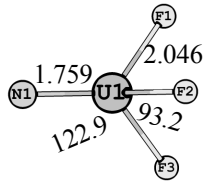
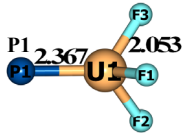 (P1-U1-F1) = 121.2 (F1-U1-F2) = 95.5 C_{3v} (i =2) E_{rel} = 0.5 kcal/mol	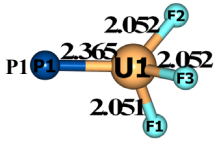 (P1-U1-F1) = 110.5 (F1-U1-F2) = 95.7 (P1-U1-F2) = 126.5 (F1-U1-F3) = 95.7 (P1-U1-F3) = 126.5 (F2-U1-F3) = 94.4 C_s (i = 0) E_{rel} = 0.5 kcal/mol	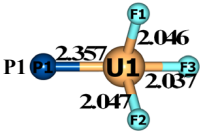 (P1-U1-F1) = 103.2 (F1-U1-F2) = 100.9 (P1-U1-F2) = 103.2 (F1-U1-F3) = 92.2 (P1-U1-F3) = 155.5 (F2-U1-F3) = 92.2 C_1 (i = 0) E_{rel} = 0.0 kcal/mol	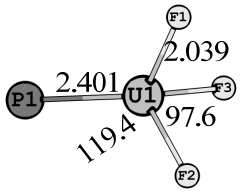
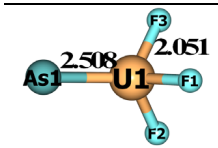 (As1-U1-F1) = 120.3 (F1-U1-F2) = 96.8 C_{3v} (i =2) E_{rel} = 0.7 kcal/mol	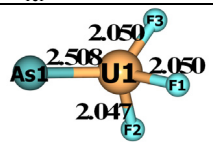 (As1-U1-F1) = 126.3 (F1-U1-F2) = 96.9 (As1-U1-F2) = 107.8 (F1-U1-F3) = 95.6 (As1-U1-F3) = 126.3 (F2-U1-F3) = 96.9 C_s (i = 1) E_{rel} = 0.7 kcal/mol	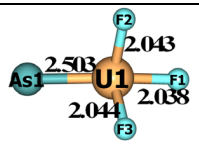 (As1-U1-F1) = 154.3 (F1-U1-F2) = 93.6 (As1-U1-F2) = 102.5 (F1-U1-F3) = 93.6 (As1-U1-F3) = 102.5 (F2-U1-F3) = 101.2 C_1 (i = 0) E_{rel} = 0.0 kcal/mol	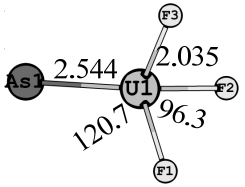
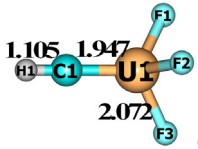 (C1-U1-F1) = 116.2 (F1-U1-F2) = 102.0 C_{3v} (i =0)			

Figure 5.5: Optimized geometries of NUF_3, PUF_3, $AsUF_3$, and $HCUF_3$ with C_{3v}, C_s, and C_1 symmetries at the BP86/TZ2P+ level of theory. Bond lengths in Å, bond angles in degrees. All of the molecules are in the singlet electronic state. Geometrical parameters at CASSCF/CASPT2 were taken from reference [16b].

5.4 Bonding Analysis of Uranium Complexes

The complexes HC≡UF_3, N≡UF_3, P≡UF_3, and As≡UF_3 in the singlet electronic state were optimized with the C_{3v} symmetry constraint at the BP86/TZ2P+ level of theory and compared with the reference geometry optimized at the CASSCF/CASPT2 level (from the literature[16b]) (Figure 5.5). The BP86/TZ2P+ level underestimates the PU and AsU bond lengths compared with the CASSCF/CASPT2 level of theory. The C_{3v}-symmetric geometries of the complexes have two imaginary frequencies of smaller magnitude. The geometries optimized without any symmetry constraint (C_1 symmetry) are minima on the PES. However, the relative energy between the C_{3v}- and C_1-symmetric geometries of the complexes are very small, so that the C_{3v}-symmetric geometries are used for EDA. The geometries of the model complexes HN=UF_3 (in the doublet electronic state) and HO-UF_3 (in the triplet electronic state) deviate from C_{3v} symmetry, with H-N-U and H-O-U bending angles of 175.7 and 169.9°, respectively. The smaller bending angle shows the possibility of multiple bonding in the NU and OU bonds. The energies required to symmetrize the complexes $HOUF_3$ and $HNUF_3$ are only 1 and 0.4 kcal/mol, respectively. Therefore, the C_{3v}-symmetric geometries are used for EDA.

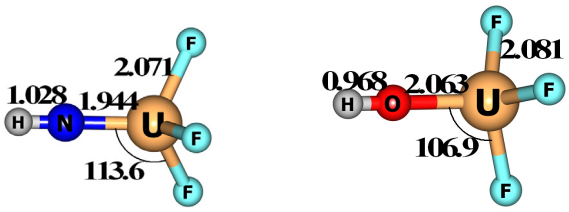

Figure 5.6: Optimized geometries of $HNUF_3$ (in the doublet electronic state) and $HOUF_3$ (in the triplet electronic state), with C_{3v} symmetry at the BP86/TZ2P+ level.

Table 5.2 shows the results of EDA of the complexes HC≡UF_3, N≡UF_3, P≡UF_3, As≡UF_3, HN=UF_3, and HO-UF_3 between the quartet (Q) electronic state fragments HC, N, P, As, and UF_3. The fragment HN in the triplet (T) electronic state interacts with the quartet (Q) electronic UF_3, resulting in the doublet (D) electronic species, HN=UF_3. EDA of the complex HO-UF_3 is done between fragments $(OH)^-$ and $(UF_3)^+$ in the singlet and triplet electronic states, respectively. The ΔE_{orb} contribution to the triple bond and the triplet triple bonds in the C_{3v}-symmetric molecules are divided into σ, π, and δ contributions, based on the irreducible representation of the contributing orbitals to the bond (Equation 5.1).

$$\Delta E_{orb}(C_{3v}) = \Delta E_{\sigma}\,(A1) + \Delta E_{\pi}\,(E) + \Delta E_{\delta}\,(A2) \qquad (5.1)$$

Table 5.2: EDA at the BP86/TZ2P+ level.

Interacting fragments	$HC{\equiv}UF_3$ (S)	$N{\equiv}UF_3$ (S)	$P{\equiv}UF_3$ (S)	$As{\equiv}UF_3$ (S)	$HN{=}UF_3$ (D)	$HO\text{-}UF_3$ (T)
	HC (Q) ; UF_3 (Q)	N (Q) ; UF_3 (Q)	P (Q) ; UF_3 (Q)	As (Q) ; UF_3 (Q)	HN (T) ; UF_3 (Q)	$(OH)^-$ (S) ; $(UF_3)^+$ (T)
Symmetry	C_{3v}	C_{3v}	C_{3v}	C_{3v}	C_{3v}	C_{3v}
ΔE_{int}	-113.1	-124.1	-43.9	-34.1	-108.0	-248.2
ΔE_{Pauli}	254.0	501.2	213.2	174.7	296.3	168.9
ΔE_{elstat}[a]	-106.9 (29.1)	-216.9 (34.7)	-109.6 (42.6)	-95.0 (45.5)	-157.6 (38.9)	-301.2 (72.2)
ΔE_{orb}[a]	-260.3 (70.9)	-408.4 (65.3)	-147.5 (57.4)	-113.8 (54.5)	-247.1 (61.1)	-115.9 (27.8)
ΔE (A1)[b]	-149.4 (57.4)	-177.8 (43.5)	-53.6 (36.4)	-41.7 (36.7)	-53.7 (21.7)	-54.9 (47.3)
ΔE (A2)[b]	0.0	0.0	0.0	0.0	0.4 (-0.1)	-1.6 (1.4)
ΔE (E)[b]	-110.9 (42.6)	-230.6 (56.5)	-93.9 (63.7)	-72.1 (63.4)	-193.7 (78.4)	-59.4 (51.3)
ΔE_{prep}	11.0	0.0	0.0	2.1	0.1	8.3
$\Delta E(= -D_e)$	-102.1	-124.1	-43.9	-32.1	-107.9	239.9
d(E-U)	1.947	1.754	2.367	2.508	1.944	2.063

[a] The values in parentheses are the percentage contributions to the total attractive interaction $\Delta E_{elstat} + \Delta E_{orb}$.
[b] The values in parentheses are the percentage contributions to the total orbital interactions ΔE_{orb}. Energy values in kcal/mol; bond lengths (d) in Å. The reference geometry and electronic state of the fragments to which the molecules dissociated are HC (D), N (Q), P (Q), As (Q), HN (T), (OH)- (S), UF_3 (Q) (C_{3v} symmetry), and $(UF_3)^+$ (T) (C_{3v} symmetry).
Q: quartet; T: triplet; D: doublet, and S: singlet electronic states.

The CU triple bond is more covalent in nature with 57.4% σ character and 42.6% π character (Table 5.2). The percentage electrostatic contributions to the CCr, CMo, and CW triple bonds in $HC{\equiv}CrF_3$, $HC{\equiv}MoF_3$, and $HC{\equiv}WF_3$ (Table 5.3) increase from Cr to W and are higher than that of the CU triple bond. The percentage σ and π contributions to the total orbital contribution of the CU (57.4% σ and 42.6% π) and CCr (56.6% σ and 43.4% π) triple bonds are almost the same and the CMo and CW triple bonds have almost the same σ and π percentage contributions to the total orbital contribution.

The instantaneous interaction energy, $\Delta E_{int,}$ and the dissociation energy, D_e, of the EU triple bonds (E = N, P, and As) decrease from N to As (Table 5.2). The EU triple bonds are weaker than the EMo and EW triple bonds.[93] The percentage π contribution of the EU triple bond increases from N to As, in contrast to the EMo and EW triple bonds, for which the percentage π contribution do not change significantly.[93] Figure 5.7 shows the plot of the valence orbital interaction between fragments As and UF_3 in $As{\equiv}UF_3$. The calculation suggests that valence f orbitals of uranium are involved in bonding with valence p orbitals of As.

The NU bond in $N{\equiv}UF_3$ is stronger than the NU bond in the model uranium–imido complex, $HN{=}UF_3$, although the percentage electrostatic contribution is higher in $HN{=}UF_3$ (Table 5.2). The NU σ bond in $HN{=}UF_3$ is weaker (with only 21.7% σ contribution) than the NU σ bond in $N{\equiv}UF_3$ (which has 43.5% σ contribution). The σ molecular orbital of $N{\equiv}UF_3$ has 38.4% contribution from the valance f orbital of U, whereas the σ molecular orbital of $HN{=}UF_3$ has only 3.9% contribution from the valance f orbital of U (Figure 5.8). In fragment HN, the σ orbital of N is shared with H and is

stabilized compared with the σ orbital on N, so that it cannot overlap with the higher energy, valence f orbital of U. In the literature, the multiple bond between the imido ligand and the uranium center is viewed by considering a formal dianionic $[N\text{-}Ar]^{2-}$ fragment interacting with the uranium 6d and 5f orbitals.[86a, 86b] However, the interaction between the charged fragments $[HN]^{2-}$ and $[UF3]^{2+}$ has a larger orbital contribution value (-381.3 kcal/mol) than the interaction between the neutral fragments (-247.1 kcal/mol) in the model uranium–imido complex $HN{=}UF_3$. The OU bond in $HO\text{-}UF_3$ is more electrostatic in nature with 51.3% π contribution. The larger π contribution to the OU bond is due to the polarization of the lone-pair electrons in the p_π orbitals of O to the empty d_π and f_π orbitals of U. The smaller (169.9°) bending angle of the H-O-U angle, in C_1 symmetry, $HO\text{-}UF_3$, is consistent with the larger π contribution.

Table 5.3: EDA at the BP86/TZ2P+ level.

	$HC{\equiv}CrF_3$	$HC{\equiv}MoF_3$	$HC{\equiv}WF_3$
Inter. Frags.	HC (Q) ; CrF_3 (Q)	HC (Q) ; MoF_3 (Q)	HC (Q) ; WF_3 (Q)
Symmetry	C_{3v}	C_{3v}	C_{3v}
ΔE_{int}	-129.8	-177.5	-198.4
ΔE_{Pauli}	244.9	293.8	313.1
ΔE_{elstat}[a]	-137.5 (36.7)	-189.8 (40.3)	-219.0 (42.8)
ΔE_{orb}[a]	-237.2 (63.3)	-281.5 (59.7)	-292.5 (57.2)
ΔE (A1)[b]	-134.3 (56.6)	-146.1 (51.9)	-148.9 (50.9)
ΔE (A2)[b]	0.0 (0.0)	0.0 (0.0)	0.0 (0.0)
ΔE (E)[b]	-103.0 (43.4)	-135.4 (48.1)	-143.6 (49.1)
ΔE_{prep}	25.0	25.3	27.4
$\Delta E(= -D_e)$	-104.8	-152.2	-171.0
d(C-M)	1.611	1.724	1.746

[a] The values in parentheses are the percentage contributions to the total attractive interaction $\Delta E_{elstat} + \Delta E_{orb}$. [b] The values in parentheses are the percentage contributions to the total orbital interactions ΔE_{orb}. Energy values in kcal/mol; bond lengths (d) in Å. The reference geometry and electronic state of the fragments to which the molecules dissociated are HC (D) and MF_3 (Q) (D_{3h} symmetry).
Q: quartet electronic state.

Table 5.4 shows the most important physical constants of the complexes $N{\equiv}UF_3$, $P{\equiv}UF_3$, $As{\equiv}UF_3$, $HC{\equiv}UF_3$, $HN{=}UF_3$, and $HO\text{-}UF_3$. The NU, PU, and AsU bonds in the complexes $N{\equiv}UF_3$, $P{\equiv}UF_3$, and $As{\equiv}UF_3$ have a Mayer bond order[94] of three. The Mayer bond order of the CU bond in $HC{\equiv}UF_3$ is less than three (2.402). The Mayer bond order of the NU bond in $HN{=}UF_3$ is less than that of the NU bond in $N{\equiv}UF_3$. The Mayer bond order of the OU bond is only 0.776. In all of the complexes studied, uranium is positively charged with a Mulliken charge of about two. $HN{=}UF_3$ has a spin density of 1.189 on uranium. The spin density, 2.018, shows the presence of two unpaired electrons on uranium in $HO\text{-}UF_3$ (Table 5.3).

$AsUF_3$	As	UF_3
8E	3E (56)	7E (29), 6E (12)
$8A_1$	$3A_1$ (52)	$7A_1$ (38)
$9A_1$	$3A_1$ (9)	$6A_1$ (58), $7A_1$ (13), $8A_1$ (18)
$2A_2$	-	$2A_2$ (100)
9E	-	6E (75), 7E(23)

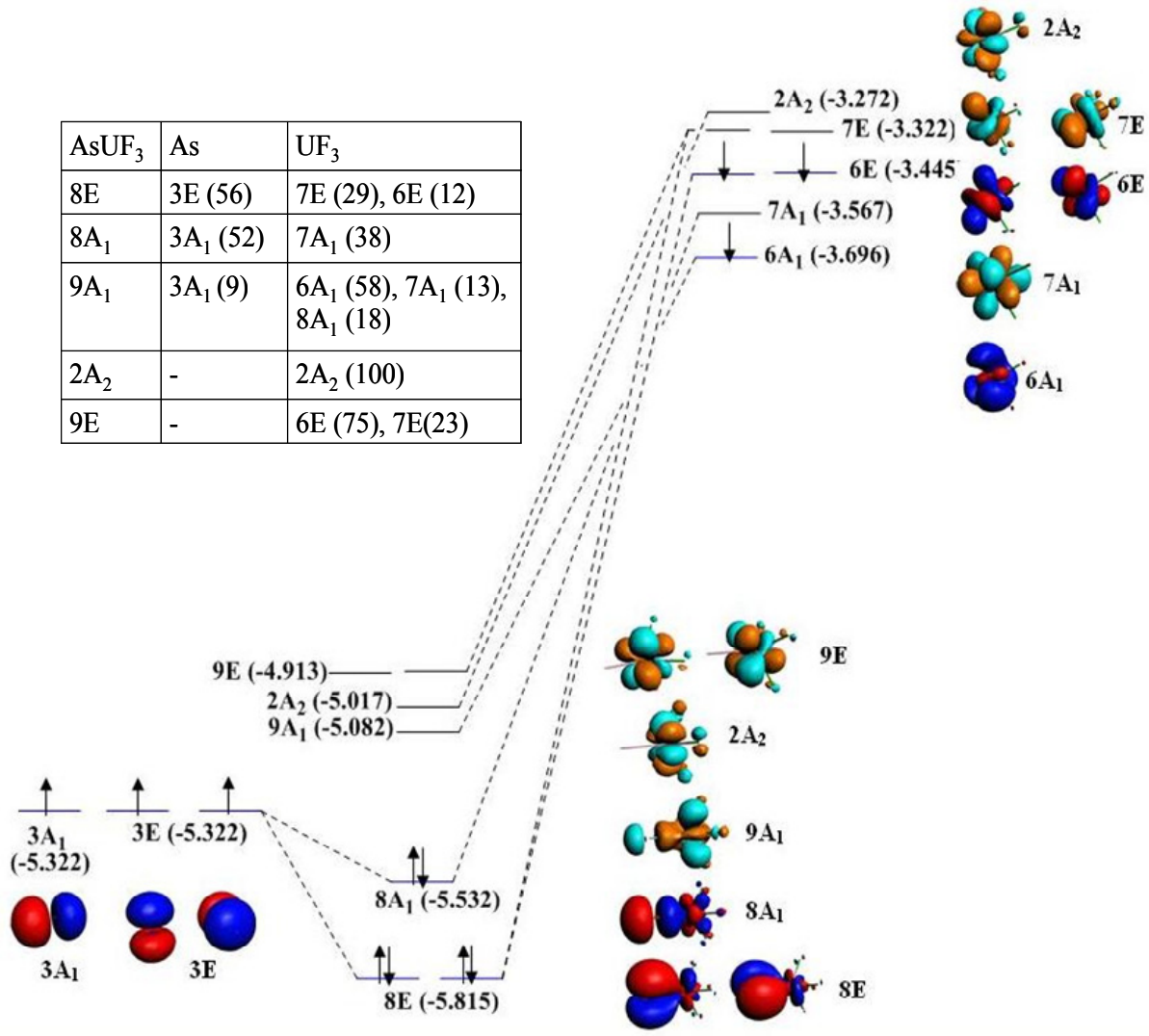

Figure 5.7: Plot of the valence orbital interaction between fragments As and UF_3 in As≡UF3 at the BP86/TZ2P+ level. Orbital energies (eV) are given in parentheses. Percentage contributions of the fragment orbitals (As and UF_3) to the bonding molecular orbitals of the AsU triple bond are given in the upper left corner of the picture.

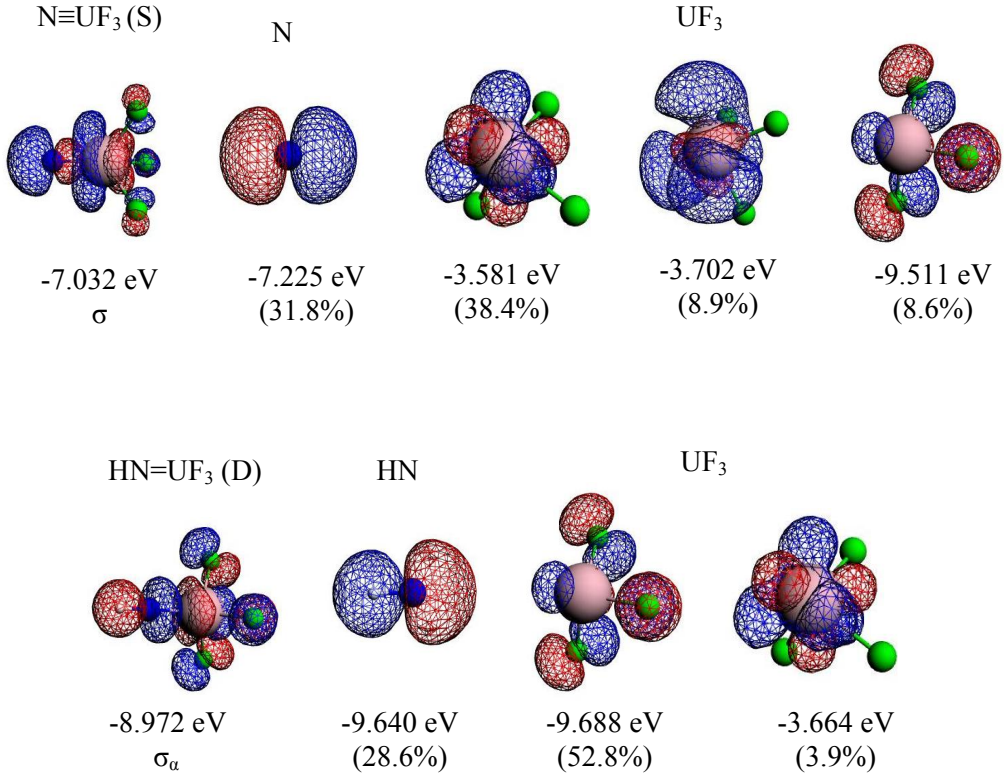

Figure 5.8: Plot of the σ molecular orbital of the NU bonds in $N{\equiv}UF_3$ and $HN{=}UF_3$ and the percentage contributions of the most important orbital of the fragments (N or HN and UF_3) at the BP86/TZ2P+ level.

Table 5.4: Selected physical constants of molecules in C_{3v} symmetry at the BP86/TZ2P+ level. E = N, P, As, C, and O.

	Mulliken charge (q)				Electron spin density on U	Dipole moment (debye)	Mayer bond order		
	H	E	U	F[a]			HE	EU	UF
$N{\equiv}UF_3$	-	-0.35	1.78	-0.48	0	1.10	-	2.989	0.778
$P{\equiv}UF_3$	-	-0.14	1.61	-0.49	0	0.28	-	3.043	0.752
$As{\equiv}UF_3$	-	-0.36	1.81	-0.48	0	0.04	-	3.058	0.746
$HC{\equiv}UF_3$	-0.23	-0.12	1.82	-0.49	0	1.23	0.992	2.402	0.727
$HN{=}UF_3$	-0.09	-0.36	1.94	-0.50	1.189	2.09	1.094	1.929	0.717
$HO{-}UF_3$	0.19	-0.64	2.02	-0.52	2.018	2.27	1.095	0.776	0.693

[a] charge on single F atom.

5.5 Bonding Analysis of Thorium and Group 4 Metal Complexes

Geometries of the triplet electronic state molecules HC÷ThF_3, FC÷MF_3, and E÷MF_3 (E = N, P, and As; M = Ti, Zr, Hf, and Th) were optimized at the BP86/TZ2P+ level, with the C_{3v} symmetry constraint (Figure 5.9). The molecules E÷MF_3 have the triplet electronic ground state.[17, 90] The two unpaired electrons in the p orbitals of C and E are shared with the empty d orbitals on the metal (M) leading to two degenerate singly occupied π molecular orbitals (Figure 5.10).

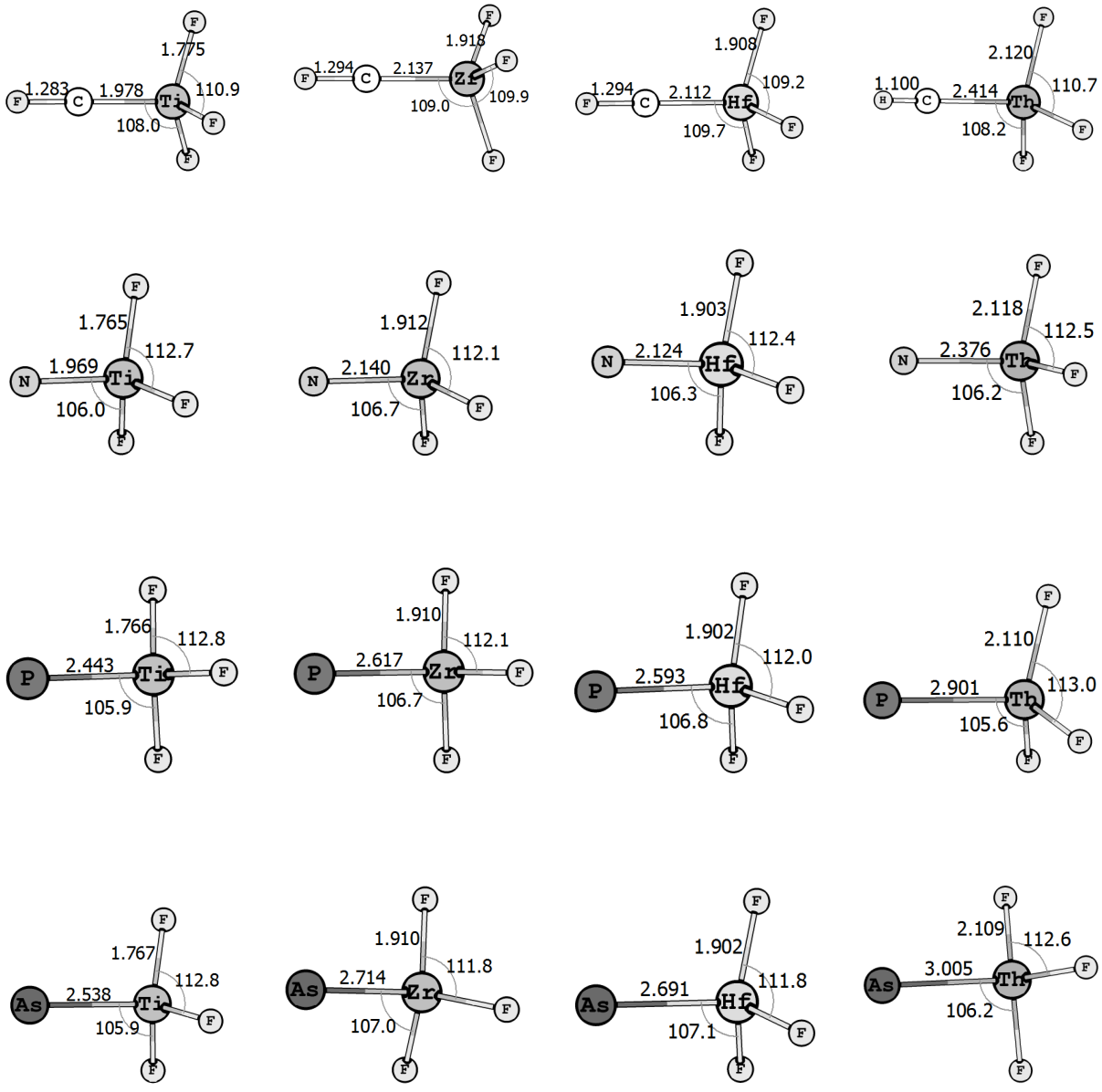

Figure 5.9: Optimized Geometries of the triplet electronic state molecules HC÷ThF_3, FC÷MF_3, and E÷MF_3 (E = N, P, and As; M = Ti, Zr, Hf, and Th) at the BP86/TZ2P+ level of theory.

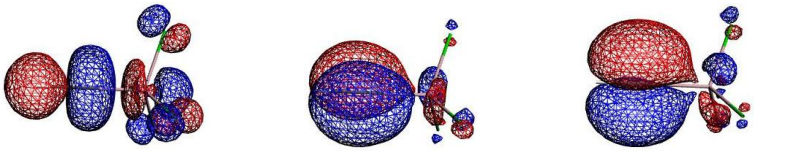

σ_α (-8.551 eV) (*1.00*) σ_β (-7.842 eV) (*1.00*) | $\pi_{\|\alpha}$ (-6.226 eV) (*1.00*) | $\pi_{\perp\alpha}$ (-6.226 eV) (*1.00*)

Figure 5.10: The σ and degenerate π molecular orbitals of the C÷Th bond in HC÷ThF_3 at the BP86/TZ2P+ level. The electron occupation is given in italics.

The percentage contributions of the valance atomic orbitals of the metals Ti and Th to the bonding (σ and π) molecular orbitals of the C÷Ti, E÷Ti, C÷Th, and E÷Th bonds are very small, relative to those of the percentage contributions coming from the valance atomic orbitals of the atoms C and E (=N to As) (Table 5.5). In C÷ThF_3 and E÷ThF_3, the 6d valance orbitals of Th are mainly involved in bonding with the valence p orbitals of C and E and the 5f orbitals of Th have only a very small contribution (Table 5.5).

Table 5.6 shows the bond lengths and EDA of the triplet triple bond in the complexes HC÷ThF_3 and E÷ThF_3. The C÷M and E÷M bond lengths calculated at the BP86/TZ2P+ (this work) and B3LYP//6-311+G(2d)/SDD (from the reference [17, 90]) levels are in good agreement with each other. However, BP86/TZ2P+ underestimates the E÷Hf bond lengths compared with the B3LYP//6-311+G(2d)/SDD level. The instantaneous interaction energy, ΔE_{int}, of the C÷M bond is almost double the instantaneous interaction energy (ΔE_{int}) of the N÷M bond, although the dissociation energies and bond lengths of the two bonds are almost the same for a metal (M) (Table 5.6). For a metal (M), the ΔE_{int} and ΔE_{Pauli} contributions decrease and the percentage π contribution of the E÷M bond increases from N to As and the percentage electrostatic contribution increases from N to As.

Table 5.7 shows EDA of the CTi, NTi, PTi, and AsTi triple bonds in the molecules HC≡Ti,[95] N≡Ti,[96] P≡Ti, and As≡Ti. EDA was performed in the doublet electronic state of the molecules. The percentage contribution of the π bonds to the C≡Ti and E≡Ti bonds (Table 5.7) are higher than the percentage contribution of the π bonds to the triplet triple bonds C÷Ti and E÷Ti (Table 5.6). The SOMO (singly occupied molecular orbital) of the molecule HC≡Ti has 68.0% 4s and 23.4% $3d_z^2$ contributions from the valence orbitals of Ti.

The instantaneous interaction energies (ΔE_{int}) of the C÷Th and C≡U bonds have almost the same values; however, ΔE_{int} of the N÷Th bond is smaller than that of the N≡U bond (Tables 5.2 and 5.6). In contrast, ΔE_{int} values of the P÷Th and As÷Th bonds are slightly higher than those of the P≡U and As≡U bonds. The Pauli repulsions of the C÷Th and E÷Th bonds are smaller than those of the C≡U and E≡U bonds.

Table 5.5: Most important percentage contributions from the atomic orbitals to the C÷M and E÷M bonds at the BP86/TZ2P+ level; M = Ti and Th; E= N, P, and As.

	FC÷TiF_3			N÷TiF_3		P÷TiF_3		As÷TiF_3	
	F	C	Ti	N	Ti	P	Ti	As	Ti
σ_α	17.2% $2P_z$	42.6% 2s, 24.5% $2p_z$	8.6% $3d_{z^2}$	3.6% 2s, 76.2% $2p_z$	13.5% $3d_{z^2}$	3.8% 3s, 66.0% $3p_z$	18.6% $3d_{z^2}$, 3.3% 4s	2.5% 4s, 69.1% $4p_z$	18.6% $3d_{z^2}$, 4.2% 4s
σ_β	8.9% $2P_z$	46.9% 2s, 22.3% $2p_z$	12.4% $3d_{z^2}$	4.8% 2s 69.5% $2p_z$	18.2% $3d_{z^2}$	4.5% 3s, 61.3% $3p_z$	23.0% $3d_{z^2}$ 3.4% 4s	2.9% 4s, 62.2% $4p_z$	24.4% $3d_{z^2}$, 4.4% 4s
$\pi_{\parallel\alpha}$	11.9% $2p_x$	59.6% $2p_x$	18.6% $3d_{xz}$	86.6% $2p_x$	4.2% $3d_{xz}$	85.8% $3p_x$	7.4% $3d_{xz}$	87.8% $4p_x$	7.2% $3d_{xz}$
$\pi_{\perp\alpha}$	11.9% $2p_y$	59.6% $2p_y$	18.6% $3d_{yz}$	86.6% $2p_y$	4.2% $3d_{yz}$	85.8% $3p_y$	7.4% $3d_{yz}$	87.8% $4p_y$	7.2% $3d_{yz}$

	HC÷ThF_3			N÷ThF_3		P÷ThF_3		As÷ThF_3	
	H	C	Th	N	Th	P	Th	As	Th
σ_α	14.4% 1s	11.0% 2s, 40.1% $2p_z$	3.3% $6p_z$, 5.6% $6d_{z^2}$, 2.9% 7s	2.1% 2s, 79.4% $2p_z$,	7.3% $6d_{z^2}$, 1.9% $5f_{z^3}$	2.6% 3s, 72.1%$3p_z$	11.4% $6d_{z^2}$, 6.6% 7s	1.8% 4s, 74.2% $4p_z$	10.9% $6d_{z^2}$, 7.3% 7s
σ_β	13.6% 1s	16.8% 2s, 37.8 % $2p_z$	2.5% $6p_z$, 9.9% $6d_{z^2}$, 5.1% 7s	2.5% 2s, 77.7% $2p_z$,	8.6% $6d_{z^2}$, 2.3% $5f_{z^3}$	2.7% 3s, 70.8% $3p_z$	12.8% $6d_{z^2}$, 7.1% 7s	1.9% 4s, 71.7% $4p_z$	12.9% $6d_{z^2}$, 8.3% 7s
$\pi_{\parallel\alpha}$	-	83.0% $2p_x$	6.7% $6d_{xz}$, 3.6% $5f_{z^2x}$	87.7% $2p_x$	3.4% $6d_{xz}$, 1.9% $5f_{z^2x}$	87.7% $3p_x$	5.6% $6d_{xz}$, 1.9% $5f_{z^2x}$	89.5% $4p_x$	5.0% $6d_{xz}$, 1.8% $5f_{z^2x}$
$\pi_{\perp\alpha}$	-	83.0% $2p_y$	6.7% $6d_{yz}$, 3.6% $5f_{z^2y}$	87.7% $2p_y$	3.4% $6d_{yz}$, 1.9% $5f_{z^2y}$	87.7% $3p_y$	5.6% $6d_{yz}$, 1.9% $5f_{z^2y}$	89.5% $4p_y$	5.0% $6d_{yz}$, 1.8% $5f_{z^2y}$

Table 5.6: EDA at the BP86/TZ2P+ level.

Interacting fragments	FC or HC ($^4\Sigma^-$); MF_3 ($^2\Sigma^+$)	N (^{4}S) ; MF_3 ($^2\Sigma^+$)	P (^{4}S) ; MF_3 ($^2\Sigma^+$)	As (^{4}S) ; MF_3 ($^2\Sigma^+$)
	FC÷TiF_3	N÷TiF_3	P÷TiF_3	As÷TiF_3
Symmetry	C_{3v}	C_{3v}	C_{3v}	C_{3v}
ΔE_{int}	-147.8	-63.1	-50.1	-47.3
ΔE_{Pauli}	74.7	148.5	101.3	99.0
ΔE_{elstat}[a]	-62.5 (28.1)	-80.4 (38.0)	-70.3 (46.4)	-73.0 (49.9)
ΔE_{orb}[a]	-160.0 (71.9)	-131.3 (62.0)	-81.1 (53.6)	-73.3 (50.1)
ΔE (A1)[b]	-133.8 (83.6)	-121.8 (92.8)	-71.3 (87.9)	-63.7 (86.9)
ΔE (A2)[b]	0.0 (0.0)	0.0 (0.0)	0.0 (0.0)	0.0 (0.0)
ΔE (E)[b]	-26.2 (16.4)	-9.5 (7.2)	-9.8 (12.1)	-9.6 (13.1)
ΔE_{prep}	93.9	6.2	4.8	4.8
$\Delta E(= -D_e)$	-53.9	-56.9	-45.3	-42.5
d(E÷M)	1.978 (1.973)[c]	1.969 (1.959)[c]	2.443 (2.426)[c]	2.538 (2.530)[c]
	FC÷ZrF_3	N÷ZrF_3	P÷ZrF_3	As÷ZrF_3
Symmetry	C_{3v}	C_{3v}	C_{3v}	C_{3v}
ΔE_{int}	-157.9	-71.7	-59.2	-56.5
ΔE_{Pauli}	86.4	176.7	125.9	125.5
ΔE_{elstat}[a]	-88.0 (36.0)	-98.0 (39.4)	-92.4 (49.9)	-98.7 (54.2)
ΔE_{orb}[a]	-156.2 (64.0)	-150.5 (60.6)	-92.7 (50.1)	-83.3 (45.8)
ΔE (A1)[b]	-131.6 (84.2)	-140.8 (93.6)	-82.4 (88.9)	-73.2 (87.8)
ΔE (A2)[b]	0.0 (0.0)	0.0 (0.0)	0.0 (0.0)	0.0 (0.0)
ΔE (E)[b]	-24.7 (15.8)	-9.7 (6.4)	-10.3 (11.1)	-10.1 (12.2)
ΔE_{prep}	93.2	5.7	4.3	4.6
$\Delta E(= -D_e)$	-64.7	-66.0	-54.9	-51.9
d(E÷M)	2.137 (2.136)[c]	2.140 (2.143)[c]	2.617 (2.606)[c]	2.714 (2.715)[c]
	FC÷HfF_3	N÷HfF_3	P÷HfF_3	As÷HfF_3
Symmetry	C_{3v}	C_{3v}	C_{3v}	C_{3v}
ΔE_{int}	-160.1	-74.0	-62.4	-59.4
ΔE_{Pauli}	244.8	186.0	133.2	131.2
ΔE_{elstat}[a]	-96.3 (23.8)	-106.4 (40.9)	-99.9 (51.1)	-104.7 (54.9)
ΔE_{orb}[a]	-308.6 (76.2)	-153.7 (59.1)	-95.7 (48.9)	-85.9 (45.1)
ΔE (A1)[b]	-283.0 (91.7)	-143.0 (93.1)	-84.5 (88.2)	-75.0 (87.4)
ΔE (A2)[b]	0.0 (0.0)	0.0 (0.0)	0.0 (0.0)	0.0 (0.0)
ΔE (E)[b]	-25.6 (8.3)	-10.7 (6.9)	-11.3 (11.8)	-10.9 (12.6)
ΔE_{prep}	94.1	6.0	4.8	5.1
$\Delta E(= -D_e)$	-66.0	-68.0	-57.6	-54.3
d(E÷M)	2.112 (2.133)[c]	2.124 (2.146)[c]	2.593 (2.609)[c]	2.691 (2.715)[c]
	HC÷ThF_3	N÷ThF_3	P÷ThF_3	As÷ThF_3
Symmetry	C_{3v}	C_{3v}	C_{3v}	C_{3v}
ΔE_{int}	-117.4	-67.2	-55.5	-53.0
ΔE_{Pauli}	105.2	145.3	106.4	105.6
ΔE_{elstat}[a]	-70.7 (31.7)	-77.0 (36.2)	-73.7 (45.6)	-79.2 (49.9)
ΔE_{orb}[a]	-152.0 (68.3)	-135.4 (63.8)	-88.1 (54.4)	-79.4 (50.1)
ΔE (A1)[b]	-139.1 (91.5)	-127.1(93.9)	-79.5 (90.3)	-71.1 (89.5)
ΔE (A2)[b]	0.0 (0.0)	0.0 (0.0)	0.0 (0.0)	0.0 (0.0)
ΔE (E)[b]	-12.9 (8.5)	-8.29 (6.1)	-8.6 (9.7)	-8.3 (10.5)
ΔE_{prep}	19.3	12.4	2.9	3.2
$\Delta E(= -D_e)$	-98.1	-54.8	-52.6	-49.8
d(E÷M)	2.414	2.376 (2.378)[c]	2.901 (2.905)[c]	3.005 (3.012)[c]

[a] The values in parentheses are the percentage contributions to the total attractive interaction ΔE_{elstat} + ΔE_{orb}. [b] The values in parentheses are the percentage contributions to the total orbital interactions ΔE_{orb}. [c] Bond lengths at the B3LYP//6-311+G(2d)/SDD level from the reference [17, 90]. Energy values in kcal/mol; bond lengths (d) in Å.

The reference geometry and electronic state of the fragments to which the molecules dissociated are HC (D), FC (D), N (Q), P (Q), As (Q), and MF_3 (D) (D_{3h} symmetry)

Table 5.7: EDA of the doublet electronic state HC≡Ti and E≡Ti (E = N, P, and As) at the BP86/TZ2P+ level.

	HC≡Ti	N≡Ti	P≡Ti	As≡Ti
Interacting fragments	HC($^4\Sigma^-$); Ti(^{5}S)	N(^{4}S) ; Ti (^{5}S)	P(^{4}S) ; Ti (^{5}S)	As(^{4}S) ; Ti (^{5}S)
ΔE_{int}	-163.9	-158.1	-99.2	-89.1
ΔE_{Pauli}	231.4	398.1	234.6	222.5
ΔE_{elstat} [a]	-154.2 (39.0)	-210.6 (37.8)	-172.0 (51.5)	-175.4 (56.3)
ΔE_{orb} [a]	-241.1 (61.0)	-345.7 (62.2)	-161.8 (48.5)	-136.2 (43.7)
ΔE (A1)[b]	-130.9 (54.3)	-161.9 (46.8)	-72.2 (44.6)	-62.3 (45.7)
ΔE (A2)[b]	0.0 (0.0)	0.0 (0.0)	0.0 (0.0)	0.0 (0.0)
ΔE (E)[b]	-110.1 (45.7)	-183.8 (53.2)	-89.6 (55.4)	-74.0 (54.3)
ΔE_{prep}	27.7	13.8	12.4	12.6
ΔE(= $-D_e$)	-136.2	-144.3	-86.8	-76.5
d(E-Ti)	1.691 (*1.728*)[c]	1.574 (*1.582*)[c]	2.078	2.191

[a] The values in parentheses are the percentage contributions to the total attractive interaction ΔE_{elstat} + ΔE_{orb}. [b] The values in parentheses are the percentage contributions to the total orbital interactions ΔE_{orb}. [c] Experimental bond lengths.[95, 96] Energy values in kcal/mol; bond lengths (d) in Å.
Note: Ground electronic states: HC($^2\Pi$), E(^{4}S), and Ti (^{3}F).

5.6 Summary

The performance of the BP86 functional was tested in predicting the geometry of complexes with triple bonds to uranium. The BP86 functional performs well, independent of the size of the basis set used. EDA of the complexes with a triple bond to uranium and complexes with triplet triple bonds to thorium and Group 4 metals is reported. The CU and EU triple bonds are weaker than the CM and EM triple bonds (E = N to As; M = Cr, Mo, and W). The NU bond in N≡UF_3 is stronger than the NU bond in the model uranium–imido complex HN=UF_3. The OU bond in HO-UF_3 is more electrostatic in nature with 51.3% π contribution. In the triplet molecules HC÷ThF_3, FC÷MF_3, and E÷MF_3 (E = N, P, and As; M = Ti, Zr, Hf, and Th), the two unpaired electrons in the p orbitals of C and E are shared with the empty d orbitals on the metal (M), leading to two degenerate singly occupied π molecular orbitals. The instantaneous interaction energy, ΔE_{int}, of the C÷M bonds is stronger than that of E÷M. The percentage π contribution of the E÷M bond increases from N to As for a metal (M). The calculations suggest that the valence f orbitals of U are involved in bonding with the valence p orbitals of As in As≡UF_3. In contrast, the percentage contribution of the valence f orbital of Th to the E÷Th bonds in E÷ThF_3 is very small. However, the participation of the valence f orbitals of actinides in chemical bonding needs to be investigated in detail.

6. Conclusion and Outlook

Compounds with potential triple-bonding character, involving the heavier main group elements, Group 4 transition metals, and the actinides uranium and thorium, have been studied by using quantum mechanical methods. The most important results of this thesis are summarized below.

Heavier Homologues of HCN–HNC

The singlet potential energy surface (PES) of the system (H, X, E), in which X = N to Bi and E = C to Pb, was explored at the CCSD(T)/TZVPP and BP86/TZ2P+ levels of theory. The BP86 level performs as well as CCSD(T), but it fails to predict *lin*-HSiBi as the global minimum of the (H, Bi, Si) system. The PESs of systems involving the first-row elements C and N, that is, the (H, N, E) and (H, X, C) systems, are different from the PESs of heavier homologues. *lin*-HNE is the global minimum and *lin*-HEN is the local minimum for E = Si to Pb. In contrast, *lin*-HCN is lower in energy than *lin*-HNC. A planar transition state (TS) connects the two minima. No bent structures were observed as minima on the PES of the (H, N, E) system, whereas *bent*-HXE and *lin*-HEX were minima and *lin*-HXE was a second-order saddle point in the case of (H, X, E) for X = P to Bi and E = Si to Pb. *bent*-HXE is the global minimum and *lin*-HEX is the local minimum, except *bent*-HBiSi which is 3.1 kcal/mol higher in energy than *lin*-HSiBi. In *bent*-HBiSi, the 1s orbital of H prefers to overlap more with the 2p orbital of Si than the more diffuse 5p orbital of Bi. The natural partial atomic (NPA) charges on the atoms of the (H, X, E) system follow the periodic trend. Changes in the Wiberg bond index values are consistent with the structural changes of the system (H, X, E).

The nature of the EX bond in *lin*-HEX involves one σ and two π-electron-sharing bonds, between the quartet electronic state fragments ($^4\Sigma^-$) HE and (^{4}S) X. However, for X = Bi, the fragment HE interacting in the ($^2\Pi$) electronic ground state, with the (^{2}P) Bi, also becomes valid. In *bent*-HXE, there are σ and π-electron-sharing bonds between X and E and a donor–acceptor interaction between the HX bond pair and the empty p orbital on E and the donor–acceptor interaction increases from P to Bi. Apart from the size, charge, and electronegativity differences between the atoms involved in the system (H, X, E), the electronic state of the interacting fragments (HX, HE, E, and X) in the stationary points also influence the nature of the PES of the system.

The heavier homologues of HCN and HNC could be potential targets for spectroscopic characterization and may also be astronomically interesting.

Compounds with Triple Bonds to Sulfur

The nature of the triple-bonding character to sulfur in HCSF, HCSH, HCSOH, F_5SCSF_3, HSiSF, HSiSH, NSF, NSH, NSOH, PSF, PSH, and PSOH was studied. All of the molecules studied have a planar, bent structure. Linear geometries are not minima on the PES. *cis*-HCSF is a potential target with CS triple-bond character, however, *trans*-HCSF is not minimum on the PES. The CS triple-bond character in *cis,cis*-HCSOH is weaker than in *cis*-HCSF. *trans*-HCSH is a carbene with a CS

single bond, however, the $p_{\pi\perp}$ lone-pair electrons on S delocalize toward the empty $p_{\pi\perp}$ orbital on C, giving a 19.3% $\Delta E_{\pi\perp}$ contribution to the total orbital contribution of the CS bond. The SH bond in *trans*-HCSH is covalent in nature and has a higher excitation energy ($^2\Pi \rightarrow {}^4\Sigma^-$) than the SF bond in *cis*-HCSF. The nature of the SiS bond in HSiSF and HSiSH involves a dative σ bond and an electron-sharing π bond, in which the fragments HSi and SF (or SH) interact in their ground electronic states. However, the description of the SiS bond in terms of an electron-sharing σ bond and donor–acceptor π bond is not negligible in HSiSH. The NS and PS bonds in NSF and PSF also have triple-bond character. NSH and PSH have NS and PS electron-sharing σ bonds with significant ΔE_π contributions due to the donor–acceptor interaction between the filled and empty π-type orbitals of N or P and S.

Compounds with Triple Bonds to Uranium, Thorium and Group 4 Transition Metals

Energy decomposition analysis of the complexes $HC{\equiv}UF_3$, $HN{=}UF_3$, $HO\text{-}UF_3$, $E{\equiv}UF_3$, $HC{\div}MF_3$, and $E{\div}MF_3$ (E = N, P, and As; M = Ti, Zr, Hf, and Th), with a triple bond to uranium and triplet triple bonds to thorium and Group 4 metals, was performed. The CU and EU triple bonds are weaker than the CM and EM triple bonds, for E = N to As and M = Cr, Mo, and W. The NU bond in $N{\equiv}UF_3$ is stronger than the NU bond in the model uranium–imido complex $HN{=}UF_3$. The OU bond in $HO\text{-}UF_3$ is more electrostatic in nature with 51.3% π contribution. In the triplet molecules $HC{\div}ThF_3$, $FC{\div}MF_3$, and $E{\div}MF_3$ (E = N, P, and As; M = Ti, Zr, Hf, and Th), the two unpaired electrons in the p orbitals of C and E are shared with the empty d orbitals on the metal (M), leading to two degenerate singly occupied π molecular orbitals. The instantaneous interaction energy, ΔE_{int}, of the C÷M bonds is stronger than that of the E÷M bonds. The percentage π contribution of the E÷M bond increases from N to As, for a metal (M). Calculations suggest that the valence f orbitals of U are involved in bonding with the valence p orbitals of As in $As{\equiv}UF_3$. In contrast, the percentage contribution of the valence f orbital of Th to the E÷Th bonds in $E{\div}ThF_3$ is very small. However, the participation of the valence f orbitals of actinides in chemical bonding needs to be investigated in detail.

7. References

[1] M. Lein, A. Krapp, G. Frenking, *J. Am. Chem. Soc.* **2005**, *127*, 6290.

[2] a)P. P. Power, *Chem. Rev.* **1999**, *99*, 3463; b)R. C. Fischer, P. P. Power, *Chem. Rev.* **2010**, *110*, 3877.

[3] a)L. E. Snyder, D. Buhl, *Astrophys. J.* **1971**, *163*, L47; b)S. Green, P. Thaddeus, *Astrophys. J.* **1974**, *191*, 653; c)W. M. Irvine, F. P. Schloerb, *Astrophys. J.* **1984**, *282*, 516; d)J. Cernicharo, M. J. Barlow, E. GonzalezAlfonso, P. Cox, P. E. Clegg, NguyenQrieu, A. Omont, M. Guelin, X. W. Liu, R. J. Sylvester, T. Lim, M. J. Griffin, B. M. Swinyard, S. J. Unger, P. A. R. Ade, J. P. Baluteau, E. Caux, M. Cohen, R. J. Emery, J. Fischer, I. Furniss, W. M. Glencross, M. A. Greenhouse, C. Gry, M. Joubert, D. Lorenzetti, B. Nisini, R. Orfei, D. Pequignot, P. Saraceno, G. Serra, C. J. Skinner, H. A. Smith, W. A. Towlson, H. J. Walker, C. Armand, M. Burgdorf, D. Ewart, A. DiGiorgio, S. Molinari, M. Price, S. Sidher, D. Texier, N. Trams, *Astron. Astrophys.* **1996**, *315*, L201; e)T. Hirota, S. Yamamoto, H. Mikami, M. Ohishi, *Astrophys. J.* **1998**, *503*, 717.

[4] a)M. Bogey, C. Demuynck, J. L. Destombes, A. Walters, *Astron. Astrophys.* **1991**, *244*, L47; b)G. Maier, J. Glatthaar, *Angew. Chem. Int. Ed.* **1994**, *33*, 473.

[5] a)T. E. Gier, *J. Am. Chem. Soc.* **1961**, *83*, 1769; b)J. K. Tyler, *J. Chem. Phys.* **1964**, *40*, 1170.

[6] V. Lattanzi, S. Thorwirth, D. T. Halfen, L. A. Muck, L. M. Ziurys, P. Thaddeus, J. Gauss, M. C. McCarthy, *Angew. Chem. Int. Ed.* **2010**, *49*, 5661.

[7] D. B. Chesnut, *Chem. Phys.* **2005**, *315*, 59.

[8] E. K. Moltzen, K. J. Klabunde, A. Senning, *Chem. Rev.* **1988**, *88*, 391.

[9] a)B. Pötter, K. Seppelt, *Angew. Chem.* **1984**, *96*, 138; b)B. Poetter, K. Seppelt, A. Simon, E. M. Peters, B. Hettich, *J. Am. Chem. Soc.* **1985**, *107*, 980; c)J. Buschmann, R. Damerius, R. Gerhardt, D. Lentz, P. Luger, R. Marschall, D. Preugschat, K. Seppelt, A. Simon, *J. Am. Chem. Soc.* **1992**, *114*, 9465.

[10] a)R. Gerhardt, T. Grelbig, J. Buschmann, P. Luger, K. Seppelt, *Angew. Chem.* **1988**, *100*, 1592; b)K. Seppelt, *Angew. Chem. Int. Ed.* **1991**, *30*, 361.

[11] P. R. Schreiner, H. P. Reisenauer, J. Romanski, G. Mloston, *Angew. Chem. Int. Ed.* **2009**, *48*, 8133.

[12] D. Bourissou, O. Guerret, F. P. Gabbaï, G. Bertrand, *Chem. Rev.* **1999**, *100*, 39.

[13] E. O. Fischer, G. Kreis, C. G. Kreiter, J. Muller, G. Huttner, H. Lorenz, *Angew. Chem. Int. Ed.* **1973**, *12*, 564.

[14] G. Balazs, L. J. Gregoriades, M. Scheer, *Organometallics* **2007**, *26*, 3058.

[15] J. T. Lyon, H. S. Hu, L. Andrews, J. Li, *Proc. Natl. Acad. Sci.* **2007**, *104*, 18919.

[16] a)L. Andrews, X. F. Wang, R. Lindh, B. O. Roos, C. J. Marsden, *Angew. Chem. Int. Ed.* **2008**, *47*, 5366; b)L. Andrews, X. F. Wang, B. O. Roos, *Inorg. Chem.* **2009**, *48*, 6594.

[17] a)X. Wang, J. T. Lyon, L. Andrews, *Inorg. Chem.* **2009**, *48*, 6297; b)X. F. Wang, L. Andrews, *Dalton Trans.* **2009**, 9260.

[18] a)A. Szabo, N. S. Ostlund, *Modern Quantum Chemisty*, Dover Publications, Mineola, New York, **1996**; b)F. Jensen, *Computational Chemistry*, Wiley, Chichester, **1999**; c)I. N. Levine, *Quantum Chemistry*, Prentice Hall, Engelwoods Cliffs, **1991**; d)C. J. Cramer, *Essentials of Computational Chemistry*, Wiley, Chichester, **2003**.

[19] a)E. Schrodinger, *Ann. Phys.* **1926**, *80*, 437; b)E. Schrodinger, *Ann. Phys.* **1926**, *79*, 489; c)E. Schrodinger, *Ann. Phys.* **1926**, *79*, 734; d)E. Schrodinger, *Ann. Phys.* **1926**, *79*, 361; e)E. Schrodinger, *Ann. Phys.* **1926**, *81*.

[20] M. Born, R. Oppenheimer, *Ann. Phys.* **1927**, *84*, 0457.

[21] W. Pauli, *Z. Phys.* **1925**, *31*, 765.

[22] a)D. R. Hartree, *Proc. Cambridge Phil. Soc.* **1928**, *24*, 426; b)D. R. Hartree, *Proc. Cambridge Phil. Soc.* **1928**, *24*, 111; c)D. R. Hartree, *Proc. Cambridge Phil. Soc.* **1928**, *24*, 89; d)V. Fock, *Z. Phys.* **1930**, *61*, 126.

[23] J. C. Slater, *Phys. Rev.* **1929**, *34*, 1293.

[24] a)G. G. Hall, *Proc. Roy. Soc. A* **1951**, *205*, 541; b)C. C. J. Roothaan, *Rev. Mod. Phys.* **1951**, *23*, 69.

[25] C. Moller, M. S. Plesset, *Phys. Rev.* **1934**, *46*, 0618.

[26] a)R. J. Bartlett, *J. Phys. Chem.* **1989**, *93*, 1697; b)J. Cizek, *Adv. Chem. Phys.* **1969**, *15*, 35.

[27] E. Fermi, *Rend. Accad. Naz. Lincei.* **1927**, *6*, 602.

[28] L. H. Thomas, *Proc. Cambridge Phil. Soc.* **1927**, *23*, 542.

[29] P. Hohenberg, W. Kohn, *Phys. Rev. B* **1964**, *136*, B864.

[30] W. Kohn, L. J. Sham, *Phys. Rev.* **1965**, *140*, 1133.

[31] P. A. M. Dirac, *Proc. Cambridge Phil. Soc.* **1930**, *26*, 376.

[32] J. C. Slater, *Phys. Rev.* **1951**, *81*, 385.

[33] S. H. Vosko, L. Wilk, M. Nusair, *Can. J. Phys.* **1980**, *58*, 1200.

[34] J. P. Perdew, A. Zunger, *Phys. Rev. B* **1981**, *23*, 5048.

[35] S. F. Sousa, P. A. Fernandes, M. J. Ramos, *J. Phys. Chem. A* **2007**, *111*, 10439.

[36] A. D. Becke, *Phys. Rev. A* **1988**, *38*, 3098.

[37] J. P. Perdew, W. Yue, *Phys. Rev. B* **1986**, *33*, 8800.

[38] C. Adamo, V. Barone, *J. Chem. Phys.* **1998**, *108*, 664.

[39] A. D. Becke, *J. Chem. Phys.* **1986**, *84*, 4524.

[40] J. P. Perdew, *Phys. Rev. B* **1986**, *33*, 8822.

[41] J. P. Perdew, K. Burke, M. Ernzerhof, *Phys. Rev. Lett.* **1996**, *77*, 3865.

[42] C. Adamo, V. Barone, *J. Chem. Phys.* **2002**, *116*, 5933.

[43] A. D. Becke, *J. Chem. Phys.* **1988**, *88*, 1053.

[44] C. Lee, W. Yang, R. G. Parr, *Phys. Rev. B* **1988**, *37*, 785.

[45] A. D. Becke, *J. Chem. Phys.* **1996**, *104*, 1040.

[46] J. Tao, J. P. Perdew, V. N. Staroverov, G. E. Scuseria, *Phys. Rev. Lett.* **2003**, *91*, 146401.

[47] T. Van Voorhis, G. E. Scuseria, *J. Chem. Phys.* **1998**, *109*, 400.

[48] Y. Zhao, N. E. Schultz, D. G. Truhlar, *J. Chem. Theory Comput.* **2006**, *2*, 364.

[49] Y. Zhao, D. G. Truhlar, *Theor. Chem. Acc.* **2008**, *120*, 215.

[50] J. C. Slater, *Phys. Rev.* **1930**, *36*, 0057.

[51] S. F. Boys, *Proc. Roy. Soc. A* **1950**, *200*, 542.

[52] W. J. Hehre, R. F. Stewart, J. A. Pople, *J. Chem. Phys.* **1969**, *51*, 2657.

[53] J. C. Phillips, L. Kleinman, *Phys. Rev.* **1959**, *116*, 287.

[54] H. Hellmann, *J. Chem. Phys.* **1935**, *3*, 61.

[55] a)V. Bonifacic, S. Huzinaga, *J. Chem. Phys.* **1976**, *65*, 2322; b)V. Bonifacic, S. Huzinaga, *J. Chem. Phys.* **1976**, *64*, 956.

[56] A. Bergner, M. Dolg, W. Kuchle, H. Stoll, H. Preuss, *Mol. Phys.* **1993**, *80*, 1431.

[57] P. Schwerdtfeger, T. Fischer, M. Dolg, G. Igelmann, A. Nicklass, H. Stoll, A. Haaland, *J. Chem. Phys.* **1995**, *102*, 2050.

[58] W. C. Davidon, *SIAM J. Optim.* **1991**, *1*, 1.

[59] A. E. Reed, L. A. Curtiss, F. Weinhold, *Chem. Rev.* **1988**, *88*, 899.

[60] P. O. Lowdin, *Phys. Rev.* **1955**, *97*, 1474.

[61] a)K. B. Wiberg, *Tetrahedron* **1968**, *24*, 1083; b)L. Pauling, L. O. Brockway, J. Y. Beach, *J. Am. Chem. Soc.* **1935**, *57*, 2705.

[62] a)M. Lein, G. Frenking, in *Theory and Applications of Computational Chemistry* (Eds.: E. D. Clifford, F. Gernot, S. K. Kwang, E. S. Gustavo), Elsevier, Amsterdam, **2005**, pp. 291; b)G. Frenking, K. Wichmann, N. Frohlich, C. Loschen, M. Lein, J. Frunzke, V. M. Rayon, *Coord. Chem. Rev.* **2003**, *238*, 55.

[63] K. Morokuma, *J. Chem. Phys.* **1971**, *55*, 1236.

[64] a)T. Ziegler, A. Rauk, *Inorg. Chem.* **1979**, *18*, 1755; b)T. Ziegler, A. Rauk, *Inorg. Chem.* **1979**, *18*, 1558.

[65] M. P. Mitoraj, A. Michalak, T. Ziegler, *J. Chem. Theory Comput.* **2009**, *5*, 962.

[66] a)M. Mitoraj, A. Michalak, *J. Mol. Model.* **2008**, *14*, 681; b)A. Michalak, M. Mitoraj, T. Ziegler, *J. Phys. Chem. A* **2008**, *112*, 1933; c)M. Mitoraj, A. Michalak, *Organometallics* **2007**, *26*, 6576.

[67] a)R. F. W. Bader, *Acc. Chem. Res.* **1985**, *18*, 9; b)R. F. W. Bader, *Chem. Rev.* **1991**, *91*, 893.

[68] a)O. Kwon, Y. Kwon, *J. Mol. Struc-Theochem* **1999**, *460*, 213; b)M. C. Lind, F. C. Pickard, J. B. Ingels, A. Paul, Y. Yamaguchi, H. F. Schaefer, *J. Chem. Phys.* **2009**, *130*.

[69] a)J. C. T. R. B. S. Laurent, T. A. Cooper, H. W. Kroto, J. F. Nixon, O. Ohashi, K. Ohno, *J. Mol. Struct.* **1982**, *79*, 215; b)A. M. Arif, A. R. Barron, A. H. Cowley, S. W. Hall, *J. Chem. Soc., Chem. Commun.* **1988**, 171.

[70] F. Weigend, R. Ahlrichs, *Phys. Chem. Chem. Phys.* **2005**, *7*, 3297.

[71] J. G. Snijders, E. J. Baerends, P. Vernoojs, *At. Data. Nucl. Data Tables* **1982**, *26*, 483.

[72] J. Krijn, E. J. Baerends, Fit Functions in the HFS-Method, Internal Report (in Dutch), Vrije Universiteit Amsterdam, The Netherlands, **1984**.

[73] a)E. Vanlenthe, E. J. Baerends, J. G. Snijders, *J. Chem. Phys.* **1993**, *99*, 4597; b)E. Vanlenthe, E. J. Baerends, J. G. Snijders, *J. Chem. Phys.* **1994**, *101*, 9783; c)E. van Lenthe, A. Ehlers, E. J. Baerends, *J. Chem. Phys.* **1999**, *110*, 8943.

[74] H.-J. Werner, P. J. Knowles, R. Lindh, F. R. Manby, M. Schütz, MOLPRO, version 2009.1, a package of ab initio programs; see http://www.molpro.net.

[75] G. te Velde, F. M. Bickelhaupt, E. J. Baerends, C. Fonseca Guerra, S. J. A. van Gisbergen, J. G. Snijders, T. Ziegler, *J. Comput. Chem.* **2001**, *22*, 931.

[76] G. W. T. M. J. Frisch, H. B. Schlegel, G. E. Scuseria, M. A. Robb, J. R. Cheeseman, G. Scalmani, V. Barone, B. Mennucci, G. A. Petersson, H. Nakatsuji, M. Caricato, X. Li, H. P. Hratchian, A. F. Izmaylov, J. Bloino, G. Zheng, J. L. Sonnenberg, M. Hada, M. Ehara, K. Toyota, R. Fukuda, J. Hasegawa, M. Ishida, T. Nakajima, Y. Honda, O. Kitao, H. Nakai, T. Vreven, J. A. Montgomery, Jr., J. E. Peralta, F. Ogliaro, M. Bearpark, J. J. Heyd, E. Brothers, K. N. Kudin, V. N. Staroverov, R. Kobayashi, J. Normand, K. Raghavachari, A. Rendell, J. C. Burant, S. S. Iyengar, J. Tomasi, M. Cossi, N. Rega, J. M. Millam, M. Klene, J. E. Knox, J. B. Cross, V. Bakken, C. Adamo, J. Jaramillo, R. Gomperts, R. E. Stratmann, O. Yazyev, A. J. Austin, R. Cammi, C. Pomelli, J. W. Ochterski, R. L. Martin, K. Morokuma, V. G. Zakrzewski, G. A. Voth, P. Salvador, J. J. Dannenberg, S. Dapprich, A. D. Daniels, Ö. Farkas, J. B. Foresman, J. V. Ortiz, J. Cioslowski, and D. J. Fox, Gaussian 09, Revision A.02.

[77] R. F. W. Bader, *Atoms in Molecules:A Quantum Theory*, Oxford University Press, Oxford, **1990**.

[78] AIMPAC, http://www.chemistry.mcmaster.ca/aimpac.

[79] a)G. Kleemann, K. Seppelt, *Angew. Chem.* **1978**, *90*, 547; b)B. Potter, G. Kleemann, K. Seppelt, *Chem. Ber.* **1984**, *117*, 3255; c)I. Weiss, H. Oberhammer, R. Gerhardt, K. Seppelt, *J. Am. Chem. Soc.* **1990**, *112*, 6839; d)J. P. Pique, J. Manners, G. Sitja, M. Joyeux, *J. Chem. Phys.* **1992**, *96*, 6495; e)P. O. Tchir, R. D. Spratley, *Can. J. Chem.* **1975**, *53*, 2318; f)P. O. Tchir, R. D. Spratley, *Can. J. Chem.* **1975**, *53*, 2331; g)P. V. Bharatam, Amita, D. Kaur, *J. Phys. Org. Chem.* **2003**, *16*, 183; h)P. V. Bharatam, A. Kumar, P. S. Kumar, *Bull. Chem. Soc. Jpn.* **2003**, *76*, 1911.

[80] H. S. Rzepa, *J. Chem. Theory Comput.* **2011**, *7*, 97.

[81] T. Wong, J. K. Terlouw, H. Keck, W. Kuchen, P. Tommes, *J. Am. Chem. Soc.* **1992**, *114*, 8208.

[82] T. R. Cundari, M. S. Gordon, *J. Am. Chem. Soc.* **1991**, *113*, 5231.

[83] a)T. Kudo, S. Nagase, *J. Am. Chem. Soc.* **1985**, *107*, 2589; b)L. Nyulaszi, A. Belghazi, S. K. Szetsi, T. Veszpremi, J. Heinicke, *J. Mol. Struc-Theochem* **1994**, *119*, 73;

[84] a)J. Olah, T. Veszpremi, *J. Organomet. Chem.* **2003**, *686*, 112; b)J. Olah, F. De Proft, T. Veszpremi, P. Geerlings, *J. Phys. Chem. A* **2005**, *109*, 1608.

[85] M. T. Nguyen, *Chem. Phys.* **1987**, *117*, 91.

[86] a)R. A. Andersen, *Abstr. Pap. Am. Chem. S.* **1985**, *190*, 329; b)C. R. Graves, P. Yang, S. A. Kozimor, A. E. Vaughn, D. L. Clark, S. D. Conradson, E. J. Schelter, B. L. Scott, J. D. Thompson, P. J. Hay, D. E. Morris, J. L. Kiplinger, *J. Am. Chem. Soc.* **2008**, *130*, 5272; c)R. E. Cramer, F. Edelmann, A. L. Mori, S. Roth, J. W. Gilje, K. Tatsumi, A. Nakamura, *Organometallics* **1988**, *7*, 841; d)J. G. Brennan, R. A. Andersen, *J. Am. Chem. Soc.* **1985**, *107*, 514.

[87] R. K. Thomson, T. Cantat, B. L. Scott, D. E. Morris, E. R. Batista, J. L. Kiplinger, *Nat. Chem.* **2010**, *2*, 723.

[88] R. K. Thomson, C. R. Graves, B. L. Scott, J. L. Kiplinger, *Eur. J. Inorg. Chem.* **2009**, 1451.

[89] S. J. Kraft, J. Walensky, P. E. Fanwick, M. B. Hall, S. C. Bart, *Inorg. Chem.* **2010**, *49*, 7620.

[90] J. T. Lyon, L. Andrews, *Inorg. Chem.* **2006**, *45*, 9858.

[91] R. Ahlrichs, M. Bär, M. Häser, H. Horn, C. Kölmel, *Chem. Phys. Lett.* **1989**, *162*, 165.

[92] a)K. Eichkorn, O. Treutler, H. Öhm, M. Häser, R. Ahlrichs, *Chem. Phys. Lett.* **1995**, *242*, 652; b)F. Weigend, *Phys. Chem. Chem. Phys.* **2006**, *8*, 1057.

[93] K. K. Pandey, G. Frenking, *Eur. J. Inorg. Chem.* **2004**, 4388.

[94] A. J. Bridgeman, G. Cavigliasso, L. R. Ireland, J. Rothery, *J. Chem. Soc., Dalton Trans.* **2001**, 2095.

[95] M. Barnes, A. J. Merer, G. F. Metha, *J. Mol. Spectrosc.* **1997**, *181*, 168.

[96] T. M. Dunn, L. K. Hanson, K. A. Rubinson, *Can. J. Phys.* **1970**, *48*, 1657.

Appendix

Heavier Homologues of HCN-HNC

Compounds with Triple bonds to Sulfur

Compounds with Triple Bonds to Uranium, Thorium, and Group 4 metals

Heavier Homologues of HCN-HNC: Coordinates (in Å) of the optimized geometries at the CCSD(T)/TZVPP level of theory, total energies (*E*) in a.u, and the frequencies in cm^{-1}.

lin-HEN	TS (*lin*-HEN → *lin*-HNE)	*lin*-HNE
lin-HCN *E* = -93.27773446	TS *E* = -93.20169001	*lin*-HNC *E* = -93.20169001
C 0.000000000 0.000000000 -1.348169013	N 0.001938823 -0.022575552 1.701979127	N 0.000000000 0.000000000 1.677821577
H 0.000000000 0.000000000 -0.280186780	C -0.002163526 0.025193732 0.509573055	C 0.000000000 0.000000000 0.503299290
N 0.000000000 0.000000000 -2.507684520	H -0.097190304 1.131713905 0.924682055	H 0.000000000 0.000000000 2.674781500
1 718.83 in plane bending	1 -1196.33 Imaginary frequency	1 466.06 in plane bending
2 718.83 out of plane bending		2 466.06 out of plane bending
3 2114.08 (E-N) stretching		3 2047.70 (N-E) stretching
4 3436.29 (H-E) stretching		4 3818.83 (H-N) stretching
lin-HSiN *E* = -344.19908337	TS *E* = -344.18098153	*lin*-HNSi *E* = -344.30665385
Si 0.000000000 0.000000000 -1.083321077	N 2.125909902 0.171674413 0.000000000	N 0.000000000 0.000000000 1.744237523
H 0.000000000 0.000000000 0.402833296	Si 0.508239213 0.040811887 0.000000000	Si 0.000000000 0.000000000 0.185049546
N 0.000000000 0.000000000 -2.669619472	H 0.542017125 1.554942833 0.000000000	H 0.000000000 0.000000000 2.744713284
1 64.10 in plane bending	1 -803.52 Imaginary frequency	1 538.17 in plane bending
2 64.10 out of plane bending		2 538.17 out of plane bending
3 1148.43 (E-N) stretching		3 1205.94 (N-E) stretching
4 2191.02 (H-E) stretching		4 3750.96 (H-N) stretching
lin-HGeN *E* = -2130.62073262	TS *E* = -2130.59586174	*lin*-HNGe *E* = -2130.72399734
Ge 0.000000000 0.000000000 -1.023601610	N -1.426455656 -0.045783173 0.000000000	N 0.000000000 0.000000000 1.739036536
H 0.000000000 0.000000000 0.512262689	Ge 0.306826529 0.049255267 0.000000000	Ge 0.000000000 0.000000000 0.067015725
N 0.000000000 0.000000000 -2.697148321	H 0.176068056 -1.537354210 0.000000000	H 0.000000000 0.000000000 2.742837082
1 270.84 in plane bending	1 -789.64 Imaginary frequency	1 411.58 in plane bending
2 270.84 out of plane bending		2 411.58 out of plane bending
3 973.90 (E-N) stretching		3 975.82 (N-E) stretching
4 2105.38 (H-E) stretching		4 3705.92 (H-N) stretching
lin-HSnN *E* = -268.57842163	TS *E* = -268.54995425	*lin*-HNSn *E* = -268.68951501
Sn 0.000000000 0.000000000 -0.990564925	N 0.002108036 -0.024543485 2.411623659	N 0.000000000 0.000000000 1.898111799
H 0.000000000 0.000000000 0.719608851	Sn 0.001678907 -0.019553571 0.446140869	Sn 0.000000000 0.000000000 0.013599231
N 0.000000000 0.000000000 -2.870580164	H -0.147941955 1.722684183 0.766091746	H 0.000000000 0.000000000 2.905949334
1 243.43 in plane bending	1 -721.08 Imaginary frequency	1 332.39 in plane bending
2 243.43 out of plane bending		2 332.39 out of plane bending
3 795.05 (E-N) stretching		3 814.47 (N-E) stretching
4 1858.16 (H-E) stretching		4 3651.84 (H-N) stretching
lin-HPbN *E* = -247.02703467	TS *E* = -246.99239651	*lin*-HNPb *E* = -247.14097664
Pb 0.000000000 0.000000000 -0.973341835	N -1.961641200 0.002935777 0.000000000	N 0.000000000 0.000000000 1.988425884
H 0.000000000 0.000000000 0.778582246	Pb 0.179426479 -0.009509988 0.000000000	Pb 0.000000000 0.000000000 -0.042276491
N 0.000000000 0.000000000 -2.940685648	H 0.073993592 1.841065349 0.000000000	H 0.000000000 0.000000000 3.009720981
1 380.41 in plane bending	1 -513.28 Imaginary frequency	1 248.57 in plane bending
2 380.41 out of plane bending		2 248.57 out of plane bending
3 655.65 (E-N) stretching		3 656.19 (N-E) stretching
4 1719.71 (H-E) stretching		4 3587.49 (H-N) stretching

lin-HEP	TS (lin-HEP → bent-HPE)	*bent*-HPE	*lin*-HPE
lin-HCP *E* = -379.48152010 C 0.000000000 0.000000000 -1.199708097 H 0.000000000 0.000000000 -0.126914831 P 0.000000000 0.000000000 -2.748544380	-	-	*lin*-HPC P 0.000000000 0.000000000 1.936710325 C 0.000000000 0.000000000 0.315547582 H 0.000000000 0.000000000 3.359975517
1 694.45 in plane bending 2 694.45 out of plane bending 3 1290.81 (E-P) stretching 4 3346.95 (H-E) stretching			1 -348.81 Imaginary frequency 2 -348.81 Imaginary frequency 3 1117.04 (P-E) stretching 4 2306.45 (H-P) stretching
lin-HSiP *E* = -630.48386466 Si 0.000000000 0.000000000 -0.929391203 H 0.000000000 0.000000000 0.550196227 P 0.000000000 0.000000000 -2.902564272	TS *E* = -630.46085157 P 0.017836383 -0.998881125 0.000000000 Si 0.062284807 1.046871440 0.000000000 H -1.459002294 0.940395760 0.000000000	*bent*-HPSi *E* = -630.50023324 P -2.071301922 0.006147770 0.000000000 Si -0.009206152 -0.005775460 0.000000000 H -1.336574184 -1.289913407 0.000000000	*lin*-HPSi *E* = -630.48155699 P 0.000000000 0.000000000 2.034502837 Si 0.000000000 0.000000000 0.029477405 H 0.000000000 0.000000000 3.438581174
1 247.25 in plane bending 2 247.25 out of plane bending 3 714.69 (E-P) stretching 4 2244.59 (H-E) stretching	1 -745.14 Imaginary frequency	1 637.24 (P-E) stretching 2 776.67 H wagging from P to E 3 2018.00 H wagging toward P	1 -282.28 Imaginary frequency 2 -282.28 Imaginary frequency 3 669.57 (P-E) stretching 4 2469.36 (H-P) stretching
lin-HGeP *E* = -2416.91963109 Ge 0.000000000 0.000000000 -0.943814081 H 0.000000000 0.000000000 0.589159421 P 0.000000000 0.000000000 -2.979635592	TS *E* = -2416.89457727 P -0.006474479 1.435650905 0.000000000 Ge 0.057221407 -0.695889547 0.000000000 H -1.537295040 -0.602776347 0.000000000	*bent*-HPGe *E* = -2416.94412675 P -1.041768362 0.017214136 0.000000000 Ge 1.114374809 0.016994428 0.000000000 H -0.451039477 -1.328454662 0.000000000	*lin*-HPGe *E* = -2416.92682286 P 0.000000000 0.000000000 -0.503367491 Ge 0.000000000 0.000000000 1.587984391 H 0.000000000 0.000000000 -1.909727963
1 278.46 in plane bending 2 278.46 out of plane bending 3 572.91 (E-P) stretching 4 2146.06 (H-E) stretching	1 -700.80 Imaginary frequency	1 470.14 (P-E) stretching 2 569.91 H wagging from P to E 3 2114.10 H wagging toward P	1 -278.73 Imaginary frequency 2 -278.73 Imaginary frequency 3 515.40 (P-E) stretching 4 2453.23 (H-P) stretching
lin-HSnP *E* = -554.89120533 Sn 0.000000000 0.000000000 -0.921079264 H 0.000000000 0.000000000 0.783633587 P 0.000000000 0.000000000 -3.146430571	TS *E* = -554.86712026 P -0.010752248 1.786663837 0.000000000 Sn 0.047381377 -0.560598254 0.000000000 H -1.727918257 -0.424710523 0.000000000	*bent*-HPSn *E* = -554.93371316 P -1.202548238 0.007019738 0.000000000 Sn 1.163471930 0.036451305 0.000000000 H -0.829214758 -1.391880144 0.000000000	*lin*-HPSn *E* = -554.91756476 P 0.000000000 0.000000000 -0.656619574 Sn 0.000000000 0.000000000 1.627648359 H 0.000000000 0.000000000 -2.063127869
1 235.08 in plane bending 2 235.08 out of plane bending 3 480.10 (E-P) stretching 4 1918.23 (H-E) stretching	1 -616.59 Imaginary frequency	1 354.97 (P-E) stretching 2 444.94 H wagging from P to E 3 2221.66 H wagging toward P	1 -285.28 Imaginary frequency 2 -285.28 Imaginary frequency 3 430.69 (P-E) stretching 4 2454.84 (H-P) stretching
lin-HPbP *E* = -533.35059096 Pb 0.000000000 0.000000000 -0.938281435 H 0.000000000 0.000000000 0.812182147 P 0.000000000 0.000000000 -3.217182964	TS *E* = -533.32764799 P -0.011051470 2.050901905 0.000000000 Pb 0.037373941 -0.401271300 0.000000000 H -1.813998605 -0.461633515 0.000000000	*bent*-HPPb *E* = -533.40869798 P -1.301183984 0.002620032 0.000000000 Pb 1.159204123 0.039757552 0.000000000 H -1.021721227 -1.411100687 0.000000000	*lin*-HPPb *E* = -533.39297812 P 0.000000000 0.000000000 -0.744527239 Pb 0.000000000 0.000000000 1.628964364 H 0.000000000 0.000000000 -2.153537221
1 298.24 in plane bending 2 298.24 out of plane bending 3 438.48 (E-P) stretching 4 1805.92 (H-E) stretching	1 -460.65 Imaginary frequency	1 338.77 (P-E) stretching 2 431.40 H wagging from P to E 3 2259.39 H wagging toward P	1 -261.02 Imaginary frequency 2 -261.02 Imaginary frequency 3 381.76 (P-E) stretching 4 2441.35 (H-P) stretching

lin-HEAs	TS	*bent*-HAsE	*lin*-HAsE
lin-HCAs *E* = -2272.91026568			*lin*-HAsC *E* = -2272.78711673
C 0.000000000 0.000000000 -1.146291519			As 0.000000000 0.000000000 2.008311518
H 0.000000000 0.000000000 -0.070885457	-	-	C 0.000000000 0.000000000 0.276553042
As 0.000000000 0.000000000 -2.815702329			H 0.000000000 0.000000000 3.531671880
1 636.90 in plane bending			1 -219.59 Imaginary frequency
2 636.90 out of plane bending			2 -219.59 Imaginary frequency
3 1060.29 (E-As) stretching			3 933.83 (As-E) stretching
4 3314.64 (H-E) stretching			4 2089.71 (H-As) stretching
lin-HSiAs *E* = -2523.93727477	TS *E* = -2523.91623554	*bent*-HAsSi *E* = -2523.94482115	*lin*-HAsSi *E* = -2523.92245392
Si 0.000000000 0.000000000 -0.827847391	As 0.013732328 -1.026802306 0.000000000	As -1.005779380 0.027828682 0.000000000	As 0.000000000 0.000000000 2.063038974
H 0.000000000 0.000000000 0.653447872	Si 0.062218654 1.130388781 0.000000000	Si 1.167776214 0.003882738 0.000000000	Si 0.000000000 0.000000000 -0.038036065
As 0.000000000 0.000000000 -2.906590714	H -1.460925087 1.017187610 0.000000000	H -0.066953827 -1.301582516 0.000000000	H 0.000000000 0.000000000 3.565078513
1 221.47 in plane bending	1 -712.62 Imaginary frequency	1 506.39 (As-E) stretching	1 -215.61 Imaginary frequency
2 221.47 out of plane bending		2 878.66 H wagging from As to E	2 -215.61 Imaginary frequency
3 561.90 (E-As) stretching		3 1756.99 H wagging toward As	3 536.12 (As-E) stretching
4 2232.52 (H-E) stretching			4 2258.28 (H-As) stretching
lin-HGeAs *E* = -4310.37554364	TS *E* = -4310.35303134	*bent*-HAsGe *E* = -4310.39065522	*lin*-HAsGe *E* = -4310.37035343
Ge 0.000000000 0.000000000 -0.856792164	As 0.005202480 -1.084147601 0.000000000	As -1.076035109 0.025648974 0.000000000	As 0.000000000 0.000000000 2.112601749
H 0.000000000 0.000000000 0.679509749	Ge 0.078546118 1.153439392 0.000000000	Ge 1.184829791 0.010348711 0.000000000	Ge 0.000000000 0.000000000 -0.070841653
As 0.000000000 0.000000000 -2.993609824	H -1.518168706 1.072029295 0.000000000	H -0.253513693 -1.352971785 0.000000000	H 0.000000000 0.000000000 3.618428332
1 264.96 in plane bending	1 -669.56 Imaginary frequency	1 355.03 (As-E) stretching	1 -230.04 Imaginary frequency
2 264.97 out of plane bending		2 659.45 H wagging from As to E	2 -230.04 Imaginary frequency
3 412.05 (E-As) stretching		3 1832.12 H wagging toward As	3 376.21 (As-E) stretching
4 2132.39 (H-E) stretching			4 2239.50 (H-As) stretching
lin-HSnAs *E* = -2448.35158482	TS *E* = -2448.33002685	*bent*-HAsSn *E* = -2448.38300530	*lin*-HAsSn *E* = -2448.36447632
	As 0.014551018 -1.240693197 0.000000000	As -1.210477925 0.020370274 0.000000000	As 0.000000000 0.000000000 2.241028059
Sn 0.000000000 0.000000000 -0.818282144	Sn 0.072557918 1.205660875 0.000000000	Sn 1.250203099 0.029565056 0.000000000	Sn 0.000000000 0.000000000 -0.131301213
H 0.000000000 0.000000000 0.890023339	H -1.704390059 1.089298402 0.000000000	H -0.582210215 -1.426494434 0.000000000	H 0.000000000 0.000000000 3.748151596
As 0.000000000 0.000000000 -3.140048427			
1 217.50 in plane bending	1 -574.39 Imaginary frequency	1 279.66 (As-E) stretching	1 -243.51 Imaginary frequency
2 217.50 out of plane bending		2 434.68 H wagging from As to E	2 -243.51 Imaginary frequency
3 332.91 (E-As) stretching		3 1936.38 H wagging toward As	3 302.01 (As-E) stretching
4 1909.37 (H-E) stretching			4 2238.53 (H-As) stretching
lin-HPbAs *E* = -2426.81227531	TS *E* = -2426.79279628	*bent*-HAsPb *E* = -2426.85957474	*lin*-HAsPb *E* = -2426.84187443
Pb 0.000000000 0.000000000 -0.856089190	As 0.022367055 -1.361610195 0.000000000	As -1.311300196 0.014555361 0.000000000	As 0.000000000 0.000000000 2.337824720
H 0.000000000 0.000000000 0.901835629	Pb 0.071245007 1.183291319 0.000000000	Pb 1.241620890 0.046894315 0.000000000	Pb 0.000000000 0.000000000 -0.120315733
As 0.000000000 0.000000000 -3.231544681	H -1.776042190 1.294676960 0.000000000	H -0.817406760 -1.467987783 0.000000000	H 0.000000000 0.000000000 3.848373472
1 268.62 in plane bending	1 -424.22 Imaginary frequency	1 235.86 (As-E) stretching	1 -223.75 Imaginary frequency
2 268.63 out of plane bending		2 387.60 H wagging from As to E	2 -223.74 Imaginary frequency
3 292.46 (E-As) stretching		3 2000.95 H wagging toward As	3 258.08 (As-E) stretching
4 1787.95 (H-E) stretching			4 2227.34 (H-As) stretching

lin-HESb	TS	*bent*-HSbE	*lin*-HSbE
lin-HCSb *E* = -277.93668906			*lin*-HSbC *E* = -277.81369999
C 0.000000000 0.000000000 -0.971457757			Sb 0.000000000 0.000000000 2.039646990
H 0.000000000 0.000000000 0.107677291	-	-	C 0.000000000 0.000000000 0.102765536
Sb 0.000000000 0.000000000 -2.847522815			H 0.000000000 0.000000000 3.753778920
1 559.05 in plane bending			1 - 28.77 Imaginary frequency
2 559.05 out of plane bending			2 -28.77 Imaginary frequency
3 883.34 (E-Sb) stretching			3 776.41 (Sb-E) stretching
4 3268.21 (H-E) stretching			4 1822.44 (H-Sb) stretching
lin-HSiSb *E* = -528.98768444	TS *E* = -528.96883953	*bent*-HSbSi *E* = -528.98618144	*lin*-HSbSi *E* = -528.95678060
Si 0.000000000 0.000000000 -0.649342228	Si -0.009128029 -0.606084932 0.000000000	Sb -1.289548456 1.630268790 0.000000000	Sb 0.000000000 0.000000000 2.095332637
H 0.000000000 0.000000000 0.833296873	H 0.810614946 0.687697499 0.000000000	Si 1.077519034 1.927891526 0.000000000	Si 0.000000000 0.000000000 -0.208591134
Sb 0.000000000 0.000000000 -2.924436853	Sb 2.116013303 -1.657049687 0.000000000	H -0.175429608 3.120836190 0.000000000	H 0.000000000 0.000000000 3.783812926
1 213.62 in plane bending	1 -640.68 Imaginary frequency	1 419.95 (Sb-E) stretching	1 -186.81 Imaginary frequency
2 213.62 out of plane bending		2 1030.10 H wagging from Sb to E	2 -186.81 Imaginary frequency
3 469.97 (E-Sb) stretching		3 1480.24 H wagging toward Sb	3 443.05 (Sb-E) stretching
4 2225.95 (H-E) stretching			4 1978.47 (H-Sb) stretching
lin-HGeSb *E* = -2315.42916993	TS *E* = -2315.41034098	*bent*-HSbGe *E* = -2315.43492479	*lin*-HSbGe *E* = -2315.40942896
Ge 0.000000000 0.000000000 -0.706939201	Ge -0.056362629 -0.612674637 0.000000000	Sb -1.383494813 1.620558395 0.000000000	Sb 0.000000000 0.000000000 2.170693376
H 0.000000000 0.000000000 0.833626933	H 0.731867400 0.781703936 0.000000000	Ge 1.060305466 1.917710891 0.000000000	Ge 0.000000000 0.000000000 -0.207945773
Sb 0.000000000 0.000000000 -3.034142952	Sb 2.153600443 -1.653861411 0.000000000	H -0.360740704 3.146960220 0.000000000	H 0.000000000 0.000000000 3.862437838
1 235.96 in plane bending	1 -591.12 Imaginary frequency	1 285.65 (Sb-E) stretching	1 -198.98 Imaginary frequency
2 235.96 out of plane bending		2 852.35 H wagging from Sb to E	2 -198.98 Imaginary frequency
3 330.03 (E-Sb) stretching		3 1515.10 H wagging toward Sb	3 299.90 (Sb-E) stretching
4 2115.92 (H-E) stretching			4 1970.27 (H-Sb) stretching
lin-HSnSb *E* = -453.41004304	TS *E* = -453.39262280	*bent*-HSbSn *E* = -453.42994781	*lin*-HSbSn *E* = -453.40763671
Sn 0.000000000 0.000000000 -0.670845380	Sn -0.114383343 -0.571520299 0.000000000	Sb -1.520595683 1.608678100 0.000000000	Sb 0.000000000 0.000000000 2.298248290
H 0.000000000 0.000000000 1.042184793	H 0.758927504 0.980059148 0.000000000	Sn 1.114599983 1.913479887 0.000000000	Sn 0.000000000 0.000000000 -0.265666979
Sb 0.000000000 0.000000000 -3.178687625	Sb 2.265727059 -1.731826949 0.000000000	H -0.644294379 3.188875521 0.000000000	H 0.000000000 0.000000000 3.991187145
1 190.16 in plane bending	1 -500.13 Imaginary frequency	1 225.16 (Sb-E) stretching	1 -215.08 Imaginary frequency
2 190.16 out of plane bending		2 619.43 H wagging from Sb to E	2 -215.08 Imaginary frequency
3 260.54 (E-Sb) stretching		3 1588.42 H wagging toward Sb	3 234.79 (Sb-E) stretching
4 1897.76 (H-E) stretching			4 1973.18 (H-Sb) stretching
lin-HPbSb *E* = -431.87300460	TS *E* = -431.85904601	*bent*-HSbPb *E* = -431.90851128	*lin*-HSbPb *E* = -431.88822783
Pb 0.000000000 0.000000000 -0.734902865	Pb -0.102733135 -0.584225206 0.000000000	Sb -1.642133649 1.597468789 0.000000000	Sb 0.000000000 0.000000000 2.412031327
H 0.000000000 0.000000000 1.033094481	H 0.515643360 1.155511485 0.000000000	Pb 1.077756143 1.893887524 0.000000000	Pb 0.000000000 0.000000000 -0.229846698
Sb 0.000000000 0.000000000 -3.295472842	Sb 2.355455985 -1.781093370 0.000000000	H -0.887501603 3.216783194 0.000000000	H 0.000000000 0.000000000 4.107785847
1 228.99 in plane bending	1 -353.48 Imaginary frequency	1 187.76 (Sb-E) stretching	1 -208.69 Imaginary frequency
2 228.99 out of plane bending		2 486.82 H wagging from Sb to E	2 -208.69 Imaginary frequency
3 222.82 (E-Sb) stretching		3 1658.07 H wagging toward Sb	3 196.81 (Sb-E) stretching
4 1765.87 (H-E) stretching			4 1970.48 (H-Sb) stretching

lin-HEBi	TS	*bent*-HBiE	*lin*-HBiE
lin-HCBi *E* = -252.21602824 C 0.000000000 0.000000000 -0.885835098 H 0.000000000 0.000000000 0.196441524 Bi 0.000000000 0.000000000 -2.855922694	-	-	*lin*-HBiC *E* = -252.09101531 Bi 0.000000000 0.000000000 2.050940994 C 0.000000000 0.000000000 0.042161042 H 0.000000000 0.000000000 3.845059413
1 506.24 in plane bending 2 506.24 out of plane bending 3 786.47 (E-Bi) stretching 4 3231.72 (H-E) stretching			1 166.85 in plane bending 2 166.85 out of plane bending 3 704.57 (Bi-E) stretching 4 1642.46 (H-Bi) stretching
lin-HSiBi *E* = -503.28042008 Si 0.000000000 0.000000000 -0.548139884 H 0.000000000 0.000000000 0.937424768 Bi 0.000000000 0.000000000 -2.903435073	TS *E* = -503.26309641 Bi 0.291549778 0.032176378 0.000000000 Si -1.032477109 -2.034583248 0.000000000 H 0.333963300 -2.726649487 0.000000000	*bent*-HBiSi *E* = -503.27550298 Bi -1.022440987 0.029243409 0.000000000 Si 1.449809701 -0.008144870 0.000000000 H 0.406935349 -1.343416638 0.000000000	*lin*-HBiSi *E* = -503.23740776 Bi 0.000000000 0.000000000 2.087289957 Si 0.000000000 0.000000000 -0.277789418 H 0.000000000 0.000000000 3.851068888
1 218.61 in plane bending 2 218.61 out of plane bending 3 421.95 (E-Bi) stretching 4 2210.25 (H-E) stretching	1 598.97 Imaginary frequency	1 375.57 (Bi-E) stretching 2 1042.18 H wagging from Bi to E 3 1415.15 H wagging toward theBi-E bond	1 -141.59 Imaginary frequency 2 -141.59 Imaginary frequency 3 400.47 (Bi-E) stretching 4 1805.96 (H-Bi) stretching
lin-HGeBi *E* = -2289.72301577 Ge 0.000000000 0.000000000 -0.591461579 H 0.000000000 0.000000000 0.954077464 Bi 0.000000000 0.000000000 -2.998718084	TS *E* = -2289.70603599 Bi 0.313023155 0.020244388 0.000000000 Ge -1.089380168 -2.079041430 0.000000000 H 0.292182976 -2.887519332 0.000000000	*bent*-HBiGe *E* = -2289.72480970 Bi -1.103657441 0.029899369 0.000000000 Ge 1.441581948 0.003351254 0.000000000 H 0.249175536 -1.383248725 0.000000000	*lin*-HBiGe *E* = -2289.69112284 Bi 0.000000000 0.000000000 2.152212166 Ge 0.000000000 0.000000000 -0.288745269 H 0.000000000 0.000000000 3.921218540
1 230.02 in plane bending 2 230.02 out of plane bending 3 285.07 (E-Bi) stretching 4 2095.64 (H-E) stretching	1 547.97 Imaginary frequency	1 246.50 (Bi-E) stretching 2 942.03 H wagging from Bi to E 3 1368.61 H wagging toward theBi-E bond	1 -148.17 Imaginary frequency 2 -148.17 Imaginary frequency 3 260.75 (Bi-E) stretching 4 1797.14 (H-Bi) stretching
lin-HSnBi *E* = -2289.72301577 Sn 0.000000000 0.000000000 0.290083243 H 0.000000000 0.000000000 2.007938847 Bi 0.000000000 0.000000000 -2.294273090	TS *E* = -427.69090277 Bi 0.371956863 0.155224618 0.000000000 Sn -1.117842266 -2.126394150 0.000000000 H 0.410716378 -3.038551846 0.000000000	*bent*-HBiSn *E* = -427.72094463 Bi -1.216962178 0.025851957 0.000000000 Sn 1.512889271 0.013309460 0.000000000 H 0.014298931 -1.450955524 0.000000000	*lin*-HBiSn *E* = -427.69085892 Bi 0.000000000 0.000000000 -0.284904664 Sn 0.000000000 0.000000000 2.342092138 H 0.000000000 0.000000000 -2.057187474
1 230.02 in plane bending 2 230.02 out of plane bending 3 285.07 (E-Bi) stretching 4 2095.64 (H-E) stretching	1 460.83 Imaginary frequency	1 190.98 (Bi-E) stretching 2 755.51 H wagging from Bi to E 3 1407.38 H wagging toward Bi	1 -187.78 Imaginary frequency 2 -187.78 Imaginary frequency 3 198.45 (Bi-E) stretching 4 1797.70 (H-Bi) stretching
lin-HPbBi *E* = -406.17037894 Pb 0.000000000 0.000000000 0.287518219 H 0.000000000 0.000000000 2.063934814 Bi 0.000000000 0.000000000 -2.351453033	TS *E* = -406.15837349 Bi 0.228640885 0.268724111 0.000000000 Pb -1.297325875 -2.086402962 0.000000000 H 0.082598915 -3.311106537 0.000000000	*bent*-HBiPb *E* = -406.19952963 Bi -1.339599309 0.023402508 0.000000000 Pb 1.469686833 0.025459016 0.000000000 H -0.204805529 -1.499609633 0.000000000	*lin*-HBiPb *E* = -406.17228448 Bi 0.000000000 0.000000000 1.339828782 Pb 0.000000000 0.000000000 -1.366427567 H 0.000000000 0.000000000 3.115389354
1 217.34 in plane bending 2 217.34 out of plane bending 3 182.66 (E-Bi) stretching 4 1746.82 (H-E) stretching	1 323.84 Imaginary frequency	1 155.45 (Bi-E) stretching 2 612.92 H wagging from Bi to E 3 1465.15 H wagging toward Bi	1 -183.27 Imaginary frequency 2 -183.27 Imaginary frequency 3 161.20 (Bi-E) stretching 4 1802.04 (H-Bi) stretching

Compounds with triple bond to sulfur

Coordinates (in Å) of the optimized geometries at the CCSD(T)/TZVPP level of theory, total energies (*E*) in a.u.

cis-HCSF *E* = -536.01758245 C 1.470047466 0.101465306 0.000000000 H 2.144432314 -0.738765507 0.000000000 S -0.006489169 0.448708351 0.000000000 F -1.177334426 -0.780784223 0.000000000	*lin*-HCSF *E* = -535.97251611 C 0.000000000 0.000000000 1.687617130 H 0.000000000 0.000000000 2.768164000 S 0.000000000 0.000000000 0.167115150 F 0.000000000 0.000000000 -1.715977280
trans-HCSH *E* = -436.85811802 C 0.008896821 1.174356095 0.000000000 H 1.092062898 1.400679123 0.000000000 S 0.006505042 -0.486161262 0.000000000 H -1.321893777 -0.720987852 0.000000000	*cis*-HCSH *E* = -436.85538735 C 0.097686762 1.160012130 0.000000000 H -0.931178748 1.544325310 0.000000000 S 0.094486888 -0.482193683 0.000000000 H -1.195607048 -0.940523660 0.000000000
lin-HCSH *E* = -436.70812195 C 0.000000000 0.000000000 -1.155211530 H 0.000000000 0.000000000 -2.259622960 S 0.000000000 0.000000000 0.415936403 H 0.000000000 0.000000000 2.314933936	*cis,cis*-HCSOH *E* = -512.00265416 S -0.117814342 0.410713333 0.000000000 C -1.378887398 -0.478458688 0.000000000 H -1.502380058 -1.554986595 0.000000000 O 1.456414571 -0.243571729 0.000000000 H 1.385436216 -1.206926554 0.000000000
trans-HSiSF *E* = -787.07842796 Si -0.908142710 -1.073881077 0.000000000 H -2.057341388 -0.061421357 0.000000000 S 0.050417675 0.758747483 0.000000000 F 1.660219329 0.464896958 0.000000000	*cis*-HSiSF *E* = -787.07231015 Si -1.065453126 -1.043361080 0.000000000 H 0.192720805 -1.880874927 0.000000000 S 0.002992702 0.749322034 0.000000000 F 1.611584674 0.466764844 0.000000000
lin-HSiSF *E* = -787.00621481 Si 0.000000000 0.000000000 -1.644869812 H 0.000000000 0.000000000 -3.180462540 S 0.000000000 0.000000000 0.413453618 F 0.000000000 0.000000000 2.170339564	*trans*-HSiSH *E* = -687.96534960 Si -0.002559384 1.121834583 0.000000000 H -1.520582431 1.119149030 0.000000000 S 0.011697269 -1.005680535 0.000000000 H 1.344064532 -1.154999071 0.000000000
cis-HSiSH *E* = -687.96133208 Si 0.074885996 1.133249062 0.000000000 H -1.437274562 1.255699336 0.000000000 S 0.088794821 -1.006747930 0.000000000 H -1.226361444 -1.258578460 0.000000000	*lin*-HSiSH *E* = -687.84374098 Si 0.000000000 0.000000000 -1.241591303 H 0.000000000 0.000000000 -2.828421263 S 0.000000000 0.000000000 1.105082188 H 0.000000000 0.000000000 2.489473342

NSF E = -552.08426324 N 1.398062503 0.090815278 0.000000000 S -0.012176748 0.430368175 0.000000000 F -1.070996731 -0.837405477 0.000000000	*lin*-NSF E = -552.03095623 N 0.000000000 0.000000000 1.648091064 S 0.000000000 0.000000000 0.189523527 F 0.000000000 0.000000000 -1.624484575
NSH (Singlet) E = -452.89889511 N 0.046246425 1.076407405 0.000000000 S 0.045657260 -0.426635763 0.000000000 H -1.279674775 -0.909404662 0.000000000	NSH (Triplet) E = -452.88757557 N -0.032229501 1.097840296 0.000000000 S 0.082808446 -0.544993937 0.000000000 H -1.238350034 -0.812479379 0.000000000
cis-NSOH E = -528.07484892 N -0.036428124 0.037641671 0.000000000 S -1.439175476 -0.373854021 0.000000000 O -2.580858646 0.835635451 0.000000000 H -2.111681221 1.684993064 0.000000000	*trans*-NSOH E = -528.06919983 N 1.411166952 0.137916008 0.000000000 S -0.016950742 0.434443350 0.000000000 O -0.996992386 -0.926519001 0.000000000 H -1.912990939 -0.613187430 0.000000000
PSF E = -838.33262509 P -1.012051618 -0.920633454 0.000000000 S 0.016953136 0.649563077 0.000000000 F 1.686558534 0.389308386 0.000000000	*lin*-PSF E = -838.27536353 P 0.000000000 0.000000000 -1.610047340 S 0.000000000 0.000000000 0.280003788 F 0.000000000 0.000000000 2.210524619
PSH E = -739.17881152 P 0.026118645 1.051350795 0.000000000 S 0.038608809 -0.929637120 0.000000000 H -1.267420545 -1.312363764 0.000000000	PSH (Triplet) E = -739.18873631 P 0.032543074 1.111486931 0.000000000 S 0.039855944 -0.986091071 0.000000000 H -1.293777111 -1.133124936 0.000000000
cis-PSOH E = -814.32460912 P -0.993250810 -0.932351309 0.000000000 S 0.021538676 0.676683409 0.000000000 O 1.693708383 0.469154822 0.000000000 H 1.844850945 -0.488903942 0.000000000	*trans*-PSOH E = -814.32048500 P -1.034605541 -0.921608479 0.000000000 S 0.020419261 0.650795512 0.000000000 O 1.694911131 0.311272827 0.000000000 H 2.130219361 1.175543232 0.000000000

Compounds with Triple Bond to Uranium, Thorium and Group 4 metals

Coordinates (in Å) of the optimized geometries at BP86/TZ2P+ level of theory, electronic state (S: singlet, D: doublet, T: triplet), symmetry, and bond energies (in a.u).

N≡UF_3 (S) (C_{3v} symmetry) E = -1.23506006	N≡UF_3 (S) (C_1 symmetry) E = -1.23529107
U 0.000000000 0.000000000 -2.335277000 F -1.694736000 0.000000000 -1.162130000 F 0.847368000 -1.467684000 -1.162130000 F 0.847368000 1.467684000 -1.162130000 N 0.000000000 0.000000000 -4.089265000	U 0.019564000 -0.034006000 -2.335553000 F -1.748067000 -0.010924000 -1.273241000 F 0.789834000 -1.372699000 -0.995764000 F 0.889873000 1.504601000 -1.272923000 N -0.239854000 0.413972000 -4.009287000
P≡UF_3 (S) (C_{3v} symmetry) E = -1.06321854	P≡UF_3 (S) (C_1 symmetry) E = -1.06394008
U 0.000000000 0.000000000 -2.318663000 F -1.755197000 0.000000000 -1.253697000 F 0.877598000 -1.520045000 -1.253697000 F 0.877598000 1.520045000 -1.253697000 P 0.000000000 0.000000000 -4.685272000	U 0.051029000 0.092324000 -2.322219000 F -1.836342000 -0.070703000 -1.548250000 F 0.929529000 -1.591588000 -1.559923000 F 0.681627000 1.227962000 -0.752556000 P -0.254068000 -0.443155000 -4.596831000
As≡UF_3 (S) (C_{3v} symmetry) E = -1.04179722	As≡UF_3 (S) (C_1 symmetry) E = -1.04287163
U 0.000000000 0.000000000 -2.309220000 F -1.770269000 0.000000000 -1.273643000 F 0.885135000 -1.533098000 -1.273643000 F 0.885135000 1.533098000 -1.273643000 As 0.000000000 0.000000000 -4.816881000	U 0.344121000 0.089804000 0.121037000 F 1.973292000 0.756868000 1.146981000 F 1.115084000 -1.784850000 -0.138092000 F 0.910259000 0.996328000 -1.620689000 As -2.107347000 -0.277309000 -0.229437000
HN=UF_3 (D) (C_{3v} symmetry) E = -1.3921067	HN=UF_3 (D) (C_s symmetry) E = -1.39149492
U 0.000000000 0.000000000 0.054727000 F 0.949330000 1.644288000 -0.773119000 F 0.949330000 -1.644288000 -0.773119000 F -1.898661000 0.000000000 -0.773119000 N 0.000000000 0.000000000 1.998561000 H 0.000000000 0.000000000 3.026627000	U 0.071464000 0.419398180 0.000000000 F 0.929297470 1.246632320 1.697055210 F 0.929297470 1.246632320 -1.697055210 F -1.858995490 1.124233520 0.000000000 N 0.017914180 -1.504558700 0.000000000 H -0.088977640 -2.532337640 0.000000000
HO–UF_3 (T) (C_{3v} symmetry) E = -1.38264919	HO–UF_3 (T) (C_s symmetry) E = -1.38424097
U 0.000000000 0.000000000 0.005021000 F 0.995588000 1.724410000 0.610022000 F -1.991177000 0.000000000 0.610022000 F 0.995588000 -1.724410000 0.610022000 O 0.000000000 0.000000000 -2.057792000 H 0.000000000 0.000000000 -3.025634000	U 0.046593000 0.520070000 0.000000000 F 0.908218000 1.277652000 1.736579000 F 0.908218000 1.277652000 -1.736579000 F -1.865090000 1.276340000 0.000000000 O -0.152083000 -1.555905000 0.000000000 H -0.411854000 -2.489478000 0.000000000
HC≡UF_3 (S) (C_{3v} symmetry) E = -1.30366671	HC≡CrF_3 (S) (C_{3v} symmetry) E = -1.24476777
U 0.000000000 0.000000000 -2.344993000 F -1.859046000 0.000000000 -1.429940000 F 0.929523000 -1.609981000 -1.429940000 F 0.929523000 1.609981000 -1.429940000 C 0.000000000 0.000000000 -4.292437000 H 0.000000000 0.000000000 -5.397786000	Cr 0.000000000 0.000000000 -2.080994000 F -1.668855000 0.000000000 -1.626695000 F 0.834427000 -1.445271000 -1.626695000 F 0.834427000 1.445271000 -1.626695000 C 0.000000000 0.000000000 -3.692134000 H 0.000000000 0.000000000 -4.786455000
HC≡MoF_3 (S) (C_{3v} symmetry) E = -1.31317319	HC≡WF_3 (S) (C_{3v} symmetry) E = -1.32754348
Mo 0.000000000 0.000000000 -2.162074000 F -1.810931000 0.000000000 -1.701098000 F 0.905465000 -1.568312000 -1.701098000 F 0.905465000 1.568312000 -1.701098000 C 0.000000000 0.000000000 -3.886537000 H 0.000000000 0.000000000 -4.978200000	W 0.000000000 0.000000000 -2.245092000 F -1.811558000 0.000000000 -1.769043000 F 0.905779000 -1.568855000 -1.769043000 F 0.905779000 1.568855000 -1.769043000 C 0.000000000 0.000000000 -3.990820000 H 0.000000000 0.000000000 -5.078428000

FC÷TiF_3 (T) (C_{3v} symmetry) E = -1.24956153 Ti 0.000000 0.000000 -2.114018 F -1.688160 0.000000 -1.566108 F 0.844080 -1.461989 -1.566108 F 0.844080 1.461989 -1.566108 C 0.000000 0.000000 -4.091697 F 0.000000 0.000000 -5.374867	FC÷ZrF_3 (T) (C_{3v} symmetry) E = -1.29126741 Zr 0.000000 0.000000 -2.121213 F -1.812943 0.000000 -1.496054 F 0.906472 -1.570055 -1.496054 F 0.906472 1.570055 -1.496054 C 0.000000 0.000000 -4.257902 F 0.000000 0.000000 -5.552128
FC÷HfF_3 (T) (C_{3v} symmetry) E = -1.29380079 Hf 0.000000 0.000000 -2.141642 F -1.796232 0.000000 -1.498649 F 0.898116 -1.555583 -1.498649 F 0.898116 1.555583 -1.498649 C 0.000000 0.000000 -4.253334 F 0.000000 0.000000 -5.547389	HC÷ThF_3 (T) (C_{3v} symmetry) E = -1.27943764 Th 0.000000 0.000000 -2.170206 F -2.014434 0.000000 -1.508418 F 1.007217 -1.744551 -1.508418 F 1.007217 1.744551 -1.508418 C 0.000000 0.000000 -4.584140 H 0.000000 0.000000 -5.684615
N÷TiF_3 (T) (C_{3v} symmetry) E = -1.06725921 Ti 0.000000 0.000000 -2.145663 F -1.696173 0.000000 -1.658968 F 0.848086 -1.468929 -1.658968 F 0.848086 1.468929 -1.658968 N 0.000000 0.000000 -4.114208	N÷ZrF_3 (T) (C_{3v} symmetry) E = -1.10630817 Zr 0.000000 0.000000 -2.157836 F -1.831248 0.000000 -1.606723 F 0.915624 -1.585907 -1.606723 F 0.915624 1.585907 -1.606723 N 0.000000 0.000000 -4.297867
N÷HfF_3 (T) (C_{3v} symmetry) E = -1.11005578 Hf 0.000000 0.000000 -2.156576 F -1.826543 0.000000 -1.621767 F 0.913272 -1.581833 -1.621767 F 0.913272 1.581833 -1.621767 N 0.000000 0.000000 -4.280078	N÷ThF_3 (T) (C_{3v} symmetry) E = -1.12016300 Th 0.000000000 0.000000000 -2.156328000 F -2.033788000 0.000000000 -1.565945000 F 1.016894000 -1.761312000 -1.565945000 F 1.016894000 1.761312000 -1.565945000 N 0.000000000 0.000000000 -4.531853000
P÷TiF_3 (T) (C_{3v} symmetry) E = -0.99889042 Ti 0.000000 0.000000 -2.008463 F -1.698426 0.000000 -1.523384 F 0.849213 -1.470880 -1.523384 F 0.849213 1.470880 -1.523384 P 0.000000 0.000000 -4.451344	P÷ZrF_3 (T) (C_{3v} symmetry) E = -1.03870469 Zr 0.000000 0.000000 -2.035045 F -1.829718 0.000000 -1.485449 F 0.914859 -1.584582 -1.485449 F 0.914859 1.584582 -1.485449 P 0.000000 0.000000 -4.652071
P÷HfF_3 (T) (C_{3v} symmetry) E = -1.04348737 Hf 0.000000 0.000000 -2.080426 F -1.821030 0.000000 -1.531278 F 0.910515 -1.577058 -1.531278 F 0.910515 1.577058 -1.531278 P 0.000000 0.000000 -4.673371	P÷ThF_3 (T) (C_{3v} symmetry) E = -1.05447466 Th 0.000000 0.000000 -2.067202 F -2.032326 0.000000 -1.499269 F 1.016163 -1.760046 -1.499269 F 1.016163 1.760046 -1.499269 P 0.000000 0.000000 -4.968651
As÷TiF_3 (T) (C_{3v} symmetry) E = -0.98829119 Ti 0.000000 0.000000 -1.830878 F -1.699122 0.000000 -1.345668 F 0.849561 -1.471483 -1.345668 F 0.849561 1.471483 -1.345668 As 0.000000 0.000000 -4.368881	As÷ZrF_3 (T) (C_{3v} symmetry) E = -1.0278549 Zr 0.000000 0.000000 -1.852655 F -1.826991 0.000000 -1.294655 F 0.913495 -1.582220 -1.294655 F 0.913495 1.582220 -1.294655 As 0.000000 0.000000 -4.567029
As÷HfF_3 (T) (C_{3v} symmetry) E = -1.03228831 Hf 0.000000 0.000000 -1.947749 F -1.818061 0.000000 -1.389464 F 0.909031 -1.574487 -1.389464 F 0.909031 1.574487 -1.389464 As 0.000000 0.000000 -4.638371	As÷ThF_3 (T) (C_{3v} symmetry) E = -1.04408282 Th 0.000000 0.000000 -1.918214 F -2.025423 0.000000 -1.330714 F 1.012711 -1.754068 -1.330714 F 1.012711 1.754068 -1.330714 As 0.000000 0.000000 -4.923553